Advanced damage modelling for seismic assessment of timber structures

Luis Fernando Sirumbal-Zapata
Department of Civil and Environmental Engineering
Imperial College London

A thesis submitted for
the degree of Doctor of Philosophy
and the Diploma of Imperial College London
October 2018

Declaration of Originality

I declare that this thesis is the result of my own work and every part of it has been written by myself. Throughout this thesis, references and citations are provided whenever published or unpublished work of others is referred, described, used or quoted.

Copyright Declaration

The copyright of this thesis rests with the author. Unless otherwise indicated, its contents are licensed under a Creative Commons Attribution-NonCommercial 4.0 International Licence (CC BY-NC).

Under this licence, you may copy and redistribute the material in any medium or format. You may also create and distribute modified versions of the work. This is on the condition that: you credit the author and do not use it, or any derivative works, for a commercial purpose.

When reusing or sharing this work, ensure you make the licence terms clear to others by naming the licence and linking to the licence text. Where a work has been adapted, you should indicate that the work has been changed and describe those changes.

Please seek permission from the copyright holder for uses of this work that are not included in this licence or permitted under UK Copyright Law.

Dedication

To Lorena, my love and adventures partner.

To my Parents and Brother, for their support and unconditional love.

Yo me interrogo ahora
¿por qué no he amado sólo
las rosas repentinas,
las mareas de junio,
las lunas sobre el mar?

¿Por qué he debido amar
la rosa y la justicia,
el mar y la justicia,
la justicia y la luz?

JUAN GONZALO ROSE, *Carta a Maria Teresa*

Acknowledgements

I want to thank my first supervisor, Dr. Christian Málaga-Chuquitaype, for his guidance and support throughout the four years I have been carrying out my doctoral research. Christian is passionate about research, and the highest quality aspects of this thesis are in part thanks to the high standards he demands for the work carried out within the "Emerging Structural Technologies" research group he leads. Moreover, he has always been close and friendly, and I will always remember the long conversations we used to have on Perú problems and opportunities, as well as on the unpredictable Peruvian politics. Finally, I also want to thank him for believing in me and for giving me the opportunity, I would probably not have had otherwise, of working with him in a prestigious academic institution like Imperial College London.

I want to thank my second supervisor, Prof. Ahmed Elghazouli, for his advice and logistic support. His great experience and wisdom were fundamental for the definition of the overall focus and scope of the thesis. I want to thank him for being friendly and for always being available for meetings and discussions.

I wish to thank the support from Peruvian Government through its CONCYTEC-CIENCIACTIVA Program, which provided the main funding for my PhD studies. I also want to than thank the important matching funds from the PhD Felllowship provided by the Department of Civil and Environmental Engineering at Imperial College London and from the Foundation of Universidad Nacional de Ingeniería (Patronato UNI) in Perú.

I am also very grateful to DIANA FEA company for collaborating with my research through a DIANA software license and technical support throughout the duration of my PhD studies. Among all the nice people of DIANA, I want to express my special gratitude for their selfless help and friendship to Maziar Partovi, Wijtze-Pieter Kikstra, Jonna Manie, Michel van Batenburg and Kesio Palacio.

I want to deeply thank Lorena, my wife, for accepting be my partner in this travel which four years later is now concluded. I know that she had to do a lot of sacrifices and struggled with the natural difficulties of starting a new life in a different country. Nevertheless, all this time she has been there to enjoy the experience and share the moments of profound happiness. She was also there for me during the difficult times, and her love and braveness helped me to overcome those situations.

I want to thank my mother, Cecilia, for her vast love and for always being mindful of how my life is going, and my father, Lucho, for his love and for encouraging me to undertake ambitious challenges since I was a child. I know he will be particularly happy and proud for this achievement.

I want to express my gratitude to my brother, Sebastián and my sister in law, Anthuanet, for hosting me at their home during the last month of thesis writing. Without their love and support, it would not have been possible to finish the writing of this thesis on time.

Finally, I want to thank life for giving me the opportunity to know many good friends during my temporary stay in London. I will keep all of them in my thoughts, and I hope to share moments with them again many times in the future. Among them, I would like to mention my friends at the Civil and Environmental Engineering Department: Miguel Bravo, Cagatay Demirci, Callum Munro, Boris Ochoa, Rodrigo Thiers, Leena Tahir Kibriya, Zhan Lyu, Chrissa Sfynia and Eleni Minga. I also want to thank Fionnuala Ni Dhonnabhain from the General Office for her kindness and help. I would also like to make a posthumous acknowledgement of Ron Millward's valuable help in the Structures Laboratory. I will remember his friendliness and his sense of humour. To conclude, I would like to mention my amazing London friends of life, beers and football: Dennis Vega, Jorge Lopez, Omar Velazquez, Ethel Cortegana and Miguel Gómez.

Abstract

This thesis deals with the response of timber structures undergoing large deformation levels. It is motivated by the current rise in popularity of timber structures in earthquake-prone regions and contributes to a better understanding of wood's behaviour both numerically and experimentally. Although a very good seismic performance during past earthquakes has been documented for low-rise timber buildings, the seismic reliability of mid to high-rise timber-only or hybrid timber-steel buildings has not been proved yet. For these reasons, laboratory tests and advanced numerical tools which allow an accurate prediction of the structural global nonlinear response of hybrid-timber steel connections under the action of cyclic loads are investigated throughout this thesis.

First, a detailed literature review on constitutive models for wood and other brittle materials, wood failure criteria, timber structures three-dimensional FE models, experimental studies on the cyclic behaviour of timber dowelled connections, and damage mechanics applied to the seismic performance assessment of structures, was performed . As a result the main objective of the thesis was defined to be the proposal of a material constitutive model capable of accurately simulating the nonlinear behaviour of wood under large deformation levels and load reversals until failure. The model's conceptual development, its mathematical formulation, numerical coding and implementation in a commercial FE software is documented in this thesis. Moroever, the proposed wood material model was developed within the framework of Continuous Damage Mechanics (CDM) theory, which makes it ideal for damage evolution modelling and for performance-based seismic assessment of timber dowelled structures. Experimental studies available in the literature were employed to evaluate the accuracy and the overall performance of the proposed constitutive model at the material and at the structural (or component) levels.

On the other hand, an experimental investigation of the cyclic behaviour of an hybrid timber beam-to-steel column moment connection was carried out. The hysteretic response of this connection was obtained with the objective of gaining further insight into

its load-carrying capacity, energy dissipation capability, failure modes, cyclic strength and stiffness degradation, among other characteristics. Moreover, some useful modelling techniques were presented for the elaboration of a 3D continuous model of timber dowelled connections, including the formulation and implementation of a timber-steel fastener interface contact model. Additional local responses not easily identified from the experiments, like internal potential cracking and crushing zones, damage extent or plastic deformations magnitudes, were obtained from the 3D continuous model.

Finally, a simplified component-based model for the type of timber beam-to-steel column connection previously investigated was developed. The precision of this simplified model, which is inspired in the full 3D model developed herein, was assessed by comparing the numerical and experimental results. The applicability of this simplified model to the seismic performance assessment of innovative hybrid timber-steel self-centring moment connections was also demonstrated through an illustrative case study.

The proposed novel plasticity-damage model captures for the first time the key features of wood cyclic nonlinear behaviour at the material and component levels, including: i) cyclic stiffness and strength degradation, ii) brittle local failure due to tensile and shear stresses, iii) ductile local failure due to compressive stress, iv) stiffness recovery after load reversal (crack opening and closing), and v) permanent plastic deformation due to compressive stress. Overall, the ability of the proposed finite element model, including both continuous plasticity-damage and contact modelling, to simulate the behaviour of complex timber beam-to-steel column connections for different levels of deformation is demonstrated. The proposed plasticity-damage constitutive model for wood under cyclic loads relies on an efficient and reliable algorithm which is implemented in a widely-used FE software and opens the door for realistic simulations. Therefore, this thesis represents a fundamental step towards a faithful estimation of the ultimate capacity of timber structures subjected to extreme loads such as earthquakes and, as a consequence, a more reliable assessment of their performance.

Contents

Declaration of Originality **3**

Copyright Declaration **5**

Dedication **7**

Acknowledgements **9**

Abstract **11**

Table of Contents **13**

List of Tables **17**

List of Figures **19**

Notations **27**

1 Introduction **33**

1.1 Motivation 33

1.2 Objectives 34

1.3 Research description 35

1.4 Thesis organization 37

2 Literature Review **38**

2.1 Introduction 38

2.2 Seismic assessment and damage mechanics 38

2.2.1 Performance-based seismic design 39

2.2.2 Damage mechanics applied to PBSD 42

2.3 Wood constitutive models 44

2.4 Wood failure criteria 50

2.4.1 Hill failure criterion 56

2.4.2 Hoffman failure criterion . . . 57
2.4.3 Tsai-Wu failure criterion . . . 58
2.5 Three-dimensional finite element modelling of timber dowelled connections 61
2.6 Experimental studies of timber dowelled connections . . . 69
2.6.1 Embedding tests . . . 69
2.6.2 Timber dowelled connections subjected to monotonic and cyclic loads 70
2.7 Concluding remarks . . . 75

3 Plasticity-Damage Timber Material Model 79
3.1 Introduction . . . 79
3.2 Orthotropic linear-elastic behaviour of timber . . . 81
3.3 Orthotropic damage model . . . 83
3.3.1 Spectral decomposition of the effective tensor . . . 85
3.3.2 Tensile and compressive damage criteria functions . . . 86
3.3.3 Tensile and compressive damage evolution laws . . . 87
3.3.4 Damage constitutive equations . . . 91
3.4 Orthotropic plasticity model . . . 93
3.4.1 General orthotropic yield function . . . 94
3.4.2 Plastic flow rule and strain-hardening law . . . 96
3.4.3 Hardening modulus . . . 97
3.4.4 Integration of the stress-strain rate equation . . . 98
3.5 Computational implementation . . . 100
3.5.1 Numerical considerations for plasticity and damage coupling under load reversals . . . 100
3.5.2 Algorithm design . . . 103
3.5.3 Consistent plasticity-damage tangent stiffness matrix . . . 106
3.6 Energy dissipation for tensile brittle failure . . . 110
3.7 Thermodynamic consistency verification . . . 113
3.8 Wood constitutive model: Stress-strain response . . . 115
3.8.1 Uniaxial monotonic response . . . 117
3.8.2 Uniaxial cyclic response . . . 128
3.8.3 Multiaxial monotonic response . . . 131
3.9 Concluding remarks . . . 139

4 Timber Material Model Validation 143
4.1 Introduction . . . 143

4.2 Timber brace-steel plate connection subjected to axial monotonic and cyclic loads . . . 144
4.2.1 Finite element model . . . 144
4.2.2 Material model parameters selection . . . 148
4.2.3 Monotonic loading . . . 149
4.2.4 Cyclic loading . . . 149
4.2.5 Mesh-dependency analysis . . . 151
4.3 Timber beam-steel plate connection subjected to monotonic loading perpendicular to the grain . . . 154
4.3.1 Finite element model . . . 157
4.3.2 Analysis of results . . . 160
4.4 Concluding remarks . . . 168

5 Experimental Cyclic Response of Timber-Steel Joints 170
5.1 Introduction . . . 170
5.2 Experimental set-up and test specimens . . . 172
5.2.1 Test set-up . . . 172
5.2.2 Test specimens . . . 176
5.2.3 Cyclic loading protocol . . . 177
5.2.4 Material characterization . . . 177
5.3 Observations and analysis of experimental results . . . 178
5.3.1 Moment-rotation hysteretic response . . . 178
5.3.2 Failure modes . . . 184
5.3.3 Strength deterioration . . . 187
5.3.4 Ductility and stiffness degradation . . . 192
5.3.5 Energy dissipation capacity . . . 194
5.4 Concluding remarks . . . 196

6 Numerical Modelling of Timber-Steel Joints 199
6.1 Introduction . . . 199
6.2 Timber-steel interface contact model . . . 200
6.2.1 Interface contact model in the normal direction . . . 202
6.2.2 Interface friction model in the tangential direction . . . 204
6.2.3 Tangent stiffness matrix . . . 205
6.3 Finite element modelling of timber-steel dowelled connection . . . 208
6.3.1 Finite element model description . . . 208
6.3.2 Material models and input parameters selection . . . 217

6.4 Calibration procedure using embedment tests . . . 224
6.4.1 Embedment tests . . . 226
6.4.2 Calibration methodology . . . 226
6.5 Analysis of numerical results and comparison against experimental data . 246
6.5.1 Monotonic loading . . . 247
6.5.2 Cyclic loading . . . 257
6.6 Concluding remarks . . . 273

7 Simplified Component-Based Model 279
7.1 Introduction . . . 279
7.2 Description of the component based model . . . 281
7.2.1 General aspects . . . 281
7.2.2 Detailed description . . . 284
7.3 Model validation . . . 292
7.3.1 Influence of "Shell 2" thickness magnitude and timber material nonlinear behaviour . . . 292
7.3.2 Cyclic response . . . 295
7.4 Case study: Post-tensioned timber beam-to-steel column joint . . . 296
7.4.1 Model description . . . 302
7.4.2 Post-tensioning force . . . 303
7.4.3 Monotonic response . . . 305
7.4.4 Cyclic response . . . 308
7.5 Concluding remarks . . . 309

8 Conclusions 312
8.1 General conclusions . . . 312
8.2 Specific findings . . . 315
8.2.1 Performance of the wood constitutive model at the material point level . . . 315
8.2.2 Plasticity-damage model . . . 316
8.2.3 Contact interface model . . . 317
8.2.4 Experimental response of timber beam-to-steel column connections 317
8.2.5 Simplified component-based model . . . 318
8.3 Suggestions for future work . . . 319

Bibliography 321

Appendix A Derivatives of the Jacobian matrix of the plasticity algorithm 341

List of Tables

3.1 Plasticity-damage timber constitutive model algorithm 104
3.2 Plasticity-damage material model input parameters for timber 118

4.1 Mesh sensitivity analysis case studies of Specimen S19 153
4.2 Geometric dimensions (in mm) of the multi dowel timber-steel connection specimen shown in Fig. 4.8 [185] 156
4.3 Steel-timber interface elements input parameters 159
4.4 Plasticity-damage material model input parameters for the timber beam 160
4.5 Plasticity material model input parameters for steel elements 161
4.6 Experimental and numerical load-deformation curve parameters 163

5.1 Test specimens 176
5.2 Average values of the mechanical properties of the glulam GL28h beam in [MPa]. Adapted from Karagiannis [87]. 179
5.3 In-cycle strength loss variation due to local failure 191
5.4 Connection properties from the stabilized envelope curves 193

6.1 Timber-steel interface contact model algorithm in the normal direction . 209
6.2 Timber-steel interface friction model algorithm in the tangential direction 210
6.3 Timber beam plasticity-damage constitutive model input parameters values 220
6.4 Steel plasticity model input parameters values 221
6.5 Timber-steel interface model input parameters values 223
6.6 Steel-steel interface models input parameters values 224
6.7 Calibration parameters values 247

7.1 Case studies: Post-tensioned timber beam-to-steel column joint 305

List of Figures

2.1 Experimental compressive and tensile stress-strain relationships of Scandinavian Spruce [85]. . . . 46
2.2 Experimental shear stress-strain relationships of Scandinavian Spruce [85]. 46
2.3 Interface contact model in the normal direction (Figure taken from Dorn [38]). . . . 62
2.4 Timber-concrete joint shear test specimen (Figure taken from Dias et al. [36]). . . . 63
2.5 Double-shear single-dowel timber connection finite element model (Figure taken from Santos et al. [145]). . . . 64
2.6 Single-dowel T-joint (double-shear) timber connection specimen (Figure taken from Dos Santos et al. [39]). . . . 65
2.7 Timber column-to-steel beam dowelled connection finite element model (Figure taken from Xu et al. [189]). . . . 66
2.8 Composite timber beam-to-concrete slab notched connection (Figure taken from Bedon and Fragiacomo [7]). . . . 67
2.9 Steel-timber composite connection finite element model (Figure taken from Hassanieh et al. [68]). . . . 69
2.10 Embedding methods of testing: European (left) and American (right) (Figure taken from Zhou and Guan [193]). . . . 70
2.11 Cyclic loading test setup of single timber dowelled connection (Figure taken from Yang [190]). . . . 71
2.12 Dowelled PSL timber-steel connection specimens subjected to cyclic loading (Figure taken from Frenette [54]). . . . 72
2.13 Dowelled PSL timber-steel connection specimens subjected to monotonic and cyclic loading (Figure taken from Schreyer [153]). . . . 72
2.14 Dowelled glulam-steel connection specimens subjected to monotonic load: Parallel to the grain (top) and perpendicular to the grain (left) (Figure taken from Gattesco and Toffolo [57]). . . . 73

2.15 Single dowelled glulam-steel symmetric connection specimens subjected to cyclic service load in the directions parallel and perpendicular to the grain (Figure taken from Reynolds [138]). 74
2.16 Cyclic loading test setup of glulam braces-steel side plates dowelled connection (Figure taken from Popovski et al. [136]). 75
2.17 Cyclic loading test setup of a glulam beam-to-column moment resistant dowelled connection (Figure taken from Lam et al. [100]). 76
2.18 Specimen geometric details of the beam-to-column moment resistant dowelled glulam connection (Figure taken from Wang et al. [180]). 76

3.1 Main characteristics of timber nonlinear inelastic behaviour. 80
3.2 Damage evolution law for tensile softening. 89
3.3 Damage evolution law for compressive hardening. 92
3.4 Initial compressive and tensile Hill's damage surface and initial Hoffman's plasticity yield surface. 102
3.5 Key components of the plasticity-damage timber constitutive model. . . 103
3.6 Finite element models of the timber cubic specimen of 10 mm per side (symmetry with respect to the plane XY). 116
3.7 Plasticity-damage model. Monotonic stress-strain response in the direction parallel to the grain. 119
3.8 Plasticity-damage model. Monotonic stress-strain response in the direction perpendicular to the grain. 120
3.9 Influence of the exponential softening constant, n, on the tensile monotonic stress-strain response. 121
3.10 Influence of the hardening constant, β, on the compressive monotonic stress-strain response. 123
3.11 Influence of the hardening power, m, on the compressive monotonic stress-strain response. 124
3.12 Influence of the plasticity hardening modulus, h, on the compressive monotonic stress-strain response. 125
3.13 Strain localisation under uniaxial compressive loading at 45° with respect to the grain alignment. 126
3.14 Mesh-dependency due to strain localisation. Tensile monotonic stress-strain response at 45° with respect to the grain alignment ($G_f = 0.1$). . . 127
3.15 Mesh-dependency due to strain localisation. Compressive monotonic stress-strain response at 45° with respect to the grain alignment ($G_f = 0.1$). . . 128

3.16 Influence of loading angle on the tensile monotonic stress-strain response ($G_f = 0.01$). 129
3.17 Influence of loading angle on the compressive monotonic stress-strain response ($G_f = 0.01$). 130
3.18 Uniaxial reversed cyclic stress-strain response in the direction parallel to the grain. 132
3.19 Uniaxial reversed cyclic stress-strain response in the direction perpendicular to the grain. 132
3.20 Uniaxial reversed cyclic stress-strain response in the direction 45° with respect to the grain. 133
3.21 Stress-strain response under bi-axial compression. 134
3.22 Stress-strain response under bi-axial tension. 135
3.23 Biaxial mixed compression parallel to the grain-tension perpendicular to the grain. 136
3.24 Biaxial mixed tension parallel to the grain-compression perpendicular to the grain. 137
3.25 Triaxial compression: Loading applied in the direction parallel to the grain (X-axis). 138
3.26 Triaxial compression: Loading applied in the direction perpendicular to the grain (Y-axis). 139

4.1 Cyclic loading protocol [136]. 145
4.2 Timber-steel dowelled connection finite element model of Specimen S19. . 146
4.3 Timber-steel dowelled connection finite element model of Specimen S12. . 147
4.4 Timber-steel dowelled connection subjected to monotonic tension loading. Comparison of experimental [135] and numerical results. 150
4.5 Timber-steel dowelled connection subjected to cyclic loading. Comparison of experimental [135] and numerical results. 152
4.6 Specimen S19: Mesh sensitivity analysis. 155
4.7 Specimen S19: Very fine mesh of the timber zone around the dowel. . . . 155
4.8 Configuration and geometric characteristics of the timber-steel connection loaded in the direction perpendicular to the grain (Figure taken from Xu et al. [185]). 156
4.9 Multi dowel timber-steel connection FE model, boundary conditions (green arrows) and displacement load (red arrows). 157
4.10 Timber-steel interface elements: Dowel-beam and dowel-plate (left side); beam-plate (right side). 158

4.11 Multi dowel timber-steel connection loaded in the direction perpendicular to the grain. Comparison of experimental [185] and numerical results. . . 162
4.12 Plasticity-damage model: Influence of the fracture energy density parameter on the numerical load-deformation curve. 164
4.13 Contour of the timber-to-steel connection vertical displacement. 165
4.14 Plastic strains in the directions parallel (ε_{pX}) and perpendicular (ε_{pZ}) to the grain. 166
4.15 Compressive (ω^-) and tensile (ω^+) damage variables. 167

5.1 Schematic representation of specimens and set-up. 173
5.2 Experimental set-up. 174
5.3 Test specimen and set-up. 174
5.4 Geometry of the hybrid beam-to-column connection components. 175
5.5 Cyclic loading protocol. 178
5.6 Experimental moment-rotation hysteretic responses. 181
5.7 First cycle moment-rotation hysteresis loops. 182
5.8 Third cycle moment-rotation hysteresis loops. 183
5.9 Hybrid timber-steel moment connection specimens during testing. 185
5.10 Local failure in specimen S1-12D-12A. 186
5.11 Local failure modes in specimen S2-12D-15A. 188
5.12 Local failure modes in specimen S3-16D-15A. 189
5.13 Backbone envelope curves of specimens S1-12D-12A, S2-12D-15A and S3-16D-15A. 190
5.14 Stabilized envelope curves of specimens S1-12D-12A, S2-12D-15A and S3-16D-15A. 192
5.15 Cumulative energy dissipation of specimens S1-12D-12A, S2-12D-15A and S3-16D-15A. 195
5.16 Cyclic energy dissipation of specimens S1-12D-12A, S2-12D-15A and S3-16D-15A. 196

6.1 Two-dimensional interface element for timber-steel contact modelling (Figure taken from DIANA User's manual [35]). 202
6.2 Timber-steel contact hysteretic model in the normal direction to the interface plane. 202
6.3 Timber-steel friction nonlinear model in the direction tangential to the interface plane. 205
6.4 FE model 3D view of the timber beam-to-steel column dowelled connection (Specimen S3-16D-15A). 212

6.5 Steel components of the FE model (Specimen S3-16D-15A). 213
6.6 Interface elements (Specimen S3-16D-15A). 214
6.7 Bolts interface elements (Specimen S3-16D-15A). 215
6.8 Guidelines for the definition of the dowelled connection zone mesh geometry in terms of the bolt radius length. 216
6.9 Finite element mesh geometry of the steel dowel and the timber beam. . 216
6.10 Embedment test experimental set-up for 12 mm bolt diameter specimens: parallel (left) and perpendicular (right) to the grain (Figure taken from Karagiannis et al. [85]). 227
6.11 Experimental embedment curves for 12 mm and 16 mm bolt diameter specimens (Figures taken from Karagiannis et al. [85]). 228
6.12 FE models of the 12 mm bolt diameter embedment test specimens. . . . 229
6.13 Calibration of k_C based on the experimental embedment curves [85] in the direction parallel to the grain. 232
6.14 Calibration of k_C based on the experimental embedment curves [85] in the direction perpendicular to the grain. 233
6.15 Calibration of β based on the experimental embedment curves [85] in the direction parallel to the grain. 235
6.16 Calibration of β based on the experimental embedment curves [85] in the direction perpendicular to the grain. 236
6.17 Calibration of h based on the experimental embedment curves [85] in the direction parallel to the grain. 239
6.18 Calibration of h based on the experimental embedment curves [85] in the direction perpendicular to the grain. 240
6.19 Calibration of k_{UL} based on the experimental embedment curves [85] in the direction parallel to the grain. 242
6.20 Calibration of k_{UL} based on the experimental embedment curves [85] in the direction perpendicular to the grain. 243
6.21 Calibration of k_S based on the experimental embedment curves [85] in the direction parallel to the grain. 244
6.22 Calibration of k_S based on the experimental embedment curves [85] in the direction perpendicular to the grain. 245
6.23 Numerical calibrated against experimental [85] embedment curves. 246
6.24 Comparison between numerical and experimental monotonic [87] and cyclic stabilized envelope curves. 249
6.25 Timber beam lateral face tensile damage contour plot under monotonic load. 251

6.26 Timber beam lateral face compressive damage contour plot under monotonic load. . . . 252
6.27 Timber beam lateral face compressive plastic strain in the vertical direction (perpendicular to the grain) contour plot under monotonic load. . . . 254
6.28 Timber beam top face tensile damage contour plot under monotonic load. 255
6.29 Timber beam top face compressive damage contour plot under monotonic load. . . . 255
6.30 Timber beam top face plastic strain in the longitudinal (parallel to the grain) contour plot under monotonic load. . . . 256
6.31 Steel long bolt principal tensile plastic strain contour plot under monotonic load. . . . 258
6.32 Top steel angle principal tensile plastic strain contour plot under monotonic load. . . . 259
6.33 Comparison between numerical and experimental hysteretic curves. . . . 261
6.34 Timber beam lateral face tensile damage contour plot corresponding to a cyclic joint rotation amplitude of 54 mrad. . . . 263
6.35 Timber beam lateral face compressive damage contour plot corresponding to a cyclic joint rotation amplitude of 54 mrad. . . . 264
6.36 Tensile damage contour plot in timber beam top and bottom faces for a joint rotation cyclic amplitude of 40 mrad. . . . 265
6.37 Tensile damage contour plot in timber beam top and bottom faces for a joint rotation cyclic amplitude of 54 mrad. . . . 266
6.38 Compressive damage contour plot in timber beam top and bottom faces for a joint rotation cyclic amplitude of 40 mrad. . . . 267
6.39 Compressive damage contour plot in timber beam top and bottom faces for a joint rotation cyclic amplitude of 54 mrad. . . . 268
6.40 Comparison between DIC and FE vertical strain contour plots in specimen S3-16D-15A for a joint rotation amplitude of 40 mrad. . . . 270
6.41 Comparison between DIC and FE vertical strain contour plots in specimen S3-16D-15A for a joint rotation amplitude of 54 mrad. . . . 272
6.42 Numerical prediction of crack locations in specimen S3-16D-15A. . . . 274

7.1 Class-III Timoshenko beam element (Figure taken from DIANA User's manual [35]). . . . 282
7.2 Quadrilateral isoparametric shell element (Figure taken from DIANA User's manual [35]). . . . 283

7.3 General view of the component-based model proposed for timber beam-to-steel column dowelled connections. 285
7.4 Detailed view of the complete set of elements that make up the component-based model proposed for timber beam-to-steel column dowelled connections. 286
7.5 Tyings and constraints of the component-based model proposed for timber beam-to-steel column dowelled connections. 291
7.6 Specimen S1 monotonic curves: component-based model predictions compared against experimental test and 3D continuous model estimations. . 293
7.7 Specimen S2 monotonic curves: component-based model predictions compared against experimental test and 3D continuous model estimations. . 293
7.8 Specimen S3 monotonic curves: component-based model predictions compared against experimental test and 3D continuous model estimations. . 294
7.9 Specimen S1 hysteretic curves: component-based model compared against experimental test. 296
7.10 Specimen S2 hysteretic curves: component-based model compared against experimental test. 297
7.11 Specimen S3 hysteretic curves: component-based model compared against experimental test. 297
7.12 Cable element used for modelling the post-tensioned steel bar (Figure taken from DIANA User's manual [35]). 303
7.13 Lateral view of the component-based model including the post-tensioned steel bars. 304
7.14 Moment-rotation monotonic curves of specimen S1 with post-tensioning. 306
7.15 Moment-rotation monotonic curves of specimen S2 with post-tensioning. 306
7.16 Moment-rotation monotonic curves of specimen S3 with post-tensioning. 307
7.17 Specimen S1 hysteretic curves with and without post-tensioning. 308

Notations

a_{ij}	Failure criterion stress coefficients
b	Constant parameter of the tensile damage evolution law
b_{ijkl}	Tsai-Wu criterion quadratic stress coefficients
$\boldsymbol{b}$	Unknown variables vector
c	Cohesion
C	Constant
$\boldsymbol{C}^e$	Fourth-order orthotropic linear-elastic compliance tensor
d	Bolt diameter
$\boldsymbol{D}^e$	Fourth-order orthotropic linear-elastic stiffness tensor
$\boldsymbol{D}^{ep}$	Consistent elasto-plastic tangent stiffness tensor
$\boldsymbol{D}^t$	Interface element tangent stiffness matrix
$\boldsymbol{D}$	Damage tensor
E	Elastic modulus
f_d^+	Tensile damage criterion function
f_p	Yield function

f_d^-	Compressive damage criterion function
f_i^+	Tensile strength in the direction "i"
f_i^-	Compressive strength in the direction "i"
f_{ij}^+	Shear strength in the plane "ij"
f_{biax}	Biaxial strength in the plane
f_{max}^+	Uniaxial tensile strength
f_{max}^-	Uniaxial compressive strength
F_pt	Post-tensioning force
g_d^+	Tensile damage evolution law
g_d^-	Compressive damage evolution law
G	Shear modulus
G_f	Fracture energy density
$\boldsymbol{H}^+$	Hill's criterion mapping matrix for tension
$\boldsymbol{H}^-$	Hill's criterion mapping matrix for compression
h	Plasticity hardening modulus
$\boldsymbol{I}$	Unitary fourth-order tensor
$\boldsymbol{J}$	Jacobian matrix
k	Plasticity hardening variable

k_C	Interface normal stiffness in compression
k_S	Interface shear stiffness
k_T	Interface normal stiffness in tension
k_{UL}	Interface unloading stiffness
l_{ch}	Characteristic length
m	Compressive hardening power
M	Total moment strength
M_pt	Post-tensioning moment strength provided
M_s	Energy dissipation devices moment strength
$\boldsymbol{M}$	Fourth order tensor operator
n	Calibration parameter of the tensile damage evolution law
$\boldsymbol{n}$	Tensor normal to the yield surface
p	Hydrostatic pressure
$\boldsymbol{p}_i$	Eigenvectors of the effective stress tensor
$\boldsymbol{P}$	Yield function mapping matrix
$\boldsymbol{q}$	Yield function mapping vector
$\boldsymbol{Q}^+$	Consistent tangent stiffness tensile fourth-order tensor operator
$\boldsymbol{Q}^-$	Consistent tangent stiffness compressive fourth-order tensor operator
$\boldsymbol{r}$	Residuals vector

r^+	Tensile threshold variable
r^-	Compressive threshold variable
$\boldsymbol{R}_{ij}$	Second-order symmetric tensor as a function of the effective stress eigen-vectors
t	Time
t_n	Interface normal stress
t_s	Interface shear stress
$\boldsymbol{t}$	Interface stress vector
$\boldsymbol{T}$	Plastic hardening evolution matrix
T	Plastic tangent modulus
α	Fraction of the initial slope of the exponential softening curve
α_i	Ratio of tangent plastic to elastic moduli in the "i" direction
α_{ij}^+	Hill's criterion mapping matrix coefficient for tension
α_{ij}^-	Hill's criterion mapping matrix coefficient for compression
β	Compressive hardening constant
$\Delta\boldsymbol{u}$	Interface relative displacement vector
$\Delta u_{n,G}$	Interface gap relative displacement
$\Delta u_{n,M}$	Interface maximum relative displacement

$\Delta u_{n,UL}$	Interface total unloading relative displacement
ϵ_{vol}	Volumetric strain
$\boldsymbol{\epsilon}$	Strain tensor
$\boldsymbol{\epsilon}^{e^-}$	Compressive component of the elastic strain tensor
$\boldsymbol{\epsilon}^-$	Compressive component of the strain tensor
$\boldsymbol{\epsilon}^+$	Tensile component of the strain tensor
$\boldsymbol{\epsilon}^p$	Plastic strain tensor
$\dot{\gamma}^{d+}$	Damage energy dissipation rate
$\dot{\gamma}^p$	Plasticity energy dissipation rate
$\dot{\lambda}$	Plastic multiplier
μ	Friction coefficient
ν	Poisson's ratio
ω	Scalar damage variable
ω^+	Tensile damage variable
ω^-	Compressive damage variable
Ψ	Free energy potential
Ψ_0^+	Tensile elastic free energy potential
Ψ_0^-	Compressive elastic free energy potential
$\boldsymbol{\sigma}$	Cauchy stress tensor

$\bar{\boldsymbol{\sigma}}$	Effective stress tensor
$\bar{\boldsymbol{\sigma}}^{+}$	Tensile effective stress tensor
$\bar{\boldsymbol{\sigma}}^{-}$	Compressive effective stress tensor
$\bar{\sigma}_y$	Reference yield stress
$\bar{\sigma}_i$	Eigenvalues of the effective stress tensor
σ^{+}	Uniaxial Cauchy tensile stress
σ^{-}	Uniaxial Cauchy compressive stress
τ_{max}	Maximum friction stress
$\bar{\tau}^{+}$	Tensile equivalent stress
$\bar{\tau}^{-}$	Compressive equivalent stress
χ_i	Coefficients of the yield function mapping matrix and vector
:	Double dot product operator
$\otimes$	Tensor product operator

Chapter 1

Introduction

This thesis deals with the response of timber structures undergoing large deformation levels. It is motivated by the current rise in popularity of timber structures in earthquake-prone regions and contributes to a better understanding of wood's behaviour both numerically and experimentally. This introductory chapter starts with a brief exposition of the background of the research and continues with a presentation of the main objectives of the thesis. This is followed with a description of the stages in which the research work was undertaken and the methodology that was followed to achieve its objectives. The chapter concludes with an outline of the thesis.

1.1 Motivation

The housing demand in densely-populated cities is continuously increasing all over the world. It is expected that the world population will be 9772 million people by the year 2050 [173], while 68% of them (6645 million people) will be living in cities [174]. Most of these mega-cities are located in earthquake-prone areas where significant levels of ground shaking are expected [9]. Therefore, the large-scale construction that is required to satisfy the basic human need for dwellings depends on the development and application of innovative structural systems, capable of withstanding the extreme actions of nature and minimize the associated environmental impact [165]. To this end, the use of wood, from well-managed forests, constitutes a cost-effective sustainable alternative. Some timber building projects have already been constructed [172, 64], while some other more ambitious proposals are expected to be built in the coming years [6].

Wood has numerous advantages including its ability to store a great amount of carbon

dioxide during its whole life cycle. From a structural point of view, it is a robust material with high-strength to weight ratio. In particular, modern engineered wood products like glued-laminated (Glulam) timber, cross-laminated timber (CLT) or laminated veneer lumber (LVL), increase wood's reliability and make it highly dependable in comparison with other more traditional and less sustainable materials like concrete. Furthermore, other attributes like fast construction processes and aesthetics also explain the current trend to use timber over other construction materials.

Although a very good seismic performance during past earthquakes has been documented for low-rise timber buildings [88, 52], the seismic reliability of mid to high-rise timber-only or hybrid (timber-steel or timber-concrete) buildings has not been proved yet. Moreover, there is a lack of analytical tools that can enable a faithful representation of timber's nonlinear response up to the large deformation levels. This imposes important limitations to the efficient design of connections and members and to a cost-effective and reliable implementation of performance-based seismic design.

The current philosophy of seismic design relies on the structure having ductile behaviour, hence energy dissipation is allowed through the generation of adequate yielding mechanisms. At the same time, the elevated repair and business downtime costs recently experienced in earthquake-stricken cities, like Christchurch [18], have stressed the need for new high-performance structures able to experience limited damage levels and minimal residual drifts. To achieve this aim, laboratory tests and advanced numerical tools which allow an accurate prediction of the structural global nonlinear response under the action of dynamic loads are required [191, 25]. Moreover, the current focus on the attainment of predefined damage states for given earthquake intensities, as required by state-of-the-art Performance-Based Seismic Design and Assessment (PBSDA) methodologies [112, 111, 150, 156, 33] demands high fidelity simulations and numerical tools underpinned by careful experimentation and analysis.

1.2 Objectives

The following objectives were defined for this thesis:

- To gain a fundamental understanding of the non-linear hysteretic behaviour of wood under cyclic loads, including its strength, ductility, energy dissipation, and cyclic degradation.

- To gain a sound understanding, underpinned by careful physical and numerical experimentation, of the response of timber-steel moment resistant ductile connections composed of glulam beams and wide-flange steel columns.

- To provide a sound mathematical formulation and computational implementation of a plasticity-damage constitutive material model especially suited for modelling the cyclic nonlinear behaviour of wood under seismic action.

- To propose suitable modelling techniques for the elaboration of 3D FE models of timber-steel dowelled connections including an adequate representation of the interface contact which describes the interaction between the steel fasteners and the surrounding wood.

- To provide a reliable and simple component based model which can be used as a tool for the performance based seismic design of timber dowelled structural systems.

1.3 Research description

This section describes the six stages in which the research work was carried out and explains the research methodology followed to achieve the objectives set out in the previous section. In the first stage, a comprehensive literature review of the current proposals for high-rise timber buildings was performed, involving conceptual and analytical studies. This stage also included the review of previous research on hybrid timber-steel structural systems. The literature review was also extended to other relevant topics like constitutive models for wood and other brittle materials, wood failure criteria, timber structures three-dimensional FE models, experimental studies on the cyclic behaviour of timber dowelled connections, and damage mechanics applied to the seismic performance assessment of structures.

The first stage allowed the identification of research gaps to be tackled by the thesis. Accordingly, one main objective of the thesis is to propose a material constitutive model capable of accurately simulating the nonlinear behaviour of wood under large deformation levels and load reversals until failure. The proposed wood material model is developed within the framework of Continuous Damage Mechanics (CDM) theory, which makes it ideal for damage evolution modelling and for performance-based seismic assessment of timber dowelled structures. The formulation and implementation of this constitutive

model is developed in the second stage of the research project.

The third stage is the validation of the proposed model. First, the model is validated at the material level, demonstrating its correct implementation, and enabling the understanding of the role played by the most important model parameters. The second level of validation is carried out at the structural or component level. To this end, a couple of experimental studies available in the literature are employed to evaluate the accuracy and the overall performance of the proposed constitutive model.

On the other hand, the fourth stage consisted in the experimental investigation of an hybrid timber beam-to-steel column moment connection subjected to cyclic loads. The hysteretic response of the connection is obtained and further insight is gained into its load-carrying capacity, energy dissipation capability, failure modes, cyclic strength and stiffness degradation, among other characteristics.

Then, in the fifth stage some useful modelling techniques are presented for the elaboration of a 3D continuous model of timber dowelled connections, including the formulation and implementation of a timber-steel fastener interface contact model. These techniques jointly with the previously proposed wood constitutive model are applied to simulate the response of the timber beam-to-steel column connection specimens previously tested. Therefore, the experimental results obtained from the tests are also employed in the further validation of the wood constitutive model and the timber-steel fastener interface contact model. Once the model is validated, additional local responses not easily identified from the experiments, like internal potential cracking and crushing zones, damage extent or plastic deformations magnitudes, are obtained and discussed.

Finally, the sixth and last stage is the proposal of a simplified component-based model for the type of timber beam-to-steel column connection previously investigated. The precision of this simplified model, which is inspired in the full 3D model developed herein, is assessed by comparing the numerical and experimental results. Finally, the applicability of such a model to the seismic performance assessment of innovative hybrid timber-steel self-centring moment connections is demonstrated through an illustrative case study.

1.4 Thesis organization

The thesis is organized in eight chapters and one appendix. This introductory Chapter 1 contains the motivation for carrying out the investigation and the objectives to be fulfilled. The findings from the literature review are presented in Chapter 2. Subsequently, the mathematical formulation, numerical implementation details and validation, at the material level, are presented in Chapter 3. The validation of the constitutive model at the component level follows in Chapter 4. The experimental investigation conducted on the cyclic response of the timber beam-to-steel moment joint is described next in Chapter 5. The modelling details of the moment connection specimen and the formulation of the timber-steel interface contact model are found in Chapter 6. Lastly, the characteristics of the proposed component-based simplified model and its application to the analysis of the cyclic response of self-centring post-tensioned timber-steel connections are presented in Chapter 7. The conclusions, limitation and further research work are drawn in Chapter 8. Appendix A contains analytical expressions for the calculation of the partial derivatives that are required for the internal calculation process corresponding to the constitutive model.

Chapter 2

Literature Review

2.1 Introduction

This chapter offers a general overview of past and current research related to the numerical modelling of wood as applied to the seismic assessment of timber buildings. The state-of-the-art Performance-Based Seismic Design and Assessment (PBSDA) framework that motivates the need for advanced modelling techniques, such as the ones developed in this thesis, is discussed first. This is followed by a review of wood constitutive models and their ability to capture the complex failure modes observed in timber. A summary of wood failure criteria models and their mathematical formulations is presented next. Subsequently, past numerical research on the ultimate response of timber joints are explored focusing on three-dimensional finite element simulations. Finally, experimental investigations on timber dowelled connections, that will inform the experimental studies performed on this thesis, are discussed. The chapter concludes with a summary section (Section 2.7) that highlights the research gaps identified and points towards the contributions made in later chapters of this thesis.

2.2 Seismic assessment and damage mechanics

The seismic performance of timber structures is governed by their nonlinear response at the connection zones, where high deformation levels and stress concentrations are developed around the fasteners (nails, dowels or bolts). These zones are susceptible to significant load-reversals during the service life of structures due to the occurrence of earthquakes events. For this reason, the seismic assessment of timber structures requires the implementation of structural models capable of simulating the nonlinear behaviour

of timber under large deformation levels and load reversals until failure [191].

Two modelling approaches are available to simulate the nonlinear response of structures subjected to earthquake loads: lumped hysteretic models and distributed continuous models. The theoretical foundations of lumped hysteretic models capable to represent degradation and pinching behaviour can be found in [160, 48, 49] and will not be discussed here due to their lack of applicability to the assessment of timber local failure and their need of extensive calibration for each particular case study to be analysed. Contrarily, a discussion on continuous distributed damage models that have been applied to the seismic performance assessment of structures is presented in Section 2.2.2. Although 3D models are important for the accurate prediction of structural response with damage assessment purposes [25], special attention will also be given to simpler fiber beam elements that can reduce the modelling and computational effort while keeping the multidimensional character of the stresses interactions at the material level.

The application of continuous damage mechanics constitutive models to the seismic analysis of structures is particularly relevant for structural design under the framework of performance-based earthquake engineering, where a precise evaluation of damage evolution at different demand levels is important. It will be shown in Section 2.2.2 that this is an active research field which has been substantially developed for other materials like reinforced concrete. Despite a few isolated efforts to define performance-based design guidelines for timber structures [70, 113, 156, 96], and the need for research on damage assessment of timber structures within a performance-based framework [112, 111, 150, 156], much work remains to be done on this field. In particular, there is a dearth of information regarding the application of damage mechanics to the seismic assessment of timber structures. In the next section, an overview of the performance-based seismic design (PBSD) principles is offered. This is followed by a revision of damage mechanics modelling as applied to PBSD.

2.2.1 Performance-based seismic design

Principles and origins of PBSD

Performance based seismic design (PBSD) is a methodological framework which aims to deliver structures that attain pre-defined performance levels for a given set of earthquake intensities [26, 182, 97]. As an overall description, PBSD first bridges the gaps between earthquake hazard and structural response, and then between structural response and

structural performance. Both links are quantitatively performed by means of intensity measure parameters and performance metrics, respectively [97]. The accuracy of such a quantitative assessment relies on the development and use of advanced numerical modelling techniques.

Seismic design approaches which linked the magnitude of the structure deformation to three qualitative performance categories (i.e. Immediate occupancy, Life safety and Collapse) were developed initially [46]. Due to the many sources of uncertainties involved in the prediction of the structural seismic response, the new design method needed to be implemented under a probabilistic framework. More realistic and reliable results were thus obtained, based on the quantification of the probability of exceeding different performance targets under various earthquake magnitudes. Accordingly, performance objectives have been defined as the maximum allowed exceedance probability for each performance level under a determined seismic intensity level [26, 182].

PBSD theoretical framework

Krawinkler and Deierlein [97] divide the theoretical framework of PBSD in four stages:

- Earthquake hazard:

  Given the characteristics and location of the structure, the description of the earthquake magnitude is obtained in the form of a probabilistic distribution of a random variable called Intensity Measure (IM). Different IM parameters can be employed for different purposes, however the spectral acceleration, corresponding to the structure fundamental period of vibration ($S_a(T_1)$), is one of the most common IM parameters. Several other intensity measures, including information relative to ground motion frequency content, duration and multiple period correlation, have been proposed and are currently under continuous investigation. Furthermore, the IM is the reference parameter for ground motion record scaling and earthquake spectral matching [182]. The mean annual frequency distribution of the IM is graphically represented by the seismic hazard curve, which is obtained from a Probabilistic Seismic Hazard Assessment (PSHA).

- Structural analysis:

  In this part the structural response generated by the ground motion input is determined. Then, the engineering demand parameters (EDP) selected from a set of

structural responses (e.g. inter-storey drift, storey displacement and acceleration) are post-processed using statistical methods in order to determine their probability distributions. For this reason, the availability of reliable and precise advanced analysis methods and tools is critical to the success of the whole seismic performance assessment. When the analysis goes beyond the onset of structural damage and gets closer to the collapse performance level, geometric nonlinearities considering large deformations and strains become more relevant. Due to its high computational costs, structural analysis for seismic performance including these types of geometric nonlinear behaviour is rare in practice. On the other hand, mild nonlinearities can be included in the analysis by means of standard concentrated or distributed constitutive models (e.g. cracking, plasticity). For frame structural systems, concentrated constitutive models can be assigned to moment-rotation plastic hinges only, while distributed models can be employed either in linear fibre elements or in 3D continuous models. These standard modelling techniques are generally helpful to predict realistically the early damage states of a structure only. Therefore, more advanced numerical models and methods, capable of predicting the structural response at high levels of deformation and damage up to or near collapse, are required in order to achieve a reliable assessment of the structural response for all the seismic performance levels.

- Damage assessment:

  The damage assessment allows the pairing of the engineering demand parameters (EDP), calculated from the structural analysis, with damage measure (DM) parameters. Likewise, the probability distribution of the DM parameters is used to calculate the exceedance probability of some pre-defined damage thresholds through the use of fragility functions. A fragility function can be defined either globally for the whole building, or locally for each different structural or non-structural building component (e.g. walls, beams, partitions, slabs) [121]. Moreover, the construction of fragility functions requires a systematized data base of DM and damage thresholds which scope and level of precision is continuously increasing with research. For this reason, every new experimental study or real seismic event gives important additional data to extend the library of fragility functions. This also means that using the PBSD framework ensures a uniform progress in the quantitative estimation of damage. Furthermore, cost functions are tools which permit the definition of a probability distribution of the repair cost associated with each damage threshold for a particular component. Therefore, the damage assessment output is not

restricted to a qualitative description of the damage level, but goes beyond this and provides a quantitative measure of the probability of exceeding a particular performance level, or the expected total costs incurred for a given seismic intensity.

- Performance calculation:

  Complementary to the damage assessment and consequent direct monetary losses calculation, the performance decision variables are intended to be defined in terms of the overall costs generated as a consequence of the earthquake occurrence, including those indirect costs associated to casualties, injuries and function recovery time. More research work is needed, however, to quantitatively determine the values of such decision variables relying on objective criteria framework instead of subjective experts judgement. Independently of the decision variables employed, the seismic performance can be expressed as a function of the intensity of ground motion, of a specific earthquake scenario, or return period of time.

2.2.2 Damage mechanics applied to PBSD

In lumped hysteretic models the inelastic and deterioration behaviour is governed by empirical relationships and is restricted to concentrated zones. Therefore, these type of models are not able to capture highly non-linear behaviour like the one generated by localized damage [32], and in order to obtain a more realistic simulation, consistent and experimentally validated continuous constitutive models are required [77, 96]. These continuous models establish a non-linear relationship between the stress and the strain corresponding to each material point within the model. Besides, they usually employ a set of parameters which are directly obtained from the mechanical properties of the material, and a second set of parameters which need to be obtained by means of a calibration process. For this reason, continuous models are complex and demand a great computational effort [32]. It is recognized, however, that, given the fast development of computational power resources and the increasing demand for a "more reliable interpretation of inelastic damage mechanisms" [77], constitutive models at the material point level will become the standard in the near future, and a definitely most robust approach to model material non-linear behaviour in performance-based seismic design applications. In this way, it will be possible to incorporate the fundamental role that localized damage plays in the structure damping effects, hysteretic energy dissipation and local failure modes, which eventually lead to global failure or collapse.

A great amount of constitutive models for different materials and with different levels of complexity, efficiency and applicability are available in the specialized literature. Each of these models was developed to include one or more physical mechanisms. In general, and depending on the specific material, there are four mechanisms which are fundamental for the study of the nonlinear response of structures subjected to dynamic loads like earthquakes [77]: 1) Plasticity; 2) Damage; 3) Viscosity (for rate sensitivity); and 4) hardening and softening post-failure response. In the following paragraphs a brief description of a selection of Continuous Damage Mechanics (CDM) models applied to the seismic performance assessment of structures will be presented.

Legeron et al. [105] studied the application of multi-layered elements and damage mechanics material models to the seismic behaviour modelling of concrete structures. The damage model employed was previously developed by La Borderie [98]. The applicability of this model was demonstrated by simulating the response of a real bridge pier under the action of an earthquake ground acceleration record. The authors explained that performance based seismic design requires the use of computational programs capable of executing numerical models comprised by advanced and efficient element types and material models. Besides, damage models provide quantitative and precise information about structural damage accumulation, which is fundamental for the successful application of performance-based seismic design philosophy. It was concluded that the modelling approach proposed constitutes a powerful tool for seismic analysis of reinforced concrete (RC) structures.

Later, Li and Hatzigeorgiou [108] developed a modified uniaxial version of the concrete damage model developed by Faria and Oliver [44] for fiber beam-column elements. The purpose of this simplified damage model was to study the response of RC structures subjected to seismic loads. The evolution of tensile damage variables was plotted for all the structural elements for different stages of earthquake loading. The authors claimed that a fiber damage model is a direct and precise numerical tool for modelling the seismic response of RC structures.

Kang and Lee [84] went one step further and proposed a methodology to generate damage indices for seismic fragility analysis of RC structures. The index is calculated as a function of the tensile local damage variable of the plasticity-damage model previously developed by Lee and Fenves [104]. The authors noted that damage indices quantify the global structural damage by means of fragility curves and define the damage state. The performance of the proposed methodology based on local damage indices was compared

against the standard response-based indices, like Park-Ang, which is widely used in earthquake engineering. The proposed damage index was observed to increase monotonically and, for that reason, it is ideal for the construction of seismic fragility curves.

More recently, Cardona et al. [13] employed a fiber element model in combination with a damage mechanics material model to assess the structural response of concrete columns subjected to cyclic loading. Based on their numerical results, damage indices were developed and related to global demand parameters like drift and ductility. Moreover, the evolution of local damage zones was monitored, and as a consequence, it was possible to relate some response parameters, like strain and drift, to damaged-based limit states in the concrete (e.g. cracking, crushing, reinforcement yielding) and to global performance levels (e.g. collapse, life safety, operational). To overcome the limitations associated to the qualitative description of damage, the authors claimed that numerical tools should be able to quantify the structural damage state associated with a particular performance level. This is an ongoing research topic which is clearly more advanced for concrete structures than for timber.

Finally, Feng and Xu [47] proposed a fiber beam-column element for RC structural columns and beam-to-column connections under the action of cyclic loading. A multi-dimensional damage model was assigned to the concrete fibers, while a plasticity model was defined for the reinforcement steel bars. The contribution of the additional strain in the steel reinforcement due to bond-slip effect was also taken into account. The concrete damage model allowed accounting for the combined action of axial and shear stresses. This modelling strategy demonstrated to correctly reproduce the initial stiffness and pinching effect of RC structures. Moreover, the authors highlighted the importance that reliable and efficient numerical models have on earthquake engineering design.

2.3 Wood constitutive models

Wood is a quasi-brittle anisotropic material that shows strong dissimilar strength, failure modes and post-elastic behaviour under the action of tensile and compressive stresses. This means that the mechanical properties of wood (e.g. elastic moduli, shear moduli, Poisson's ratio and strength) vary with the directions (i.e. longitudinal, radial or tangential) and signs (i.e. whether in tension or compression). In general, the three most important failure modes are [188]: (i)ductile failure due to compression parallel to the grain, (ii) ductile failure due to compression perpendicular to the grain, and (iii) brittle

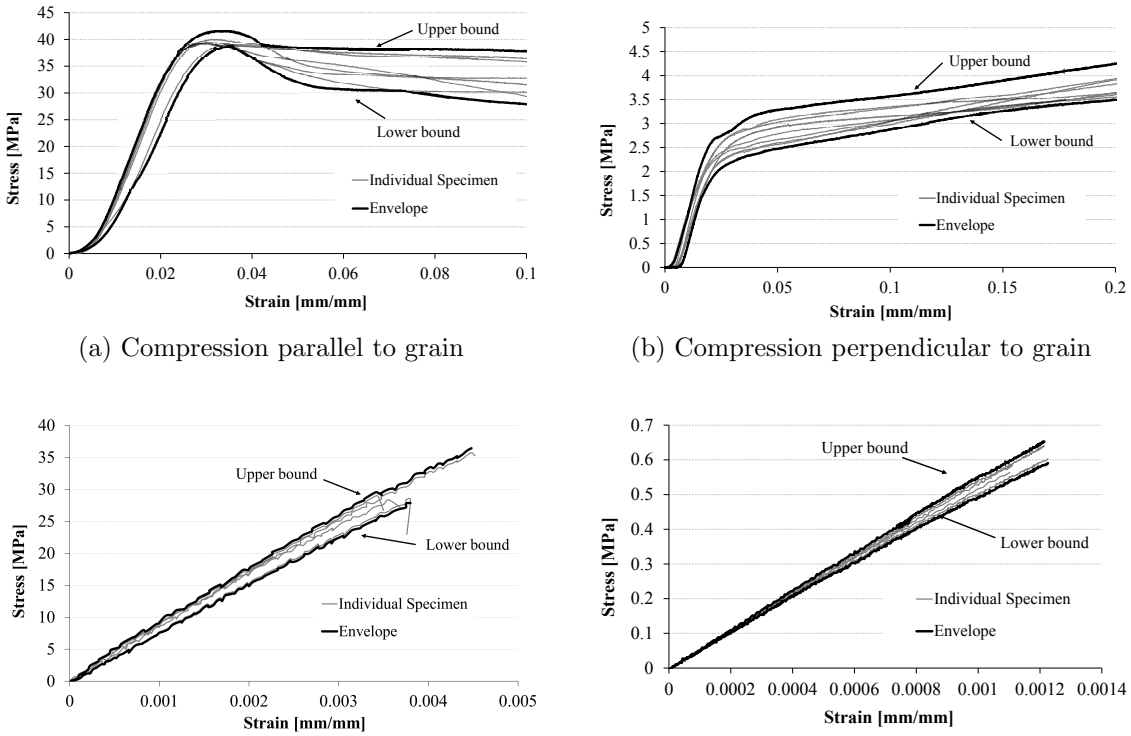
failure due to shear parallel to the grain and tension perpendicular to the grain.

Fig. 2.1 shows typical compressive and tensile stress-strain curves of Scandinavian spruce with a mean density of 430 kg/m^3 obtained experimentally by Karagiannis et al. [85]. It can be appreciated from this figure that, for the direction parallel to the grain (Fig. 2.1a), the behaviour in compression is approximately linear elastic until the compressive strength is reached at around 40 MPa. After this point, a minor stress drop is produced followed by a plastic plateau. Alternatively, the compressive stress-strain relationship in the direction perpendicular to the grain (Fig. 2.1b) shows plastic behaviour with moderate hardening. It is important to note that the compressive strength in the direction perpendicular to the grain is less than 10% of the strength in the direction parallel to the grain.

In the case of tension (Figs. 2.1c and 2.1d), an initial linear elastic response is followed by a brittle failure in both directions. Therefore, the post-elastic behaviour of wood in tension is markedly different than that in compression due to absence of plastic deformation and the sudden loss of strength at failure. Finally, even though the shear stress-strain curve in the direction parallel to the grain is nonlinear, a brittle failure is also observed in this case (Fig. 2.2).

In light of the above discussion, timber failure modes can be summarized as ductile elastic-plastic failure with large deformation due to compression stresses, and elastic brittle failure due to a combination of shear and tension stresses. This means that, in addition to the anisotropic character of timber, the numerical modelling of this material involves the challenge of reproducing completely different failure modes and nonlinear responses for tensile and compressive stress regimes. Therefore, the link of a wood failure criterion with a nonlinear post-elastic constitutive law is a complicated but necessary step towards the faithful description of, not only the failure onset, but also the post-elastic response of timber structures [89].

Although approximate phenomenological modelling has been previously attempted [51, 48, 76], rigorous three-dimensional constitutive models tailored for wood have been developed during the last ten years. The main purposes of these developments are to increase the precision of the numerical predictions and to gain further insight into the nonlinear behaviour of timber structures. Accordingly, a few attempts have been made to develop a material constitutive model for timber subjected to monotonic loading that can deal with both ductile and brittle failure modes. And while most of the available



(a) Compression parallel to grain

(b) Compression perpendicular to grain

(c) Tension parallel to grain

(d) Tension perpendicular to grain

Figure 2.1: Experimental compressive and tensile stress-strain relationships of Scandinavian Spruce [85].

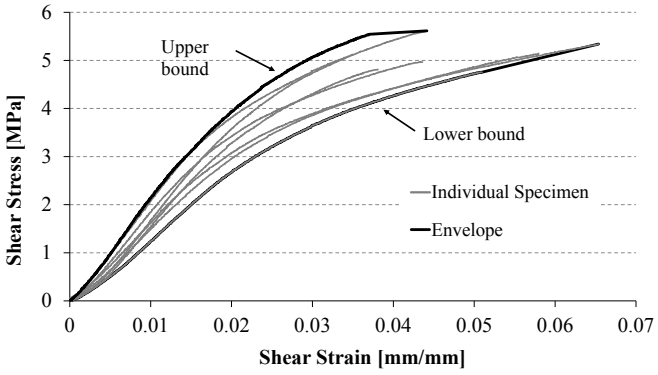


Figure 2.2: Experimental shear stress-strain relationships of Scandinavian Spruce [85].

timber models for monotonic loading employ plasticity theory for failure in compression, three different approaches have been typically followed for shear and tension related failure modes.

The first approach [183, 23, 122] is based on linear elastic fracture mechanics (LEFM) and, in combination with an appropriate failure criterion, represents the most simple technique to identify the zones where local brittle failure has taken place. However, LEFM by itself cannot model the post-elastic behaviour after brittle failure. As a consequence, it is usually complemented with some empirical methods (e.g. random strength or stiffness reduction) or more elaborated techniques like element removal and mesh updating. The second approach [53, 39] is based on nonlinear fracture theory for the development of cohesive zone models, and aims to simulate explicitly the formation and growth of cracks. The major disadvantages of this method are the complexity of the formulation and the practical difficulties associated with the determination of appropriate values for the input parameters. Furthermore, its implementation is generally feasible only for discrete crack modelling, which requires an *a priori* definition of the cracking path, severely limiting its applicability to simulate most timber joints (commonly dowelled connections) subject to cyclic loading, where the crack locations are not known in advance. The third approach is based on Continuous Damage Mechanics (CDM) theory [92, 188, 143] and represents a practical alternative for the definition of a plasticity-damage model for the analysis of timber structures subjected to load reversals. Even though this approach is not suitable for explicit modelling of cracking, it allows to monitor damage evolution and to identify the rupture zones using a smeared continuous approach.

The first wood constitutive models arose in the late nineties and followed the first approach mentioned above. At this stage, Tsai-Wu [171] was the most frequently employed criterion for modelling brittle failure and plasticity yielding of wood. For instance, Williams et al. [183] developed a linear elastic fracture mechanics model to predict the strength of recycled wood elements. To this end, plane stress elements, the Tsai-Wu failure criterion, and the element removal technique were employed. Based on the stress state, the failure criterion is evaluated for each element. The element is removed when the criterion is met at all its integration points, and a new mesh is generated for the next load step. The model was employed to predict the ultimate capacity of a timber beam with a dowel hole in a four-point bending test. The constitutive model demonstrated that accurate strength predictions can be obtained by means of the Tsai-Wu failure criterion with an interaction coefficient equal to zero.

Clouston and Lam [23] proposed a plane stress wood constitutive model based on orthotropic plasticity combined with stochastic analysis. Tsai-Wu yield criterion in combination with associative plasticity and isotropic hardening were defined for modelling compressive post-elastic ductile failure. Subsequently, an empirical approach is followed for modelling the post-elastic brittle failure as a consequence of a mixed normal-shear stress state. On the other hand, an alternative probabilistic approach, based on iterative statistical fitting and Monte Carlo simulations, was proposed to determine the values of the timber shear strength, the shear modulus and the Tsai-Wu interaction coefficients.

Finally, Moses and Prion [122] implemented a material constitutive model to analyse the failure of wooden structures. The model has two components: anisotropic plasticity for compression and probabilistic Weibull weakest link theory for tensile failure. Tsai-Wu failure criterion was also presented as an option for modelling tensile failure, although the authors decided not to use it. Under the Weibull theory, a referential stress associated to a particular probability of failure is calculated and multiplied by a referential volume of timber. Then, the stresses acting at each integration point in a specific direction are numerically integrated over the same referential volume. Failure was attained by those volumes where the total acting stress was higher than the referential stress. The model was used to study the failure mode of a notched shear block and the ultimate strength of a single-bolt connection. A reasonable agreement was found between the numerical and experimental load-displacement curves for both case studies. Nevertheless, early failure and strength under prediction were reported.

On the other hand, the second approach based on nonlinear fracture theory was followed by Dos Santos et al. [39] to study the load slip behaviour of a single-doweled timber T-connection by means of plasticity and fracture mechanics. The connection comprised one central element loaded in compression parallel to the grain and two lateral elements loaded along the direction perpendicular to the grain. A combination of Hill's anisotropic plasticity without hardening and a discrete cohesive zone damage model were employed for ductile and brittle failure modes, respectively. Also, Franke and Quenneville [53] followed the same modelling approach to study the non-linear response of a multiple-dowelled steel-timber T-connection.

Among the various existing failure surfaces for anisotropic materials, Hill [73] and Hoffman [75] have been frequently employed for modelling timber failure under monotonic loads based on the third approach (i.e. continuous damage mechanics). For example, Kharouf et al. [91] employed Hill's criterion to develop a 2D elasto-plastic orthotropic

model with anisotropic hardening, capable of simulating the biaxial (perpendicular and parallel to the grain) behaviour of timber under compression stresses only. Plastic softening and hardening was defined in the directions parallel and perpendicular to the grain, respectively. Brittle failure modes (tension or shear) were not considered by the authors and their model was applied to the analysis of the monotonic response of timber bolted connections.

Furthermore, a 3D anisotropic plasticity model for compression failure in combination with a simplified damage model based on the Tsai-Hill failure criterion for tension was implemented by Guan and Zhu [60]. Additionally, element removal techniques were used to simulate the crack initiation and growth in timber-OSB beams with openings. A similar model but including anisotropic plasticity and ductile densification for compression perpendicular to the grain was implemented by Oudjene and Khelifa [128]. This model was used to simulate the experimental results of a timber beam three-point bending test. Later, the same timber constitutive model was used by O'Loinsigh et al. [127] to study the non-linear behaviour of multi-layered wooden beams with welded dowels. An improved version of this model, within the framework of plasticity coupled with continuous damage mechanics, was developed by Khennane et al. [93] for the study of brittle failure modes in timber structures subjected to tensile and bending loading. More recently, Khelifa et al. [92] also applied this model on the study of timber-steel dowelled connections subjected to monotonic tension loading. This refined constitutive model incorporates the effects of orthotropic elasticity, anisotropic plasticity with isotropic hardening, isotropic ductile damage, and large plastic deformations. Nonetheless, the model does not consider different input strength parameters for tension and compression failure. Conversely, only one set of average strength parameters are required to be calibrated for each particular problem. Moreover, only one Hill's surface is used simultaneously as plasticity and damage criteria, making both inelastic behaviours fully dependent on each other. All these characteristics make this model unsuitable for the study of the nonlinear response of timber subjected to cyclic loading.

More recently, Sandhaas et al. [143] implemented a constitutive model for wood under monotonic loads based exclusively on CDM. The accuracy of this damage model was evaluated against experimental results of timber specimens subjected to monotonic tension, compression and dowel embedment. The model takes into account eight types of brittle and ductile failure modes, each of them associated with a different failure criterion. In spite of not including plasticity, the explicit definition of linear softening (tension) and perfectly plastic (compression) damage evolution laws, as a function of an internal

threshold variable controlling the size of the damage surface, constitutes an important contribution for the numerical modelling of wood.

On the other hand, Xu et al. [188] developed a timber model based on a combination of anisotropic plasticity with hardening for compression, and a simplified continuous damage model for shear and tension. Hill's yield criterion was used for plasticity, whereas a modified version of the same criterion, considering tension and shear stresses only, was used for the definition of the onset of damage. A simplification of the damage evolution law was introduced through a direct reduction of the elastic modulus in the three material orthogonal directions. This plasticity-damage model was used to study the behaviour of timber-steel dowelled joints subjected to monotonic tension loads only. Previously, the same model had been used to study the embedding strength of Glulam dowelled connections [187] and the nonlinear response of a timber beam-steel plate dowelled connections subjected to monotonic loading in the direction perpendicular to the grain [185]. The model prediction accuracy achieved in these studies was satisfactory. However, its lack of continuous damage evolution laws and loading-unloading conditions render this model unsuitable for cyclic loading simulation.

2.4 Wood failure criteria

The formulation of accurate wood failure criteria continues to be a very active research area for which consensus has not been reached yet [123]. The first failure criteria employed for wood strength analysis were developed in the sixties [125, 75] and early seventies [171]. Comparative studies on the determination of the best (new or existing) approaches for modelling of wood failure were carried out in the eighties [27, 66, 178, 114, 106] and have continued until now [89, 177, 12, 117, 61]. This section offers a comprehensive review of the different failure criteria employed by a number of researchers to study the strength of timber and other orthotropic materials under bi-dimensional and three-dimensional stress states. It concludes with the presentation of the formulation of three most representative timber failure criteria.

The Tsai-Wu [171] failure criterion, also known as the tensor polynomial failure criterion, is represented by a generalized quadratic surface that can be compactly expressed in tensor notation, and that incorporates a parameter, called interaction coefficient, that accounts for the interaction of normal stresses in different orthotropic directions. A methodology or analytical expression to determine an appropriate value for this parame-

ter has been one of the most difficult and recurrent subjects of study undertaken by several researchers over the last forty years [27, 66, 178, 114, 106, 168, 89, 177, 12, 117]. Despite the fact that several methodologies have been proposed, no consensus on this specific issue has been reached to date. Nevertheless, Tsai-Wu remains one of the most appealing failure criteria for timber due to its generic formulation. In fact, many widespread quadratic failure criteria frequently used in the strength analysis of timber and other orthotropic materials (e.g. Norris, Hoffman, Hill, Hankinson) can be derived as a particular cases of the Tsai-Wu criteria.

Liu [114] studied the plane stress failure surface of Sitka Spruce using the Tsai-Wu criterion. In this study the Hankinson formula [63] was proposed as a practical analytical expression for the calculation of the interaction coefficient. Liu pointed out that before Tsai and Wu developed their general tensor polynomial failure criterion for anisotropic materials in 1971, the Hankinson [63] and Norris [125] formulae were the most popular expressions for wood strength estimation. Liu's study emphasizes to the high sensitivity of the interaction coefficient values to the results obtained from biaxial loading tests. Moreover, the uncertainty associated with the determination of the interaction coefficient due to the heterogeneity of wood is highlighted.

Theocaris [167] proposed and formulated an elliptic parabolic failure surface for general transversely isotropic materials. Test data of fibre composite materials was employed to validate the proposed failure criterion. The advantages and drawbacks of other traditional failure criteria were analysed. It is stated that Hoffman's criterion "constitutes a simple and well defined failure criterion taking care of the strength differential phenomena of the materials in the correct way". The author also highlighted that despite the empirical basis of its formulation, a deeper study of Hoffman's failure surface demonstrates that, under certain stability conditions, "there is a sound physical significance for this fracture condition which is also a complete and a general one".

Theocaris and Philippidis [168] aimed to demonstrate that the Tsai-Wu theory cannot be considered a failure criterion due to the lack of an adequate definition for the interaction coefficient. The authors contended that assigning a zero value to the interaction coefficient [178] should be avoided because it leads to an ellipsoid closed failure surface whereby an artificial failure could be predicted for those materials with "infinite" strength under a specific triaxial stress state direction. However, it will be explained below that, in the case of wood-based materials, this is not a drawback but quite the opposite [89]. Theocaris and Philippidis [168], agreed that, as shown by other studies, a good agree-

ment is attained between the biaxial tests data and the Tsai-Wu criterion with a zero value for the interaction coefficient. Nevertheless, they showed that this is not case for comparisons against three-dimensional stress-state experimental results. It is important to mention, however, that the 3D stress-state experimental data used in Theocaris and Philippidis' study corresponded to anisotropic polycarbonate material.

In a separate study, Theocaris [169] employs Hoffman's criterion (denominated "elliptic paraboloid") to study the biaxial and triaxial strength of cellular solids. Since Hoffman's yield surface might be open or closed, a complementary additional cut-off surface was defined to avoid elastic buckling failure due to triaxial compression stress-state. One of the major advantages of Hoffman's criterion is that no especial tests are required to calculate the interaction coefficients. Instead, only basic uniaxial strength data is needed. On the contrary, Tsai-Wu criterion requires specialized experimental tests or the adoption of empirical rules for the definition of the interaction coefficients. In his study Theocaris [169] finds a remarkable agreement between the Hoffman failure surface described above and the experimental data. The performance of the Tsai-Wu criterion was also evaluated for two different values of the interaction coefficient. Hoffman showed a superior performance than Tsai-Wu for oriented polycarbonate subjected to hydrostatic compression. As a conclusion the authors stated that Hoffman criterion "presents a high flexibility to describe the failure of any material, brittle or ductile, failing in tension or compression and shear, isotropic or anisotropic".

In a later study, Theocaris [170] recognized that for some anisotropic materials triaxial compressive failure may occur (at some point) due to elastic buckling, and therefore, failure criteria that sustain very high loads under triaxial compression (e.g. Hoffman) are not always in agreement with the experimental evidence. For this reason, Theocaris [170] proposed and formulated a failure criterion based on a symmetric ellipsoid, which axis of symmetry is parallel to the hydrostatic axis. Contrarily to Hoffman's criterion, the interaction coefficients of the ellipsoid failure criterion proposed by Theocaris [170] cannot be directly obtained from the uniaxial strengths along the orthotropy axes, but need to be determined by means of a hydrostatic compression test. Nevertheless, the author demonstrated that the intersection of both surfaces with the principal stress planes resulted in curves that were coincidental in most regions. On the other hand, the author claimed that a significant simplification of the failure surface calculation can be achieved when using the transverse isotropy hypothesis for a general orthotropic material under the action of generic complex loading. Furthermore, the transverse isotropy hypothesis does not change significantly the shape, position and other general characteristics of the

original failure surface.

Kasal and Leichti [89] presented a comprehensive literature review of the theories and approaches available for modelling failure in wood. The authors indicated that, based on the assumption of transverse isotropy, failure criteria originally developed for composite materials have commonly been applied to the analysis and design of wood. On the other hand, it was noted that hydrostatic pressure-independent surfaces (e.g. Hill) are not valid for wood. This conclusion was based on the results obtained from an experimental campaign in which wood spheres were observed to degenerate into elliptical shapes under the action of high hydrostatic pressures. Kasal and Leichti acknowledged Norris [125] as one of the first failure criteria specifically developed for wood. Nevertheless, the authors also noted that Norris's criterion can significantly underestimate the strength of wood when subjected to combined normal and shear stress states. In contrast, Hoffman's criterion was especially developed for modelling brittle failure. A major drawback of it is that, for particular combinations of normal and shear strengths, Hoffman's failure surface can degenerate into an unbounded surface with infinite theoretical strength in a specific direction of the three dimensional stress state. Kasal and Leichti [89] also examined Tsai-Wu's failure criterion. They highlighted that a distinguished feature of this criterion is the definition of the interaction coefficient as a function of the biaxial (instead of uniaxial) compressive or tensile strength. The failure surface sensitivity to the interaction coefficient is also discussed by Kasal and Leichti [89]. They explained graphically that a small error in the experimental determination of the biaxial strength produces a large error in the estimation of the interaction coefficient. Nevertheless, the authors observed that if the interaction coefficient is properly determined, the Tsai-Wu criterion is able to precisely describe the failure bounds of wooden materials. Finally, they concluded that it is important to use a wood failure criteria graphically represented by a closed surface. This was pointed out as one of the main reasons for the popularity of Tsai-Wu tensorial strength criterion in the failure modelling of wood.

Several failure theories (e.g. maximum stress, Tsai-Wu, Hoffman, Norris, Hashin) originally developed for composites were evaluated by Murray [123] as potential wood failure surfaces. Following a comprehensive numerical assessment, her study presents a complete summary of the particular characteristics, advantages and drawbacks of each failure criterion. Off-axis, parallel and perpendicular to the grain test results were employed for this purpose. Based on the results obtained for the off-axis test data, Murray [123] asserted that the modified Hashin and Tsai-Wu failure criteria were the best candidates for assessing wood strength. Subsequently, a modified version of the Hashin

criterion [66] was used in the wood constitutive model proposed in [123]. Hashin's general failure criterion is based on five stress invariants under the hypothesis of transverse isotropy. It is assumed that failure in the directions parallel and perpendicular to the grain do not interact but are independent from each other. To this end, four surfaces corresponding to tensile and compressive failure modes in the directions parallel or perpendicular to the grain are independently evaluated. No interaction coefficient between the normal stresses in each direction is required. The two most important advantages of this failure criterion are: 1) its capability to identify different types of failure modes; and 2) the predicted strengths in the direction parallel to the grain are moderated in comparison with the very high strength magnitudes usually predicted by other failure criteria.

Sandhaas [144] recalled that quadratic, continuous, closed and convex surfaces have been used efficiently to describe wood failure surfaces with sufficient accuracy. Moreover, although there is no physical reason to justify the use of quadratic surfaces, Sandhaas [144] explained that, due to the scatter of test data characteristic of wooden materials, the use of sophisticated or more complex criteria provides no real advantage. For instance, multi-surface yield criteria [115] are able to better describe the elasticity boundaries of wooden materials; however, they are also difficult to implement and present some numerical instabilities. Alternatively, the author claimed that piecewise failure criteria are more meaningful than quadratic from a physical point of view. For this reason, Sandhaas [144] used a failure criterion composed of eight independent piecewise timber failure modes imported from the field of fibre composites.

Dorn [38] also considered that a multi-surface yield criterion is ideal for representing the markedly different wood failure modes in tension and compression. Nevertheless the complexity of this criterion was considered as an important drawback. A discussion on the mathematical formulation and the determination of the interaction coefficient of Tsai-Wu criterion was presented. Finally, Dorn [38] considered that the Tsai-Wu single surface failure criterion was precise enough and a null interaction coefficient (ellipsoid failure surface) was assumed in this study.

Cabrero et al. [12] explained that although phenomenological failure criteria are able to identify the occurrence of failure, they cannot distinguish failure modes or mechanisms. The mathematical expressions and geometrical representations of several quadratic failure surfaces were summarized and compared in [12]. Among them, Hill, Norris and tensor derived criteria like Tsai-Wu and Hoffman were discussed. Cabrero et al. [12] summarized some research works that recommend the use of tensor polynomial failure

criteria with null interaction coefficient for wood failure modelling. Moreover, the authors claimed that Hoffman's criterion can be defined as a particular case of Tsai-Wu's criterion for which a very small value (close to zero) is assigned to the interaction coefficient. Tsai-Wu's failure criterion was distinguished as the most used for wood modelling as well.

Mascia and Nicolas [116] performed an experimental study to evaluate the ability of the Tsai-Wu criterion to predict the failure of Brazilian wood species. For this purpose, the strength of several specimens under different loading conditions (e.g. tension and compression uniaxial, off-axis, biaxial and shear tests) was determined. The authors concluded that the Tsai-Wu criterion is particularly suited for the prediction of compressive uniaxial and biaxial strengths. However, the difficulties associated with the determination of the interaction coefficient were also mentioned. In theory, this coefficient could be determined by means of a biaxial test. In reality, the test data scatter makes it very difficult to obtain a representative mean value of the interaction coefficient, and for that reason, many researchers have proposed different analytical expressions to estimate it. A complete summary of several methodologies proposed to calculate the interaction coefficient was presented in [116]. Furthermore, analytical expressions for the maximum and minimum limits of the interaction coefficient values to obtain a closed failure surface were presented. This study concluded that good results were obtained using interaction coefficients equal to the maximum limit. Besides, a close fit of the biaxial test results were obtained with the interaction coefficient formula proposed by Cowin [27]. In general, Mascia and Nicolas [116] found that small values of the interaction coefficient (lower than 20% of its maximum limit) also provide good results.

Later, Mascia and Simoni [117] assessed the capability of the Hill, Hoffman, Tsai-Wu and Norris criteria to match the experimental response obtained for two brazilian wood species. The analysis of the results indicated that more stable ellipsoid failure surfaces were obtained for the Hoffman and Tsai-Wu criteria than for Hill's or Norris's. Furthermore, it was concluded that the Hoffman criterion provided the best representation of the strength of the wood species considered.

More recently, Guindos [61] presented a numerical approach for assessing the failure state of knotty wood. This approach evaluates the average stress of a group of integration points (instead of the stress at each integration point) into a phenomenological failure criteria. For this purpose, the results obtained with traditional wood failure criteria like Tsai-Wu, Hashin, Hoffman, Norris, Hill, among others, were compared against experimental data using both average and point-by-point stresses. As expected, less variable

results were obtained in most of the cases for the stress average approach. Moreover, the authors warned of the high sensitivity of the Tsai-Wu criterion to the values assigned to the interaction coefficient. Conservative results were obtained using the 45° off-axis tensile strength to determine the interaction coefficient, while the alternative approach proposed by Liu [114] resulted in a closer match of the experimental data.

From the literature review presented in this section, it can be concluded that, among the various failure criteria developed over the last fifty years, Tsai-Wu [171] and Hoffman [75] are the most frequently employed for the analysis of wood strength. Advantages and drawbacks have been reported above for both of them. Nevertheless, they have been successfully used on the analysis of timber structures. For this reason, a brief summary of the mathematical formulation of the Hoffman and Tsai-Wu criteria follows below. Being a previously developed and simpler failure criterion which has been employed several times in timber engineering, the formulation of the Hill [73] criterion is also presented for the sake of completeness.

2.4.1 Hill failure criterion

The Hill criterion, originally proposed as an extension of the Mises criterion, is defined by Eq. 2.1 for material orthotropic directions coincidental with the principal stress space axes [148]:

$$f\left(\boldsymbol{\sigma}, \bar{\sigma}_y\right) = a_{23}\left(\sigma_{22}-\sigma_{33}\right)^2 + a_{31}\left(\sigma_{33}-\sigma_{11}\right)^2 + a_{12}\left(\sigma_{11}-\sigma_{22}\right)^2 + 3a_{44}\sigma_{23}^2 + 3a_{55}\sigma_{31}^2 + 3a_{66}\sigma_{12}^2 - \bar{\sigma}_y^2 = 0 \tag{2.1}$$

where σ_{ij} are the components of the stress tensor in the principal direction axes 1, 2 and 3; a_{ij} are the stress coefficients which values are dependent on the strength of timber and the failure criterion; and $\bar{\sigma}_y$ is the non-dimensional reference yield stress. When used for modelling plasticity, $\bar{\sigma}_y$ controls the size variation of the yield surface in accordance with a hardening law, and its initial value is defined as $\bar{\sigma}_{y,0} = 1$ [34].

The expressions for calculating the material parameters (a_{ij}) are functions of the uniaxial normal strengths in the three principal directions of orthotropy (f_1, f_2, f_3) and the three shear strengths in the three principal orthotropic planes (f_{12}, f_{23}, f_{31}) [30]. Under the Hill criterion, only one uniaxial normal strength can be assigned to each orthotropic

direction. This means that by definition Hill is only applicable to materials with the same strength in tension and compression, which marks a significant departure from the observed physical response of wood. Despite this, the Hill criterion has been frequently used to analyse timber elements.

2.4.2 Hoffman failure criterion

The Hoffman criterion can be considered a modification of the Hill criterion that incorporates three additional linear stress terms and three additional uniaxial normal strength material parameters. Therefore, the Hoffman quadratic function given by Eq. 2.2 is expressed in terms of nine independent material parameters (a_{ij}):

$$f(\boldsymbol{\sigma}, \bar{\sigma}_y) = a_{23}(\sigma_{22} - \sigma_{33})^2 + a_{31}(\sigma_{33} - \sigma_{11})^2 + a_{12}(\sigma_{11} - \sigma_{22})^2 + a_{11}\sigma_{11} + a_{22}\sigma_{22} + a_{33}\sigma_{33} + 3a_{44}\sigma_{23}^2 + 3a_{55}\sigma_{31}^2 + 3a_{66}\sigma_{12}^2 - \bar{\sigma}_y^2 = 0 \tag{2.2}$$

In contrast to the Hill criterion, Hoffman's stress coefficients, a_{ij}, are defined in terms of six uniaxial tension (f_1^+, f_2^+, f_3^+) and compression (f_1^-, f_2^-, f_3^-) strengths, in addition to the three shear strengths (f_{12}, f_{23}, f_{31}). In this way, the Hoffman criterion overcomes the main limitation of Hill's, namely, not being able to take into account the difference between tensile and compressive strengths [148].

In general, it is difficult to obtain a graphical representation of anisotropic yield surfaces because they are six-dimensional hypersurfaces in the stress space [34]. Nevertheless, in the principal stress space Hill's failure surface is geometrically represented by an elliptic cylinder. The principal axis of the cylinder coincides with the hydrostatic axis, which means that the Hill criterion is pressure insensitive [148, 34]. On the other hand, the graphical representation of Hoffman's failure surface in the principal stress space is an elliptic paraboloid whose space diagonal does not coincide with the hydrostatic axis but is parallel to it. The cross section which results from the intersection of the elliptic paraboloid with the deviatoric stress plane is an ellipse which is shaped by the quadratic stress terms of Eq. 2.2, while its expansion along the space diagonal is determined by its linear stress terms [148]. This means that, in opposition to Hill's criterion, Hoffman's is pressure sensitive.

2.4.3 Tsai-Wu failure criterion

The Tsai-Wu general tensor polynomial failure criterion can be formulated as follows:

$$f\left(\boldsymbol{\sigma}, \bar{\sigma}_y\right) = a_{ij}\sigma_{ij} + b_{ijkl}\sigma_{ij}\sigma_{kl} - \bar{\sigma}_y^2 = 0 \tag{2.3}$$

where a_{ij} and b_{ijkl} are the linear and quadratic stress coefficients, respectively. Before expanding Eq. 2.3 for a three-dimensional stress state $(i, j, k, l = 1, 2, 3)$, some hypothesis based on physical considerations should be defined for both coefficients. First, the signs are relevant for normal stresses only (tension or compression). Contrarily, the signs of shear stresses are meaningless, and therefore, no linear shear stress coefficients are included:

$$a_{ij} = 0 \quad \text{if} \quad i \neq j \tag{2.4}$$

Besides, the interaction between stresses in different directions is only allowed for normal stresses. By contrast, it is assumed that the interaction of a shear stresses with any other component of the stress tensor is negligible, and consequently, the following condition on the corresponding quadratic stress coefficients is imposed:

$$b_{ijkl} = 0 \qquad \text{if} \quad [(i \neq j) \vee (k \neq l)] \quad \wedge \quad [(i \neq k) \vee (j \neq l)] \tag{2.5}$$

Finally, the remaining quadratic stress coefficients are assumed to be symmetric:

$$b_{iijj} = b_{jjii} \qquad ; \qquad b_{ijij} = b_{jiji} \tag{2.6}$$

Taking into account the conditions in Eqs. 2.4 to 2.6, the expansion of the Tsai-Wu criteria of Eq. 2.3 results in the following expression:

$$\begin{aligned} f\left(\boldsymbol{\sigma}, \bar{\sigma}_y\right) = a_{11}\sigma_{11} + a_{22}\sigma_{22} + a_{33}\sigma_{33} + b_{1111}\sigma_{11}^2 + b_{2222}\sigma_{22}^2 + b_{3333}\sigma_{33}^2 + \\ 2\left(b_{1122}\sigma_{11}\sigma_{22} + b_{2233}\sigma_{22}\sigma_{33} + b_{1133}\sigma_{11}\sigma_{33}\right) + 4\left(b_{1212}\sigma_{12}^2 + b_{2323}\sigma_{23}^2 + b_{1313}\sigma_{13}^2\right) - \bar{\sigma}_y^2 = 0 \end{aligned} \tag{2.7}$$

The linear normal stress coefficients are defined in terms of the uniaxial tensile (f_i^+) and compressive (f_i^-) strengths such that:

$$a_{11} = \frac{1}{f_1^+} - \frac{1}{f_1^-} \qquad ; \qquad a_{22} = \frac{1}{f_2^+} - \frac{1}{f_2^-} \qquad ; \qquad a_{33} = \frac{1}{f_3^+} - \frac{1}{f_3^-} \tag{2.8}$$

Likewise, the quadratic normal stress coefficients are defined as:

$$b_{1111} = \frac{1}{f_1^+ \cdot f_1^-} \quad ; \quad b_{2222} = \frac{1}{f_2^+ \cdot f_2^-} \quad ; \quad b_{3333} = \frac{1}{f_3^+ \cdot f_3^-} \tag{2.9}$$

The quadratic shear stress coefficients are defined as a function of the shear strengths (f_{ij}):

$$b_{1212} = \frac{1}{4 \cdot f_{12}^2} \quad ; \quad b_{2323} = \frac{1}{4 \cdot f_{23}^2} \quad ; \quad b_{1313} = \frac{1}{4 \cdot f_{13}^2} \tag{2.10}$$

The expressions to determine nine out of a total of twelve coefficients required for the definition of Tsai-Wu criterion in Eq. 2.7 have already been presented in Eqs. 2.8 to 2.10. The three missing coefficients are the normal stress interaction coefficients (b_{iijj}). As explained above, these coefficients cannot be straightforwardly derived from the uniaxial strengths and there is no standard methodology to calculate them. In principle, it is possible to calculate the interaction coefficients from the biaxial tensile or compressive strength (f_{biax}) by means of Eq. 2.11 [116]:

$$b_{iijj} = \frac{1}{2 \cdot f_{biax}^2} \left[1 - f_{biax} \left(a_{ii} + a_{jj}\right) - f_{biax}^2 \left(b_{ijij} + b_{iiii} + b_{jjjj}\right)\right] \tag{2.11}$$

Based on the assumption of no interaction between normal and shear stresses, the coefficient b_{ijij} can be considered equal to zero in Eq. 2.11 [89]. On the other hand, due to the well-known difficulty associated with the experimental determination of f_{biax}, a number of simplifying assumptions and analytical expressions have been proposed. For instance, a typical simplification used for modelling wood is: $f_{biax} = f_i^+$. The first analytical expression employed to estimate f_{biax} is equivalent to half the wood compressive (or tensile) strength for a load direction at 45° with respect to the grain. The Hankinson formula is employed to derive the following analytical expression based on this criterion:

$$f_{biax} = \frac{f_i^\pm \cdot f_j^\pm}{f_i^\pm + f_j^\pm} \tag{2.12}$$

However, some authors recommend against the use of Hankinson's formula to calculate the interaction coefficient [179].

Besides, the admissible values of the interaction coefficient are bounded by a mathe-

matical condition which ensures that the failure criterion surface is closed:

$$-\sqrt{b_{iiii} \cdot b_{jjjj}} \leq b_{iijj} \leq \sqrt{b_{iiii} \cdot b_{jjjj}} \tag{2.13}$$

Therefore, an alternative expression to estimate the interaction coefficient in terms of these minimum and maximum limits is:

$$b_{iijj} = r_1 \sqrt{b_{iiii} \cdot b_{jjjj}} \tag{2.14}$$

where r_1 varies from -1 to +1. Several values of r_1 have been used by different authors to calculate the interaction coefficient. The most frequently used are r_1 equal to: 0 [114, 38, 183], +1 [116] and -0.5 [126]. Nevertheless, smaller values ($|r_1| \leq 0.3$) have also been recommended [116, 23].

Another expression to determine the interaction coefficient was proposed in [170] for transversely isotropic materials:

$$b_{iijj} = r_2 \left(-b_{iiii} - b_{jjjj} - b_{kkkk}\right) \tag{2.15}$$

where values of r_2 between 0 and +0.5 are recommended. It should be noted that Hoffman's criterion is obtained from Eq. 2.7 when calculating the interaction coefficients using Eq. 2.15 with $r_2 = 0.5$.

Finally, two alternative theoretical expressions were proposed by Cowin [27] and Liu [114] to estimate the interaction coefficients as presented in Eqs. 2.16 and 2.17, respectively.

$$b_{iijj} = \sqrt{b_{iiii} \cdot b_{jjjj}} - \frac{1}{2 \cdot f_{ij}^2} \tag{2.16}$$

$$b_{iijj} = \frac{1}{2}\left(\frac{1}{f_i^+ \cdot f_j^-} + \frac{1}{f_j^+ \cdot f_i^-} - \frac{1}{f_{ij}^2}\right) \tag{2.17}$$

2.5 Three-dimensional finite element modelling of timber dowelled connections

Dorn [38] built a finite element model to study the behaviour of timber dowelled connections under the action of low amplitude cyclic vibrations at the serviceability limit state. A three-dimensional orthotropic elastoplastic constitutive model based on the Tsai-Wu yield surface with null interaction coefficient values was employed. Hardening or softening post-elastic responses were not included in the model. Furthermore, the author proposed an interface contact model to simulate the interaction between the steel bolt and the surrounding wood. A nonlinear normal pressure-deformation dependence shown in Fig. 2.3 was established for loading, whereas friction in the tangential direction was not taken into account by this model. Based on the experimentally observed non-recoverable plastic deformations, the interface stiffness during the first loading was defined to be lower than for unloading or reloading. On the other hand, timber plasticity was modelled in two stages. The first one takes place in the timber reduced zone adjacent to the steel bolt and directly affected by the interaction with it. This plastic deformation is modelled by the bolt-timber contact interface described above. Additional plasticity and permanent deformations corresponding to the second stage occur for higher levels of load. In this stage, plasticity develops in the inner timber matrix and is modelled by the orthotropic elastoplastic constitutive model. The author concluded that a proper modelling of both plasticity stages is fundamental for an accurate prediction of the unloading behaviour. Finally, some interesting remarks on the fundamental role that friction coefficients play in timber dowelled connections were drawn by Dorn [38]. For instance, the high variability of friction coefficients employed by different authors was highlighted. A wide range of friction values (from 0 to 0.7) stresses the high uncertainty associated with contact modelling in general. In his study, a friction coefficient of 0.4 was employed in the contact surface between the steel dowel and the timber beam. However, a higher friction coefficient of 0.7 was assigned to the contact surface between the steel plate and the steel bolt. Finally, contact between the steel plate and the timber element was disregarded. It was demonstrated that for dowelled connections higher timber-bolt friction coefficients results in a ductile failure mode and a higher connection capacity. On the contrary, low values of friction coefficient lead to early brittle failure.

Dias et al. [36] developed a 3D finite element model to study the nonlinear behaviour of the timber-concrete joint specimen shown in Fig. 2.4. The proposed model comprised isotropic and orthotropic plasticity for steel and timber components, respectively, contact and friction modelling for the interfaces zones between materials, and geometric

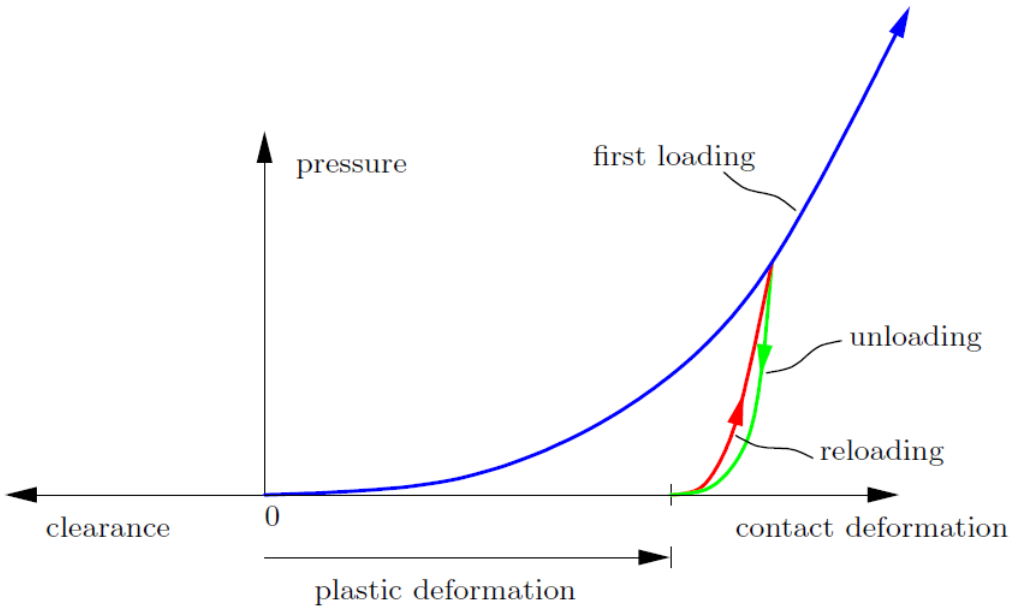


Figure 2.3: Interface contact model in the normal direction (Figure taken from Dorn [38]).

nonlinear behaviour. A dedicated wood constitutive model was not implemented in this study, leading to an overestimation of the initial stiffness and strength of the connection. Plasticity only was found inappropriate to model the brittle failure of timber under tensile stresses. The authors analyses show that the lack of stiffness degradation before the attainment of yield strength was one of the main flaws in the timber material model employed. Moreover, the timber compressive strength was assumed to be equal to the embedding strength. The authors recognized that this assumption may be unrealistic, and the actual strength of timber in compression may be lower. On the other hand, it was pointed out that the initial stiffness of timber dowelled connections could be influenced by the dowel hole clearance, especially in the case of softwood specimens. The authors concluded that further research on timber material nonlinear behaviour is required to obtain more realistic numerical results.

Santos et al. [145] constructed a three-dimensional finite element model of a double-shear single-dowel timber connection subjected to monotonic loads. For the finite element model shown in Fig. 2.5, the authors employed linear elastic material models and examined the nonlinear contact modelling between steel dowel and timber. Regarding contact in the normal direction, they stated that a high stiffness value limits the amount of penetration between timber and dowel but can lead to numerical instability and convergence difficulties. On the contrary, low stiffness values allow unrealistically high levels of pen-

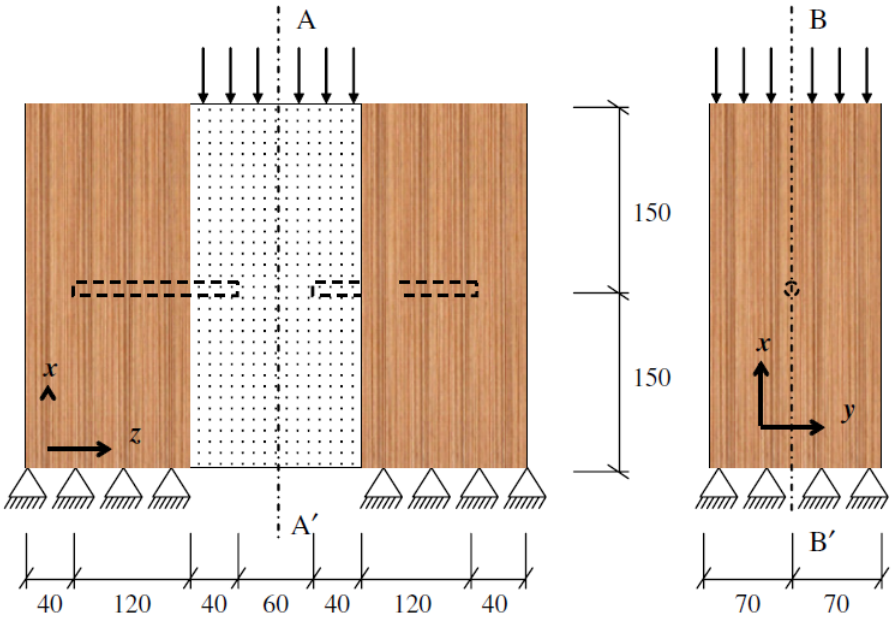


Figure 2.4: Timber-concrete joint shear test specimen (Figure taken from Dias et al. [36]).

etration leading to inaccurate numerical predictions. It was suggested that a referential value of the interface normal stiffness can be obtained from the bulk modulus of the contacted timber body. This referential stiffness value can be subsequently adjusted by multiplying it by a penalty stiffness factor ranging from 0.01 to 1. However, an analytical expression to calculate the bulk modulus of orthotropic materials like timber was not provided in [145]. Finally, the strong influence of the gap between the dowel and the hole on the contact model performance was highlighted. Based on direct measurements and the observed experimental load-slip curves, the use of gaps between 0.1 mm and 0.3 mm was recommended.

More recently, Dos Santos et al. [39] simulated the nonlinear behaviour of a single-dowel T-joint (double-shear) timber connection subjected to monotonic loading by means of a three-dimensional finite element model. The connection specimen shown in Fig. 2.6 had the geometric configuration of a T-joint with central member loaded in the direction parallel to the grain, and two simply supported side members loaded in the direction perpendicular to the grain. In addition to contact, this study incorporated timber material nonlinear modelling. A Hill orthotropic plasticity model was employed to simulate ductile failure due to compressive stresses, while a cohesive damage model was defined to simulate brittle failure modes. Three contact interfaces were defined in the model: steel dowel-timber central member, steel dowel-timber side members, and timber central-side

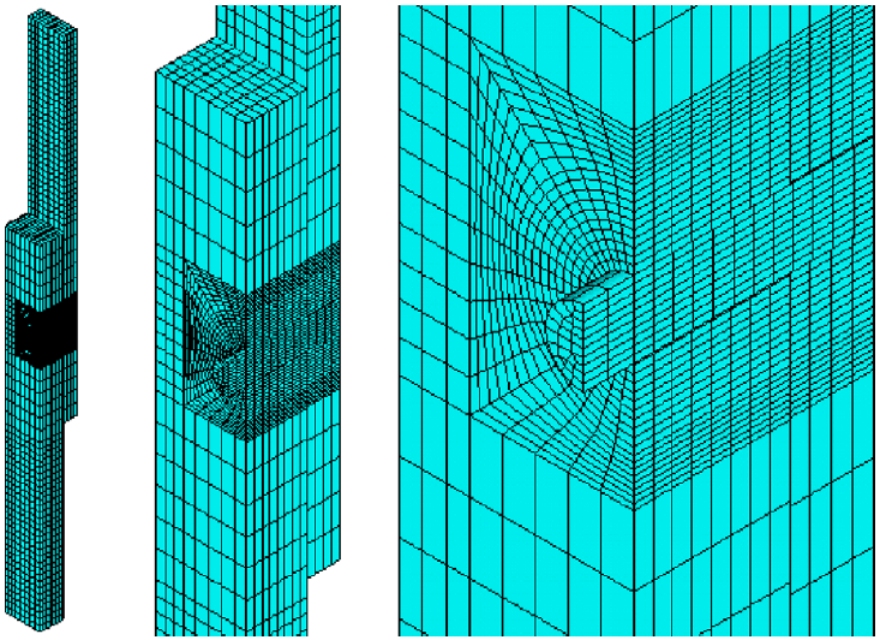


Figure 2.5: Double-shear single-dowel timber connection finite element model (Figure taken from Santos et al. [145]).

members. Different contact stiffness values were employed for each of the three contact interfaces, and a calibration process based on embedding tests was followed to determine these contact stiffness values. The authors concluded that the incorporation of elastic-plastic material model for wood accurately describes the nonlinear load-displacement response of the joint. However, plasticity was not enough to obtain the connection's ultimate capacity before collapse. On the other hand, the inclusion of a cohesive damage model allows the simulation of brittle failure modes and their associated collapse loads. However, the ductile behaviour previous to failure was not captured by the damage model itself. Therefore, the simultaneous application of plasticity and cohesive damage models was required in order to obtain a faithful representation of the connection's capacity and its nonlinear behaviour before collapse.

Following a different approach, Xu et al. [189] proposed a three-dimensional finite element model shown in Fig. 2.7 to simulate the response of a timber column-to-steel beam dowelled connection under monotonic loading. To this end, the authors developed a plasticity-damage constitutive model for wood based on a Hill's yield surface combined with a Hoffman damage function. Transverse isotropy was assumed for the definition of the timber elastic material properties. Perfectly plastic (no hardening) post-elastic behaviour was considered for compressive ductile failure modes, while a simplified empirical damage evolution law was employed for tensile brittle failure. The three-dimensional

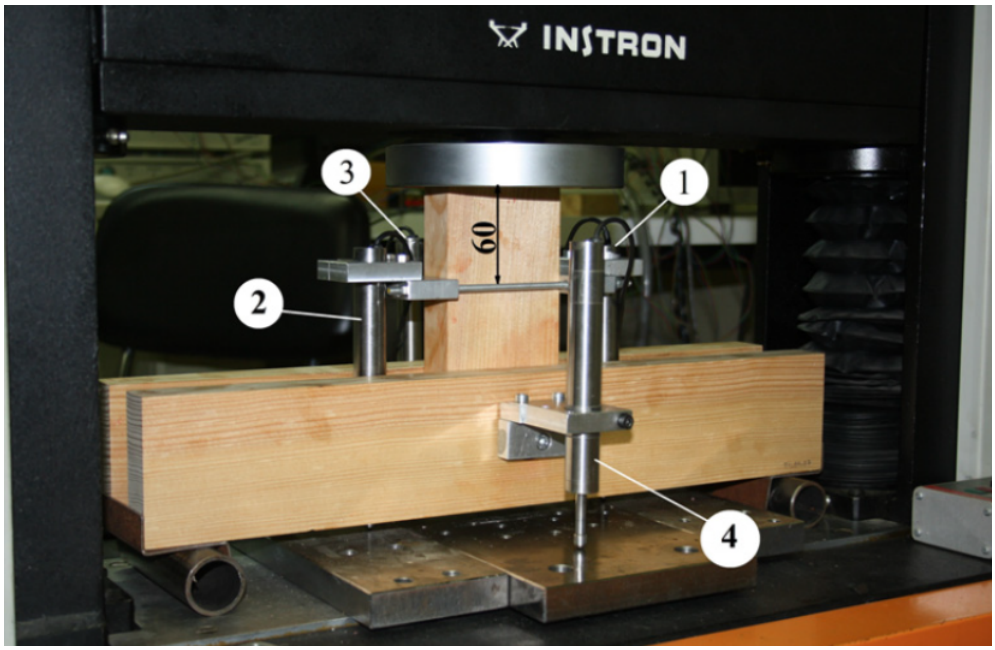


Figure 2.6: Single-dowel T-joint (double-shear) timber connection specimen (Figure taken from Dos Santos et al. [39]).

character of the nonlinear behaviour of timber dowelled connections was identified to be a consequence of the non-uniform stress distribution across the timber member thickness generated by the bending of the steel dowel, the embedding of wood and the contact between wood and steel. Three contact interfaces were considered in the model: timber column-steel plates, timber column-steel dowel, and steel plate-steel dowel. The direct constraint method was employed for contact modelling. This method consists of the imposition of a multipoint constraint between the adjacent nodes of the elements in contact. Once contact is established, sliding based on the Coulomb friction model is allowed along an imaginary line between two adjacent nodes on the surface of the contacted body. Therefore, no tangential movement is permitted until the friction resistant force is overcome. Afterwards, the tangential stiffness is set to zero and sliding occurs under a constant friction force. It was observed that considering friction between the steel dowels and the timber element did not affect the initial elastic stiffness of the connection. Contrarily, the moment capacity of the connection was significantly increased when friction was incorporated. A good agreement was observed between the experimental and numerical global moment-rotation curves. Besides, the shear failure modes were correctly predicted. The authors concluded that this type of plasticity-damage models are useful for predicting the locations of the failure zones and investigating their damage evolution with increasing load magnitudes. Moreover, the authors envisaged limiting the need of experiments by performing more realistic numerical parametric studies.

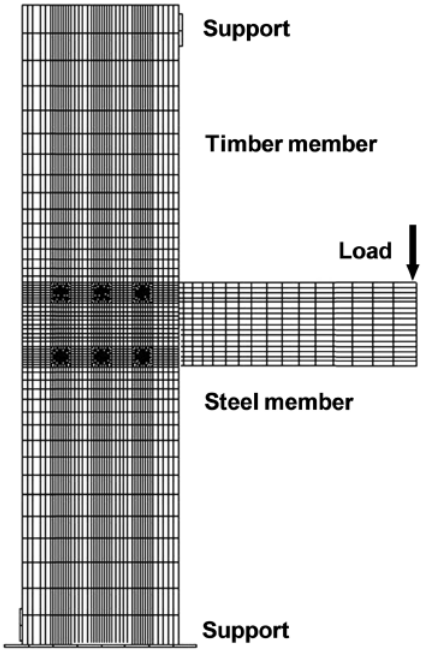


Figure 2.7: Timber column-to-steel beam dowelled connection finite element model (Figure taken from Xu et al. [189]).

Bedon and Fragiacomo [7] proposed a 3D finite element model of a composite timber beam-to-concrete slab notched connection. Fig. 2.8 shows that failure due to shear stresses parallel to the grain and tensile stresses perpendicular to the grain was modelled using cohesive damage elements along the shear failure plane of the notched connection, a wood plasticity material model and interface contact elements. Cohesive damage models provide an accurate simulation of crack propagation as long as the timber material properties are properly calibrated. The damage evolution in the cohesive element was defined in terms of mode I (tension) and mode II (shear) fracture energy density material properties. On the other hand, plastic deformations due to compressive stresses were taken into account for the whole timber beam element. However, no damage due to crushing can be modelled using a plasticity model. Therefore, timber damage was only restricted to the shear failure plane where the cohesive elements were defined. The authors stated that advanced numerical modelling is required to study the structural performance of notched connections. Despite being complex and computationally expensive, it was concluded that this type of numerical model is an appealing alternative to experimental tests. The proposed model was validated against push-out tests. The specimens tested were notched connections composed of Laminated Veneer Lumber (LVL) blocks and concrete topping connected through steel coach screws. The purpose of this study was to identify the notched connection parameters that have an effect on its stiffness and strength, as well

as to evaluate the potential applicability of the proposed FE model. Importantly, shear collapse of the concrete notch was identified as the typical failure mode of the notched connection during push-out tests. Therefore, no timber failure occurred. This was confirmed by the numerical results in the cohesive layer, in which only partial damage was observed. It can be argued that for this particular type of connection, the proper modelling of concrete nonlinear behaviour until failure is more important than an accurate modelling of timber material nonlinearity. Finally, this study highlighted the ability of monitoring damage propagation for all the model components throughout all the loading stages as an advantage of FE modelling over experimentation.

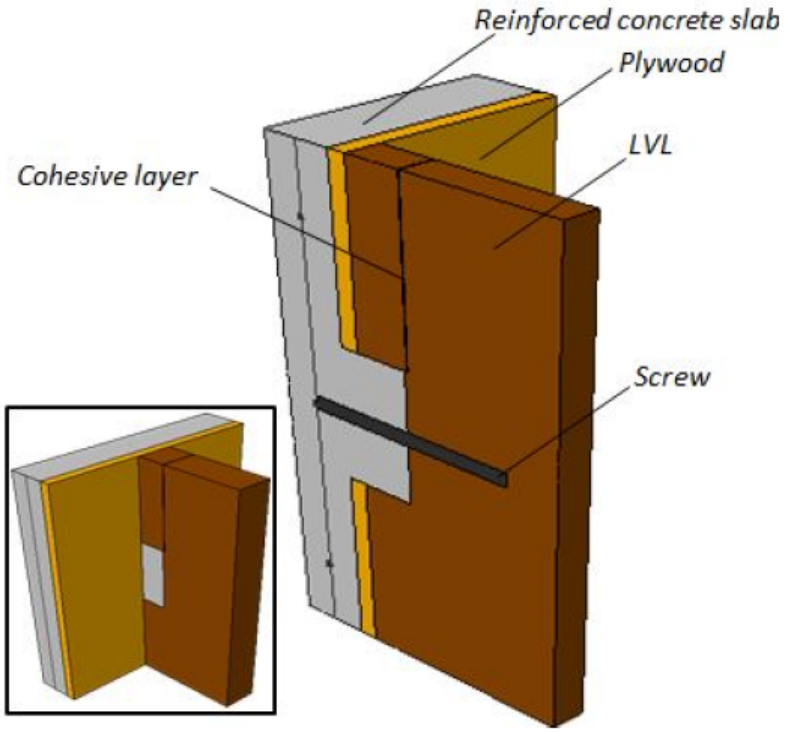


Figure 2.8: Composite timber beam-to-concrete slab notched connection (Figure taken from Bedon and Fragiacomo [7]).

Finally, Hassanieh et al. [68] developed the three-dimensional finite element model shown in Fig. 2.9 to study the nonlinear behaviour of steel-timber composite connections subjected to monotonic loading. The performance of two types of timber products, Laminated Veneer Lumber (LVL) and Cross Laminated Timber (CLT), and two types of steel fasteners, screws and bolts, was investigated. The continuous damage mechanics (CDM) wood constitutive model proposed by Sandhaas [143, 144] was employed for modelling both LVL and CLT timber products. One advantage of CDM models is their capability

to model both ductile and brittle failure modes simultaneously. To this end, two damage evolution laws corresponding to perfect plasticity and linear softening for ductile and brittle failure modes were defined. The authors asserted that a single-surface failure criterion cannot simulate both failure modes. Therefore, a multi surface failure criterion including eight failure modes associated to six damage variables was employed. Each failure mode is caused by a particular combination of normal (tension or compression) and shear stresses for both directions, parallel and perpendicular to the grain. Furthermore, the transverse isotropy hypothesis was used for the definition of the orthotropic elastic timber material properties. On the other hand, the authors stated that pre-existing damage in a timber hole produces a reduction of the timber elastic modulus in that zone. The authors referred to experimental studies which have demonstrated that the timber elastic modulus in the timber hole is smaller than its bulk modulus. This would be the reason why the numerical models tend to overestimate the load-slip initial stiffness. Based on this conclusion, the nonlinear pressure-displacement relation developed by Dorn [38] was used for the contact modelling between the steel fasteners and the timber components. This model requires two input parameters that need to be assumed or obtained via calibration: maximum contact pressure and maximum embedment. Typical average values around 0.4 mm are recommended for the former, while values of 60 MPa or 30 MPa can be used for the latter, depending on timber product to be modelled (LVL or CLT). The performance of the proposed finite element model was evaluated based on a number of experimental push-out tests conducted on timber-steel lap connections. The numerical results obtained demonstrated the models' ability to reproduce their load-slip responses and to predict their peak load capacities and failure modes. Nevertheless, the load and stiffness of the LVL specimens were slightly overestimated. The authors attributed this to the elastic-perfectly plastic post-elastic behaviour defined for timber under compressive stresses. They argued that softening due to compression should be incorporated in the wood constitutive model. However, no experimental evidence of such a compressive post-elastic response for timber was provided. Alternatively, the numerical model overestimation of the response can be related to an inadequate calculation of the stiffness degradation due to tensile and shear stresses. Finally, some parametric studies were performed. Negligible influence of bolt post-tensioning on the peak load capacity of the connection was observed. However, bolt post-tensioning influences the load at which first slip occurs between the timber-steel interface. On the other hand, the influence of the friction coefficient value on the connection's post elastic behaviour and maximum load capacity is expected to be more relevant for screwed than for bolted connections.

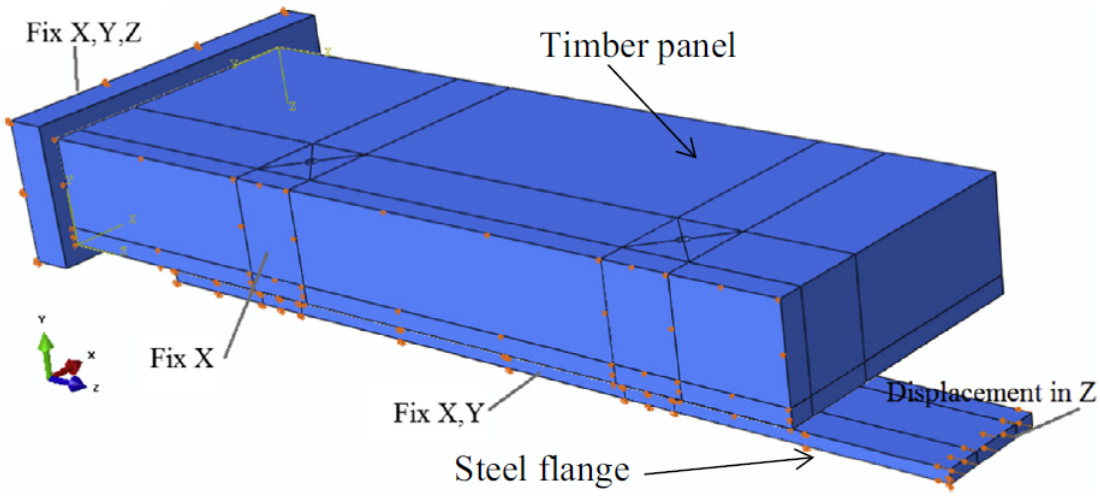


Figure 2.9: Steel-timber composite connection finite element model (Figure taken from Hassanieh et al. [68]).

2.6 Experimental studies of timber dowelled connections

2.6.1 Embedding tests

Embedding strength is a parameter that governs the response of timber dowelled connections. This parameter depends on the connection material and geometric characteristics. The "European Yield Model" based on Johansen's yield theory is employed in Eurocode 5 [14] to calculate the strength of timber dowelled connections. Johansen's theory assumes an elasto-plastic behaviour for both wood and steel dowel elements. This means that Johansen plastic model is only applicable to the prediction of the ultimate load associated with ductile failure modes [39]. However, this type of failure is not always achieved, and brittle failure may occur in timber-steel connections with large diameter bolts and low timber thickness-to-dowel diameter ratio (small dowel slenderness). For this type of brittle failure, the embedding load-displacement relation is strongly influenced by the local stress concentration in the timber around the dowel [91]. Accordingly, the prediction accuracy of Johansen's model decreases for dowels with diameters larger than 20 mm [81] and for perpendicular to the grain loads [185].

Considering that the European Yield Model is not generally applicable to every type of connections, experimental research on timber dowelled connections is generally required to characterise their nonlinear behaviour and to determine their characteristic failure

modes (e.g. ductile embedding due to compression, ductile mixed embedding-dowel plastic hinge, brittle timber splitting due to tension perpendicular to the grain and shear) [185, 10]. A large number of experimental studies of timber dowelled connections with different characteristics have been conducted to date. Zhou and Guan [193] performed a complete literature review of the experimental research programs on timber embedding strength carried out in Europe and North America more than 20 years ago. Wood density and moisture content were identified as the most important factors affecting the embedding strength of a timber specimen. Besides, additional factors like the size and slenderness of the steel fastener (bolt or nail), the loading direction with respect to the timber grain, and the method of testing and data interpretation, were also demonstrated to affect the embedding strength.

The experimental set-ups of the "European" and the "American" methodologies for embedding testing are shown in Fig. 2.10. Due to the considerable amount of factors affecting the measure of timber embedding strength, experimental studies on the isolated embedment response of timber under cyclic loads are rare [138]. Conversely, a relatively large number of experimental studies on the monotonic and cyclic behaviour of single and multiple timber-steel dowelled connections have been carried out. In the following section some of them will be reviewed.

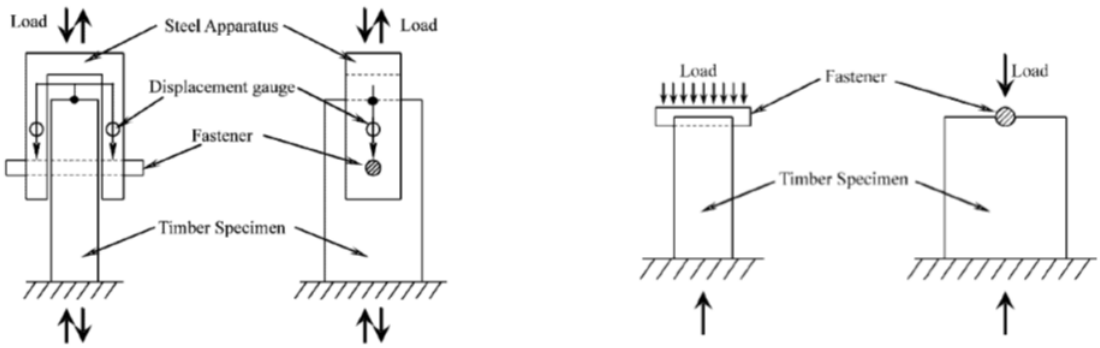


Figure 2.10: Embedding methods of testing: European (left) and American (right) (Figure taken from Zhou and Guan [193]).

2.6.2 Timber dowelled connections subjected to monotonic and cyclic loads

Yang [190] conducted cyclic loading tests on a single timber dowelled connection. 50 mm thick timber plates and 16 mm bolts were employed. The test set-up used in this study

and shown in Fig. 2.11 is similar to the European embedding test scheme (Fig. 2.10). The only difference is that a hold-down connection, composed by four dowels of 13 mm diameter, was needed to resist load reversals.

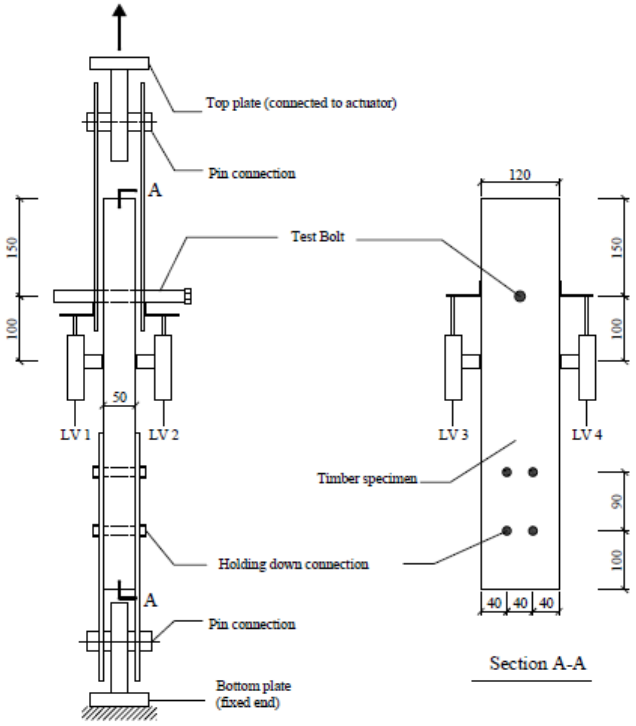


Figure 2.11: Cyclic loading test setup of single timber dowelled connection (Figure taken from Yang [190]).

Frenette [54] conducted cyclic loading tests on the dowelled connections shown in Fig. 2.12, which incorporated a parallel strand lumber (PSL) specimen and a slotted-in steel plate. The thickness of the PSL specimen was 177 mm, while the steel dowel diameter and plate thickness were 12.7 mm and 12 mm, respectively. Schreyer [153] also carried out a similar type of test for the dowelled PSL specimen shown in Fig. 2.13. The thickness of the PSL specimen was 133 mm, while slender fasteners with dowels diameters between 5 mm and 7 mm were employed. For stability reasons, two dowels, instead of one, were used to connect the the PSL specimen and the 6 mm thick steel plate in the central slot. Five identical specimens were tested under monotonic loading and five more under cyclic loading.

Gattesco and Toffolo [57] conducted monotonic tests on the nine types of dowelled glulam-steel connections shown in Fig. 2.14. Five of them were tested in the direction

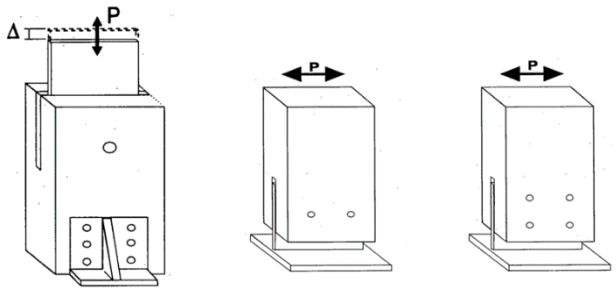


Figure 2.12: Dowelled PSL timber-steel connection specimens subjected to cyclic loading (Figure taken from Frenette [54]).

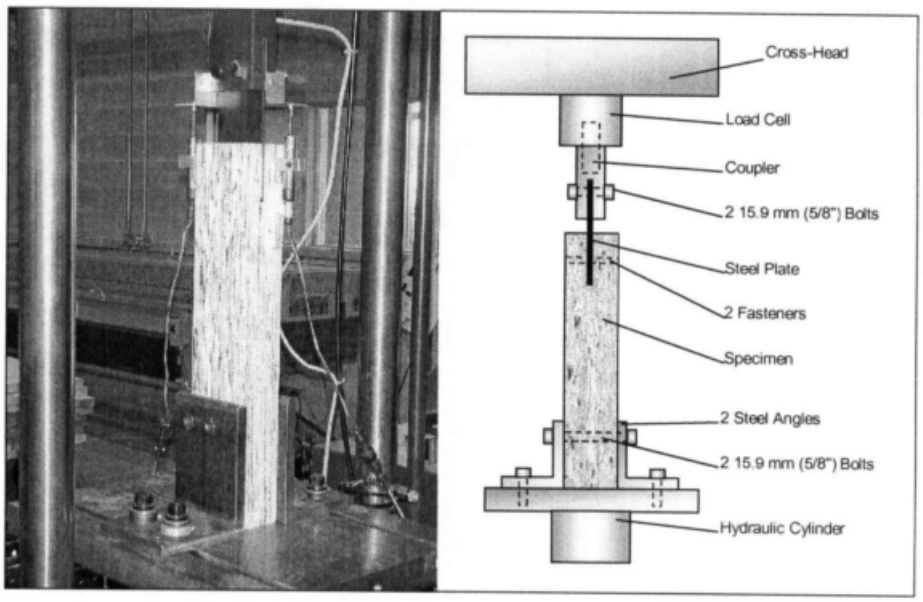


Figure 2.13: Dowelled PSL timber-steel connection specimens subjected to monotonic and cyclic loading (Figure taken from Schreyer [153]).

parallel to the grain, whereas the other four were loaded in the direction perpendicular to the grain. Tests were repeated five times per each specimen, which makes a total of 45 tests carried out. The thickness of the parallel and perpendicular to grain glulam specimens were 110 mm and 120 mm, respectively. The diameter of the steel bolts was 16 mm, while the steel plate thickness was 9 mm.

Reynolds [138] conducted cyclic loading tests on the single dowelled glulam connections shown in Fig. 2.15. The tests were carried out in the directions parallel (3 specimens) and perpendicular (3 specimens) to the grain. However, the specimens were subjected to small levels of displacement corresponding to serviceability limit state only. A symmetrical test configuration was employed to avoid the need for an anchor connection. The

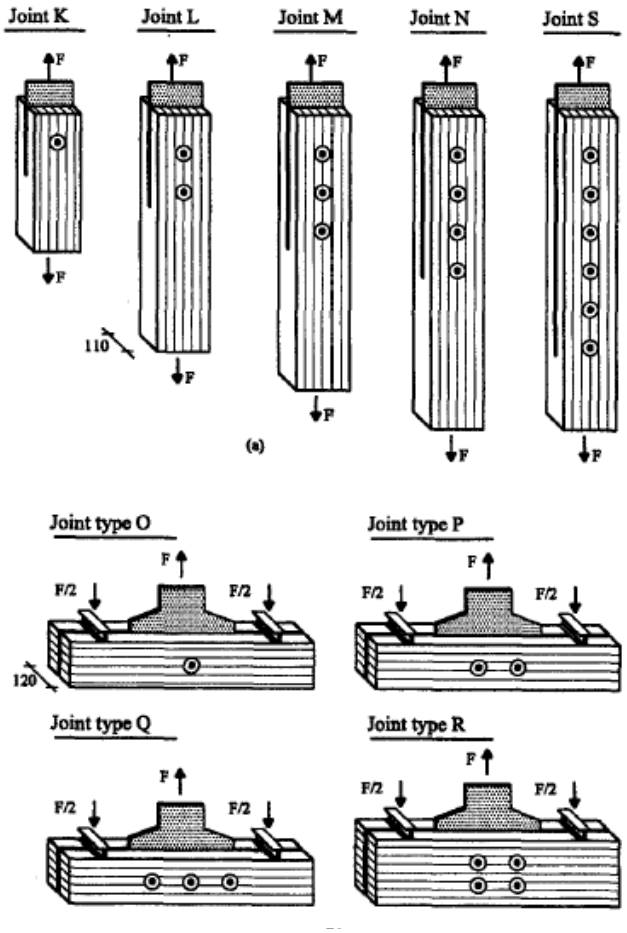


Figure 2.14: Dowelled glulam-steel connection specimens subjected to monotonic load: Parallel to the grain (top) and perpendicular to the grain (left) (Figure taken from Gattesco and Toffolo [57]).

glulam specimen thickness was 185 mm, while the dowel diameter was 12 mm.

The monotonic and cyclic behaviour of timber dowelled connections with two steel side plates was studied by Popovski et al. [136]. A glulam brace with cross section dimensions of 130 mm x 152 mm was connected to two external 12 mm thickness steel plates through steel bolts. Three different types of specimens with 9.5 mm, 12.7 mm and 19 mm bolts were tested three times under monotonic loading and three times under cyclic loading, making a total of 18 specimens. The test set-up employed is shown in Fig. 2.16. The hold-down connection in the bottom part and the load cell in the top part of the test frame were attached to pins in order to minimize the influence of secondary bending moments. Moreover, two roller supports were located in the middle of the timber braces to prevent out-of-plane displacements during compression.

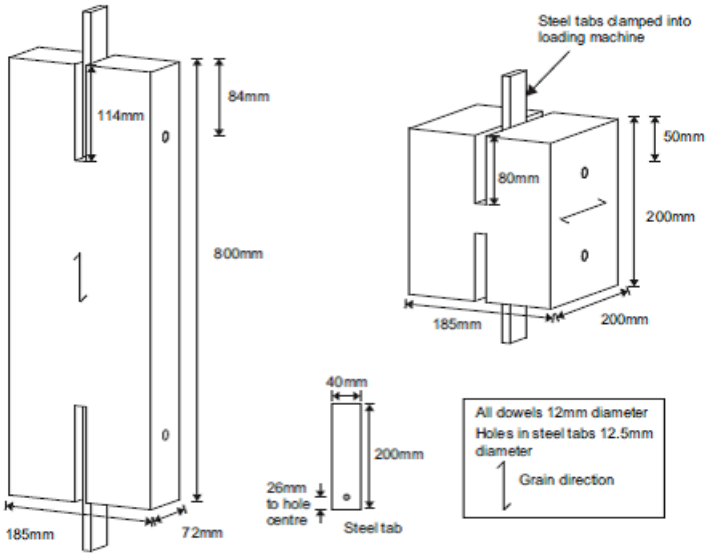


Figure 2.15: Single dowelled glulam-steel symmetric connection specimens subjected to cyclic service load in the directions parallel and perpendicular to the grain (Figure taken from Reynolds [138]).

Lam et al. [100] conducted a cyclic lateral loading test on the timber-steel dowelled connection shown in Fig. 2.17 which is commonly used in beam-to-column moment resistant joints. The column element, which was fixed to the base using steel anchor bolts, was composed of two glulam members with cross section dimensions of 130 mm x 305 mm. On the other hand, the vertically positioned beam was formed by a single glulam element with the same cross section dimensions as the column. A 9.5 mm thick steel plate was located in the middle of the two column members and connected to the beam element through a central slot. Four bolts connected the steel plate to the beam and another four bolts connected it to the column. The diameter of the eight bolts was 20 mm. It is important to notice that the load actuator applying the lateral displacement to the free end of the beam was attached to the load cell through a pinned connection. This allows the end of the beam to freely rotate when the lateral load is being applied.

More recently, Wang et al. [180] carried out a set of monotonic and cyclic tests on a similar moment resistant glulam connection as shown in Fig. 2.18. Five specimens were built for monotonic tests, and another five for cyclic tests. The test setup and loading method employed was the same as Fig. 2.17 [100].

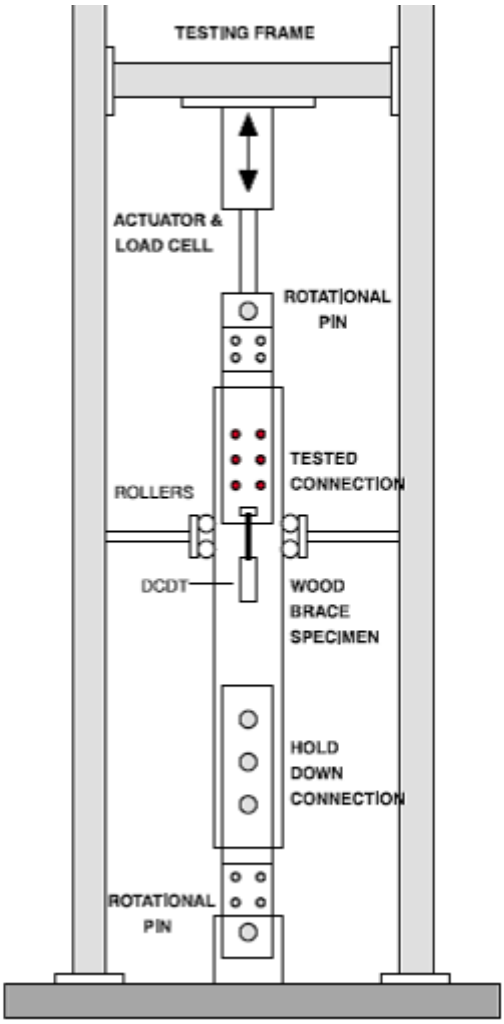


Figure 2.16: Cyclic loading test setup of glulam braces-steel side plates dowelled connection (Figure taken from Popovski et al. [136]).

2.7 Concluding remarks

In general, continuum 3D FE models have shown to be an important tool for acquiring a better understanding of wood's nonlinear behaviour, especially when dealing with highly localized nonlinear phenomena. Furthermore, when properly defined, continuum 3D FE models can be an accurate and useful tool for the study of the structural seismic response at ultimate deformation levels up to collapse, as required by state-of-the-art Performance-Based Seismic Design and Assessment (PBSDA) methodologies. In the case of timber structures, continuum 3D FE modelling is even more important because it is the only consistent numerical approach for: 1) predicting the location and size of potential cracking zones; and 2) assessing the influence of local damage and plastic deformations on the global response of the structure. In those circumstances, it can be stated that 3D FE

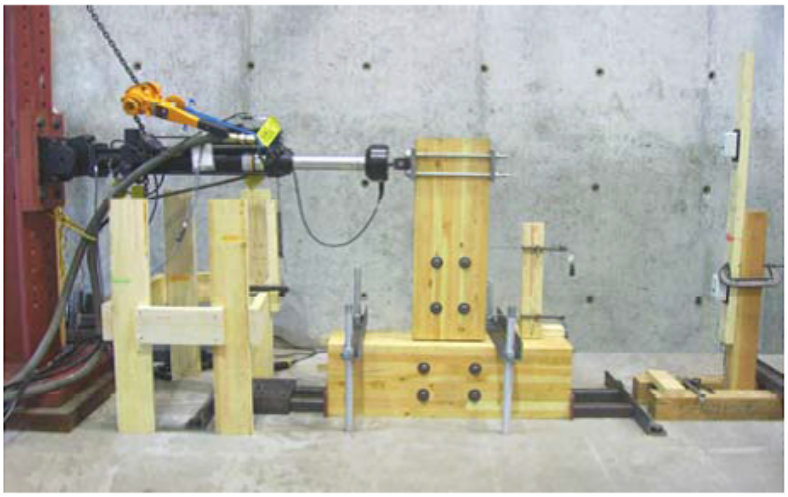


Figure 2.17: Cyclic loading test setup of a glulam beam-to-column moment resistant dowelled connection (Figure taken from Lam et al. [100]).

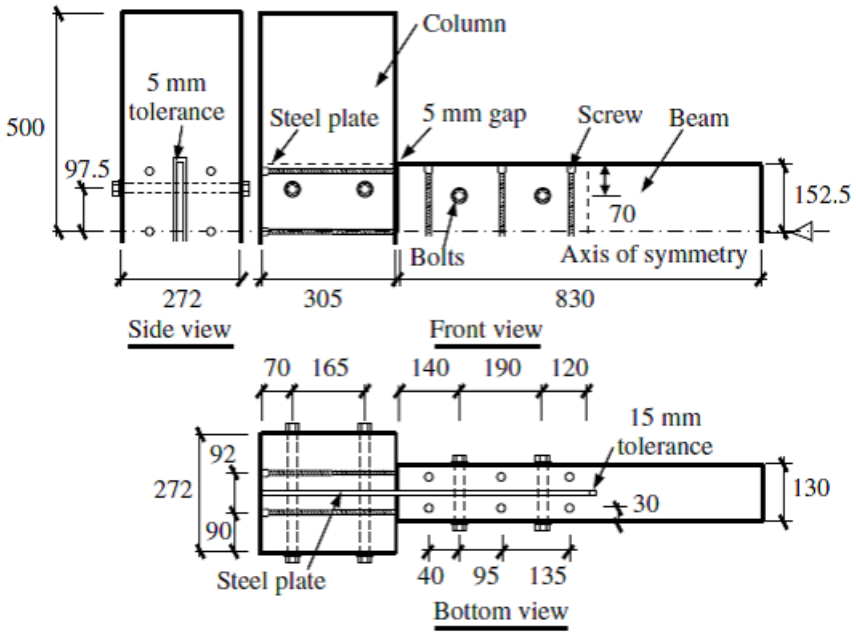


Figure 2.18: Specimen geometric details of the beam-to-column moment resistant dowelled glulam connection (Figure taken from Wang et al. [180]).

modelling is the only numerical approach that is a realistic alternative to experimental investigations.

This chapter has reviewed the few attempts made in recent years to develop an anisotropic material constitutive model for timber that can deal with both ductile and brittle failure modes. However, to the author's knowledge, no timber constitutive model

tailored to the reproduction of the cyclic response of wood, expected during earthquake action, has been proposed yet. Most of the available modelling alternatives are restricted to monotonic loads and employ plasticity theory for simulating ductile failure under compressive stresses. On the other hand, different approaches have been followed to model brittle failure related to shear and tensile stresses, namely, linear elastic fracture mechanics (LEFM), nonlinear fracture theory and continuous damage mechanics (CDM). Following the literature review presented above, it is concluded that CDM offers a fair combination of accuracy and versatility, making it the most efficient approach for capturing both global and local nonlinear behaviour, particularly when dealing with cyclic loading conditions. Therefore, a plasticity-damage constitutive model, especially suited for modelling the cyclic nonlinear behaviour of wood under seismic action, will be formulated, coded and verified in this thesis.

The variety of wood failure criteria used during the last decades for the design of timber structures has also been outlined. It was noted that no general consensus exists to date on which of these failure surfaces provides the most faithful description of timber elastic boundary when subjected to generic loading. Nevertheless, among the different types of quadratic yield surfaces analysed above, the Tsai-Wu and Hoffman criteria have emerged as the most frequently employed for timber strength characterization. Good predictions of experimental results have been reported for both of these criteria under particular boundary and loading conditions. However, it is indispensable that the analyst should be aware of the advantages and drawbacks associated with each of them.

Hoffman's criterion is a particular case of the more general Tsai-Wu criterion when a small value of the interaction coefficient is employed. In addition to its good performance and theoretical consistency, the main advantage of Hoffman's criterion lies in the closed-form expression in terms of uniaxial strengths available for the calculation of the interaction coefficients. This overcomes the need to conduct complex biaxial or off-axis experiments to characterise the interaction coefficient. Nonetheless, Hoffman's failure surface may become unbounded for certain combinations of strength parameters, meaning that for a particular triaxial stress direction the theoretical strength will become infinite.

On the other hand, it is concluded from the literature review that, in timber structures, the use of an appropriate contact model is as important as a suitable wood constitutive model. An accurate description of the interaction between the steel fasteners and the surrounding wood is required in order to capture the large localized plastic deformations,

and to accurately quantify the friction forces generated between the different connection components. These friction forces can contribute significantly to the global capacity of the structure.

The literature review conducted also draws attention to the lack of numerical studies on the cyclic response of timber. What is more, the small number of papers presented (or accepted) in timber-related conferences, like WCTE or INTER, that use three-dimensional continuous models is particularly notorious. This stands in striking contrast with other more traditional materials like concrete or steel and bears witness to the lack of adequate modelling tools.

This relative dearth of information is also translated to experimental studies, where cyclic embedment tests on dowelled connections are limited. Embedment tests are useful for the investigation of the local nonlinear behaviour of wood under the action of concentrated stresses generated by steel fasteners. Although embedment tests are relatively simple to implement for monotononic loading, the test configuration is not naturally suited for the application of cyclic loads. For this reason, the cyclic response of wood is usually investigated within more elaborated tests involving timber dowelled connections which response does not rely solely on the nonlinear response of wood, but depends also on the behaviour of the steel components. It was concluded that there is a lack of experimental investigations on the cyclic response of timber dowelled specimens in general, and of hybrid timber-steel components in particular. The experimental campaign carried out as part of this thesis aims to contribute towards the database of tests available.

Chapter 3

Plasticity-Damage Timber Material Model

3.1 Introduction

Several constitutive models especially developed for the analysis of timber structures were presented in the literature review in Section 2.3. However, there is a lack of three-dimensional wood constitutive models able to accurately reproduce the nonlinear cyclic response and failure modes of timber dowelled connections. For this reason, the objective of this chapter is to develop and present the formulation and implementation of a plasticity-damage model able to simulate the complex behaviour of wood under three-dimensional stress conditions, within a continuum mechanics approach and with a good level of precision. The model is based on the most relevant characteristics of timber inelastic behaviour when subjected to reversed cyclic loading, which were presented in Section 2.3 and are schematically summarized in Fig. 3.1. Building upon previous developments available for other quasi-brittle materials such as concrete [45, 58, 79], the consistent and detailed 3D plasticity-damage material constitutive model for wood presented herein is able to simulate its most important failure modes, while considering plastic deformations and cyclic stiffness and strength degradation, simultaneously.

The plasticity component of the model simulates the ductile nonlinear behaviour and permanent deformations of timber under compressive stresses. A general orthotropic plasticity yield surface with isotropic hardening is employed to incorporate the timber plastic flow in compression. Besides, modelling of brittle shear and tensile failure is based on Continuum Damage Mechanics (CDM) theory which, although not suitable for explicit crack representation, allows the monitoring of damage evolution and the identification of

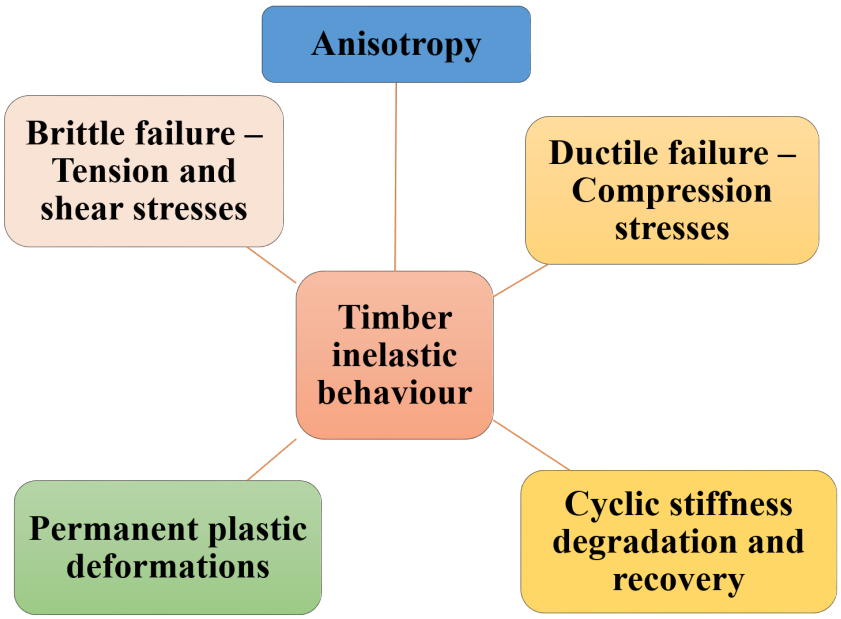


Figure 3.1: Main characteristics of timber nonlinear inelastic behaviour.

potential rupture zones through a smeared continuous approach. In the model proposed herein, the damage evolution process is handled by two independent scalar variables for tension and compression post-elastic responses, respectively.

The coupling of plasticity and damage models is particularly attractive for materials with an inelastic behaviour characterized by the simultaneous occurrence of plastic flow and crack formation. Moreover, plasticity-damage models are able to accurately reproduce the material stiffness degradation characteristic of cyclic loading problems subjected to extensive stress redistribution [79, 31]. Nevertheless, in order to obtain reliable results, the thermodynamic consistency of the model should be verified to ensure that energy is dissipated and that the introduction of spurious energy into the system is avoided [58].

This chapter presents the theoretical basis and constitutive equations required for the computational implementation and coupling of the elasticity, damage and plasticity components of the proposed model. The numerical issues related to the computational implementation of the model are discussed, including the plasticity return mapping iterative algorithm, the global plasticity-damage model algorithm and the derivation of a closed-form expression for the algorithmic plasticity-damage consistent tangent operator. Subsequently, the energy dissipation for tensile brittle failure is studied and the thermodynamic consistency of the model is verified. Finally, the ability of the model to simulate the uniaxial cyclic stress-strain response of a cubic timber specimen in the

directions parallel and perpendicular to the grain is illustrated. To perform this and all the other simulations hereafter presented, the proposed plasticity-damage model for timber structures was coded and implemented in DIANA FEA software [35] by means of a general material model User-Supplied Subroutine (USS). The contents of this chapter are based on the plasticity-damage model developed and validated in [159].

3.2 Orthotropic linear-elastic behaviour of timber

Before yielding (compression) or failure (tension and shear) is produced, the strain-stress constitutive equation of wood can be defined as:

$$\boldsymbol{\epsilon} = \boldsymbol{C}^e : \boldsymbol{\sigma} \tag{3.1}$$

where $\boldsymbol{C}^e$ is the fourth-order orthotropic linear-elastic compliance tensor, defined as a 6 by 6 matrix in Voigt's notation such that:

$$\boldsymbol{C}^e = \begin{bmatrix} \frac{1}{E_X} & -\frac{\nu_{YX}}{E_Y} & -\frac{\nu_{ZX}}{E_Z} & 0 & 0 & 0 \\ -\frac{\nu_{XY}}{E_X} & \frac{1}{E_Y} & -\frac{\nu_{ZY}}{E_Z} & 0 & 0 & 0 \\ -\frac{\nu_{XZ}}{E_X} & -\frac{\nu_{YZ}}{E_Y} & \frac{1}{E_Z} & 0 & 0 & 0 \\ 0 & 0 & 0 & \frac{1}{G_{XY}} & 0 & 0 \\ 0 & 0 & 0 & 0 & \frac{1}{G_{YZ}} & 0 \\ 0 & 0 & 0 & 0 & 0 & \frac{1}{G_{ZX}} \end{bmatrix} \tag{3.2}$$

Accordingly, the inverse of $\boldsymbol{C}^e$ is the fourth-order orthotropic linear-elastic stiffness tensor $\boldsymbol{D}^e$, defined as a 6 by 6 matrix in Voigt's notation as:

$$\boldsymbol{D}^e = \begin{bmatrix} \frac{E_X(1-\nu_{YZ}\nu_{ZY})}{\Delta} & \frac{E_X(\nu_{YX}+\nu_{ZX}\nu_{YZ})}{\Delta} & \frac{E_X(\nu_{ZX}+\nu_{YX}\nu_{ZY})}{\Delta} & 0 & 0 & 0 \\ \frac{E_Y(\nu_{XY}+\nu_{ZY}\nu_{XZ})}{\Delta} & \frac{E_Y(1-\nu_{XZ}\nu_{ZX})}{\Delta} & \frac{E_Y(\nu_{ZY}+\nu_{XY}\nu_{ZX})}{\Delta} & 0 & 0 & 0 \\ \frac{E_Z(\nu_{XZ}+\nu_{YZ}\nu_{XY})}{\Delta} & \frac{E_Z(\nu_{YZ}+\nu_{XZ}\nu_{YX})}{\Delta} & \frac{E_Z(1-\nu_{XY}\nu_{YX})}{\Delta} & 0 & 0 & 0 \\ 0 & 0 & 0 & G_{XY} & 0 & 0 \\ 0 & 0 & 0 & 0 & G_{YZ} & 0 \\ 0 & 0 & 0 & 0 & 0 & G_{ZX} \end{bmatrix} \tag{3.3}$$

with:

$$\Delta = 1 - \nu_{XY}\nu_{YX} - \nu_{YZ}\nu_{ZY} - \nu_{XZ}\nu_{ZX} - 2\nu_{YX}\nu_{ZY}\nu_{XZ} \tag{3.4}$$

The orthotropic directions X, Y and Z correspond to the longitudinal, tangential and radial timber local axes, respectively. It is assumed that the longitudinal axis runs parallel to the grain of the timber material, while the tangential and radial axes lay in the cross-section plan and act in the direction perpendicular to the grain. Notice that due to timber anisotropy the values of the elastic moduli, the shear moduli and the Poisson's ratios are different for each of the three orthogonal axes or planes. However, due to the symmetry property of $\boldsymbol{C}^e$ and $\boldsymbol{D}^e$, the following numerical modelling conditions (not necessarily true from a physical point of view) hold:

$$\frac{\nu_{XY}}{E_X} = \frac{\nu_{YX}}{E_Y}; \quad \frac{\nu_{YZ}}{E_Y} = \frac{\nu_{ZY}}{E_Z}; \quad \frac{\nu_{XZ}}{E_X} = \frac{\nu_{ZX}}{E_Z} \tag{3.5}$$

Consequently, in order to define the linear-elastic orthotropic behaviour of timber, a total of nine mechanical material parameters are required: three elastic moduli, three shear moduli and three Poisson's ratios. A transverse isotropy hypothesis is generally accepted and frequently employed for wood constitutive models [90, 188, 175, 74]. Accordingly, average values of the mechanical properties are assigned to both perpendicular to the grain directions, resulting in a simpler and more reliable numerical modelling approach without significant loss of precision. In the model here proposed, transverse isotropy is assumed, and therefore, the number of independent parameters can be reduced to five (E_X, E_Z, G_{ZX}, ν_{XZ}, ν_{ZY}), by means of the following additional set of relationships:

$$E_Y = E_Z; \quad G_{XY} = G_{ZX}; \quad \nu_{XZ} = \nu_{XY}; \quad G_{YZ} = \frac{E_Z}{2(1+\nu_{ZY})} \tag{3.6}$$

3.3 Orthotropic damage model

Brittle failure due to tension and shear stresses generates voids and micro cracks in the timber matrix which not only lead to a sudden reduction of the material strength, but also cause a gradual degradation of its mechanical properties, including its stiffness. When further loads are applied, the micro-cracks grow and their coalescence produces macro-crack zones and irreversible damage [92]. Continuous Damage Mechanics (CDM), based on the Thermodynamics of Irreversible Processes theory, has been widely used for modelling the nonlinear behaviour of different brittle materials, like concrete, rock [158], and more recently, timber [143]. In elastic strain-based CDM models, the level of damage in the material is directly linked to the magnitude of its elastic strains. Moreover, the model formulation relies on the concept of Effective Stress and the hypothesis of Strain Equivalence. The former is defined as the stress acting in the reduced undamaged net surface area of the material, without considering the portion of area taken by the micro-cracks and voids. Taking into account that the total force acting in the material body is constant, the magnitude of the effective stress acting in the reduced undamaged area is higher than the magnitude of the Cauchy stress acting over the total nominal surface area. On the other hand, the hypothesis of strain equivalence states that the strain associated with the Cauchy stress in the damaged state is equivalent to the strain associated with the effective stress in the undamaged state [158]. In summary, two stress spaces, namely, nominal and effective, which correspond to the damaged and undamaged states, respectively, are defined for the same material point.

The effective stress tensor, $\bar{\boldsymbol{\sigma}}$, is transformed into the Cauchy stress tensor, $\boldsymbol{\sigma}$, by means of the fourth-order tensor $\boldsymbol{M}$, which is a function of the damage tensor, $\boldsymbol{D}$ [83]:

$$\boldsymbol{\sigma} = \boldsymbol{M}(\boldsymbol{D}) : \bar{\boldsymbol{\sigma}} \tag{3.7}$$

Depending on the characteristics of the damage model, $\boldsymbol{D}$ can be defined either as a second-order or fourth-order tensor. Besides, each coefficient of $\boldsymbol{D}$ is a function of one or more scalar damage variables. Based on the number of independent damage variables used to describe the material deterioration process, the damage models can be classified as isotropic or anisotropic. In the case of anisotropic damage models, more than one scalar damage variables are assigned to monitor different types (normal or shear) and directions of material deterioration. The directions of damage anisotropy are influenced by several factors, like the specimen geometry, the material axes of anisotropy, the loading direction or the cracks formation, among others.

A straightforward criterion for the definition of the directions of wood damage anisotropy is to fix them to the material orthotropic axes (longitudinal, radial and tangential). Nevertheless, there are two main disadvantages associated with this criterion for timber material models, a physical and a numerical one. First, the evolution laws for the damage variables corresponding to each orthotropic direction are not known and are difficult to obtain through experimental tests. Second, the strain equivalence hypothesis is not valid for this type of anisotropic damage, and therefore, it is not possible to obtain a mechanically consistent anisotropic damage tensor ($\boldsymbol{D}$) without losing the symmetry of either the Cauchy or the effective stress tensors. Given that, by definition, the Cauchy stress tensor is symmetric, a non-symmetric effective stress tensor would need to be utilised [176]. The advantages of keeping the symmetry of the effective stress tensor will become clear latter.

In light of the above discussion, a different and simpler approach, and the one followed herein, consists in replacing the tensor $\boldsymbol{M}$ in Eq. 3.7 by a scalar expression [58, 79, 132, 133] such that:

$$\boldsymbol{\sigma} = (1 - \omega)\bar{\boldsymbol{\sigma}} \tag{3.8}$$

where ω is the scalar damage variable. This scalar damage model, in combination with the spectral decomposition technique (see Section 3.3.1), allows the modelling of damage-induced anisotropy [17] in timber structures by taking into account the orthotropic nature of its elastic behaviour (see Section 3.2), but not being restricted to it.

The damage process starts with the attainment of the damage criterion condition. Once this criterion is met, the value of the damage variable increases gradually and monotonically from 0 (undamaged state) to 1 (total damage state). It is important to mention that the scalar damage model as defined in Eq. 3.8 implies that the degradation ratios of the elastic and shear moduli terms in Eqs. 3.2 and 3.3 assume a value of $(1-\omega)$. Conversely, it is assumed that no degradation occurs in the Poisson's ratios, remaining constant throughout the analysis. The later is an inherent characteristic of all scalar damage models [83] which is generally accepted for two reasons: first, it avoids the numerical complexities of tensor-defined anisotropic damage models which have a documented restriction on their applicability in engineering practice [184]; second, it evades the set of assumptions on the Poisson's ratio degradation rules that lack physical or experimental justification for most of the materials, and would be necessary to keep the symmetry of the fourth-order tensor $\boldsymbol{M}$ if this type of complex anisotropic damage approach was fol-

lowed [118]. Furthermore, in isotropic damage models the same amount of damage that occurs in one direction is extended to all the other directions. This is thought to be a suitable modelling assumption for wood, considering that there is no evidence of damage decoupling between normal (or shear) stresses in the directions (or planes) parallel and perpendicular to the grain [144]. Thus, the relationships between the mechanical properties of the virgin and the damaged materials for the elastic moduli, the shear moduli and the Poisson's ratio in isotropic scalar damage models are:

$$E^d = (1-\omega)E^0; \quad G^d = (1-\omega)G^0; \quad \nu^d = \nu^0 \tag{3.9}$$

3.3.1 Spectral decomposition of the effective tensor

A timber material constitutive model for cyclic loading should be capable of reproducing the different inelastic responses of wood in tension and compression as described in the literature review in Section 2.3. This does not only include the different strengths and failure modes, but also the different post-elastic and stiffness degradation responses. The latter is particularly important in order to adequately capture the unloading-stiffness degradation and the stiffness recovery after load reversal when passing from tension to compression stress states and *viceversa* [79, 118, 43].

For this reason, a split of the effective stress tensor into a tensile ($\bar{\boldsymbol{\sigma}}^+$) and a compressive ($\bar{\boldsymbol{\sigma}}^-$) components is performed such that [42]:

$$\bar{\boldsymbol{\sigma}}^+ = \sum_{i=1}^{3} \langle \bar{\sigma}_i \rangle \boldsymbol{p}_i \otimes \boldsymbol{p}_i \tag{3.10}$$

$$\bar{\boldsymbol{\sigma}}^- = \bar{\boldsymbol{\sigma}} - \bar{\boldsymbol{\sigma}}^+ \tag{3.11}$$

where $\boldsymbol{p}_i$ and $\bar{\sigma}_i$ are the eigenvectors and eigenvalues of the effective stress tensor, respectively. In order to obtain the principal values of the effective stress tensor ($\bar{\sigma}_i$) and their associated eigenvectors ($\boldsymbol{p}_i$), a spectral decomposition is carried out. This is the first reason why the selection of a symmetric effective stress tensor, and thus, of a scalar damage model, is preferred over a tensor damage model. The Macaulay brackets operator $\langle \cdot \rangle$ in Eq. 3.10 returns the positive values and sets the negative ones to zero. Thus, only the eigenvectors associated to positive (tensile) principal stresses are retained.

Hence, the constitutive equation of the damage model in Eq. 3.8 can be reformulated

in terms of the tensile and compressive components of the effective stress tensor as:

$$\boldsymbol{\sigma} = (1-\omega^{+})\bar{\boldsymbol{\sigma}}^{+} + (1-\omega^{-})\bar{\boldsymbol{\sigma}}^{-} \tag{3.12}$$

where ω^{+} and ω^{-} are the tensile and compressive damage variables, respectively. Each damage variable monitors and quantifies the level of damage of either the tensile or the compressive components of the effective stress tensor. This strategy allows tone o handle the damage mechanisms for tension and compression independently [45], and therefore, to indirectly model the crack opening-closing mechanism, as well as the cyclic stiffness recovery characteristic of brittle materials under reversible loads [132]. Furthermore, under this approach the directions of damage in the three-dimensional space are orthogonal and coincident with the current principal axis of the effective stress tensor [17]. This means that, in spite of using scalar damage variables, this model is able to capture damage-induced orthotropy, for which the damage magnitudes in the three orthogonal directions are controlled by either the tensile or the compressive damage variable, depending on the sign of the corresponding principal effective stresses. During the last years this modelling strategy has been successfully employed by many authors for different applications, structures and materials [184, 134, 120, 132, 17, 13, 142]. It is important to notice that, in general, the orthotropic damage directions are not the same as the timber material orthotropic directions (longitudinal, transversal and radial), except in the cases of triaxial compression or triaxial tension, for which the damage model is reduces to its isotropic version.

3.3.2 Tensile and compressive damage criteria functions

The initiation of the damage evolution process (when the damage variable $\omega^{\pm}$ starts its gradual growth from 0 to 1) is determined by the damage criteria function defined as:

$$f_d^{\pm}(\bar{\boldsymbol{\sigma}}^{\pm}, r^{\pm}) = \bar{\tau}^{\pm} - r^{\pm} \tag{3.13}$$

where $\bar{\tau}^{\pm}$ are the equivalent stresses, while $r^{\pm}$ are the threshold variables. The equivalent stresses are scalar functions of the effective stress tensor components that define the shape of the damage failure surface. On the other hand, the threshold variable is a parameter whose magnitude indicates the current size of the damage function surface, and therefore, the current damage level. Notice that Eq. 3.13 encompasses two damage functions with different equivalent stresses and threshold variables for each independent tension and compression damage process. Due to the anisotropy, complex stresses interaction and failure characteristics of wood, a multidimensional, orthotropic and pressure-independent

damage surface based on Hill's criterion [73] is adopted herein. Hence, the associated equivalent stress of the Hill's damage criterion is defined in Voigt's notation as:

$$\bar{\tau}^{\pm} = \sqrt{\frac{1}{2}\bar{\boldsymbol{\sigma}}^{\pm T}\boldsymbol{H}^{\pm}\bar{\boldsymbol{\sigma}}^{\pm}} \tag{3.14}$$

where the equivalent stress, $\bar{\tau}^{\pm}$, is defined in terms of its corresponding effective stress tensor, $\bar{\boldsymbol{\sigma}}^{\pm}$ and the Hill's mapping matrix $\boldsymbol{H}^{\pm}$ for both tension and compression. The definitions of the coefficients $\alpha_{ij}^{\pm}$ of the matrix $\boldsymbol{H}^{\pm}$ in terms of the wood normal (tension or compression) and shear strengths for each of the three orthotropic directions ($f_X^{\pm}$, $f_Y^{\pm}$, $f_Z^{\pm}$, f_{XY}, f_{YZ}, f_{ZX}) are given as:

$$\boldsymbol{H}^{\pm} = \begin{bmatrix} \alpha_{11}^{\pm} & -\alpha_{12}^{\pm} & -\alpha_{13}^{\pm} & 0 & 0 & 0 \\ -\alpha_{21}^{\pm} & \alpha_{22}^{\pm} & -\alpha_{23}^{\pm} & 0 & 0 & 0 \\ -\alpha_{31}^{\pm} & -\alpha_{32}^{\pm} & \alpha_{33}^{\pm} & 0 & 0 & 0 \\ 0 & 0 & 0 & \alpha_{44} & 0 & 0 \\ 0 & 0 & 0 & 0 & \alpha_{55} & 0 \\ 0 & 0 & 0 & 0 & 0 & \alpha_{66} \end{bmatrix} \tag{3.15}$$

$$\begin{cases} \alpha_{11}^{\pm} = \frac{2}{\left(f_X^{\pm}\right)^2}; \quad \alpha_{22}^{\pm} = \frac{2}{\left(f_Y^{\pm}\right)^2}; \quad \alpha_{33}^{\pm} = \frac{2}{\left(f_Z^{\pm}\right)^2} \\ \alpha_{44} = \frac{2}{\left(f_{XY}\right)^2}; \quad \alpha_{55} = \frac{2}{\left(f_{YZ}\right)^2}; \quad \alpha_{66} = \frac{2}{\left(f_{ZX}\right)^2} \\ \alpha_{12}^{\pm} = \alpha_{21}^{\pm} = \left(\frac{1}{\left(f_X^{\pm}\right)^2} + \frac{1}{\left(f_Y^{\pm}\right)^2} - \frac{1}{\left(f_Z^{\pm}\right)^2}\right) \\ \alpha_{13}^{\pm} = \alpha_{31}^{\pm} = \left(\frac{1}{\left(f_X^{\pm}\right)^2} + \frac{1}{\left(f_Z^{\pm}\right)^2} - \frac{1}{\left(f_Y^{\pm}\right)^2}\right) \\ \alpha_{23}^{\pm} = \alpha_{32}^{\pm} = \left(\frac{1}{\left(f_Y^{\pm}\right)^2} + \frac{1}{\left(f_Z^{\pm}\right)^2} - \frac{1}{\left(f_X^{\pm}\right)^2}\right) \end{cases} \tag{3.16}$$

3.3.3 Tensile and compressive damage evolution laws

The variation of the damage variables, $\omega^{\pm}$, as a function of the threshold variables, $r^{\pm}$, is determined by the damage evolution law defined as:

$$\omega^{\pm} = g_d^{\pm}\left(r^{\pm}\right) \tag{3.17}$$

The mathematical expression of this monotonically increasing function is related to the type of post-elastic stress-strain behaviour of the material (e.g. softening, perfect plas-

ticity, hardening) by means of Eq. 3.8. This relationship is more clearly expressed for a uniaxial stress state in terms of the initial threshold variable, $r_0^{\pm}$, and the uniaxial strength, $f_{max}^{\pm}$, as:

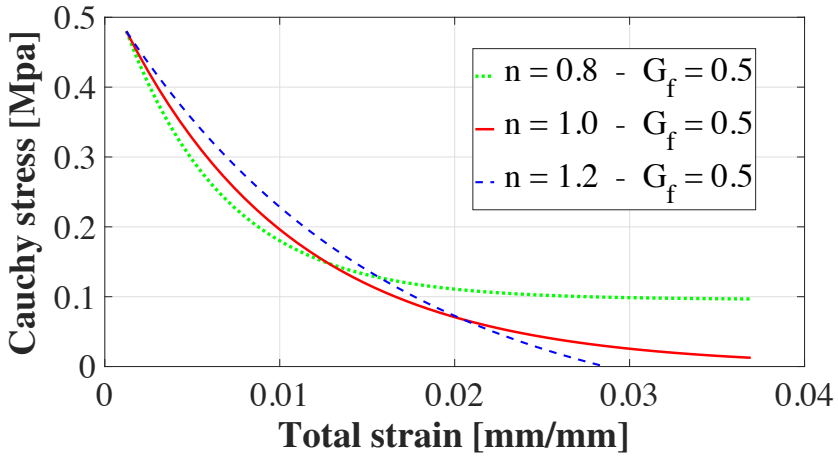
$$\sigma^{\pm} = \frac{r^{\pm}}{r_0^{\pm}} f_{max}^{\pm} \left(1 - g_d^{\pm}\left(r^{\pm}\right)\right) \tag{3.18}$$

Softening post-elastic behaviour with a sharp decrease of strength is characteristic of timber brittle failure under tensile stresses. Thus, the damage evolution law proposed by De Borst et al. [31], capable of modelling different types of exponential softening, is assumed herein for simulating the tensile post-elastic behaviour of wood:

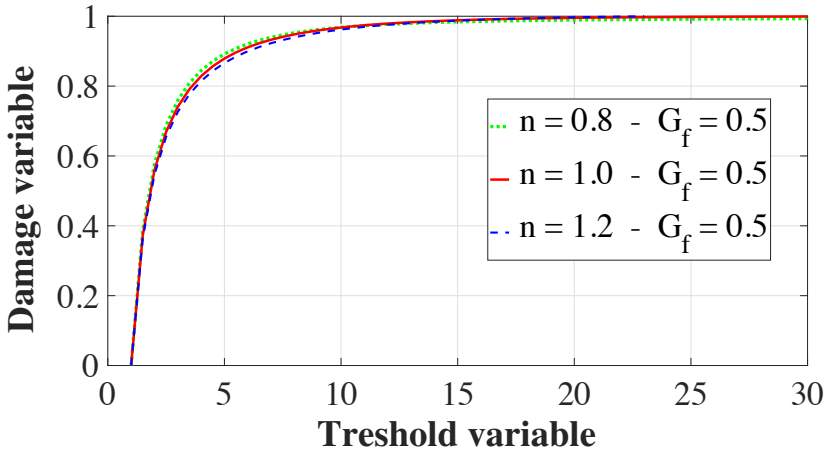
$$g_d^{+}\left(r^{+}\right) = 1 - \frac{r_0^{+}}{r^{+}}\left(1 - n + ne^{-b\left(r^{+} - r_0^{+}\right)}\right) \tag{3.19}$$

where r_0 is the initial value of the threshold variable, n is a calibration parameter and b is a constant dependent on the material mechanical properties and the finite element mesh size. The influence of n in the damage evolution of the Cauchy tensile stress, σ^{+} (Eq. 3.18), and the tensile damage variable, ω^{+} (Eq. 3.19), is explored in Figs. 3.2a and 3.2b, respectively. Fig. 3.2b shows that n has almost no influence on the growth rate of the damage variable. However, for n smaller or equal to 1, an asymptotically exponential softening of the Cauchy stress is appreciated (Fig. 3.2a). The lower the value of n, the higher the residual stress obtained even for widespread damage levels. On the other hand, for values $n > 1$ there is no asymptotic behaviour and the stress rapidly decays to zero.

The value of the constant b in Eq.3.19 depends on the energy dissipated by the material during post-elastic deformation from the moment in which the maximum strength is reached until a local failure is produced. The energy dissipation capability of brittle materials is graphically represented by the area under the softening curve in Fig. 3.2a, and is directly proportional to the fracture energy density (G_f), a mechanical property of wood which varies with the type of failure and, in the particular case of timber, with the material orthotropic plane in which fracture occurs. In light of the experimental response discussed in Section 2.3, the most frequent brittle failure for wood is a consequence of a combination of tensile stress perpendicular to the grain and shear stress parallel to the grain. Therefore, this constitutive model adopts a mixed-mode fracture energy density corresponding to the combination of failure mode-I in the direction perpendicular to the grain and failure mode-II in the direction parallel to the grain, as the most relevant for timber dowelled connections [80]. Hence, b can be expressed in terms of the wood material



(a) Cauchy stress, σ^+.



(b) Damage variable, ω^+.

Figure 3.2: Damage evolution law for tensile softening.

properties through a parameter H defined as:

$$H = \frac{\left(f_{Y-Z}^{+}\right)^2 \times l_{ch}}{2 \times G_f \times E_{Y-Z}} \tag{3.20}$$

where f_{Y-Z}^{+} and E_{Y-Z} are the tensile strength and the modulus of elasticity, respectively, in the direction perpendicular to the grain. Moreover, in order to satisfy the requirement of mesh objectivity, G_f needs to be normalized by the characteristic length, l_{ch}, which is a parameter related to the size of the finite element model discretization [5]. Accordingly, depending of the value of n, the constant b is defined as:

$$\begin{cases} \text{For } n \geq 1, & b = \frac{A}{r_0^+}\left[1 + (n-1) \times ln\left(\frac{n-1}{n}\right)\right]; & A = \frac{2H}{1-H} \\ \text{For } n < 1, & b = \frac{A}{r_0^+}\left[(\alpha n + n - 1) \times ln(\alpha) + 2n(1-\alpha)\right]; & A = \frac{H}{1-n(1-\alpha)H} \end{cases} \tag{3.21}$$

where α is a constant parameter. A detailed discussion on energy dissipation for tensile brittle failure and the derivation of Eqs. 3.20 and 3.21 is offered in Section 3.6.

In the case of compressive post-elastic behaviour, the definition of the damage evolution law is straightforward. Even though perfectly plastic post-elastic behaviour has been frequently assumed when modelling timber ductile compressive failure [143, 181], hardening can be appreciated in the experimental stress-strain curves (Fig. 2.1), particularly when the compressive stress is applied in the direction perpendicular to the grain. Therefore, the compressive damage evolution law, $g_d^{-}\left(r^{-}\right)$, is defined as:

$$g_d^{-}\left(r^{-}\right) = \beta \times \left(1 - \frac{r_0^{-}}{r^{-}}\right)^m \tag{3.22}$$

where β and m are calibration parameters.

The exponent m, which by definition must be higher or equal to one, diminishes the growth rate of the damage variable and determines the order of the uniaxial post-elastic stress-strain curve. On the other hand, the constant β influences the post-elastic stiffness and the maximum value attainable by the compressive damage variable. Fig. 3.3 shows the influence of β on the evolution of the compressive damage variable, ω^{-}, and the Cauchy stress, σ^{-}, for a linear hardening post-elastic behaviour ($m = 1$). Depending of the value of β, which can vary from 0 to 1, the post-elastic stiffness can be zero (perfectly plastic) or higher than zero (hardening) (Fig. 3.3a). Similarly, Fig. 3.3b shows that the maximum allowable value of ω^{-} (maximum level of damage in compression) is equal to β.

For instance, $\beta = 1$ reduces the compressive damage evolution law to a perfectly plastic post-elastic stress-strain response.

Based on these considerations, β and m should be calibrated against experimental monotonic (hardening slope) and cyclic (maximum stiffness degradation) tests on wood specimens under compressive loads. However, this kind of tests are seldom available for the particular type of timber material to be analysed. Therefore, a practical methodology for the calibration of the parameter β will be proposed in Chapter 6, where it will also be shown that the other two calibration parameters, m and n, can be safely assumed based on the typical compressive and tensile post-elastic responses of timber. Finally, it is worth noting that wood does not show softening behaviour in compression (Fig. 2.1). Therefore, in this case there is no need to incorporate a fracture energy density property in the damage evolution law, nor a characteristic length parameter to satisfy the mesh objectivity requirement.

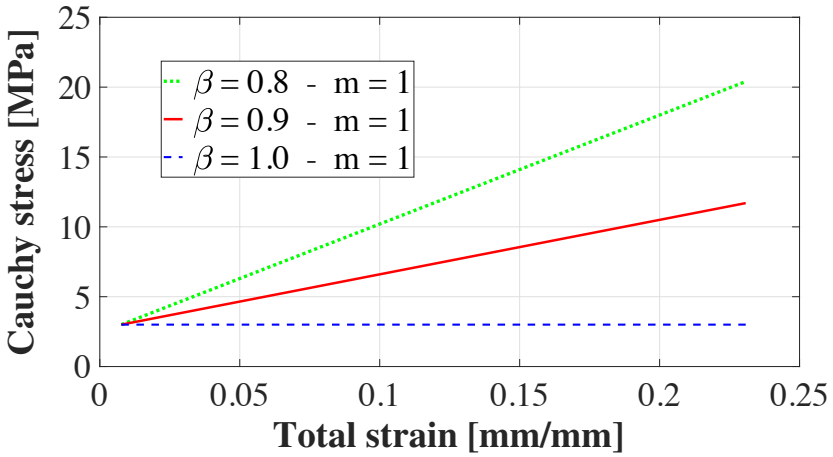
3.3.4 Damage constitutive equations

The damage model is completely defined by the damage criteria function (Eq. 3.13), the damage evolution law (Eq. 3.17), and the loading-unloading (Kuhn-Tucker) conditions defined as:

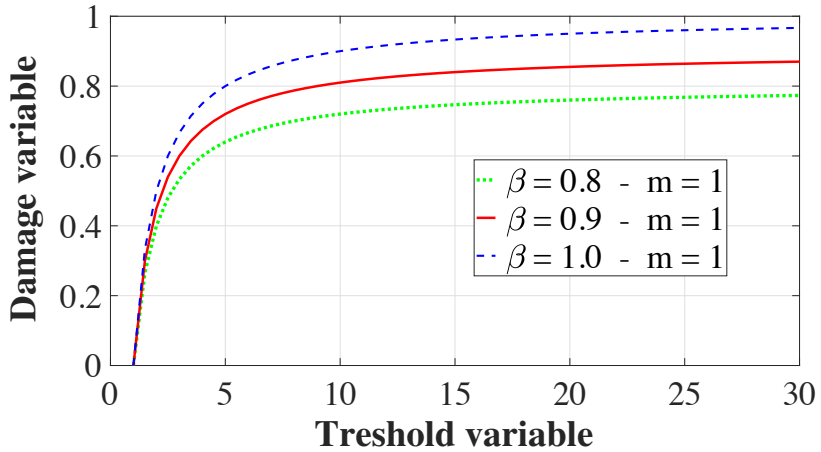
$$f_d^{\pm} \leq 0; \qquad \dot{r}^{\pm} \geq 0; \qquad \dot{r}^{\pm} f_d^{\pm} = 0 \tag{3.23}$$

It follows from Eq. 3.23 that, in addition to define the start of the damage evolution process, the damage function accomplishes two other important tasks. First, it identifies the loading and unloading states, and second, it controls the activation and deactivation of the damage variable growth [43]. Lastly, it can be concluded from Eqs. 3.13 and 3.23 that the value of the damage threshold variables for a time t can be defined as:

$$r^{\pm} = max\left\{r_0^{\pm}, max_{(0\leq x\leq t)}\left(\bar{\tau}_x^{\pm}\right)\right\} \tag{3.24}$$



(a) Cauchy stress, σ^-.



(b) Damage variable, ω^-.

Figure 3.3: Damage evolution law for compressive hardening.

3.4 Orthotropic plasticity model

It was previously observed in Chapter 2 that wood local failure in compression is ductile. Moreover, mild hardening and permanent deformation accumulation take place before crushing occurs. A pure damage model is perfectly capable of simulating the nonlinear responses associated with both brittle and ductile failure mode types. However, if the magnitude of the permanent deformations generated during the compressive post-elastic regime needs to be quantified, a plasticity model should also be incorporated. Two alternative approaches are possible for the coupling of plasticity and damage in light of the definition of the two parallel stress spaces (nominal and effective) discussed above, depending on whether the plasticity part is formulated in the nominal Cauchy stress space or the effective stress space. From a physical point of view, plasticity in compression occurs in the material matrix, between voids and cracks, leading to local hardening behavior [28]. In this sense, the effective stress tensor, which is defined to act only over the undamaged material matrix, offers a more consistent stress space for plasticity formulation [158].

There are also some numerical considerations which favour the definition of plasticity in the effective stress space. In order to obtain a unique solution (Local Uniqueness Condition), plasticity algorithms based on nominal stresses require the introduction of strong hardening [58]. However, Fig. 2.1 shows that slight hardening plasticity is the characteristic behaviour of timber under compressive stresses. Therefore, a nominal stress based plasticity model, which requires the introduction of strong hardening in order to be numerically stable, is not a suitable alternative for wood. By contrast, hardening plasticity is not a requirement of Local Uniqueness in the effective stress space [58]. In light of this, the wood constitutive model employed herein computes the plastic strains and updates the compressive stress component in the effective stress space, before assessing the damage state. This configures a second important reason for ensuring the symmetry of the effective stress tensor, by coupling the plasticity model with a scalar (instead of a tensor) damage model. Therefore, based on the characteristic strain tensor decomposition of plasticity theory, the relationship between the compressive components of the effective stress tensor, $\bar{\boldsymbol{\sigma}}^{-}$, the total strain tensor, $\boldsymbol{\epsilon}^{-}$, the elastic strain tensor, $\boldsymbol{\epsilon}^{e^{-}}$, and the plastic strain tensor, $\boldsymbol{\epsilon}^{p}$, is defined as:

$$\bar{\boldsymbol{\sigma}}^{-} = \boldsymbol{D}^{e} : \boldsymbol{\epsilon}^{e^{-}} = \boldsymbol{D}^{e} : \left(\boldsymbol{\epsilon}^{-} - \boldsymbol{\epsilon}^{p}\right) \tag{3.25}$$

3.4.1 General orthotropic yield function

The three components of the plasticity model are the yield function, the plasticity flow rule and the hardening variable evolution law. The general orthotropic yield criterion proposed by Oller et al. [126] in combination with isotropic hardening is adopted herein for the compressive component of the effective stress tensor ($\bar{\boldsymbol{\sigma}}^-$) such that:

$$f_p = \frac{1}{2}\bar{\boldsymbol{\sigma}}^{-T}\boldsymbol{P}(k)\bar{\boldsymbol{\sigma}}^- + \bar{\boldsymbol{\sigma}}^{-T}\boldsymbol{q}(k) - \bar{\sigma}_y^2(k) \tag{3.26}$$

where the reference yield stress, $\bar{\sigma}_y$, the mapping matrix, $\boldsymbol{P}$, and the mapping vector, $\boldsymbol{q}$, are functions of the isotropic plastic hardening variable, k. It should be noted that hereafter all the equations are formulated in Voigt's notation, except when indicated otherwise:

$$\boldsymbol{P} = \bar{\sigma}_y^2(k)\begin{bmatrix} \boldsymbol{\Omega} & 0 \\ 0 & \boldsymbol{\Gamma} \end{bmatrix}; \boldsymbol{\Omega} = \begin{bmatrix} \chi_1 & -\chi_4 & -\chi_5 \\ -\chi_4 & \chi_2 & -\chi_6 \\ -\chi_5 & -\chi_6 & \chi_3 \end{bmatrix}; \boldsymbol{\Gamma} = \begin{bmatrix} \chi_7 & 0 & 0 \\ 0 & \chi_8 & 0 \\ 0 & 0 & \chi_9 \end{bmatrix} \tag{3.27}$$

$$\boldsymbol{q} = \bar{\sigma}_y^2(k)\begin{bmatrix} \chi_{10} & \chi_{11} & \chi_{12} & 0 & 0 & 0 \end{bmatrix}^T \tag{3.28}$$

The coefficients χ_i $(i = 1, ..., 12)$ are defined in terms of timber anisotropic yield stresses $\left(f_X^{\pm}, f_Y^{\pm}, f_Z^{\pm}, f_{XY}, f_{XY}, f_{ZX}\right)$ and the parameters λ_{XY}, λ_{XZ}, λ_{XY}, β_X, β_Y and β_Z such that:

$$\begin{cases} \chi_1 = \frac{2}{f_X^+(k)\cdot f_X^-(k)}, & \chi_2 = \frac{2}{f_Y^+(k)\cdot f_Y^-(k)}, & \chi_3 = \frac{2}{f_Z^+(k)\cdot f_Z^-(k)}, \\ \chi_4 = \frac{\lambda_{XY}}{\sqrt{f_X^+(k)\cdot f_X^-(k)\cdot f_Y^+(k)\cdot f_Y^-(k)}}, & \chi_5 = \frac{\lambda_{XZ}}{\sqrt{f_X^+(k)\cdot f_X^-(k)\cdot f_Z^+(k)\cdot f_Z^-(k)}}, & \chi_6 = \frac{\lambda_{YZ}}{\sqrt{f_Y^+(k)\cdot f_Y^-(k)\cdot f_Z^+(k)\cdot f_Z^-(k)}}, \\ \chi_7 = \frac{2}{f_{XY}^2(k)}, & \chi_8 = \frac{2}{f_{YZ}^2(k)}, & \chi_9 = \frac{2}{f_{ZX}^2(k)}, \\ \chi_{10} = \frac{2\beta_X}{\sqrt{f_X^+(k)\cdot f_X^-(k)}}, & \chi_{11} = \frac{2\beta_Y}{\sqrt{f_Y^+(k)\cdot f_Y^-(k)}}, & \chi_{12} = \frac{2\beta_Z}{\sqrt{f_Z^+(k)\cdot f_Z^-(k)}} \end{cases} \tag{3.29}$$

The values assigned to the parameters λ and β [126] reduce the general formulation of Eq. 3.26 to several classic quadratic orthotropic yield functions, frequently employed as failure criterion for timber structures (e.g. Hill, Hoffman, Tsai-Wu). The types of quadratic yield surfaces that can be obtained by this general formulation are diverse

(e.g. open, closed, pressure-dependent, pressure-independent). However, as discussed in Section 2.4, currently there is no general consensus on which of these orthotropic failure surfaces provides a better approximation of timber elastic boundary when subjected to a general loading. Nonetheless, good prediction of experimental test results have been reported for particular boundary and loading conditions, which led to valuable recommendations for choosing a proper timber failure criteria [114, 24, 89, 123, 117]. As a matter of fact, the definition of a general timber yield surface is an ongoing research topic that requires much more experimental and numerical work to be carried out.

In agreement with the observed experimental behaviour (Fig. 2.1) and the material model hypothesis adopted, the plasticity constitutive relation in Eq. 3.25 and the yield function in Eq. 3.26 are defined in terms of the compressive part of the effective stress tensor only. Thus, the proposed model considers a damage-only behaviour in tension with no plastic response. However, the incorporation of tensile yield stresses (f_X^+, f_Y^+, and f_Z^+) is still required for the definition of pressure-dependent yield criteria [110].

On the other hand, linear hardening functions are defined for each of the timber yield stresses and the reference yield stress, in terms of the isotropic hardening variable k and the hardening moduli ($h_X^\pm$, $h_Y^\pm$, $h_Z^\pm$, h_{XY}, h_{YZ}, h_{ZX}, and h) such that:

$$\begin{cases} f_X^\pm = f_{X,0}^\pm + h_X^\pm \cdot k, & f_Y^\pm = f_{Y,0}^\pm + h_Y^\pm \cdot k, & f_Z^\pm = f_{Z,0}^\pm + h_Z^\pm \cdot k, \\ f_{XY} = f_{XY,0} + h_{XY} \cdot k, & f_{YZ} = f_{YZ,0} + h_{YZ} \cdot k, & f_{ZX} = f_{ZX,0} + h_{ZX} \cdot k \end{cases} \tag{3.30}$$

$$\bar{\sigma}_y = \bar{\sigma}_{y,0} + h \cdot k \tag{3.31}$$

Besides, proportional hardening is assumed in all directions [110] for easiness of numerical implementation:

$$\frac{h_X^\pm}{f_X^\pm} = \frac{h_Y^\pm}{f_Y^\pm} = \frac{h_Z^\pm}{f_Z^\pm} = \frac{h_{XY}}{f_{XY}} = \frac{h_{YZ}}{f_{YZ}} = \frac{h_{ZX}}{f_{ZX}} = \frac{h}{\bar{\sigma}_y} \tag{3.32}$$

which, combined with Eqs. 3.30 and 3.31 leads to:

$$\frac{f_{X,0}^\pm}{f_X^\pm} = \frac{f_{Y,0}^\pm}{f_Y^\pm} = \frac{f_{Z,0}^\pm}{f_Z^\pm} = \frac{f_{XY,0}}{f_{XY}} = \frac{f_{YZ,0}}{f_{YZ}} = \frac{f_{ZX,0}}{f_{ZX}} = \frac{\bar{\sigma}_{y,0}}{\bar{\sigma}_y} \tag{3.33}$$

Finally, replacing Eqs. 3.33 and 3.29 in Eqs. 3.27 and 3.28:

$$\boldsymbol{P} = \bar{\sigma}_{y,0}^2 \begin{bmatrix} \boldsymbol{\Omega} & 0 \\ 0 & \boldsymbol{\Gamma} \end{bmatrix}; \boldsymbol{\Omega} = \begin{bmatrix} \chi_{1,0} & -\chi_{4,0} & -\chi_{5,0} \\ -\chi_{4,0} & \chi_{2,0} & -\chi_{6,0} \\ -\chi_{5,0} & -\chi_{6,0} & \chi_{3,0} \end{bmatrix}; \boldsymbol{\Gamma} = \begin{bmatrix} \chi_{7,0} & 0 & 0 \\ 0 & \chi_{8,0} & 0 \\ 0 & 0 & \chi_{9,0} \end{bmatrix} \tag{3.34}$$

$$\boldsymbol{q} = \bar{\sigma}_y(k) \cdot \bar{\sigma}_{y,0} \begin{bmatrix} \chi_{10,0} & \chi_{11,0} & \chi_{12,0} & 0 & 0 & 0 \end{bmatrix}^T \tag{3.35}$$

which renders $\boldsymbol{P}$ independent from the reference yield stress, while $\boldsymbol{q}$ becomes a linear (not quadratic any more) function of the reference yield stress. Moreover, the condition in Eq. 3.33 allows the definition of the coefficients $\chi_{i,0}$ (as per Eq. 3.29) to be maintained, but now in terms of the initial yield stresses, instead of the current yield stresses. This means that the coefficients $\chi_{i,0}$ become constants and independent from the hardening variable k. Furthermore, the initial value of the reference yield stress is equal to one (e.g. $\bar{\sigma}_{y,0} = 1$ MPa). Accordingly, based on the new definition of the mapping matrix and vector, the general orthotropic yield function with isotropic proportional hardening becomes:

$$f_p = \frac{1}{2} \bar{\boldsymbol{\sigma}}^{-T} \boldsymbol{P} \bar{\boldsymbol{\sigma}}^{-} + \bar{\boldsymbol{\sigma}}^{-T} \boldsymbol{q}(k) - \bar{\sigma}_y^2(k) \tag{3.36}$$

3.4.2 Plastic flow rule and strain-hardening law

The flow rule for associated plasticity is given by:

$$\dot{\boldsymbol{\epsilon}}^p = \dot{\lambda} \boldsymbol{n} \left(\bar{\boldsymbol{\sigma}}^{-}, k \right) \tag{3.37}$$

$$\boldsymbol{n} = \left(\frac{\partial f_p \left(\bar{\boldsymbol{\sigma}}^{-}, k \right)}{\partial \bar{\boldsymbol{\sigma}}^{-}} \right)^T = \boldsymbol{P} \bar{\boldsymbol{\sigma}}^{-} + \boldsymbol{q}(k) \tag{3.38}$$

where $\dot{\lambda}$ is the plastic multiplier and $\boldsymbol{n}$ is the tensor normal to the yield surface. Likewise, the normalized strain-hardening evolution law is defined as:

$$\dot{k} = \dot{\lambda} \sqrt{\boldsymbol{n}^T \boldsymbol{T} \boldsymbol{n}} \tag{3.39}$$

where $\boldsymbol{T}$ defined as:

$$\boldsymbol{T} = diag\,[0,\ 1,\ 1,\ 0,\ 1/2,\ 0] \tag{3.40}$$

ensures that only the normal and shear plastic strain components in the direction perpendicular to the grain contribute to the increment of the plasticity hardening variable. Finally, to complete the formulation of the plasticity model, the following loading-unloading conditions are assumed:

$$f_p \leq 0; \quad \dot{\lambda} \geq 0; \quad \dot{\lambda} f_p = 0 \tag{3.41}$$

3.4.3 Hardening modulus

The hardening modulus can be expressed (from Eqs. 3.30 and 3.31) as:

$$\begin{cases} \frac{\mathrm{d}f_X^{\pm}}{\mathrm{d}k} = h_X^{\pm}, & \frac{\mathrm{d}f_Y^{\pm}}{\mathrm{d}k} = h_Y^{\pm}, & \frac{\mathrm{d}f_Z^{\pm}}{\mathrm{d}k} = h_Z^{\pm}, \\ \frac{\mathrm{d}f_{XY}}{\mathrm{d}k} = h_{XY}, & \frac{\mathrm{d}f_{YZ}}{\mathrm{d}k} = h_{YZ}, & \frac{\mathrm{d}f_{ZX}}{\mathrm{d}k} = h_{ZX}, \\ & \frac{\mathrm{d}\bar{\sigma}_y}{\mathrm{d}k} = h & \end{cases} \tag{3.42}$$

Therefore, the hardening modulus is an input parameter of the plasticity model which can be directly obtained from the uniaxial stress-strain diagram of the material in any of the orthotropic directions. In the case of wood, it is appropriate to define the value of the hardening modulus using the compressive stress-strain curve in the direction perpendicular to the grain (Y or Z axes). Besides, in line with the plasticity consistency condition, plastic flow can take place only if the value of the yield function is equal to zero and remains constant for at least one instant of time ($f_p = 0 \ \wedge \ \dot{f}_p = 0$) [29], the following plasticity condition can be obtained from Eq. 3.36 for a uniaxial compressive stress state in the Z direction:

$$\dot{f}_p = \bar{\sigma}_{y,0}^2 \cdot \chi_{3,0} \cdot \bar{\sigma}_Z \cdot \dot{\bar{\sigma}}_Z + \bar{\sigma}_{y,0} \cdot \chi_{12,0} \cdot \left(\dot{\bar{\sigma}}_Z \cdot \bar{\sigma}_y + \bar{\sigma}_Z \cdot \frac{\mathrm{d}\bar{\sigma}_y}{\mathrm{d}k} \dot{k} \right) - 2\bar{\sigma}_y \frac{\mathrm{d}\bar{\sigma}_y}{\mathrm{d}k} \dot{k} = 0 \tag{3.43}$$

By recalling the definition of hardening modulus (Eq.3.42), and re-arranging for the

particular case of uniaxial plasticity, the following expression can be obtained:

$$h = \frac{\bar{\sigma}_{y,0} \cdot \chi_{12,0} + \bar{\sigma}_{y,0}^2 \cdot \chi_{3,0} \left(\frac{\bar{\sigma}_Z}{\bar{\sigma}_y}\right)}{\bar{\sigma}_{y,0} \cdot \chi_{12,0} \left(\frac{\bar{\sigma}_Z}{\bar{\sigma}_y}\right) - 2} \cdot \frac{\partial \bar{\sigma}_Z}{\partial \epsilon_Z^p} \tag{3.44}$$

where

$$\frac{\bar{\sigma}_Z}{\bar{\sigma}_y} = \frac{1}{\bar{\sigma}_{y,0}} \frac{-\chi_{12,0} - \sqrt{(\chi_{12,0})^2 + 2\chi_{3,0}}}{\chi_{3,0}} \tag{3.45}$$

And since $\bar{\sigma}_Z$ is negative (compression) and the reference yield stress is always higher or equal to one ($\bar{\sigma}_y \geq 1$), the ratio $\frac{\bar{\sigma}_Z}{\bar{\sigma}_y}$ corresponds to the negative root of the yield function ($f_p = 0$). The substitution of the coefficients $\chi_{3,0}$ and $\chi_{12,0}$ (Eq. 3.29) in Eqs. 3.44 and 3.45 leads to:

$$h = \frac{\bar{\sigma}_{y,0}}{f_{Z,0}^-} \frac{\partial \bar{\sigma}_Z}{\partial \epsilon_Z^p} \tag{3.46}$$

Finally, the following expression can be used to calculate the derivative of the uniaxial effective stress with respect to the plastic strain in terms of the elastic (E_Z) and plastic tangent (T_Z) moduli:

$$\frac{\partial \bar{\sigma}_Z}{\partial \epsilon_Z^p} = \frac{E_Z \cdot T_Z}{E_Z - T_Z} \tag{3.47}$$

3.4.4 Integration of the stress-strain rate equation

The backward Euler method is employed herein to integrate the stress-strain rate equations. To this end, the finite increment counterpart of the plasticity flow rule in Eq. 3.37 is expressed as:

$$\Delta \boldsymbol{\epsilon}^p = \Delta\lambda \boldsymbol{n} \left(\bar{\boldsymbol{\sigma}}^-, k\right) \tag{3.48}$$

Correspondingly, Eq. 3.25 is also reformulated for the compressive component of the effective stress as:

$$\Delta \bar{\boldsymbol{\sigma}}^- = \boldsymbol{D}^e \Delta \boldsymbol{\epsilon}^- - \Delta\lambda \boldsymbol{D}^e \boldsymbol{n} \left(\bar{\boldsymbol{\sigma}}^-, k\right) \tag{3.49}$$

Before the load increment is applied, the compressive component of the total strain increment, $\Delta\boldsymbol{\epsilon}^{-}$, the compressive component of the initial effective stress, $\bar{\boldsymbol{\sigma}}_{j}^{-}$, and the hardening modulus, h, are known. The addition of $\bar{\boldsymbol{\sigma}}_{j}^{-}$ to both sides of Eq. 3.49 makes it possible to obtain the final compressive effective stress, $\bar{\boldsymbol{\sigma}}_{j+1}^{-}$, as an elastic predictor-plastic corrector process in which $\bar{\boldsymbol{\sigma}}^{e^{-}}$ is the trial elastic compressive effective stress:

$$\bar{\boldsymbol{\sigma}}_{j+1}^{-} = \bar{\boldsymbol{\sigma}}^{e^{-}} - \Delta\lambda_{j+1}\boldsymbol{D}^{e}\boldsymbol{n}\left(\bar{\boldsymbol{\sigma}}_{j+1}^{-}, k_{j+1}\right); \quad \bar{\boldsymbol{\sigma}}^{e^{-}} = \bar{\boldsymbol{\sigma}}_{j}^{-} + \boldsymbol{D}^{e}\Delta\boldsymbol{\epsilon}_{j+1}^{-} \tag{3.50}$$

Substituting Eq. 3.38 into Eq. 3.50:

$$\bar{\boldsymbol{\sigma}}_{j+1}^{-} = \boldsymbol{A}^{-1}\left(\Delta\lambda_{j+1}\right)\left[\boldsymbol{D}^{e^{-1}}\bar{\boldsymbol{\sigma}}^{e^{-}} - \Delta\lambda_{j+1}\boldsymbol{q}(k_{j+1})\right]; \;\; \boldsymbol{A} = \boldsymbol{D}^{e^{-1}} + \Delta\lambda_{j+1}\boldsymbol{P} \tag{3.51}$$

Besides, two additional equations can be derived from the hardening law (Eq. 3.39) and the yield function (Eq. 3.36) such that:

$$\Delta k_{j+1} = \Delta\lambda_{j+1}\sqrt{\boldsymbol{n}^{T}\left(\bar{\boldsymbol{\sigma}}_{j+1}^{-}, k_{j+1}\right)\boldsymbol{T}\boldsymbol{n}\left(\bar{\boldsymbol{\sigma}}_{j+1}^{-}, k_{j+1}\right)} \tag{3.52}$$

$$f_{p} = \frac{1}{2}{\bar{\boldsymbol{\sigma}}_{j+1}^{-}}^{T}\boldsymbol{P}\bar{\boldsymbol{\sigma}}_{j+1}^{-} + {\bar{\boldsymbol{\sigma}}_{j+1}^{-}}^{T}\boldsymbol{q}\left(k_{j+1}\right) - \bar{\sigma}_{y}^{2}\left(k_{j+1}\right) \tag{3.53}$$

In this way, the system of three equations (Eqs. 3.51 to 3.53) with three unknowns ($\bar{\boldsymbol{\sigma}}_{j+1}^{-}, k_{j+1}$ and $\Delta\lambda_{j+1}$) is completely defined. This system can be reduced to one system of two equations with two unknowns (Δk_{j+1} and $\Delta\lambda_{j+1}$):

$$\begin{cases} F = \Delta k_{j+1} - \Delta\lambda_{j+1}\sqrt{\boldsymbol{n}^{T}\left(\Delta\lambda_{j+1}, \Delta k_{j+1}\right)\boldsymbol{T}\boldsymbol{n}\left(\Delta\lambda_{j+1}, \Delta k_{j+1}\right)} = 0 \\ f_{p} = \frac{1}{2}{\bar{\boldsymbol{\sigma}}_{j+1}^{-}}^{T}\left(\Delta\lambda_{j+1}, \Delta k_{j+1}\right)\boldsymbol{P}\bar{\boldsymbol{\sigma}}_{j+1}^{-}\left(\Delta\lambda_{j+1}, \Delta k_{j+1}\right) + {\bar{\boldsymbol{\sigma}}_{j+1}^{-}}^{T}\left(\Delta\lambda_{j+1}, \Delta k_{j+1}\right)\boldsymbol{q}\left(\Delta k_{j+1}\right) \\ \qquad\qquad - \bar{\sigma}_{y}^{2}\left(\Delta k_{j+1}\right) = 0 \end{cases} \tag{3.54}$$

which implies the following relationship between the final hardening variable and its increment:

$$k_{j+i} = k_{j} + \Delta k_{j+1} \tag{3.55}$$

The solution of Eq. 3.54 can be obtained by means of an iterative method like Newton-Raphson as outlined in Appendix A.

3.5 Computational implementation

3.5.1 Numerical considerations for plasticity and damage coupling under load reversals

Some numerical aspects need to be accounted for when formulating a coupled damage-plasticity model such as the well-known mesh-dependency problem of finite element approximations with softening inelastic behaviour [28]. This issue is not relevant for wood in compression since hardening plasticity and hardening damage evolution are considered. However, for wood in tension, the development of fracture zones produces softening [59] which is expressed mathematically by the damage evolution law in Eq. 3.19. In order to avoid mesh-dependency, a crack band regularization technique [5] is employed here. Accordingly, the softening damage evolution law is adjusted through the incorporation of the characteristic length (l_{ch}) in Eq. 3.20, which is assumed to be equal to the cubic root of the volume of the finite elements of the model mesh.

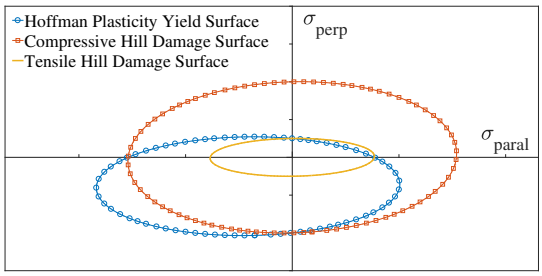
Additionally, the damage criterion functions formulated only in terms of the total strain (without considering the influence of plastic strains) can generate spurious high tensile strengths. This artificial rise of the tensile strength delays the start of the damage process when a tension reversal loading is applied after the occurrence of a plastic flow in compression [58]. This is the reason why the equivalent stress defined in Eq. 3.14 is expressed in terms of the effective stress tensor, which is a function of the elastic strain or, analogously, of both the total and plastic strains [79]. This approach is essential for an appropriate definition of the damage function for cyclic loading applications.

Furthermore, it is proposed that the coupling of damage and plasticity formulations occurs exclusively in the compressive component of the effective stress space. Conversely, the tensile component of the effective stress is governed by a pure damage model (no plasticity), and as a consequence, there is no need of coupling between damage and plasticity. This is grounded on the typical post-elastic behaviour of wood in both tensile and compressive stress states, as particularly important and original to the proposed model.

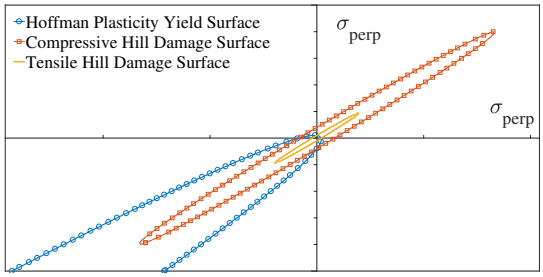
Since there is no experimental evidence for an equivalent behaviour to the Bauschinger effect in wood subjected to cyclic loading, there is no reason for incorporating a kinematic hardening rule in the plasticity part of the model. Besides, considering that in the pro-

posed model plasticity would only be valid for the compressive component of the stress tensor, the relevance of such a kinematic hardening would be arguable. Nevertheless, the different progressions of the elastic boundaries in tension and compression are governed by the two damage variables. Likewise, the influence of loading in one direction on the elasticity boundary on the alternative direction is defined by the concepts of "structural damage", characteristic of tensile failure, and "constitutive damage", characteristic of compressive failure [132]. The structural damage in tension does not affect the stiffness degradation or the strength of the material when a load reversal is applied in compression (stiffness recovery). In contrast, constitutive damage or crushing does reduce the tensile capacity of the material when a reverse loading from compression to tension occurs [118], meaning that the tensile damage variable should not be less than the compressive damage variable (i.e. $\omega^+ \geq \omega^-$). Numerical difficulties may arise, however, if based on the constitutive damage concept, an update of the tensile damage variable in function of the compressive damage variable is intended even when the tensile damage function is not activated (i.e. $f_d^+ < 0$). Therefore, it is better to perform this update only if the tensile damage function is already activated.

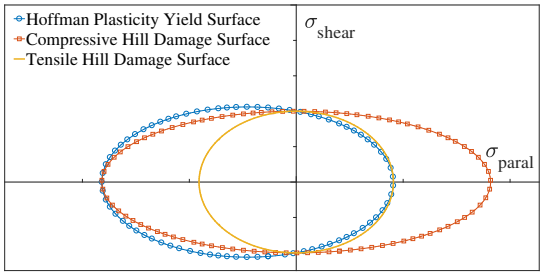
Fig. 3.4 shows the initial ($r^{\pm} = r_0^{\pm} = 1$) elastic boundaries in tension and compression according to Hill's damage criteria (Eqs. 3.13 and 3.14), and the initial plasticity surface ($k = 0$) according to Hoffman particular case of the general orthotropic yield function in Eq. 3.36. All curves in Fig. 3.4 represent the intersection of these multidimensional surfaces with two-dimensional planes (shear stresses and normal stresses parallel and perpendicular to the grain) of the effective stress space. Fig. 3.4a shows that under biaxial compression in the directions parallel and perpendicular to the grain, damage occurs before plasticity, while for mixed tension-compression stress states, an interaction between plasticity in compression and damage in tension prevails. Similarly, for biaxial compression in the plane perpendicular to the grain, Fig. 3.4b shows that damage occurs before plasticity as well. What is more, due to the elliptic paraboloid shape and the pressure dependency of the Hoffman surface, plasticity is unlikely to occur for a hydrostatic compression. In this plane, an interaction between tensile damage and plasticity can also be appreciated for mixed biaxial tension-compression stress state. Finally, Figs. 3.4c and 3.4d show the interaction of shear with normal stresses in both parallel and perpendicular to the grain directions, respectively. In the same way than in the previous cases, damage is activated earlier than plasticity when compression normal stresses interact with shear stresses. However, the distance between both compressive damage and plasticity surfaces is considerably smaller than in the case of biaxial normal stress (in the direction parallel to the grain, Fig. 3.4c, both surfaces are almost coincident in compression). This



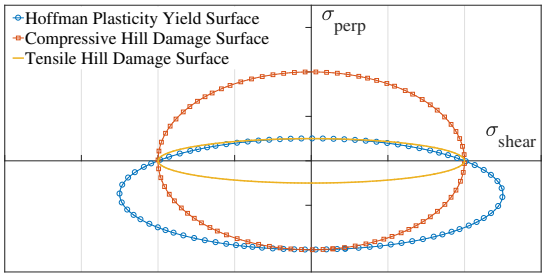
(a) Plane of normal stresses in the directions parallel and perpendicular to the grain.



(b) Plane of normal stresses in the directions perpendicular to the grain.



(c) Plane of normal stress in the direction parallel to the grain and shear stress.



(d) Plane of normal stress in the direction perpendicular to the grain and shear stress.

Figure 3.4: Initial compressive and tensile Hill's damage surface and initial Hoffman's plasticity yield surface.

clearly indicates that for this type of plasticity yield function a stress state including shear stresses is more critical than one of normal stresses only. In the tension zone, the interaction of shear and normal stresses is governed exclusively by the tensile damage surface.

All the characteristics discussed above are consistent with the expected behaviour of wood where compressive behaviour, with or without shear, is governed by the combination of plasticity and damage, with the latter occurring before the former. It is also expected that a combination of shear stresses with compression stresses produce a ductile failure in which plasticity plays the most important role. By contrast, a hydrostatic biaxial compression is assumed to cause failure due to crushing, and therefore, damage plays the most important role. On the other hand, in any stress state in which tension normal stresses are present, the tensile damage surface clearly prevails over the other two. Noticeably, these initial surfaces will expand once the applied stresses magnitudes reach them and the inelastic behaviour starts.

3.5.2 Algorithm design

Fig. 3.5 shows a schematic representation of the three key components of the proposed plasticity-damage constitutive model for timber, and the particular characteristics of timber nonlinear behaviour which are captured by each of them. Furthermore, a detailed scheme of the plasticity-damage model algorithm is presented in Table 3.1. First, the total elastic trial effective stress is calculated (Step 1). Then the spectral decomposition of this stress tensor is performed and its eigenvalues and eigenvectors are saved (Step 2). In the next step the compressive component of the trial effective stress is evaluated into the yield function to determine if there is plasticity or not. In case of plasticity, the Newton-Raphson algorithm is executed, the compressive effective stress, the plastic multiplier and the hardening variable are updated, while the increment of the plastic strain vector is calculated (Step 3). Then, both effective compressive and tensile stress components are evaluated in their corresponding damage functions. If there is damage for any of the stress components, the value of the damage variable is updated using the corresponding damage evolution law (Step 4). The Cauchy nominal stress is calculated (Step 5) and delivered as the main output parameter of the constitutive model. Finally, the total and plastic strains are updated (Step 6), while the consistent plasticity-damage tangent stiffness matrix (Step 7) is calculated to be delivered as output parameter of the model.

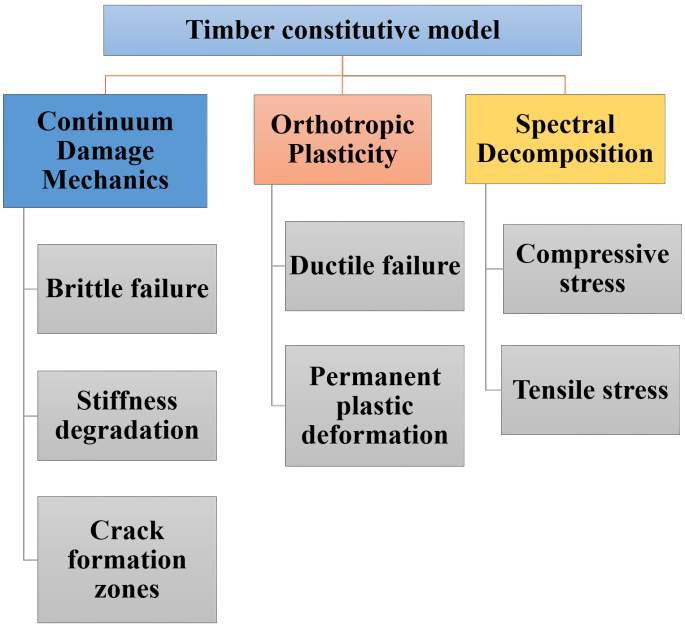


Figure 3.5: Key components of the plasticity-damage timber constitutive model.

Table 3.1: Plasticity-damage timber constitutive model algorithm

Initial values: $\boldsymbol{\epsilon}_0 = \mathbf{0}$; $\boldsymbol{\epsilon}_0^p = \mathbf{0}$; $\bar{\boldsymbol{\sigma}}_0^{\pm} = \mathbf{0}$; $k_0 = 0$; $\omega_0^{\pm} = 0$; $r_0^{\pm} = 1$

Load step input parameters: $\Delta\boldsymbol{\epsilon}_{j+1}$, $\boldsymbol{\epsilon}_j$, $\boldsymbol{\epsilon}_j^p$, $\bar{\boldsymbol{\sigma}}_j^{\pm}$, k_j, $\omega_j^{\pm}$, $r_j^{\pm}$

1. Calculate the total elastic trial effective stress tensor:

$$\bar{\boldsymbol{\sigma}}^e = \bar{\boldsymbol{\sigma}}_j^+ + \bar{\boldsymbol{\sigma}}_j^- + \boldsymbol{D}^e \Delta\boldsymbol{\epsilon}$$

2. Spectral decomposition of the total elastic trial effective stress tensor:

   2.1. Obtain the eigenvalues and eigenvectors for $i = 1, 2, 3$

   2.2. Calculate the compressive and tensile components:

$$\text{Eq. 3.10} \rightarrow \bar{\boldsymbol{\sigma}}_{j+1}^+ \qquad \text{Eq. 3.11} \rightarrow \bar{\boldsymbol{\sigma}}_{j+1}^-$$

3. Plasticity verification for the compressive component only:

   3.1. Evaluate the yield function

$$\text{Eq. 3.36} \rightarrow f_p(\bar{\boldsymbol{\sigma}}_{j+1}^-, k_j) = \tfrac{1}{2} {\bar{\boldsymbol{\sigma}}_{j+1}^-}^T \boldsymbol{P} \bar{\boldsymbol{\sigma}}_{j+1}^- + {\bar{\boldsymbol{\sigma}}_{j+1}^-}^T \boldsymbol{q}(k_j) - \bar{\sigma}_y^2(k_j) \ < 0 \ ?$$

   3.2. YES $\rightarrow$ No plasticity

$$\Delta\lambda_{j+1} = 0; \ \ k_{j+1} = k_j; \ \ \Delta\boldsymbol{\epsilon}_{j+1}^p = \mathbf{0}$$

   3.3. NO $\rightarrow$ Plasticity algorithm

      3.3.1. Assign the compressive elastic trial effective stress tensor

$$\bar{\boldsymbol{\sigma}}^{e^-} = \bar{\boldsymbol{\sigma}}_{j+1}^-$$

      3.3.2. Initiation of the unknown variables

$$\Delta\lambda_{j+1}^0 = 0; \ \ \Delta k_{j+1}^0 = 0$$

      3.3.3. Calculate $\Delta\lambda_{j+1}$ and Δk_{j+1}: Newton-Raphson algorithm for

iteration i

Eq. 3.55 $\rightarrow k_{j+1}^{i} = k_j + \Delta k_{j+1}^{i}$

Eq. 3.31 $\rightarrow \bar{\sigma}_{y,j+1}^{i} = \bar{\sigma}_{y,0} + h \cdot k_{j+1}^{i}$

Eq. 3.35 $\rightarrow \boldsymbol{q}\left(\Delta k_{j+1}^{i}\right)$

Eq. 3.51 $\rightarrow \bar{\boldsymbol{\sigma}}_{j+1}^{-\,i}\left(\Delta\lambda_{j+1}^{i}, \Delta k_{j+1}^{i}\right)$

Eq. 3.38 $\rightarrow \boldsymbol{n}_{j+1}^{i}\left(\bar{\boldsymbol{\sigma}}_{j+1}^{-\,i}, \Delta k_{j+1}^{i}\right)$

$\boldsymbol{b}_{j+1}^{i+1} = \boldsymbol{b}_{j+1}^{i} - (\boldsymbol{J}_{j+1}^{i})^{-1}\boldsymbol{r}_{j+1}^{i}$

where $\boldsymbol{b}$, $\boldsymbol{r}$, and $\boldsymbol{J}$ are the unknown variables vector, the residuals vector, and the Jacobian matrix, respectively (Appendix A)

Do while $\left|\boldsymbol{r}_{j+1}^{i+1}\right| >$ tolerance

3.3.4. Calculate the compressive effective stress tensor and the plastic strain tensor increment:

Eq. 3.51 $\rightarrow \bar{\boldsymbol{\sigma}}_{j+1}^{-}\left(\Delta\lambda_{j+1}, k_{j+1}\right)$
Eq. 3.48 $\rightarrow \Delta\boldsymbol{\epsilon}_{j+1}^{p}\left(\bar{\boldsymbol{\sigma}}_{j+1}^{-}, \Delta\lambda_{j+1}, k_{j+1}\right)$

4. Damage verification for the tensile and compressive stress components:

4.1. Calculate the equivalent stress and evaluate the damage function

Eq. 3.14 $\rightarrow \bar{\tau}^{\pm} = \sqrt{\frac{1}{2}\bar{\boldsymbol{\sigma}}_{j+1}^{\pm\,T}\boldsymbol{H}^{\pm}\bar{\boldsymbol{\sigma}}_{j+1}^{\pm}}$
Eq. 3.13 $\rightarrow f_d^{\pm}(\bar{\boldsymbol{\sigma}}_{j+1}^{\pm}, r_j^{\pm}) = \bar{\tau}^{\pm} - r_j^{\pm} < 0$?

4.2. YES $\rightarrow$ No damage

$$r_{j+1}^{\pm} = r_j^{\pm};\;\; \omega_{j+1}^{\pm} = \omega_j^{\pm}$$

4.3. NO $\rightarrow$ Damage algorithm

$$r_{j+1}^{\pm} = \bar{\tau}^{\pm}$$
Eq. 3.19 $\rightarrow \omega_{j+1}^{+} = g_d^{+}(r_{j+1}^{+})$
Eq. 3.22 $\rightarrow \omega_{j+1}^{-} = g_d^{-}(r_{j+1}^{-})$

5. Calculate the Cauchy stress tensor:

$$\text{Eq. 3.12} \rightarrow \boldsymbol{\sigma}_{j+1} = (1-\omega^{+}_{j+1})\bar{\boldsymbol{\sigma}}^{+}_{j+1} + (1-\omega^{-}_{j+1})\bar{\boldsymbol{\sigma}}^{-}_{j+1}$$

6. Calculate the total strain and plastic strain tensors:

$$\boldsymbol{\epsilon}_{j+1} = \boldsymbol{\epsilon}_{j} + \Delta\boldsymbol{\epsilon}_{j+1}; \;\; \boldsymbol{\epsilon}^{p}_{j+1} = \boldsymbol{\epsilon}^{p}_{j} + \Delta\boldsymbol{\epsilon}^{p}_{j+1}$$

7. Calculate the consistent plasticity-damage tangent stiffness matrix (Section 3.5.3):

   7.1. Calculate the consistent elasto-plastic tangent stiffness matrix for the compressive stress component ($\boldsymbol{D}^{ep}_{j+1}$)

   7.2. Calculate the compressive and tensile fourth-order tensor operators ($\boldsymbol{Q}^{\pm}_{j+1}$)

   7.3. Calculate the consistent plasticity-damage tangent stiffness matrix ($\boldsymbol{D}^{pd}_{j+1}$)

Output parameters: $\boldsymbol{\sigma}_{j+1}$, $\boldsymbol{D}^{pd}_{j+1}$, $\boldsymbol{\epsilon}_{j+1}$, $\boldsymbol{\epsilon}^{p}_{j+1}$, $\bar{\boldsymbol{\sigma}}^{\pm}_{j+1}$, k_{j+1}, $\omega^{\pm}_{j+1}$, $r^{\pm}_{j+1}$

3.5.3 Consistent plasticity-damage tangent stiffness matrix

The consistent plasticity-damage tangent stiffness matrix, $\boldsymbol{D}^{pd}$, sets the relation between the Cauchy nominal stress rate, $\Delta\boldsymbol{\sigma}$, and the total strain rate, $\Delta\boldsymbol{\epsilon}$. This matrix is employed in the calculation of the global structural tangent stiffness matrix, which ensures the robustness of the Newton-Raphson method by maintaining its quadratic convergence rate [102]. The particular characteristics of the consistent tangent stiffness matrix depend on each constitutive model and may be non-symmetric in many cases, which increases the computational time and numerical complexity. For this reason, some authors recommend the adoption of a nonlinear equation solver which employs only the initial elastic stiffness matrix during the entire analysis, particularly when performing seismic analysis of massive structures [45]. In spite of saving computational time for some specific applications, the use of a unique tangent stiffness matrix is not suitable for problems where high levels of nonlinear post-peak behaviour are expected. In these cases a consistent tangent stiffness matrix needs to be derived, not only to attain the high deformation levels required but also to drastically curtail the number of iterations needed [42].

For the plasticity-damage model proposed herein the consistent tangent stiffness matrix is obtained from the Cauchy stress, Eq. 3.12, as a function of the compressive and tensile threshold variables ($r^{\pm}$) and the total strain tensor increments ($\Delta\boldsymbol{\epsilon}^{\pm}$):

$$\boldsymbol{\sigma} = \left[1-\omega^{+}\left(r^{+}\right)\right]\bar{\boldsymbol{\sigma}}^{+}\left(\Delta\boldsymbol{\epsilon}^{+}\right) + \left[1-\omega^{-}\left(r^{-}\right)\right]\bar{\boldsymbol{\sigma}}^{-}\left(\Delta\boldsymbol{\epsilon}^{-}\right) \tag{3.56}$$

Likewise, the tangent stiffness matrix (in tensor notation) can be defined as:

$$\frac{\mathrm{d}\boldsymbol{\sigma}}{\mathrm{d}\boldsymbol{\epsilon}} = \frac{\partial\boldsymbol{\sigma}}{\partial r^{+}}\otimes\frac{\partial r^{+}}{\partial\boldsymbol{\epsilon}} + \frac{\partial\boldsymbol{\sigma}}{\partial r^{-}}\otimes\frac{\partial r^{-}}{\partial\boldsymbol{\epsilon}} + \frac{\partial\boldsymbol{\sigma}}{\partial\boldsymbol{\epsilon}^{+}}:\frac{\partial\boldsymbol{\epsilon}^{+}}{\partial\boldsymbol{\epsilon}} + \frac{\partial\boldsymbol{\sigma}}{\partial\boldsymbol{\epsilon}^{-}}:\frac{\partial\boldsymbol{\epsilon}^{-}}{\partial\boldsymbol{\epsilon}} \tag{3.57}$$

Based on Eqs. 3.17 and 3.56, the partial differentiation of the Cauchy stress tensor with respect to the threshold variables leads to:

$$\frac{\partial\boldsymbol{\sigma}}{\partial r^{\pm}} = \frac{\partial\boldsymbol{\sigma}}{\partial\omega^{\pm}}\frac{\partial\omega^{\pm}}{\partial r^{\pm}} = -\bar{\boldsymbol{\sigma}}^{\pm}\frac{\partial g_d^{\pm}}{\partial r^{\pm}} \tag{3.58}$$

while on the basis of Eqs. 3.13 and 3.14, the partial differentiation of the threshold variables with respect to the total strain tensor is:

$$\frac{\partial r^{\pm}}{\partial\boldsymbol{\epsilon}} = \frac{\partial r^{\pm}}{\partial\bar{\tau}^{\pm}}\frac{\partial\bar{\tau}^{\pm}}{\partial\bar{\boldsymbol{\sigma}}^{\pm}}:\frac{\mathrm{d}\bar{\boldsymbol{\sigma}}^{\pm}}{\mathrm{d}\boldsymbol{\epsilon}^{\pm}}:\frac{\partial\boldsymbol{\epsilon}^{\pm}}{\partial\boldsymbol{\epsilon}} \tag{3.59}$$

It should be noted, from Eq. 3.24, that $\frac{\partial r^{\pm}}{\partial\bar{\tau}^{\pm}}$ can only be equal to 1, when damage occurs, or 0, when there is no damage. Subsequently, the partial differentiation of the Cauchy stress tensor with respect to the tensile and compressive components of the total strain tensor leads to:

$$\frac{\partial\boldsymbol{\sigma}}{\partial\boldsymbol{\epsilon}^{\pm}} = \frac{\partial\boldsymbol{\sigma}}{\partial\bar{\boldsymbol{\sigma}}^{\pm}}:\frac{\mathrm{d}\bar{\boldsymbol{\sigma}}^{\pm}}{\mathrm{d}\boldsymbol{\epsilon}^{\pm}} = \left(1-\omega^{\pm}\right)\boldsymbol{I}:\frac{\mathrm{d}\bar{\boldsymbol{\sigma}}^{\pm}}{\mathrm{d}\boldsymbol{\epsilon}^{\pm}} \tag{3.60}$$

where $\boldsymbol{I}$ is the unitary fourth-order tensor.

The tensile and compressive components of the effective stress tensor are obtained based on elasticity and plasticity formulations, respectively. Therefore, their total derivatives in function of the corresponding tensile and compressive components of the total strain tensor are precisely the linear-elastic stiffness tensor, $\boldsymbol{D}^{e}$, and the consistent elasto-plastic tangent stiffness tensor, $\boldsymbol{D}^{ep}$:

$$\frac{\mathrm{d}\bar{\boldsymbol{\sigma}}^{+}}{\mathrm{d}\boldsymbol{\epsilon}^{+}} = \boldsymbol{D}^{e} \tag{3.61}$$

$$\frac{\mathrm{d}\bar{\boldsymbol{\sigma}}^{-}}{\mathrm{d}\boldsymbol{\epsilon}^{-}} = \boldsymbol{D}^{ep} \tag{3.62}$$

Therefore, from Eqs. 3.57 to 3.62, the following expression for the consistent plasticity-damage tangent stiffness matrix can be obtained:

$$\begin{aligned}\frac{\mathrm{d}\boldsymbol{\sigma}}{\mathrm{d}\boldsymbol{\epsilon}} = &\left[\left(1-\omega^{+}\right)\boldsymbol{I} - \frac{\partial r^{+}}{\partial \bar{\tau}^{+}}\frac{\partial g_d^{+}}{\partial r^{+}}\bar{\boldsymbol{\sigma}}^{+}\otimes\frac{\partial \bar{\tau}^{+}}{\partial \bar{\boldsymbol{\sigma}}^{+}}\right] : \boldsymbol{D}^{e} : \frac{\partial \boldsymbol{\epsilon}^{+}}{\partial \boldsymbol{\epsilon}} \\ &+ \left[\left(1-\omega^{-}\right)\boldsymbol{I} - \frac{\partial r^{-}}{\partial \bar{\tau}^{-}}\frac{\partial g_d^{-}}{\partial r^{-}}\bar{\boldsymbol{\sigma}}^{-}\otimes\frac{\partial \bar{\tau}^{-}}{\partial \bar{\boldsymbol{\sigma}}^{-}}\right] : \boldsymbol{D}^{ep} : \frac{\partial \boldsymbol{\epsilon}^{-}}{\partial \boldsymbol{\epsilon}}\end{aligned} \tag{3.63}$$

Consistent elasto-plastic tangent stiffness matrix

The elasto-plastic tangent stiffness matrix is obtained consistently with respect to the stress update procedure followed in the corresponding local return mapping algorithm [157, 65]. Noting that the compressive effective stress (Eq. 3.51) is a function of the plastic multiplier increment, $\Delta\lambda$, the hardening variable increment, Δk, and the compressive total strain tensor increment, $\Delta\boldsymbol{\epsilon}^{-}$, then:

$$\bar{\boldsymbol{\sigma}}^{-} = \boldsymbol{A}^{-1}\left(\Delta\lambda\right)\left[\boldsymbol{D}^{e^{-1}}\bar{\boldsymbol{\sigma}}^{e^{-}}\left(\Delta\boldsymbol{\epsilon}^{-}\right) - \Delta\lambda\boldsymbol{q}\left(\Delta k\right)\right] \tag{3.64}$$

The tangent stiffness matrix is obtained from the total differentiation of the compressive effective stress tensor, $\bar{\boldsymbol{\sigma}}^{-}$, with respect to the compressive total strain tensor, $\boldsymbol{\epsilon}^{-}$:

$$\frac{\mathrm{d}\bar{\boldsymbol{\sigma}}^{-}}{\mathrm{d}\boldsymbol{\epsilon}^{-}} = \frac{\partial\bar{\boldsymbol{\sigma}}^{-}}{\partial\boldsymbol{\epsilon}^{-}} + \frac{\partial\bar{\boldsymbol{\sigma}}^{-}}{\partial\Delta\lambda}\frac{\partial\Delta\lambda}{\partial\boldsymbol{\epsilon}^{-}} + \frac{\partial\bar{\boldsymbol{\sigma}}^{-}}{\partial\Delta k}\frac{\partial\Delta k}{\partial\boldsymbol{\epsilon}^{-}} \tag{3.65}$$

On the other hand, based on the Newton-Raphson iterative algorithm for plasticity, the derivative of the plastic multiplier and the hardening variable increments with respect to the compressive total strain can be obtained in terms of the Jacobian matrix, $\boldsymbol{J}$, as follows (see Appendix A):

$$\begin{bmatrix} \frac{\partial\Delta\lambda}{\partial\boldsymbol{\epsilon}^{-}} \\ \frac{\partial\Delta k}{\partial\boldsymbol{\epsilon}^{-}} \end{bmatrix} = \frac{\partial\boldsymbol{b}}{\partial\boldsymbol{\epsilon}^{-}} = -\boldsymbol{J}^{-1}\frac{\partial\boldsymbol{r}}{\partial\boldsymbol{\epsilon}^{-}} = -\boldsymbol{J}^{-1}\begin{bmatrix} \frac{\partial f_p}{\partial\boldsymbol{\epsilon}^{-}} \\ \frac{\partial F}{\partial\boldsymbol{\epsilon}^{-}} \end{bmatrix} \tag{3.66}$$

The substitution of Eq. 3.66 into Eq. 3.65 leads to the expression for the consistent elasto-plastic tangent stiffness matrix D^{ep}:

$$\frac{\mathrm{d}\bar{\boldsymbol{\sigma}}^{-}}{\mathrm{d}\boldsymbol{\epsilon}^{-}} = \boldsymbol{D}^{ep} = \frac{\partial\bar{\boldsymbol{\sigma}}^{-}}{\partial\boldsymbol{\epsilon}^{-}} - \begin{bmatrix} \frac{\partial\bar{\boldsymbol{\sigma}}^{-}}{\partial\Delta\lambda} & \frac{\partial\bar{\boldsymbol{\sigma}}^{-}}{\partial\Delta k} \end{bmatrix}\boldsymbol{J}^{-1}\begin{bmatrix} \frac{\partial f_p}{\partial\boldsymbol{\epsilon}^{-}} \\ \frac{\partial F}{\partial\boldsymbol{\epsilon}^{-}} \end{bmatrix} \tag{3.67}$$

The expressions to calculate the derivatives in Eq. 3.67 and the coefficients of the Jacobian

matrix are derived in Appendix A.

Partial derivatives of the tensile and compressive components of the total strain tensor with respect to the total strain tensor

In order to obtain the expressions of partial the derivatives of the tensile and compressive strain components with respect to the total strain tensor, first the fourth-order tensor operators, $\boldsymbol{Q}^{\pm}$, must be defined:

$$\dot{\boldsymbol{\sigma}}^{e^{\pm}} = \boldsymbol{Q}^{\pm} : \dot{\boldsymbol{\sigma}}^{e} \tag{3.68}$$

$$\boldsymbol{Q}^{-} = \boldsymbol{I} - \boldsymbol{Q}^{+} \tag{3.69}$$

Notice that the previous expressions are defined to be valid in the elastic stress state only, before any plasticity correction is performed for the compressive effective stress component. Therefore, the time derivatives of the elastic effective stresses are defined as follows:

$$\dot{\boldsymbol{\sigma}}^{e} = \boldsymbol{D}^{e} : \dot{\boldsymbol{\epsilon}} \tag{3.70}$$

$$\dot{\boldsymbol{\sigma}}^{e^{\pm}} = \boldsymbol{D}^{e} : \dot{\boldsymbol{\epsilon}}^{\pm} \tag{3.71}$$

From Eq. 3.10, the total differentiation of the tensile elastic effective stress, in tensor notation, is:

$$\mathrm{d}\bar{\boldsymbol{\sigma}}^{e^{+}} = \sum_{i=1}^{3} \left[H\left(\bar{\sigma}_i\right) \left(\boldsymbol{p}_i \otimes \boldsymbol{p}_i\right) \mathrm{d}\bar{\sigma}_i + \langle \bar{\sigma}_i \rangle \mathrm{d}\left(\boldsymbol{p}_i \otimes \boldsymbol{p}_i\right) \right] \tag{3.72}$$

where $H(\cdot)$ is the Heaviside function. The total derivatives of the eigenvalues, $\bar{\sigma}_i$, and eigenvectors, $\boldsymbol{p}_i$, of the elastic effective stress tensor, $\bar{\boldsymbol{\sigma}}^{e}$, can be expressed as [42]:

$$\mathrm{d}\bar{\sigma}_i = \boldsymbol{R}_{ii} : \mathrm{d}\bar{\boldsymbol{\sigma}}^{e} \tag{3.73}$$

$$\mathrm{d}\left(\boldsymbol{p}_i \otimes \boldsymbol{p}_i\right) = 2 \sum_{\substack{j=1 \\ j \neq i}}^{3} \left[\frac{1}{\bar{\sigma}_i - \bar{\sigma}_j} \left(\boldsymbol{R}_{ij} \otimes \boldsymbol{R}_{ij}\right) : \mathrm{d}\bar{\boldsymbol{\sigma}}^{e} \right] \tag{3.74}$$

where the second-order symmetric tensor $\boldsymbol{R}_{ij}$ is defined as:

$$\boldsymbol{R}_{ij} = \frac{1}{2}\left(\boldsymbol{p}_i \otimes \boldsymbol{p}_j + \boldsymbol{p}_j \otimes \boldsymbol{p}_i\right) \tag{3.75}$$

Replacing Eqs. 3.73 and 3.74 into Eq. 3.72, and from the definition given in Eq. 3.68, the tensile fourth-order tensor operator is obtained [42]:

$$\boldsymbol{Q}^{+} = \sum_{i=1}^{3}\left[H\left(\bar{\sigma}_i\right)\left(\boldsymbol{R}_{ii} \otimes \boldsymbol{R}_{ii}\right)\right] + 2\sum_{i=1}^{3}\sum_{\substack{j=1 \\ j \neq i}}^{3}\left[\frac{\langle \bar{\sigma}_i \rangle}{\bar{\sigma}_i - \bar{\sigma}_j}\left(\boldsymbol{R}_{ij} \otimes \boldsymbol{R}_{ij}\right)\right] \tag{3.76}$$

Finally, after substituting Eqs. 3.70 and 3.71 into Eq. 3.68, the derivative of the tensile and compressive strain tensor components as a function of the total strain tensor is obtained as:

$$\frac{\partial \boldsymbol{\epsilon}^{\pm}}{\partial \boldsymbol{\epsilon}} = \boldsymbol{D}^{e^{-1}} : \boldsymbol{Q}^{\pm} : \boldsymbol{D}^{e} \tag{3.77}$$

where $\boldsymbol{Q}^{+}$ and $\boldsymbol{Q}^{-}$ are given by Eqs. 3.76 and 3.69, respectively.

Consistent plasticity-damage tangent stiffness matrix formulation

The final expression of the consistent plasticity-damage tangent stiffness matrix in Voigt's notation can be obtained by replacing Eq. 3.77 into Eq. 3.63:

$$\begin{aligned} \boldsymbol{D}^{pd} = &\left[\left(1-\omega^{+}\right)\boldsymbol{I} - \frac{\partial r^{+}}{\partial \bar{\tau}^{+}}\frac{\partial g_d^{+}}{\partial r^{+}}\bar{\boldsymbol{\sigma}}^{+}\frac{\partial \bar{\tau}^{+}}{\partial \bar{\boldsymbol{\sigma}}^{+}}\right]\boldsymbol{Q}^{+}\boldsymbol{D}^{e} \\ &+\left[\left(1-\omega^{-}\right)\boldsymbol{I} - \frac{\partial r^{-}}{\partial \bar{\tau}^{-}}\frac{\partial g_d^{-}}{\partial r^{-}}\bar{\boldsymbol{\sigma}}^{-}\frac{\partial \bar{\tau}^{-}}{\partial \bar{\boldsymbol{\sigma}}^{-}}\right]\boldsymbol{D}^{ep}\left(\boldsymbol{D}^{e}\right)^{-1}\left(\boldsymbol{Q}^{-}\right)\boldsymbol{D}^{e} \end{aligned} \tag{3.78}$$

3.6 Energy dissipation for tensile brittle failure

The energy dissipated in the post-elastic region after tensile brittle failure can be expressed as the fracture energy density (G_f) of wood normalized by the characteristic

length (l_{ch}) of the finite element discretization such that:

$$\frac{G_f}{l_{ch}} = \int_0^\infty \dot{\gamma}^{d+} \mathrm{d}t \tag{3.79}$$

where the tensile component of the damage energy dissipation rate, $\dot{\gamma}^{d+}$, is:

$$\dot{\gamma}^{d+} = \Psi_0^+ \dot{\omega}^+ \tag{3.80}$$

On the other hand, the effective stress for a uniaxial tensile stress state is expressed as:

$$\bar{\sigma}^+ = \frac{r^+}{r_0^+} f_{max}^+ \tag{3.81}$$

while the total strain is:

$$\epsilon = \frac{1}{E} \frac{r^+}{r_0^+} f_{max}^+ \tag{3.82}$$

And since there is no plastic strain for uniaxial tensile stresses, from Eqs. 3.81 and 3.82 the tensile elastic free energy potential is:

$$\Psi_0^+ = \frac{1}{2E} \left(\frac{r^+}{r_0^+} f_{max}^+ \right)^2 \tag{3.83}$$

The time derivative of the tensile damage variable is defined as:

$$\dot{\omega}^+ = \frac{\partial g_d^+}{\partial r^+} \dot{r}^+ \tag{3.84}$$

Therefore, replacing Eqs. 3.83 and 3.84 into Eq. 3.80:

$$\dot{\gamma}^{d+} = \frac{{f_{max}^+}^2}{2E \left(r_0^+\right)^2} \left(r^+\right)^2 \frac{\partial g_d^+}{\partial r^+} \dot{r}^+ \tag{3.85}$$

Finally, after substituting Eq. 3.85 into Eq. 3.79, the energy dissipation due to tensile failure is obtained through the solution of the following integral:

$$\frac{G_f}{l_{ch}} = \frac{{f_{max}^+}^2}{2E \left(r_0^+\right)^2} \int_{r_0^+}^{r_u^+} \left(r^+\right)^2 \frac{\partial g_d^+}{\partial r^+} \mathrm{d}r^+ \tag{3.86}$$

which integration by parts leads to:

$$\frac{G_f}{l_{ch}} = \frac{{f_{max}^+}^2}{2Er_0^+}\left[\left(r_u^+ - r_0^+\right)(1-n) - n\left(r_u^+ + \frac{2}{b}\right)e^{-b\left(r_u^+ - r_0^+\right)} + n\left(r_0^+ + \frac{2}{b}\right)\right] \tag{3.87}$$

for the particular tensile damage evolution law of Eq. 3.19. Depending on the value of the parameter n, the expressions to calculate the maximum value of the threshold variable, r_u^+, are:

$$\begin{cases} \text{For } n \geq 1 & r_u^+ = -\frac{1}{b}\ln\left(\frac{n-1}{n}\right) + r_0^+ \\ \text{For } n < 1 & r_u^+ = -\frac{1}{b}\ln\left(\alpha\right) + r_0^+ \end{cases} \tag{3.88}$$

where α denotes a fraction of the initial slope of the exponential softening curve. Accordingly, for $n < 1$, r_u^+ is defined to occur at the point where the slope of the exponential curve equals α times the initial slope ($\alpha \leq 0.01$).

The demonstration of Eq.3.21 can be accomplished by substituting Eq.3.88 into Eq. 3.87 and re-arranging for b:

$$\begin{cases} \text{For } n \geq 1 & b = \dfrac{2\left[1+(n-1)\ln\left(\frac{n-1}{n}\right)\right]}{r_0^+\left[\dfrac{2EG_f}{\left(f_{max}^+\right)^2 l_{ch}} - 1\right]} \\ \text{For } n < 1 & b = \dfrac{(\alpha n + n - 1)\ln\alpha + 2n(1-\alpha)}{r_0^+\left[\dfrac{2EG_f}{\left(f_{max}^+\right)^2 l_{ch}} - n(1-\alpha)\right]} \end{cases} \tag{3.89}$$

Finally, to ensure that the tensile damage evolution law in Eq.3.19 corresponds to an exponential softening function, the parameter b should be positive. This condition implies a mathematical restriction for the maximum characteristic length of the finite element discretization, l_{ch}, such that:

$$\begin{cases} \text{For } n \geq 1 & l_{ch} < \dfrac{2EG_f}{\left(f_{max}^+\right)^2} \\ \text{For } n < 1 & l_{ch} < \dfrac{2EG_f}{\left(f_{max}^+\right)^2 n(1-\alpha)} \end{cases} \tag{3.90}$$

3.7 Thermodynamic consistency verification

The verification of the thermodynamic consistency of a constitutive model is a necessary requirement to guard against the danger of spurious energy generation, and is particularly important for cyclic material models like the one presented herein [58]. The first step is to define the elastic free energy potential in tensor notation as [45]:

$$\Psi_0 = \frac{1}{2}\bar{\boldsymbol{\sigma}} : \boldsymbol{\epsilon}^e = \frac{1}{2}\bar{\boldsymbol{\sigma}} : (\boldsymbol{\epsilon} - \boldsymbol{\epsilon}^p) \tag{3.91}$$

Based on Eq. 3.11, the elastic free energy potential can be expressed as:

$$\Psi_0 = \frac{1}{2}\left(\bar{\boldsymbol{\sigma}}^+ + \bar{\boldsymbol{\sigma}}^-\right) : \boldsymbol{\epsilon}^e = \frac{1}{2}\bar{\boldsymbol{\sigma}}^+ : (\boldsymbol{\epsilon} - \boldsymbol{\epsilon}^p) + \frac{1}{2}\bar{\boldsymbol{\sigma}}^- : (\boldsymbol{\epsilon} - \boldsymbol{\epsilon}^p) = \Psi_0^+ + \Psi_0^- \tag{3.92}$$

Therefore, under the assumption of isothermal conditions and uniform temperature, the free energy potential of the plasticity-damage model developed herein can be expressed in terms of the free ($\boldsymbol{\epsilon}$) and internal ($\boldsymbol{\epsilon}^p$, ω^+, ω^-) variables as follows:

$$\Psi\left(\boldsymbol{\epsilon}, \boldsymbol{\epsilon}^p, \omega^+, \omega^-\right) = \left(1 - \omega^+\right)\Psi_0^+\left(\boldsymbol{\epsilon}, \boldsymbol{\epsilon}^p\right) + \left(1 - \omega^-\right)\Psi_0^-\left(\boldsymbol{\epsilon}, \boldsymbol{\epsilon}^p\right) \tag{3.93}$$

In order to fulfil the second principle of thermodynamics, the total energy introduced to the system should be higher than the total energy dissipated [45]. This condition is mathematically expressed by the Clausius-Duheim inequality [158] such that:

$$\dot{\gamma} = \boldsymbol{\sigma} : \dot{\boldsymbol{\epsilon}} - \dot{\Psi} \geq 0 \tag{3.94}$$

The time derivative of the free energy potential is:

$$\dot{\Psi} = \frac{\partial \Psi}{\partial \boldsymbol{\epsilon}} : \dot{\boldsymbol{\epsilon}} + \frac{\partial \Psi}{\partial \boldsymbol{\epsilon}^p} : \dot{\boldsymbol{\epsilon}}^p + \frac{\partial \Psi}{\partial \omega^+}\dot{\omega}^+ + \frac{\partial \Psi}{\partial \omega^-}\dot{\omega}^- \tag{3.95}$$

And, from Eq. 3.93, the partial derivatives of the free energy potential in function of the free and internal variables are:

$$\frac{\partial \Psi}{\partial \boldsymbol{\epsilon}} = \left(1 - \omega^+\right)\frac{\partial \Psi_0^+}{\partial \boldsymbol{\epsilon}} + \left(1 - \omega^-\right)\frac{\partial \Psi_0^-}{\partial \boldsymbol{\epsilon}} \tag{3.96}$$

$$\frac{\partial \Psi}{\partial \boldsymbol{\epsilon}^p} = \left(1 - \omega^+\right)\frac{\partial \Psi_0^+}{\partial \boldsymbol{\epsilon}^p} + \left(1 - \omega^-\right)\frac{\partial \Psi_0^-}{\partial \boldsymbol{\epsilon}^p} \tag{3.97}$$

$$\frac{\partial \Psi}{\partial \omega^{\pm}} = -\Psi_0^{\pm} \tag{3.98}$$

It can also be shown that [45]:

$$\frac{\partial \Psi_0^{\pm}}{\partial \boldsymbol{\epsilon}} = \bar{\boldsymbol{\sigma}}^{\pm} \tag{3.99}$$

$$\frac{\partial \Psi_0^{\pm}}{\partial \boldsymbol{\epsilon}^p} = -\bar{\boldsymbol{\sigma}}^{\pm} \tag{3.100}$$

The substitution of Eq. 3.95 into Eq. 3.94 leads to:

$$\dot{\gamma} = \left(\boldsymbol{\sigma} - \frac{\partial \Psi}{\partial \boldsymbol{\epsilon}}\right) : \dot{\boldsymbol{\epsilon}} - \left(\frac{\partial \Psi}{\partial \boldsymbol{\epsilon}^p} : \dot{\boldsymbol{\epsilon}}^p + \frac{\partial \Psi}{\partial \omega^+}\dot{\omega}^+ + \frac{\partial \Psi}{\partial \omega^-}\dot{\omega}^-\right) \geq 0 \tag{3.101}$$

Given that the condition in Eq. 3.101 must be fulfilled at all time steps and under any loading condition, the first term, which is a function of the free variable, should always equal zero:

$$\boldsymbol{\sigma} = \frac{\partial \Psi}{\partial \boldsymbol{\epsilon}} \tag{3.102}$$

Therefore, the substitution of Eqs. 3.96 and 3.99 into Eq. 3.102 confirms the model constitutive law previously defined in Eq. 3.12. Moreover, substituting Eqs. 3.97, 3.98 and 3.100 into Eq. 3.101 allows the energy dissipation condition to be expressed in terms of the plasticity and damage dissipation rates as:

$$\dot{\gamma} = \dot{\gamma}^p + \dot{\gamma}^d \geq 0 \tag{3.103}$$

$$\dot{\gamma}^p = \left[\left(1-\omega^+\right)\bar{\boldsymbol{\sigma}}^+ + \left(1-\omega^-\right)\bar{\boldsymbol{\sigma}}^-\right] : \dot{\boldsymbol{\epsilon}}^p = \boldsymbol{\sigma} : \dot{\boldsymbol{\epsilon}}^p \geq 0 \tag{3.104}$$

$$\dot{\gamma}^d = \Psi_0^+\dot{\omega}^+ + \Psi_0^-\dot{\omega}^- \geq 0 \tag{3.105}$$

It can be shown that $\Psi_0^{\pm}$ is positive [45], while by definition $\dot{\omega}^{\pm}$ is always positive as well. Therefore, thermodynamic consistency is always ensured for the damage component of energy dissipation rate $\dot{\gamma}^d$. However, some additional conditions should be met in order to ensure that the plasticity part of the energy dissipation rate is positive as well. From Eq. 3.104 it can be concluded that the scalar multiplication of the effective stress components and the plastic strain tensor should be non-negative. For this to be true, it

is sufficient, but not necessary, that the plastic yield surface in Eq. 3.36 is convex, and the plastic flow rule in Eq. 3.38 is associated [133, 58]. Both condition are met by the plasticity model developed herein, hence verifying its thermodynamic consistency.

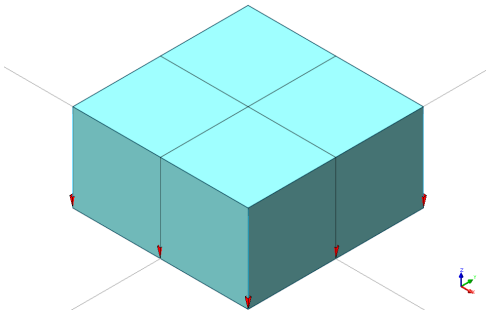
3.8 Wood constitutive model: Stress-strain response

The newly proposed timber plasticity-damage model was coded in FORTRAN and implemented in the finite element software DIANA [35] by means of a user-supplied subroutine (USS). In order to display the performance of the material model exclusively, a simple timber cubic specimen of 10 mm per side is modelled in this section by means of hexahedral finite solid elements with linear interpolation. The Newton-Raphson iterative algorithm is employed for the solution of the finite element method system of nonlinear equations. Geometric nonlinear analysis is not included in this set of numerical simulations.

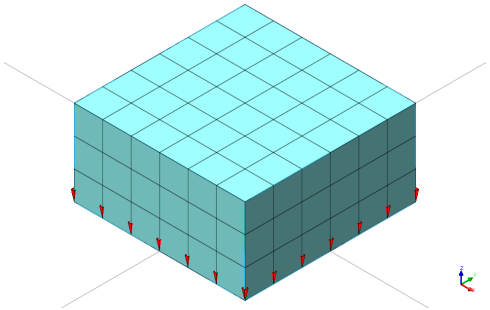
Fig. 3.6 presents the three different mesh sizes used to evaluate the mesh sensitivity of the model. The element sizes of the coarse mesh M1 (Fig. 3.6a), the intermediate mesh M3 (Fig. 3.6b) and the fine mesh M5 (Fig. 3.6c) are 5 mm, 1.67 mm and 1 mm, respectively. Moreover, the timber material orthotropic directions coincide with the global axes X (parallel to the grain), Y (perpendicular to the grain) and Z (perpendicular to the grain). Except when indicated otherwise, for the case studies presented along this section the loads are applied parallel to the plane XY. Therefore, for those cases the symmetry condition with respect to the plane XY (graphically represented in Fig. 3.6 by the displacement restraints in Z-direction) applies, and only one half of the timber cubic specimen needs to be modelled.

Displacement control loading is applied to the wood cube along three directions. The loading direction angles with respect to the timber grain orientation (X-axis) considered for the analysis are: 0° (parallel to the grain), 90° (perpendicular to the grain) and 45°. The influence of the loading direction, the model mesh size and the values of the material model parameters on the timber specimen stress-strain response is evaluated. Finally, the monotonic stress-strain response under biaxial and triaxial stress states are presented. For these studies the symmetry condition does not hold and complete models of the cubic specimen were employed.

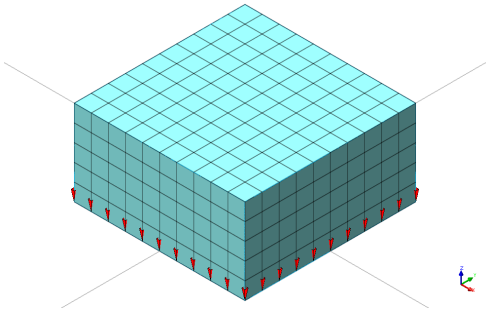
In addition to the standard classical orthotropic plasticity models input parame-



(a) Coarse mesh M1.



(b) Intermediate mesh M3.



(c) Fine mesh M5.

Figure 3.6: Finite element models of the timber cubic specimen of 10 mm per side (symmetry with respect to the plane XY).

ters (i.e. Young's moduli, shear moduli, Poisson's ratios, compressive strengths, tensile strengths and shear strengths), the proposed plasticity-damage model requires a total of 6 additional parameters. One of these additional parameters is the mixed-mode fracture energy density of timber (G_f) which has been briefly discussed in Sections 3.3.3 and 3.6. Despite being a material property, the fracture energy density is difficult to determine experimentally, and it varies considerably with the type of failure mode and the loading direction. Nevertheless, for modelling purposes some referential values can be obtained from previous studies like Jensen and Quenneville [80], among others [154, 7, 149, 53, 123]. Another parameter is the characteristic length (l_{ch}), which was introduced in Section 3.3.3 as the cubic root of the volume of the finite elements of the model mesh (see Section 3.5.1). Finally, the other four parameters required are the exponential softening constant (n), the plasticity hardening modulus (h), the compressive hardening constant (β) and the compressive hardening power (m). Due to the difficulty of obtaining them from experimental data, or to link them to other material properties, these parameters are obtained by means of a calibration process.

The set of material model parameters used for the simulations presented in this section are provided in Table 3.2. The values of the 18 standard parameters are consistent with the assumption of orthotropic behaviour with transverse isotropy (see Section 3.2), and can be considered as generic for Glulam GL32h. For illustration purposes only, a very small value was assigned to the fracture energy density (G_f), making it possible to visualize the exponential softening of the material model due to tensile and shear failure. The exclusive purpose of this section is to show the performance and particular characteristics of the proposed timber constitutive model. Therefore, no attempt of discussion on the parameters calibration procedure or the selection criteria for the yield surface and the material properties was made at this stage. These important issues are discussed in detail in Chapters 4 and 6.

3.8.1 Uniaxial monotonic response

First, the specimens shown in Fig. 3.6 were subjected to a monotonic load in the directions parallel (X-axis) and perpendicular (Y-axis) to the timber grain alignment under displacement-control conditions. This is achieved by applying displacement restraints to the nodes located in the faces of the cubic specimen perpendicular to the corresponding loading direction axes. The translational degrees of freedom in the loading direction are set to zero in one face, whereas a prescribed uniform increasing (in case of tension) or

Table 3.2: Plasticity-damage material model input parameters for timber

Poisson's ratios	$\nu_{XY} = 0.41$	$\nu_{YZ} = 0.37$	$\nu_{XZ} = 0.41$
Shear moduli [MPa]	$G_{XY} = 690$	$G_{YZ} = 125.9$	$G_{ZX} = 690$
Young's moduli [MPa]	$E_X = 9936$	$E_Y = 345$	$E_Z = 345$
Compressive strengths [MPa]	$f_X^- = 40$	$f_Y^- = 4$	$f_Z^- = 4$
Tensile strengths [MPa]	$f_X^+ = 20$	$f_Y^+ = 1$	$f_Z^+ = 1$
Shear strengths [MPa]	$f_{XY} = 4$	$f_{YZ} = 4$	$f_{ZX} = 4$
Fracture energy density [N/mm]		$G_f = 0.01$	
Characteristic length [mm]	$l_{ch,M1} = 5$	$l_{ch,M3} = 1.67$	$l_{ch,M5} = 1$
Exponential softening parameter		$n = 1$	
Hardening modulus [MPa]		$h = 12.9$	
Compressive hardening constant		$\beta = 0.85$	
Compressive hardening power		$m = 1$	
Orthotropic yield criterion		Hoffman	

decreasing (in case of compression) displacement is assigned to the nodes in the opposite face. Tension and compression monotonic loading was applied in both, parallel and perpendicular to the grain directions, for each of the three models presented in Fig. 3.6.

Considering that no strain localization is generated under the previously mentioned loading cases, the numerical results obtained from these simulations are not expected to suffer from mesh-dependency issues [144]. For this reason, the crack band regularization technique is deactivated for this first set of simulations. This is easily achieved by overriding the default values of the characteristic length l_{ch} in Table 3.2 with a value of 1 mm for the three models (M1, M3 and M5).

Figs. 3.7 and 3.8 show the monotonic stress-strain responses of the cubic timber specimens when subjected to uniaxial loading in the directions parallel and perpendicular to

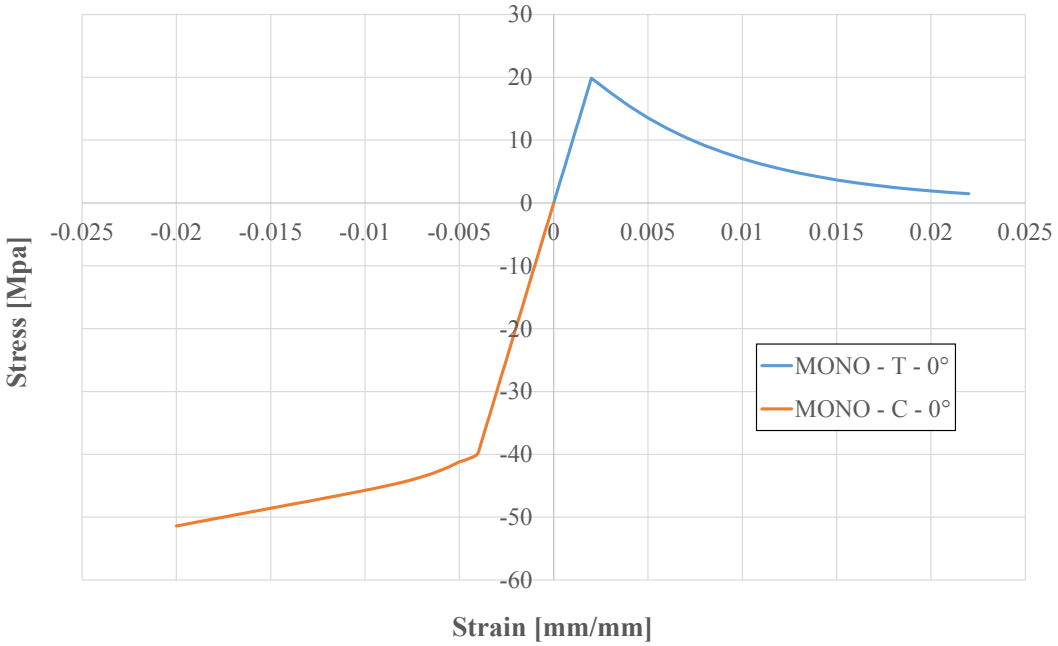


Figure 3.7: Plasticity-damage model. Monotonic stress-strain response in the direction parallel to the grain.

the grain, respectively. As expected, there were no mesh-dependency issues, and therefore, exactly the same stress-strain graphic was obtained in both directions for the three models, not being required the activation of the crack band regularization technique. It can be observed from these figures that the responses under tensile and compressive stress states are markedly different. The tensile inelastic response is characterized by an exponential softening behaviour, while the compressive counter-part features plasticity with limited hardening. Finally, in addition to the considerable difference between the timber strengths in the directions parallel and perpendicular to the grain (which are consistent with the input parameters values in Table 3.2), it is interesting to note that in compression perpendicular to the grain the strain related to the onset of the nonlinear range is twice the corresponding strain in compression parallel to the grain. Obviously, the reason for this is the characteristic low stiffness of timber in the direction perpendicular to the grain.

Response sensitivity to model parameters

The same modelling hypothesis of the previous section were used to evaluate the influence of the four calibration parameters mentioned above (n, β, m and h) on the stress-strain response. Fig. 3.9 shows the monotonic loading-unloading tensile stress-strain response for three different values of the exponential softening constant parameter, n. When

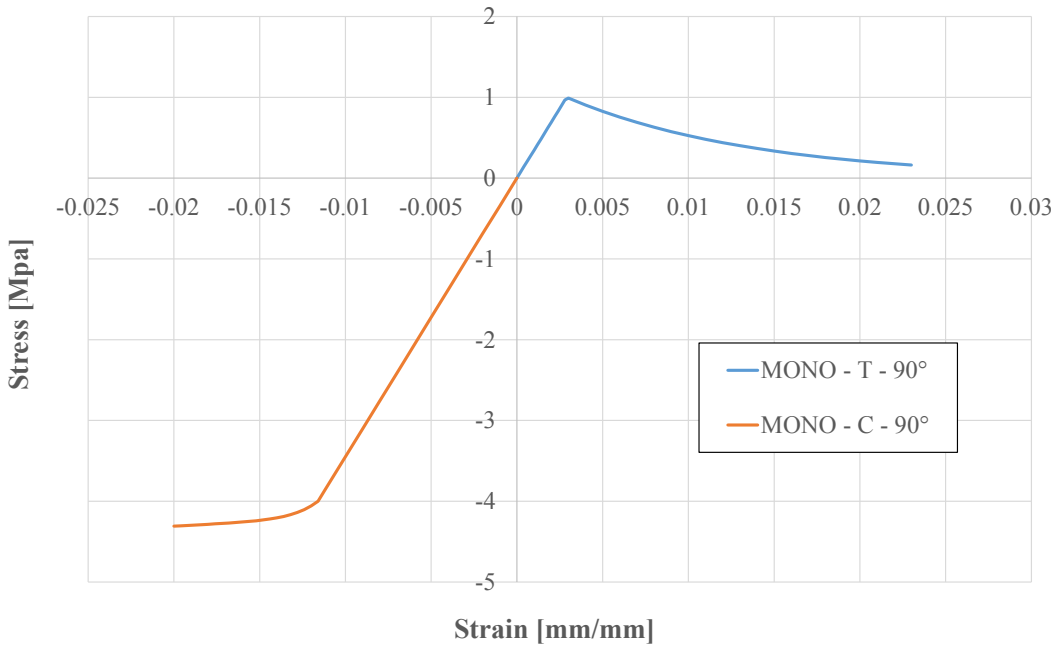
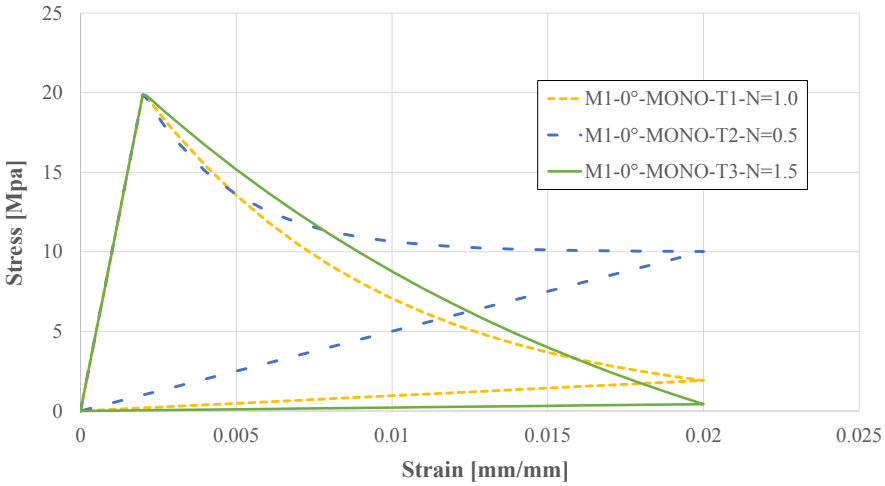


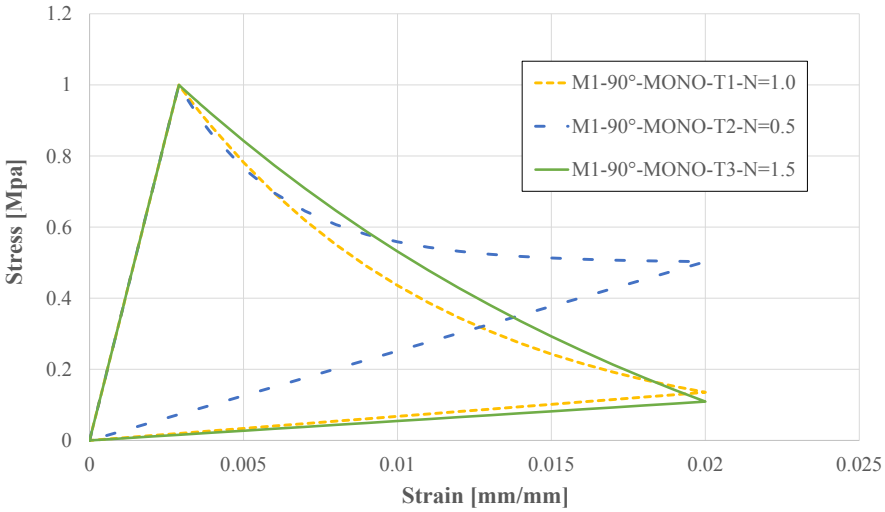
Figure 3.8: Plasticity-damage model. Monotonic stress-strain response in the direction perpendicular to the grain.

$n = 1$ a very sharp stress decay is appreciated immediately after the maximum strength is reached. The softening rate diminishes progressively, leading to an asymptotic response towards a zero-stress value. The response for $n = 0.5$ is similar to the case where $n = 1$, with the only difference being that the asymptotic behaviour tends to a stress value higher than zero. For this particular case, the value of $n = 0.5$ implies that the residual stress is equal to half the timber strength in the corresponding direction. Lastly, the third case ($n = 1.5$) leads to a tensile behaviour that resembles a linear softening response. No asymptotic behaviour is obtained, and therefore, a total local failure occurs when a zero-stress value is reached for a finite strain level. The behaviour shown in Fig. 3.9 is consistent with the discussion presented in Section 3.3.3 with respect to Fig. 3.2a. The only difference between both graphs is that the latter was directly obtained from Eqs. 3.18 and 3.19, while the former is the result of a finite element simulation of the implemented constitutive model.

Fig. 3.10 shows the influence of the hardening constant, β, on the compressive loading-unloading stress-strain response of the timber constitutive model. As mentioned in Section 3.3.3, β varies between 0 (no damage) and 1 (full damage). The higher the value of β, the higher the maximum damage allowed. Fig. 3.10 shows that the parameter β has a direct effect on the post-elastic compressive hardening slope. A value of $\beta = 1$ ensures a perfectly plastic response. The lower the value of β, the larger the hardening slope. In



(a) Parallel to the grain.



(b) Perpendicular to the grain

Figure 3.9: Influence of the exponential softening constant, n, on the tensile monotonic stress-strain response.

a similar way to the exponential softening parameter, Fig. 3.10 is consistent with Fig. 3.3a.

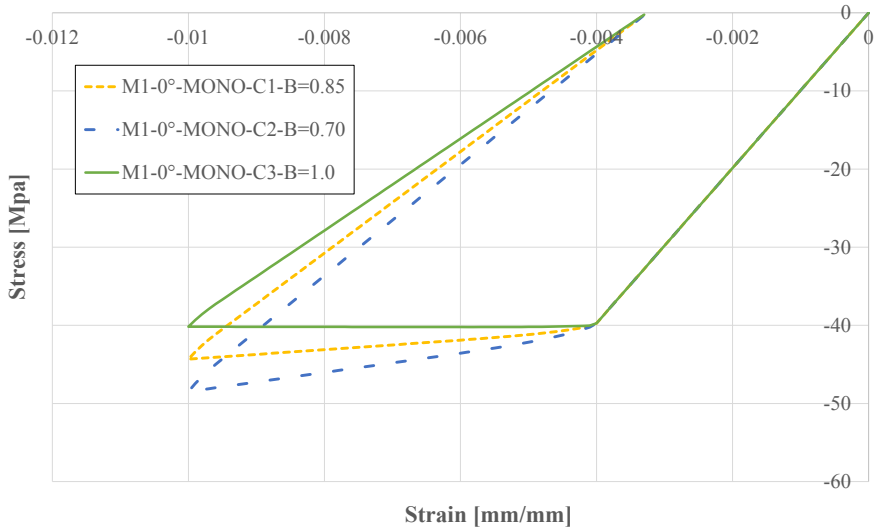
Fig. 3.11 shows that the effect of the hardening power, m, on the post-elastic compressive stress-strain response is noteworthy. A change in the order of the compressive damage evolution law from a linear ($m = 1$) to a quadratic ($m = 2$) or cubic ($m = 3$) function produces an increment of around five times the hardening slope. For this reason, a linear damage evolution in compression is the most suitable option for a wood material model using nominal hardening values.

Finally, the influence of the plasticity hardening modulus, h, on the compressive post-elastic loading-unloading material behaviour is illustrated in Fig. 3.12. Even though its effect on the hardening slope increment is minor, the most important and distinctive feature of the parameter h is its direct relationship with the magnitude of plastic strains generated in the wood. This can be observed from Fig. 3.12 by noting the different amount of permanent deformations obtained after unloading for each of the three different magnitudes of h. The stress-strain response of the model with the highest plasticity hardening modulus ($h = 25$) shows smaller plastic strains and higher stiffness degradation (lower unloading branch slope). In contrast, a small plasticity hardening modulus ($h = 1$) generates larger plastic strains and slight stiffness degradation.

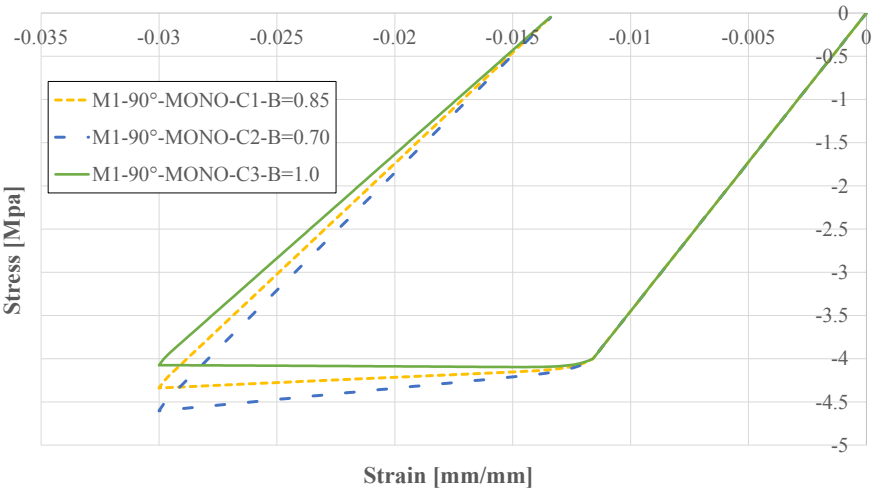
Mesh sensitivity due to strain localization

It was demonstrated in Section 3.8.1 that the cubic specimen models shown in Fig. 3.6 do not experience mesh-dependency under uniaxial loading in the directions parallel or perpendicular to the grain. In order to evaluate the performance of the crack band regularization method incorporated into the proposed constitutive model, a investigation of the stress-strain response of the cubic specimen models in Fig. 3.6 under alternative loading condition causing strain localisation is performed. To this end, the local material axes of the cubic specimen models are rotated 45° around the Z-axis. In this way, a uniaxial load in the direction 45° with respect to the grain alignment is applied to the three mesh size models (M1, M3 and M5) in tension and compression.

Fig. 3.13 shows the principal strains field generated by a compressive loading applied at 45° with respect to the grain alignment. The concentration of tensile and compressive strains generated in the two opposite corners of the cubic specimen, and in the diagonal which joins them, is characteristic of a mixed normal-shear stress state, which can

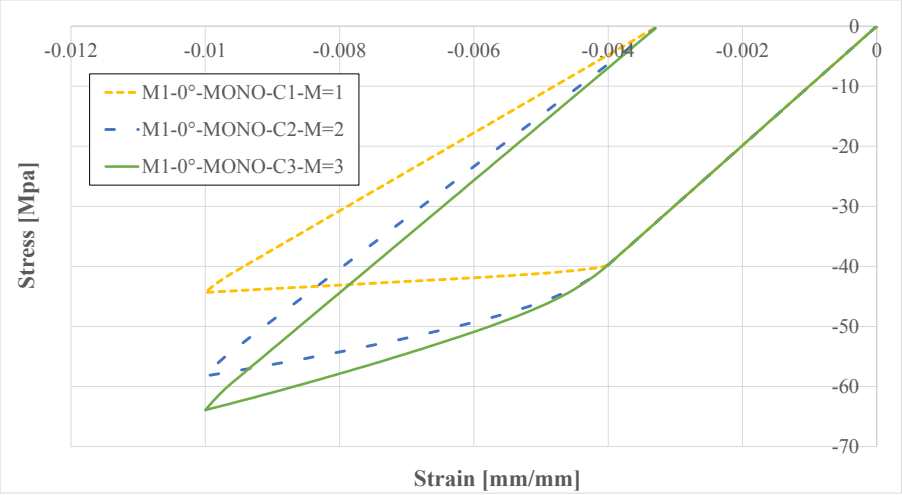


(a) Parallel to the grain.

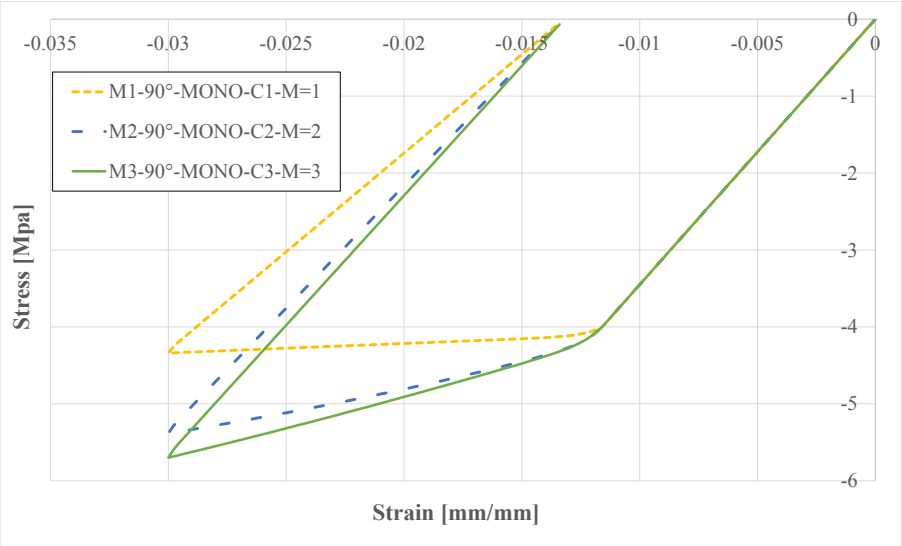


(b) Perpendicular to the grain

Figure 3.10: Influence of the hardening constant, β, on the compressive monotonic stress-strain response.

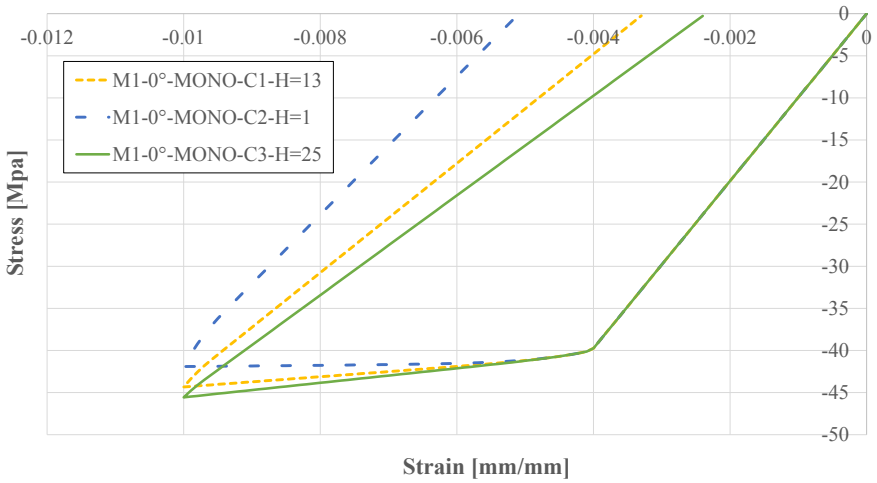


(a) Parallel to the grain.

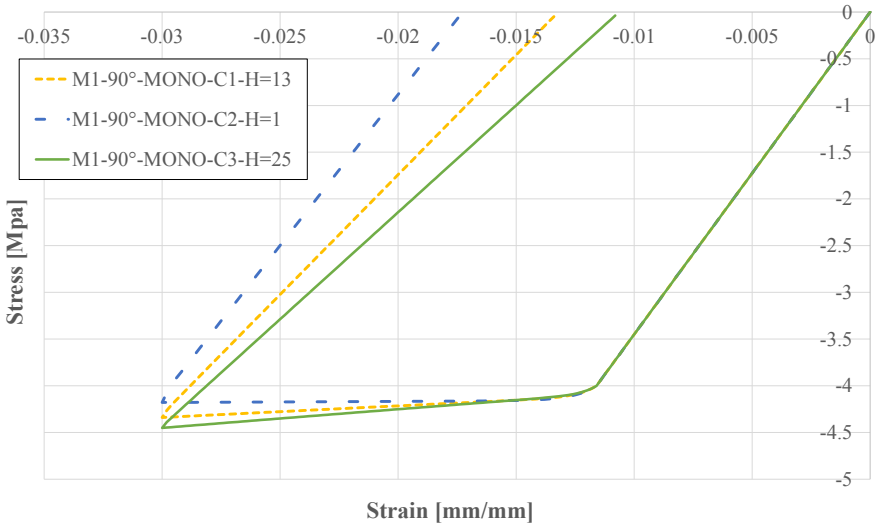


(b) Perpendicular to the grain

Figure 3.11: Influence of the hardening power, m, on the compressive monotonic stress-strain response.

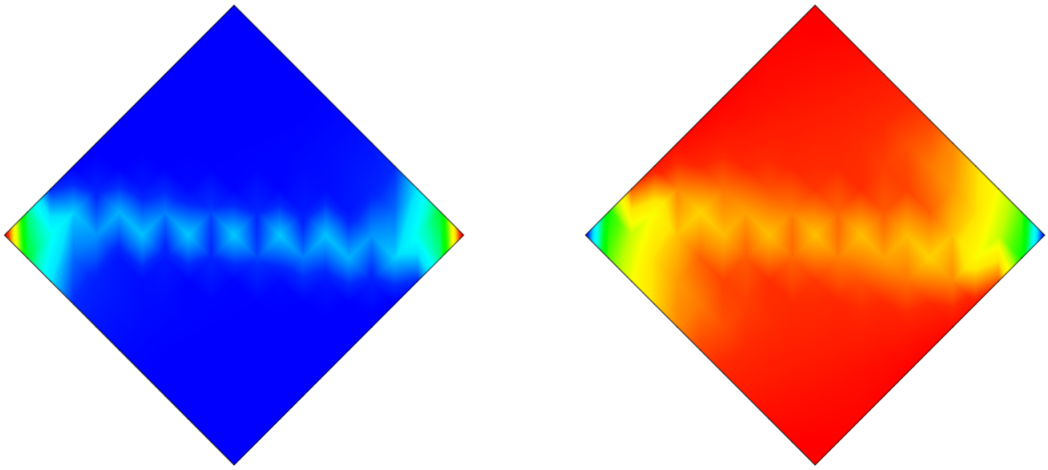


(a) Parallel to the grain.



(b) Perpendicular to the grain

Figure 3.12: Influence of the plasticity hardening modulus, h, on the compressive monotonic stress-strain response.



(a) Maximum principal strains. (b) Minimum principal strains.

Figure 3.13: Strain localisation under uniaxial compressive loading at 45° with respect to the grain alignment.

eventually lead to strain localisation and mesh-dependency issues. The tensile and compressive stress-strain response corresponding to this loading condition was obtained for the three mesh sizes described above. The normal stresses and strains were measured in the same direction of the applied load. Due to the presence of mesh-dependency, the crack band regularization method was activated by assigning to each of the three models the corresponding values of the characteristic length parameter specified in Table 3.2. Accordingly, the value of the fracture energy density, G_f, given in the same Table 3.2, had to be replaced by a more realistic value ($G_f = 0.1$) for this set of simulations only.

Fig. 3.14 shows the tensile softening loading-unloading stress-strain response of the three models with different mesh sizes. In comparison with models M3 and M5, higher tensile strength and greater energy dissipation are obtained with the coarser mesh of model M1. It can also be seen that the curves obtained with the intermediate and fine meshes M3 and M5, respectively, are very similar to each other.

On the other hand, Fig. 3.15 shows the compressive hardening loading-unloading stress-strain response for the same models. A higher strength and hardening slope is obtained with the coarser mesh M1, while very similar responses are obtained for models M3 and M5. In conclusion, Figs 3.14 and 3.15 clearly demonstrate that strain localisation produces mesh dependency, and that the crack band regularization method works well provided that the mesh is fine enough. The appropriate mesh size depends on the dimensions of the structure (or structural component) to be analysed. For each particular

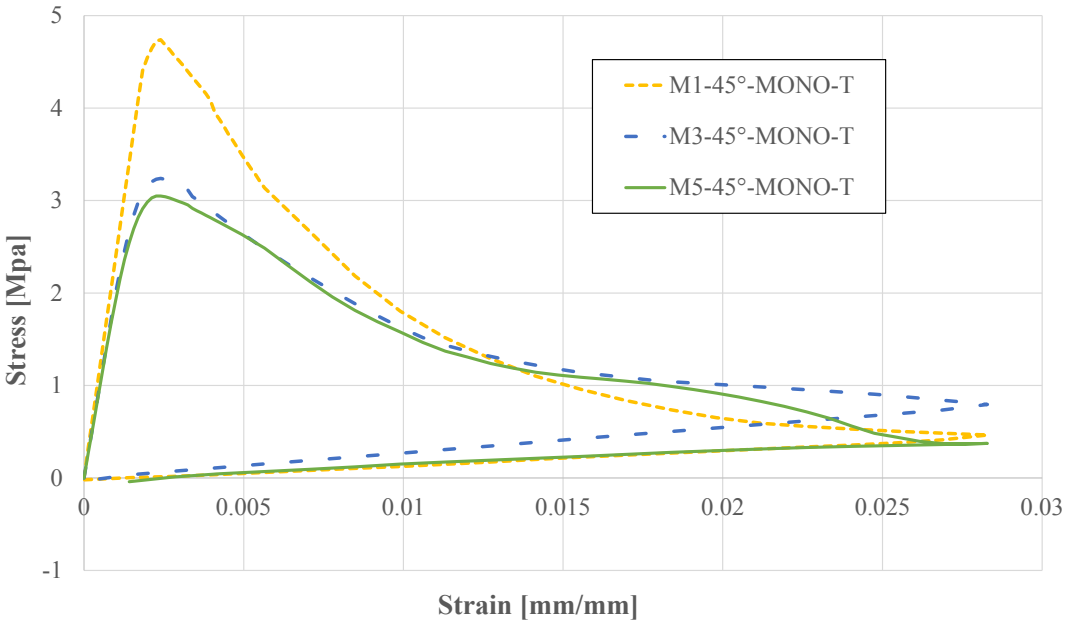


Figure 3.14: Mesh-dependency due to strain localisation. Tensile monotonic stress-strain response at 45° with respect to the grain alignment ($G_f = 0.1$).

case study, a mesh refinement exercise similar to the one presented in this section should be carried out. For instance, for this particular case it is clear that the mesh size of model M3 is good enough. By contrast, model M1 is too coarse to provide accurate results.

Influence of the loading angle

The monotonic stress-strain responses obtained with the fine-mesh model M5 (Fig. 3.6c) are plotted in Figs. 3.16 and 3.17 for three different load angles. The angles measured with respect to the timber grain are: 0° (parallel to the grain), 90° (perpendicular to the grain) and 45°. Figs. 3.16 and 3.17 show the influence of the loading angle on the tensile and compressive stress-strain responses obtained with the proposed timber constitutive model. The considerably greater strength of timber in the parallel to the grain direction, with respect to the other two directions, is clearly noticed in Figs. 3.16a and 3.17a. The stress-strain curves corresponding to 45° and 90° loading angles are better appreciated in Figs. 3.16b and 3.17b, where they are reproduced without the curve of the loading angle parallel to the grain.

It can be seen in Figs. 3.16b and 3.17b that the tensile and compressive strengths for a load applied at 45° from the grain direction are around twice the strengths in the

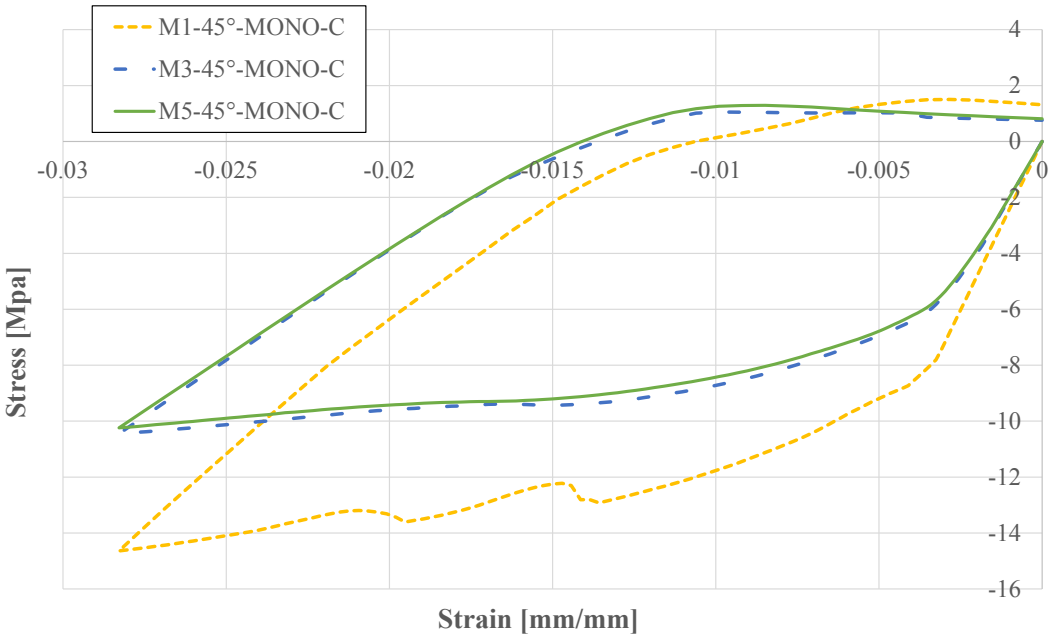
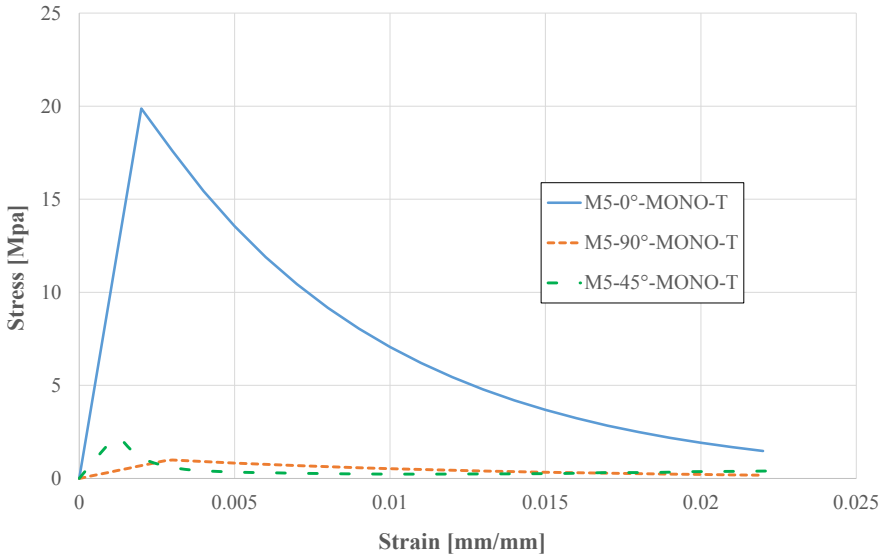


Figure 3.15: Mesh-dependency due to strain localisation. Compressive monotonic stress-strain response at 45° with respect to the grain alignment ($G_f = 0.1$).

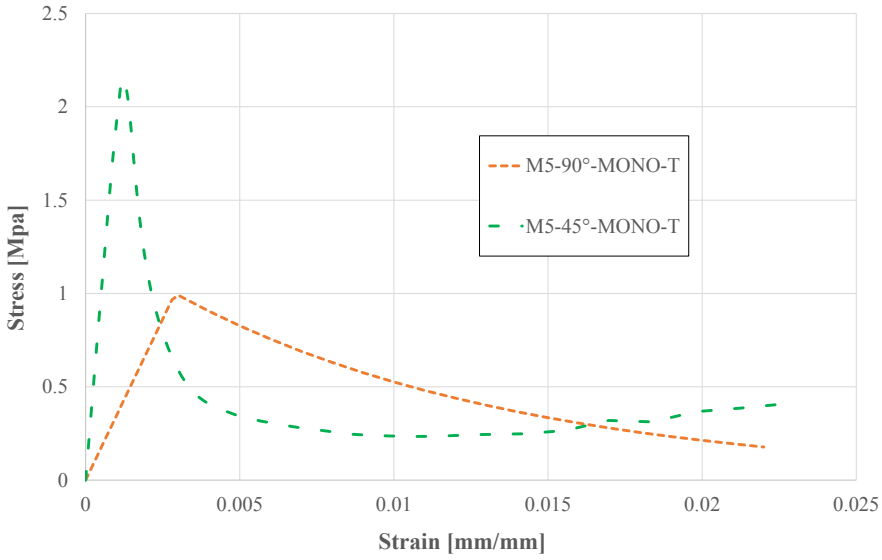
direction perpendicular to the grain. Besides, it is interesting to note that the tensile response corresponding to a 45° load inclination shows mild hardening for large levels of deformation, after the occurrence of softening. Likewise, a sudden partial loss of strength occurs in the post-elastic compressive regime corresponding to the same loading direction. It can be concluded that the mixed normal-shear stress state generated by a load at 45° introduces a mix of hardening and softening post-elastic response which is consistent with the simultaneous presence of compressive and tensile stresses in different directions.

3.8.2 Uniaxial cyclic response

Figs. 3.18, 3.19 and 3.20 show the reversed cyclic stress-strain responses of the wooden cube (model M5, Fig. 3.6c) under loading directions parallel, perpendicular and at 45° with respect to the grain alignment. Some interesting features of the proposed plasticity-damage model for wood are depicted in these graphics. First, permanent plastic deformations occur in the negative side of the strain axis when the stress passes from compression to tension. On the contrary, absolutely no plastic deformations are produced in the positive (tension) side of the strain axis. Second, the stiffness recovery after load reversal from tension to compression demonstrates that the "structural damage" concept introduced in Section 3.5.1 was successfully incorporated in the constitutive model. Moreover,

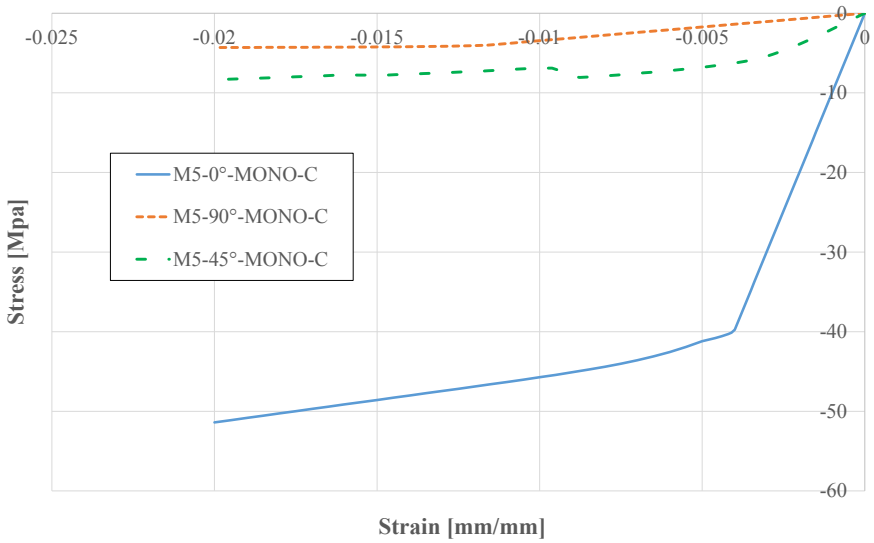


(a) 0°, 45° and 90°.

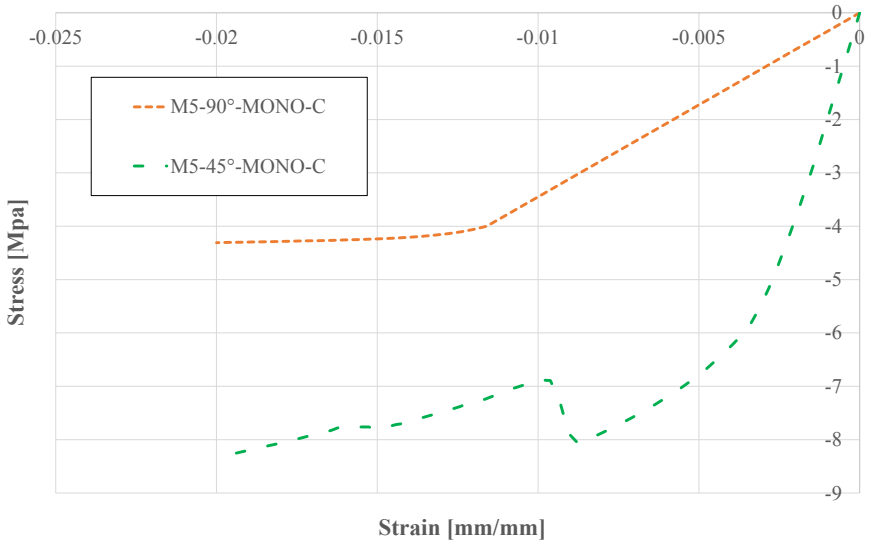


(b) 45° and 90° only

Figure 3.16: Influence of loading angle on the tensile monotonic stress-strain response ($G_f = 0.01$).



(a) 0°, 45° and 90°.



(b) 45° and 90° only

Figure 3.17: Influence of loading angle on the compressive monotonic stress-strain response ($G_f = 0.01$).

it can be seen in Figs 3.18 to 3.20 that the level of stiffness degradation in tension (structural damage) is significantly higher than in compression (constitutive damage). This is clearly appreciated by comparing the slopes of the unloading branches in both tensile and compressive zones. The lower strength and damage-only (no plasticity) characteristic response of wood in tension accelerates its stiffness degradation, causing a significant decrease of the secant unloading branch slope that invariably returns to the current highest permanent plastic strain in the negative axis. On the other hand, the higher strength in compression and the inclusion of plasticity generates a milder stiffness degradation with an unloading stiffness lying in-between the elastic and the secant branches, although considerably closer to the former than the latter.

Similar to the monotonic loading case (See Fig. 3.17b), there is a sudden loss of strength in the compressive side of the cyclic stress-strain response corresponding to a loading direction of 45° with respect to the grain alignment (Fig. 3.20). This means that the mixed normal-shear stress state generated by this loading condition, and its associated combined brittle-ductile failure mode are well represented by the model under both monotonic and cyclic loads. Overall, the proposed model captures the key characteristics of the cyclic behaviour of timber material, namely, its anisotropic behaviour, tensile softening brittle failure, stiffness cyclic degradation and recovery after load-reversal, and its compressive permanent plastic deformation due to ductile failure.

3.8.3 Multiaxial monotonic response

The fine-mesh model M5 in Fig. 3.6c is also employed to study the performance of the plasticity-damage constitutive model under multiaxial stress interaction. First, the stress-strain response under biaxial compression along the X (parallel to the grain) and Y (perpendicular to the grain) axes is shown in Fig. 3.21. As in the case of uniaxial stress state, biaxial compression shows a plastic hardening post-elastic behaviour in both X and Y axes. It has been mentioned above that, due to the low Young's modulus in the direction perpendicular to the grain, the compressive yielding strain is higher in this direction than in the direction parallel to the grain (see Figs. 3.7 and 3.8). Accordingly, in the direction parallel to the grain, the yield stress of both uniaxial and biaxial compression are almost the same (around 40 MPa). On the contrary, the uniaxial compressive yield stress in the direction perpendicular to the grain is twice the corresponding biaxial yield stress.

On the other hand, the behaviour of the wood cube under biaxial tension is shown in

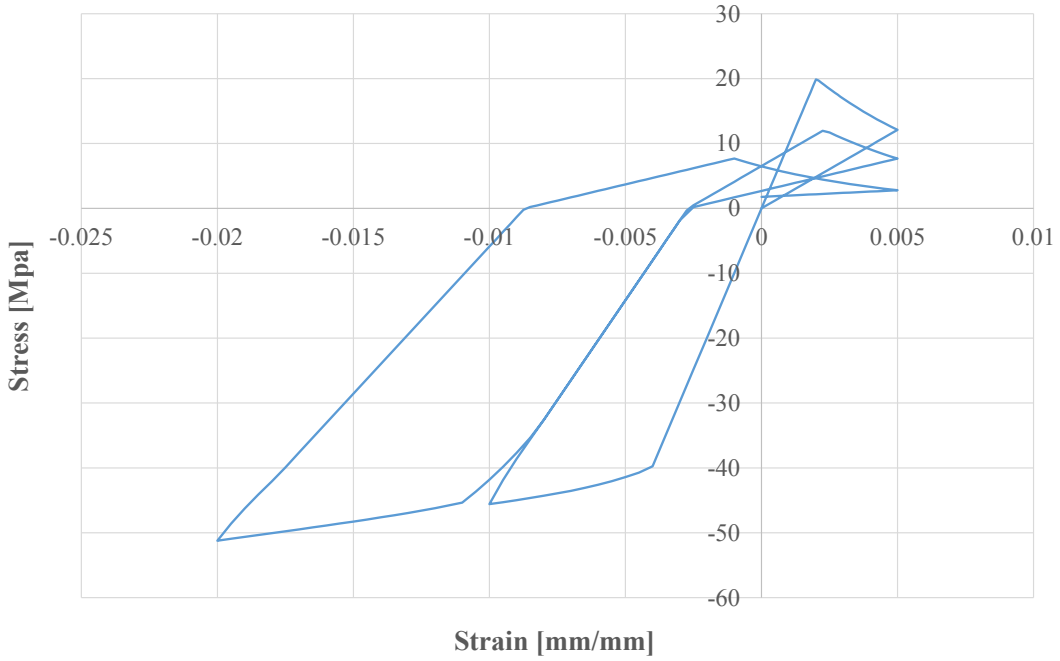


Figure 3.18: Uniaxial reversed cyclic stress-strain response in the direction parallel to the grain.

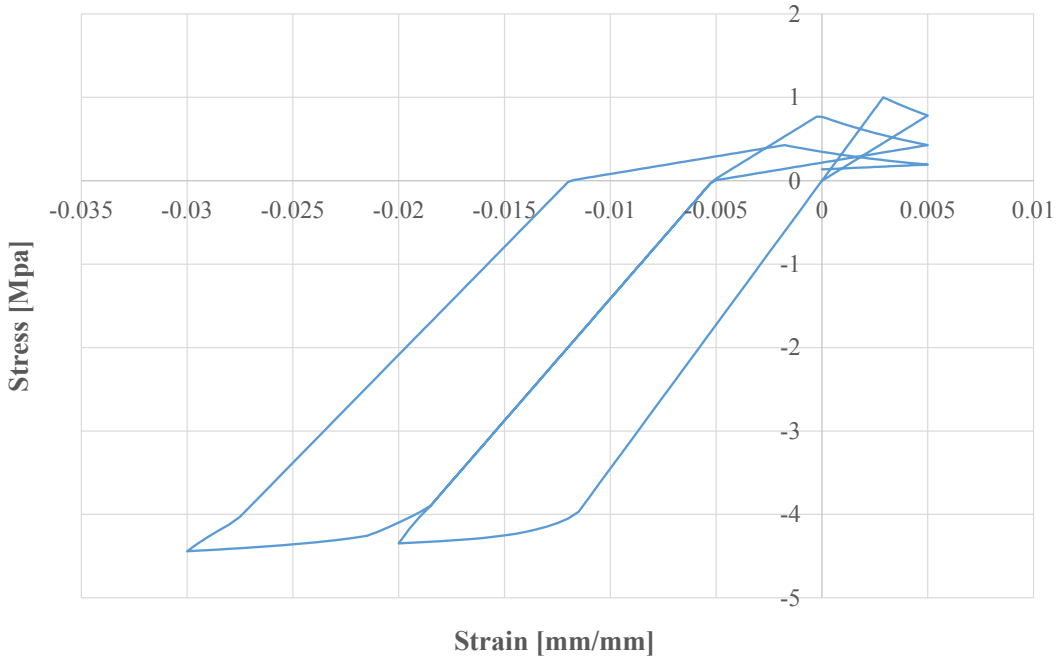


Figure 3.19: Uniaxial reversed cyclic stress-strain response in the direction perpendicular to the grain.

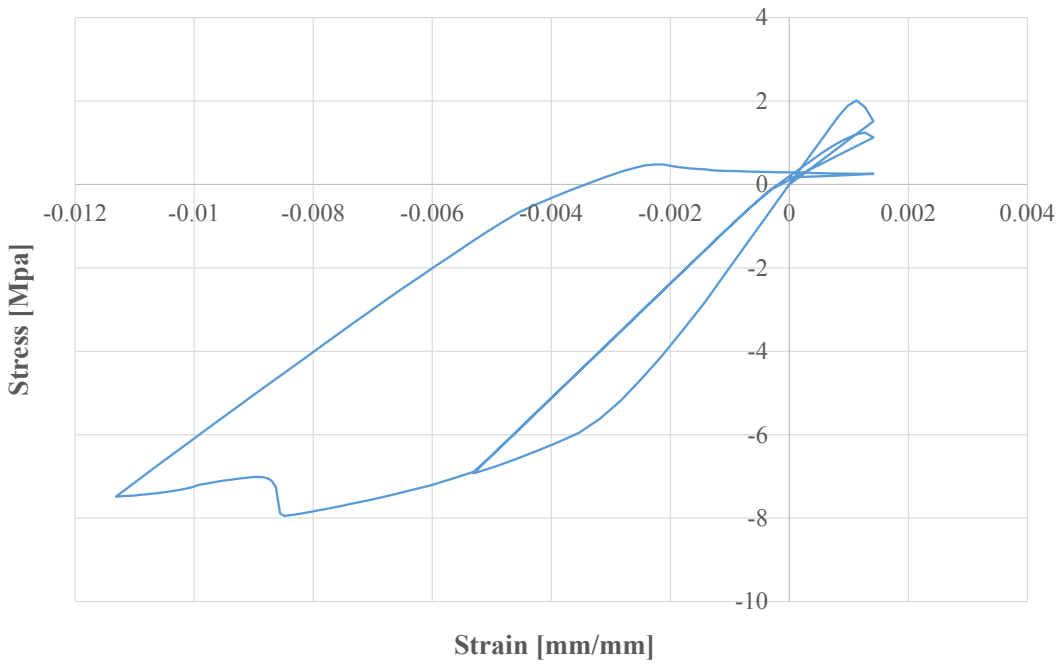
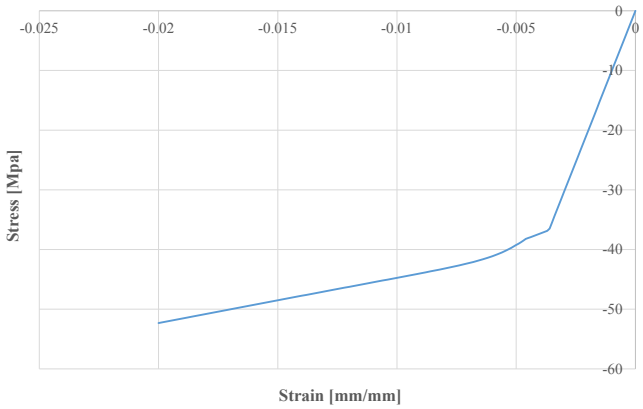


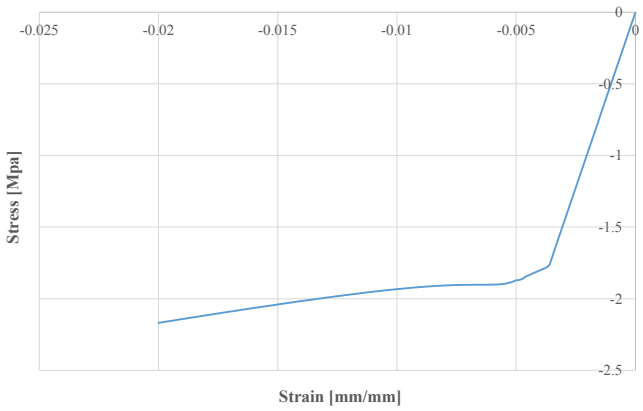
Figure 3.20: Uniaxial reversed cyclic stress-strain response in the direction 45° with respect to the grain.

Fig. 3.22. The brittle exponential softening stress-strain responses in both parallel and perpendicular to the grain axes are similar to those presented in Figs. 3.7 and 3.8 for a uniaxial stress state. Nevertheless, under biaxial tension the tensile strength in both directions is diminished with respect to the uniaxial case. A reduction of around 30% of the unixial tensile strength is appreciated from Fig. 3.22.

The response of the timber cubic specimen under a biaxial mixed tension-compression stress state is explored with reference to Figs. 3.23 and 3.24. The first case study consists on compression stress applied along the X-axis (parallel to the grain) and tension stress applied along the Y-axis (perpendicular to the grain) simultaneously. These results are shown in Fig. 3.23 for both directions. By comparing Figs. 3.7 and 3.23a, it can be noticed that there is no difference between the responses obtained for the uniaxial and the mixed biaxial stress states in the direction parallel to the grain. On the other hand, the mixed biaxial stress-strain response in the direction perpendicular to the grain shown in Fig. 3.23b is completely different from its uniaxial counterpart. First, a decrease of the elastic tensile stiffness occurs as a consequence of the additional tensile deformation generated by the compressive deformation in the direction parallel to the grain (Poisson's effect). And second, before reaching the tensile strength, the beginning of plasticity in the direction parallel to the grain produces stress unloading and a change of the stress

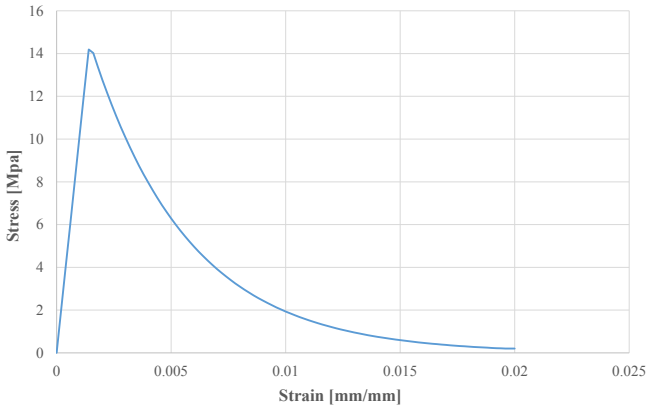


(a) Direction parallel to the grain (X-axis).

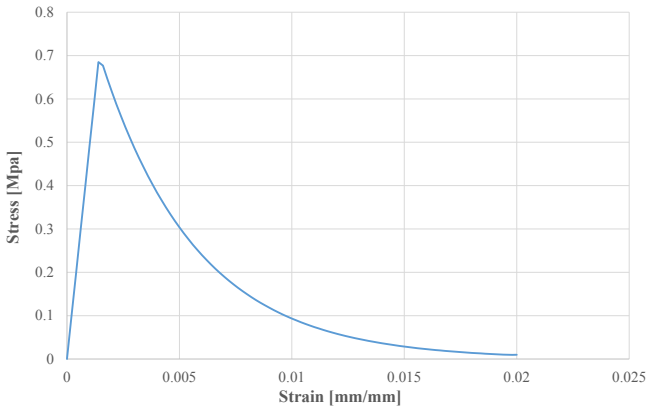


(b) Direction perpendicular to the grain (Y-axis).

Figure 3.21: Stress-strain response under bi-axial compression.

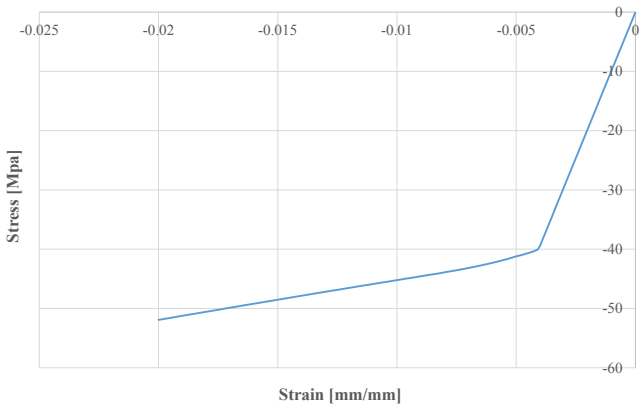


(a) Direction parallel to the grain (X-axis).

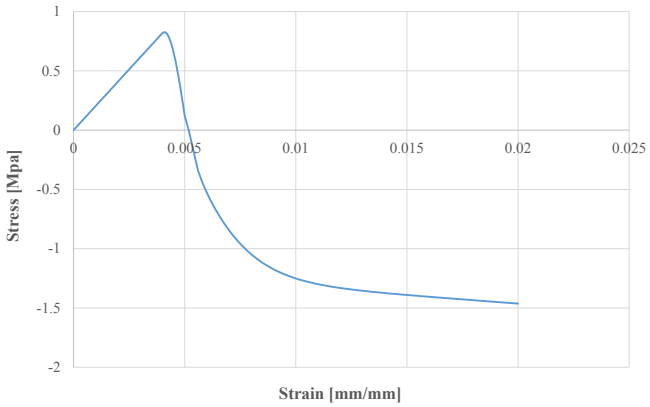


(b) Direction perpendicular to the grain (Y-axis).

Figure 3.22: Stress-strain response under bi-axial tension.



(a) Compressive stress-strain response in the direction parallel to the grain (X-axis).

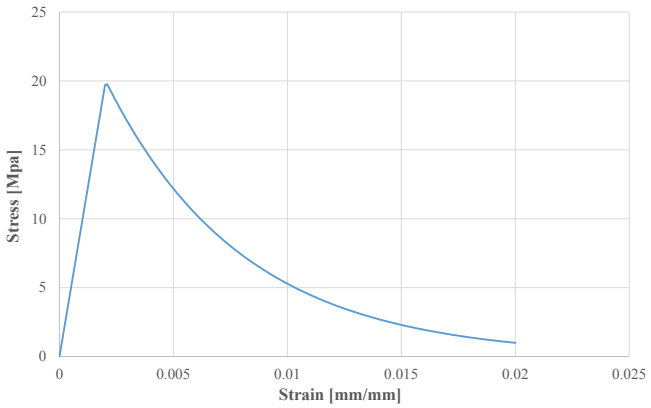


(b) Tensile-compressive stress-strain response in the direction perpendicular to the grain (Y-axis).

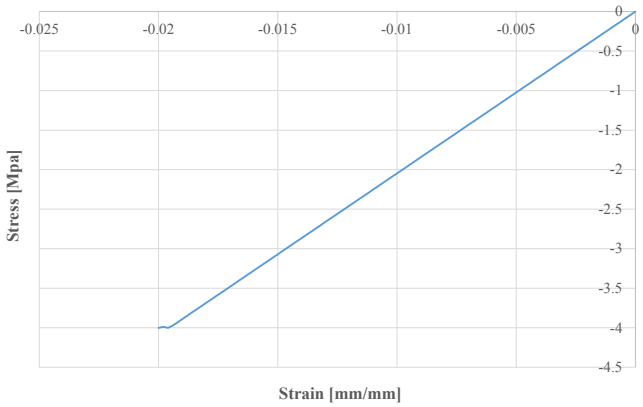
Figure 3.23: Biaxial mixed compression parallel to the grain-tension perpendicular to the grain.

sign from tension to compression in the alternative direction. This means that towards the end the mixed biaxial stress state changes to a pure compressive biaxial stress state.

The opposite mixed biaxial stress state where the tensile stress is applied in the parallel to the grain direction (while the compressive stress in the perpendicular to the grain direction) was also explored, and the results are shown in Fig. 3.24. The same observations made for the previous loading configuration are valid in this case. First, the response in the direction parallel to the grain is very similar to the one corresponding to the uniaxial stress state. Besides, a reduction of the elastic compressive stiffness in the direction perpendicular to the grain as a consequence of the Poisson's ratio effect is also noticed. Nevertheless there is one important difference with respect to the stress-strain response in the direction perpendicular to the grain: no stress unloading occurs after reaching the tensile maximum strength in the direction parallel to the grain.



(a) Tensile stress-strain response in the direction parallel to the grain (X-axis).

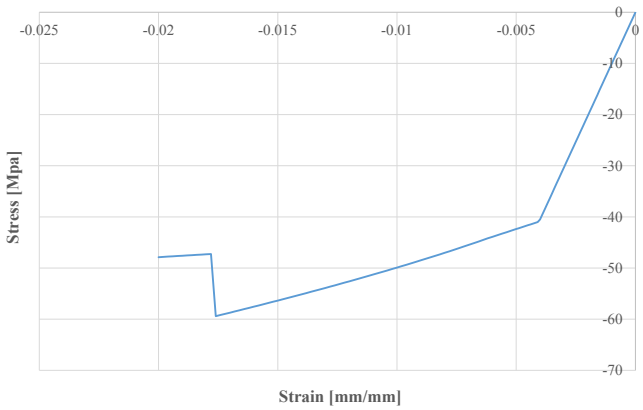


(b) Compressive stress-strain response in the direction perpendicular to the grain (Y-axis).

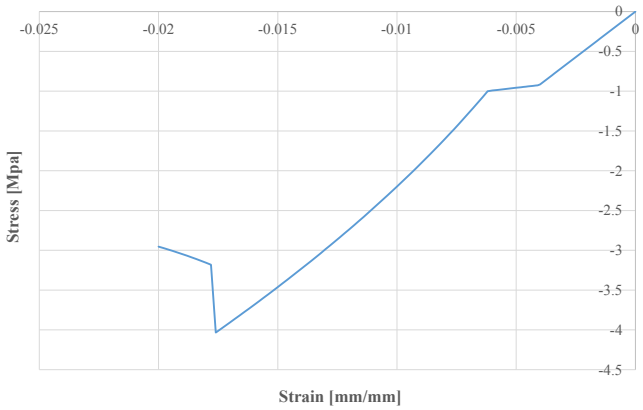
Figure 3.24: Biaxial mixed tension parallel to the grain-compression perpendicular to the grain.

On the contrary, the linear-elastic compressive response continues until reaching the corresponding compressive strength at around 4 MPa (the beginning of the plasticity range).

Finally, the performance of the constitutive model under a triaxial stress state is investigated by applying a compressive load in one direction, while restraining the translation in the other two directions. In this way, the prevention of the lateral expansion generated by the applied compressive load leads to a triaxial stress situation. The first triaxial stress case study corresponds to an applied compressive loading in the direction parallel to the grain. Fig. 3.25 shows the compressive stress-strain response obtained in both parallel (Fig. 3.25a) and perpendicular (Fig. 3.25b) to the grain directions. It can be noticed that compressive yielding in both directions is governed by the strength in the direction parallel to the grain, along which the load is directly applied. Interestingly, a recovery of the post-yielding hardening stiffness to a magnitude larger than the initial



(a) Compressive stress-strain response in the direction parallel to the grain (X-axis).

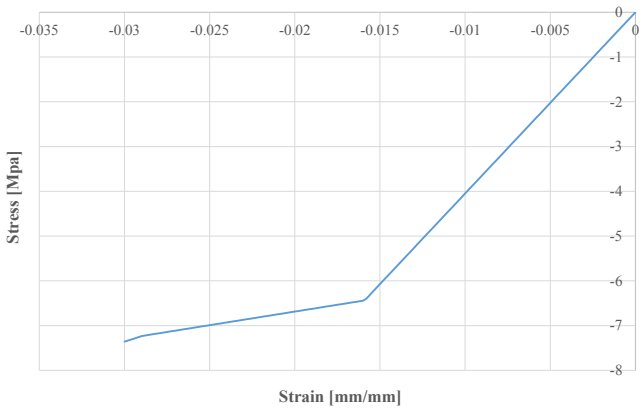


(b) Compressive stress-strain response in the direction perpendicular to the grain (Y-Z-axes).

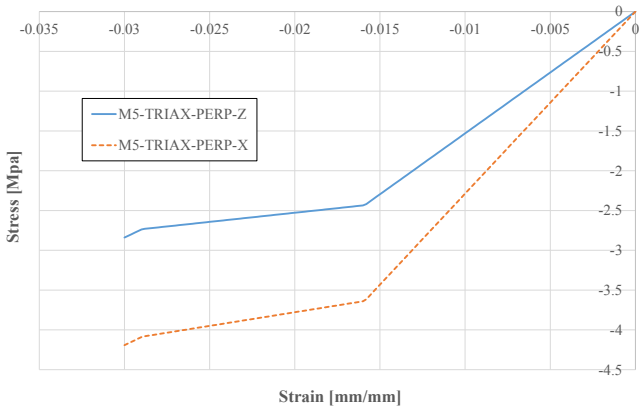
Figure 3.25: Triaxial compression: Loading applied in the direction parallel to the grain (X-axis).

elastic stiffness is observed in the direction perpendicular to the grain (Fig 3.25b). Such a phenomenon is explained by the substantial strain magnitudes in this direction that need to be neutralized after yielding occurs by the lateral expansion restriction imposed by the boundary conditions. Lastly, crushing failure occurs at a total strain of around 0.018. Immediately after, the high level of accumulated damage produces a strength drop of around 20%.

In the second triaxial stress case study the compressive load is applied along the Y-axis (perpendicular to the grain), while the displacement in the other two directions (X and Z axes) are set to zero. Fig. 3.26 shows the stress-strain responses obtained under this configuration. The yielding point is defined by the interaction between the stress components in the axes along the directions perpendicular to the grain (Y and Z axes). Mild



(a) Compressive stress-strain response in the direction perpendicular to the grain (Y-axis).



(b) Compressive stress-strain response in the directions parallel (X-axis) and perpendicular (Z-axis) to the grain.

Figure 3.26: Triaxial compression: Loading applied in the direction perpendicular to the grain (Y-axis).

hardening generated by compressive damage only takes place after the yielding point. At the end, the onset of plasticity increases the stresses generated by the lateral expansion restriction as shown in Fig. 3.26b.

3.9 Concluding remarks

A complete three-dimensional plasticity-damage constitutive model for timber materials is conceptually developed, mathematically formulated and numerically coded and implemented in the FE software DIANA under the framework of a user-supplied subroutine (USS). The thermodynamic consistency of the model developed was also demonstrated. Moreover, its correct formulation and implementation were successfully tested at the ma-

terial level by means of several simple case studies corresponding to different stress states (tension, compression, shear, uniaxial, biaxial and triaxial), loading conditions (monotonic and cyclic) and directions (0°, 45° and 90°) with respect to the grain alignment.

The conceptual core of the model formulation is based on three theoretical components: continuum damage mechanics (CDM), orthotropic plasticity theory and spectral decomposition technique. Each of them accomplishes key functions that joined together build up the model's overall performance. CDM is responsible for the incorporation of brittle failure, stiffness degradation and crack formation zones identification. Plasticity makes it possible to model ductile failure and permanent plastic deformations due to compressive stresses. Finally, spectral decomposition is a numerical method which allows the definition of different independent models for tension and compression. Thanks to spectral decomposition, the plasticity formulation of the model here proposed could be limited to the compressive component of the effective stress space exclusively. As far as the author's knowledge, this "compression-only" plasticity formulation has not been employed in other plasticity-damage constitutive models yet. Therefore, this is an original characteristic of this model, which is grounded on the typical wood post-elastic behaviour.

On the other hand, a thorough mathematical expression to calculate the consistent plasticity-damage tangent stiffness matrix is derived. The contribution of each of the three model components described above (CDM, orthotropic plasticity and spectral decomposition) can be clearly identified from the mathematical expression. The function of the material consistent tangent stiffness matrix is to build the global stiffness matrix of the structure, which is used by the FE program to calculate the displacement increment vector in each iteration. Therefore, the quadratic convergence rate of Newton-Raphson iterative method depends on the proper formulation of the consistent tangent stiffness matrix. A correct functioning of the plasticity-damage model consistent tangent stiffness matrix was verified when testing the USS at the material level, through simple models like the ones shown in Fig 3.6. However, some numerical instabilities which led to divergence were encountered for larger and more complex models. For these cases, better numerical performance was obtained when replacing the matrices $\boldsymbol{Q}^{\pm}$ by an identity matrix. Despite the consequent decrease of the convergence rate, the accuracy of the results was not affected at all.

In addition to the standard input parameters of classical orthotropic plasticity models, the proposed plasticity-damage model requires a total of six additional parameters: mixed-mode fracture energy density (G_f), characteristic length (l_{ch}), exponential soft-

ening constant (n), plasticity hardening modulus (h), compressive damage hardening constant (β) and compressive hardening power (m). The fracture energy density material property is difficult to be experimentally obtained in general, and particularly for wood, since it varies for each different failure mode and for each loading direction. The characteristic length is an input parameter of the crack band method (method employed to diminish mesh dependency), and its value depends on the model mesh size.

The other four parameters should be obtained from a calibration process. The exponential softening parameter influences the shape of the tensile softening post-elastic response. A value of $n = 1$ results in a better match of the experimental data of timber subjected to tensile stresses. The compressive damage hardening constant controls the maximum level of damage and varies from 0 (no damage) to 1 (full damage). A value of $\beta = 1$ generates a perfect plastic response. Therefore, in order to simultaneously incorporate both compressive damage and moderate hardening characteristic of timber, a value of β slightly lower than 1 (around 0.9) is recommended as a starting point for the calibration process. In turn, the compressive damage hardening power parameter defines the order of the hardening slope. From timber experimental evidence, a linear ($m = 1$) hardening slope is recommended as a default initial choice. Finally, the fourth calibration parameter is the plasticity modulus, which is related to the post-elastic hardening in compression and with the material capability to produce plastic deformations. Analytical expressions to estimate the initial value of h were given in Eqs. 3.46 and 3.47.

About the preliminary numerical results obtained from the case studies at the material level, it is demonstrated that strain localization produces mesh dependency, whereas the crack band method can efficiently avoid it as long as the mesh size is fine enough. Besides, stiffness recovery when passing from tension to compression demonstrates that the "structural damage" concept, introduced in Section 3.5.1, was successfully incorporated into the constitutive model. On the other hand, the results obtained from the uniaxial cyclic loading case studies prove that the lower strength and the lack of plasticity (damage-only) characteristic of wood in tension produce high levels of stiffness degradation. By contrast, in compression, the higher strength and the inclusion of plasticity significantly reduce the stiffness degradation. Accordingly, the slope of the unloading branches of the stress-strain curve in the compressive zone lay in-between the slopes of the elastic and secant lines.

The mixed normal-shear stress state generated by a load at 45° introduces a mix of hardening and softening post-elastic response which is consistent with the simultaneous

presence of compressive and tensile stresses acting in different directions. It was demonstrated that the combined brittle-ductile failure mode associated to this stress-state is well represented by the model under both monotonic and cyclic loads. Moreover, mixed three-dimensional stress states (biaxial and triaxial in tension and compression) are also successfully simulated by the proposed timber constitutive model. Overall, the proposed model captures the key characteristics of the cyclic behaviour of timber at the material level, namely, its anisotropic behaviour, tensile softening brittle failure, stiffness cyclic degradation and recovery after load-reversal, and its compressive permanent plastic deformation due to ductile failure. Nevertheless, the complete validation of the constitutive model requires its performance assessment at the structural component level. This task is undertaken in the following chapter.

Chapter 4

Timber Material Model Validation

4.1 Introduction

The literature review carried out on Sections 2.3 and 2.5 leads to conclude that the validation of a constitutive model for timber structures should be performed at two scale levels: material and component. The former is important to corroborate the correctness of the model implementation by verifying its capability to reproduce the basic material nonlinear behaviour hypothesis. The validation of the plasticity-damage model proposed herein at the material level was presented in Section 3.8. On the other hand, the latter type of validation at the component level aims to prove the accuracy and the applicability of the model to real engineering structures. In general, the latter type of validation is more challenging than the former. This chapter presents a validation at the component level of the plasticity-damage constitutive model for timber structures proposed in Chapter 3.

The literature review carried out in Section 2.2 highlighted the need of introducing damage mechanics into the seismic assessment of timber structures, in a similar way it has been performed since many years ago for concrete or steel structures. Therefore, besides demonstrating the model's capabilities, this chapter emphasises the advantages of including damage modelling into the analysis of timber structures.

Although there is a dearth of information regarding cyclic experimental results for wood at the material level, a large amount of experimental research has been carried out on the response of timber elements and timber connections of various types at the component level, including studies on their global cyclic behaviour (see Section 2.6). Available previous studies containing experimental data on dowelled timber-steel connec-

tion specimens subjected to monotonic and cyclic loading were selected for the model validation. Accordingly, two experimental case studies are employed in this chapter. The first one involves the timber braces studied by Popovski et al. [136] which are connected to steel plates through bolts, and loaded in the direction parallel to the timber grain. Two specimens with different bolt arrangements subjected to both monotonic and cyclic loads are presented in Section 4.2. The second case presented in Section 4.3 is a timber beam studied by Xu et al. [185]. The beam is transversally loaded in the direction perpendicular to the grain through an embedded steel plate inserted in the beam midspan. Even though this study considered monotonic loading only, its unusual loading direction and experimental set-up make it valuable for the evaluation of the proposed constitutive model.

4.2 Timber brace-steel plate connection subjected to axial monotonic and cyclic loads

In this section, the experimental results obtained by Popovski et al. [136] are employed to validate the newly proposed plasticity-damage constitutive model for wood. These tests were conducted on timber-steel dowelled connections between glulam braces and steel side plates using steel bolts. In particular, two specimens with 12 mm and 19 mm diameter bolts, respectively, are employed to assess the influence of the dowel diameter size on the wood constitutive model performance.

4.2.1 Finite element model

The glulam brace under consideration had a length of 1.5 m and a cross section of 130 mm x 152 mm; the steel plates were 12 mm thick. The first specimen, S19, had one row of two 19 mm diameter bolts. The spacing between them was 76 mm, while the end distance was 228 mm. On the other hand, the second specimen, S12, is composed of two rows of three 12 mm diameter bolts. The spacing between bolts was 51 mm, the distance between the rows of bolts is 40 mm, and the end distance was 152 mm.

The load was applied to the connection in the axial direction of the brace (parallel to the grain) through a servo-controlled actuator attached to the steel side plates. Fig. 4.1 shows the cyclic loading protocol in terms of the yield displacement (Δ_y) which was determined to be equal to 1.65 mm and 2.14 mm for the specimens S19 and S12, respectively, based on the monotonic experimental test [136]. Further details about the test set-up,

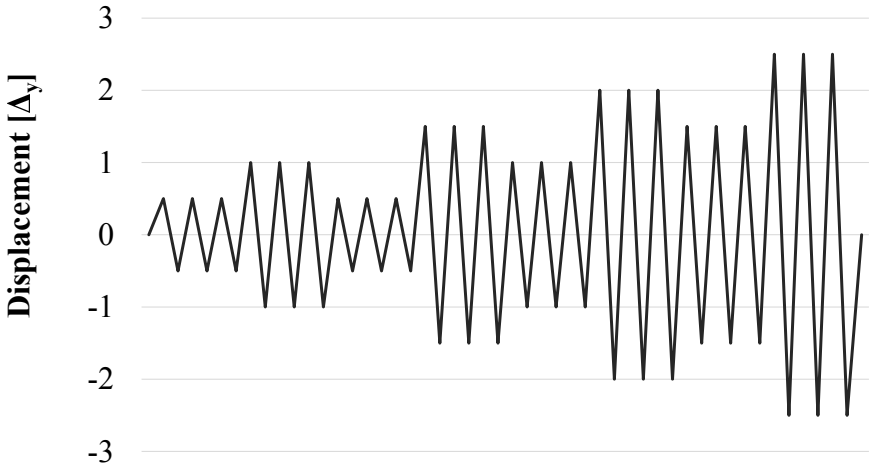
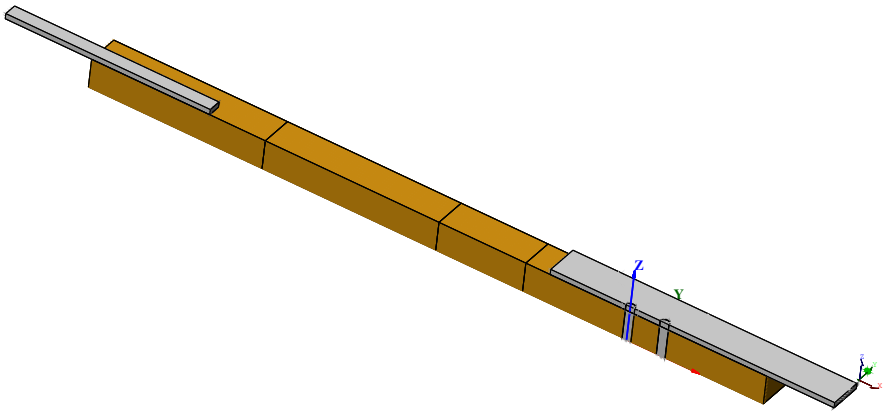


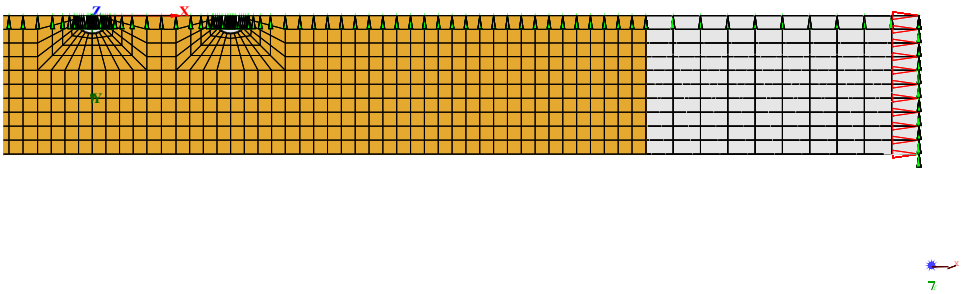
Figure 4.1: Cyclic loading protocol [136].

specimens geometry, material properties and the cyclic testing protocol can be found in [136, 135].

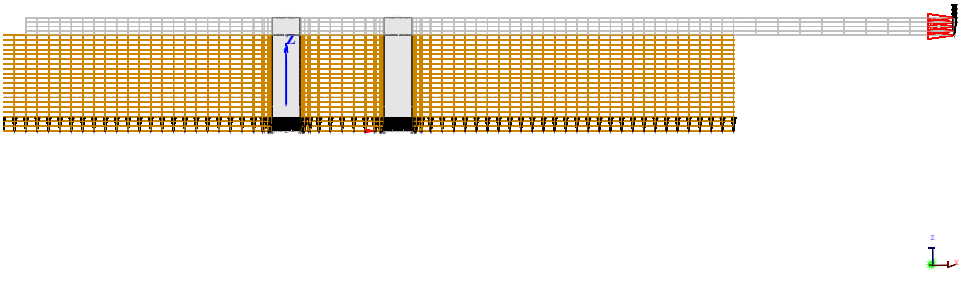
Figs. 4.2 and 4.3 show the finite element models developed in DIANA of specimens S19 and S12, respectively, including the boundary conditions and the nodes where the load was applied. The models take into account symmetry considerations as depicted in Figs. 4.2 and 4.3. The glulam brace as well as the steel plate and dowels were modelled using hexahedral solid elements with linear interpolation. The wood plasticity-damage model developed in Chapter 3 was assigned to the timber brace by means of an user-supplied subroutine (USS), while a standard Mises plasticity model was assigned to the steel dowels. Following experimental observation, the steel side plates are expected to work mainly under the linear elastic range. The interaction between the dowel and the timber surrounding was handled by a bi-dimensional interface element (for a graphical reference, see Fig 4.10) which accounted for the contact nonlinearity between both components. A thorough discussion of the characteristics and formulation of the contact interface model which simulates the timber-steel interaction is presented in Chapter 6. Lastly, a displacement-control approach was followed as represented by the arrows in Figs. 4.2 and 4.3. Geometric nonlinear behaviour due to large displacements was also considered in the analysis, and the Newton-Raphson iterative algorithm was employed for the solution of the system of nonlinear equations.



(a) 3D view

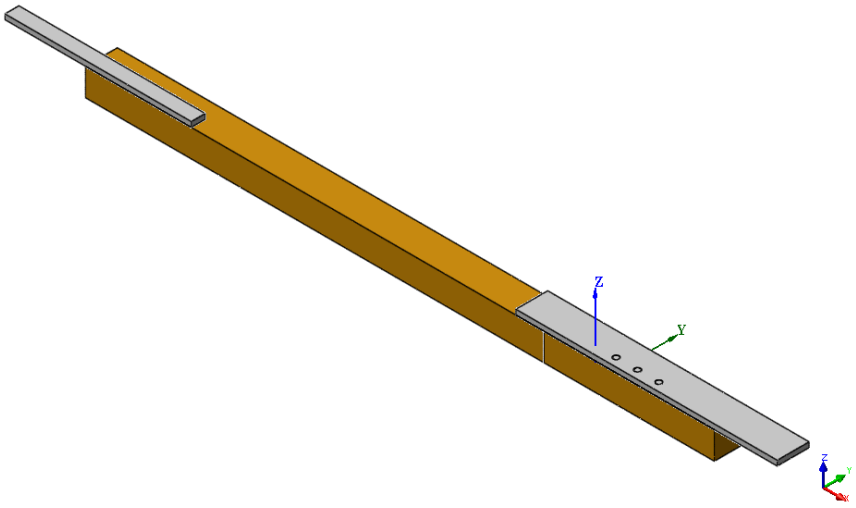


(b) Plan view, boundary conditions (green arrows) and applied load (red arrows)

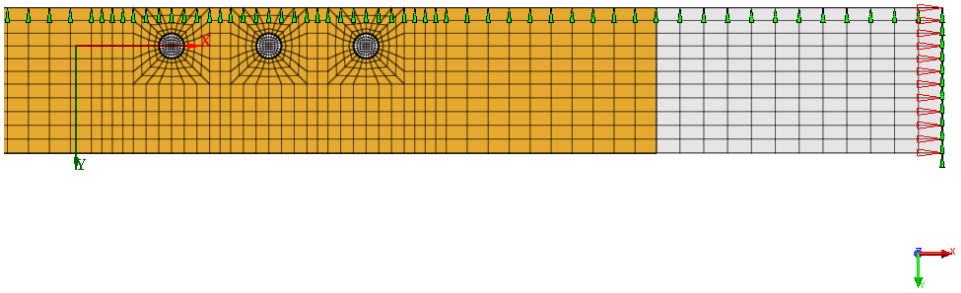


(c) Lateral view, boundary conditions (black arrows) and applied load (red arrows)

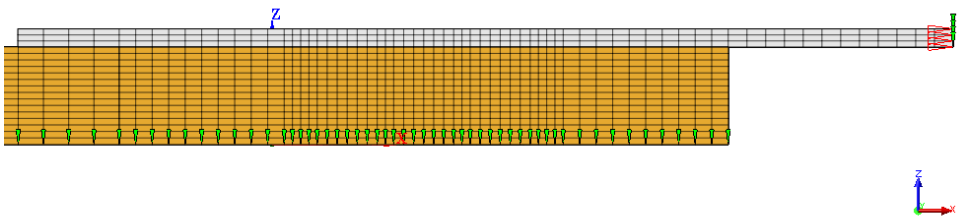
Figure 4.2: Timber-steel dowelled connection finite element model of Specimen S19.



(a) 3D view



(b) Plan view, boundary conditions (green arrows) and applied load (red arrows)



(c) Lateral view, boundary conditions (black arrows) and applied load (red arrows)

Figure 4.3: Timber-steel dowelled connection finite element model of Specimen S12.

4.2.2 Material model parameters selection

An elastic modulus in the direction parallel to the grain equal to 9936 MPa was the only material property of the glulam brace reported in [136, 135]. Therefore, the timber constitutive model parameters presented before in Table 3.2 (Section 3.8) are also employed for this simulation. A fracture energy density (G_f) of 1 N/mm corresponding to a mixed tension-shear failure mode [80] was used. Furthermore, based on the finite element mesh geometry of specimens S19 (Fig. 4.2) and S12 (Fig. 4.3), a characteristic length parameter (l_{ch}) of 2.65 mm was assigned in both cases.

It has been mentioned in Section 3.8 that all the parameters listed in Table 3.2, except the exponential softening parameter (n), the plasticity hardening modulus (h), the compressive damage hardening constant (β) and power (m) parameters, are directly related to the mechanical properties of the timber material, or to the geometric characteristics of the finite element model in the case of l_{ch}. Therefore, only the values of the four previously mentioned parameters need to be assumed or obtained by means of a calibration process. For this particular case study, a value of n equal to 1 was assumed based on typical material tensile and shear tests in timber specimens (see Figs. 2.1 and 2.2). These tests show that wood has no residual strength after brittle failure. Moreover, a value of n higher than 1 was not considered adequate following the discussion offered in Sections 3.3.3 and 3.8.1, and illustrated by Figs. 3.2 and 3.9, respectively, given that it would imply the definition of a post-failure ultimate strain which cannot be recalled from the available experimental data.

On the other hand, in a dowelled connection the interaction of both compressive hardening parameters (h and β) has a direct influence on the maximum capacity of the connection. Besides, h defines the level of plastic deformation in the timber zone around the dowels, while β limits the maximum level of stiffness degradation in compression. However, experimentally observed plastic deformations in timber are rarely reported due to the complexity associated with their measurement. Similarly, cyclic tests on timber specimens at the material level to determine the maximum level of stiffness degradation in compression are unusual. Under these circumstances, it is desirable to calibrate the parameters h and β on the basis of experimental force-displacement relationships of the more common embedment tests in the directions parallel and perpendicular to the grain.

For the case study under consideration, embedment tests were not available, and therefore, the monotonic experimental curves of the dowelled connection were employed

for the calibration of β. It is recognised that this is not an ideal solution but it was considered fit for the purpose at hand. A more rigorous calibration process for another batch of timber glulam beams based on available embedment tests results is described in detail in Section 6.4.

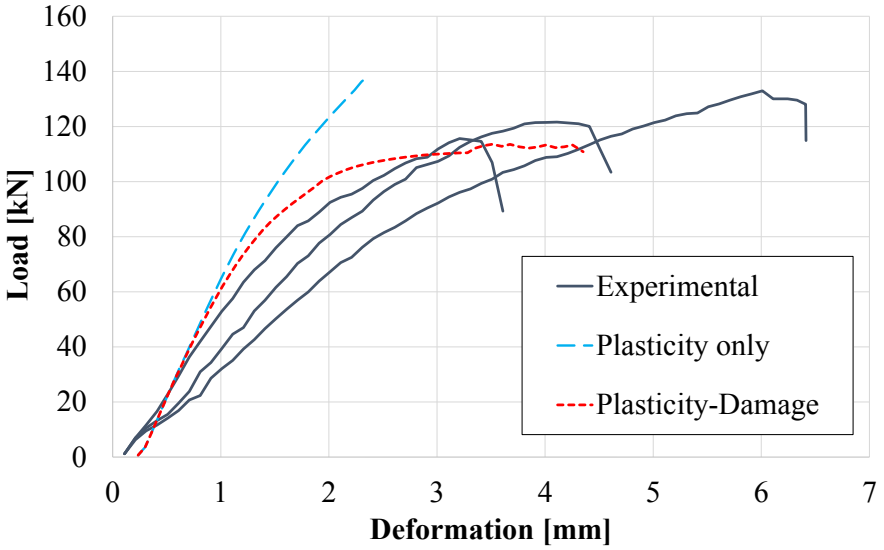
Finally, the value of h was determined by means of Eqs. 3.46 and 3.47, for which a plastic tangent moduli equal to the 13% of the elastic moduli was assumed [187]. A linear hardening damage evolution law for compressive post-elastic behaviour was employed [143, 181], meaning that the value of the power parameter m was defined as 1.

4.2.3 Monotonic loading

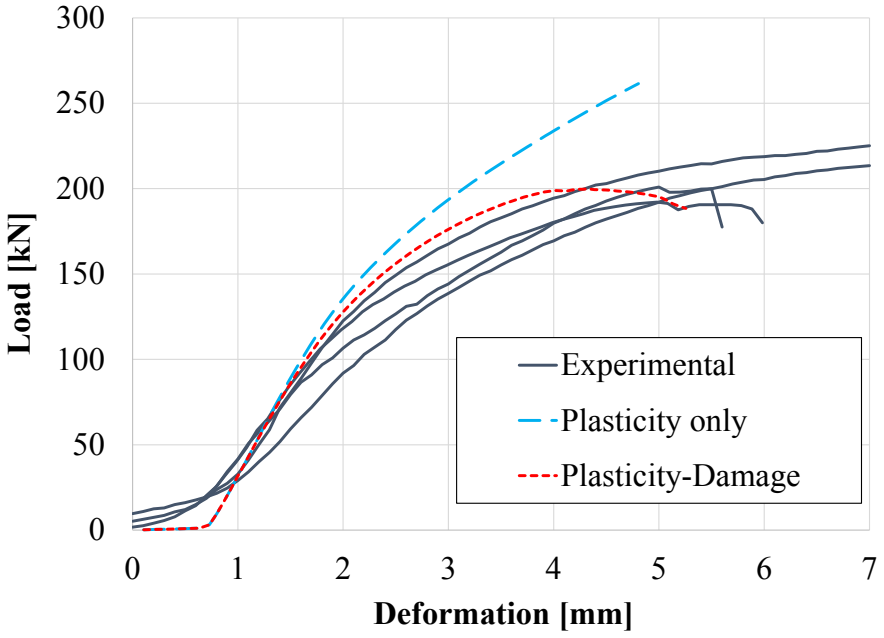
Figs. 4.4a and 4.4b compare the experimental and numerical results of the timber-steel dowelled connection specimens S19 and S12, respectively, subjected to tensile monotonic loading. In addition to the load-deformation response obtained by means of the new plasticity-damage model proposed herein, the corresponding curve for a plasticity-only model has also been included in Fig. 4.4. In both models the Hoffman orthotropic yield surface was employed. It can be observed from these figures that the plasticity-damage model is able to reproduce the stiffness degradation experienced by the specimen, eventually reaching a maximum load plateau and ulterior failure. Moreover, the prediction of the maximum load and the ultimate deformation is good. In fact, the numerical curves obtained with the new plasticity-damage model closely resemble one of the three experimental curves in the case of specimen S19 (Fig. 4.4a), and two of the four experimental curves in the case of specimen S12 (Fig. 4.4b). On the other hand, the plasticity-only model shows a stiffer response which makes the numerical and experimental load-deformation curves diverge at an early stage. Consequently, their load-deformation curves show no ductile behavior (brittle failure) and higher failure loads than the experimental ones. In general, the overall nonlinear monotonic response of the timber-steel dowelled connection is accurately predicted by the new plasticity-damage model.

4.2.4 Cyclic loading

Figs. 4.5a and 4.5b show the experimental and numerical load-deformation hysteretic curves of the timber-steel dowelled connection specimens S19 and S12, respectively. It can be observed from these figures that the numerical results obtained by means of the new constitutive material model reproduce fairly well the cycle-to-cycle stiffness degra-



(a) Specimen S19.



(b) Specimen S12.

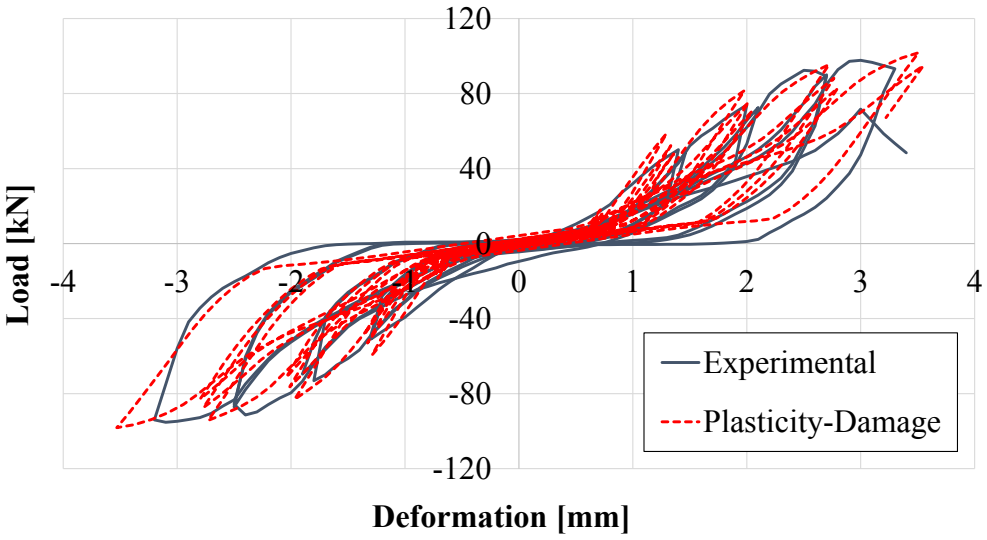
Figure 4.4: Timber-steel dowelled connection subjected to monotonic tension loading. Comparison of experimental [135] and numerical results.

dation. Furthermore, the maximum load per cycle and the in-cycle strength degradation are also accurately predicted. The loading and reloading slopes corresponding to each hysteretic loop of both specimens S19 and S12 are precisely captured by the model. For specimen S19, the unloading slope is also very well captured, while in the case of specimen S12 the experimental vertical unloading branch cannot be reproduced by the numerical curve with the same level of precision. It should be noted, however, that such a sharp unloading slope (Fig. 4.5b) is related to a greater extent to the contact mechanics between the steel dowel and the surrounding timber than to the actual nonlinear behaviour of the wood. Besides, the connection pinching behaviour and plastic deformations also play an important role. Specimen S19 hysteretic response (Fig. 4.5a) shows a well defined pinching behaviour with negligible permanent deformations that are accurately captured by the numerical model. Conversely, the hysteretic response of specimen S12 indicates less pinching and higher permanent deformations than specimen S19. This kind of behaviour is directly linked to the higher amount of plastic deformation produced in the 12 mm diameter steel dowels of specimen S12. Thus, a faithful simulation of pinching and permanent deformations of timber-steel dowelled connection relies on the numerical model capacity to accurately reproduce the steel dowel plastic strains, and to its effectiveness in transferring the stresses from the damaged wood to the steel dowels. These aspects are further discussed in Chapter 6.

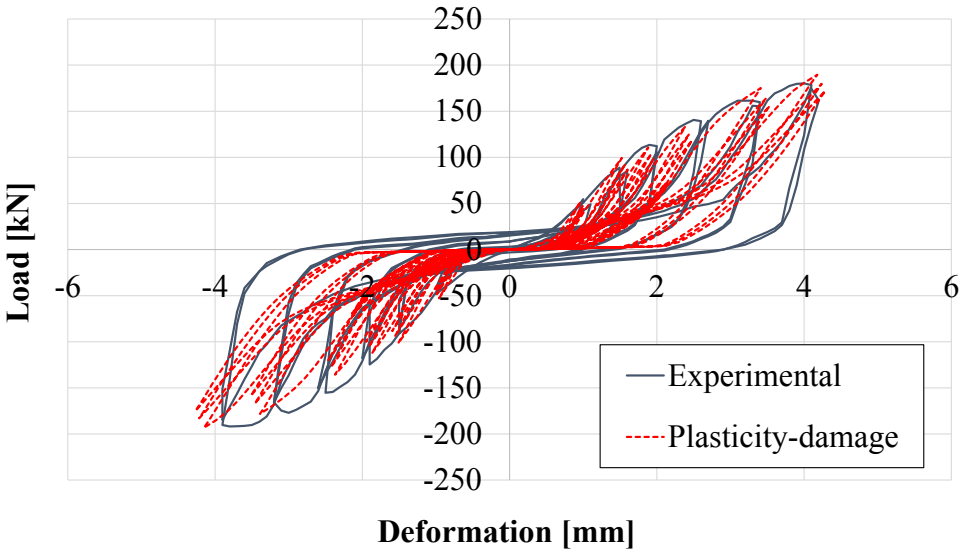
4.2.5 Mesh-dependency analysis

A mesh sensitivity analysis was carried out to assess the model mesh-dependency and to determine an appropriate mesh size. In order to do this, the monotonic numerical results obtained for specimen S19 (Fig. 4.2) are presented herein for different levels of mesh refinement (and characteristic lengths). Two coarser and two finer mesh configurations were taken into account. Besides, two different criteria were followed for the definition of the mesh configurations. The first criterion was to change the number of finite elements in the timber brace thickness direction, while the second criterion was to change the element dimensions in the zone around the dowel. A description of the original mesh and the four additional mesh configurations analysed, including the values of their corresponding characteristic length parameters (l_{ch}), is presented in Table 4.1.

Fig. 4.6 shows the five monotonic load-displacement curves corresponding to the case studies summarized in Table 4.1. A broad agreement among the original and the other four mesh configuration variations can be noted. Besides, it can be concluded from



(a) Specimen S19.



(b) Specimen S12.

Figure 4.5: Timber-steel dowelled connection subjected to cyclic loading. Comparison of experimental [135] and numerical results.

Table 4.1: Mesh sensitivity analysis case studies of Specimen S19

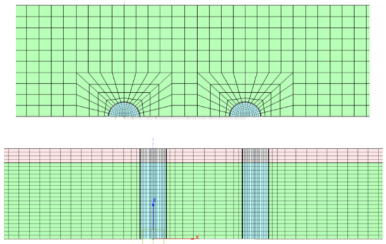
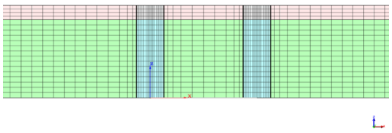
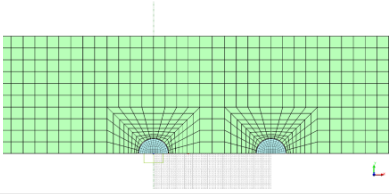
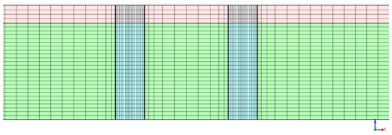
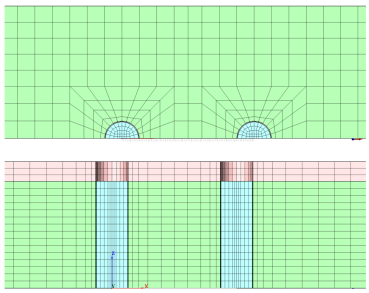
Model ID	**Description**	**Mesh geometry**	**Char. length** (l_{ch}) [mm]
Mesh0	Original mesh		2.65
Mesh1	Coarser mesh in the thickness direction		2.92
Mesh2	Finer mesh around the dowel		2.00
Mesh3	Finer mesh in the thickness direction		2.45
Mesh4	Coarser mesh around the dowel and in the thickness direction		3.16

Fig. 4.6 that the variations of the number of finite elements along the thickness (Mesh1 and Mesh3) has a minor influence on the global numerical force-displacement response of the type of connection under investigation. It can also be appreciated that when a finer mesh is employed for the timber zone around the dowel (Mesh2), the predicted strength and deformation capacities of the connection are underestimated. Conversely, when a coarser mesh size is defined for the timber zone around the dowel (Mesh 4), the precision of the predicted force-displacement curve is not affected.

In conclusion, the results obtained were observed to have limited mesh dependency. However, very small elements in the timber zone around the dowels should be avoided due to their potential to generate spurious stress concentrations in the contact zones, which can hinder the stress transfer. This is a widespread characteristic of finite element models that leads to unrealistic reductions in the predicted maximum capacity of the connection. In general, and regardless of the material model employed, it is recommended that the smallest elements in the timber zone be larger than any element in the dowels, thus avoiding the presence of free nodes.

For instance, a very fine mesh for specimen S19 is shown in Fig. 4.7a. It can be seen that the timber elements around the dowel are smaller than the dowel elements, and therefore, some of the timber elements nodes are not connected. The monotonic load-displacement curves corresponding to this mesh configuration and the original are shown in Fig. 4.7b. It is demonstrated that the employment of such a too fine mesh results in a considerable underestimation of the connection maximum capacity.

4.3 Timber beam-steel plate connection subjected to monotonic loading perpendicular to the grain

In the previous section the capability of the timber plasticity-damage model to simulate the monotonic and cyclic response of a timber-steel dowelled connection has been demonstrated. Nevertheless, it is also important to assess the response of the model to a connection loaded in the direction perpendicular to the grain. Considering the greater strength of timber along the grain, timber dowelled connections are rarely designed to resist loads in the direction perpendicular to the grain. Consequently, experimental studies on dowelled connections under this particular type of loading condition are scarce.

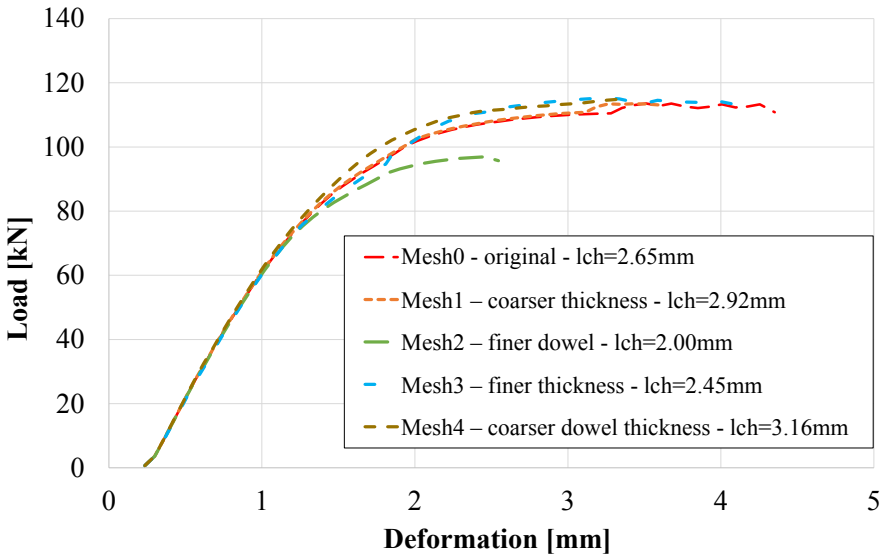
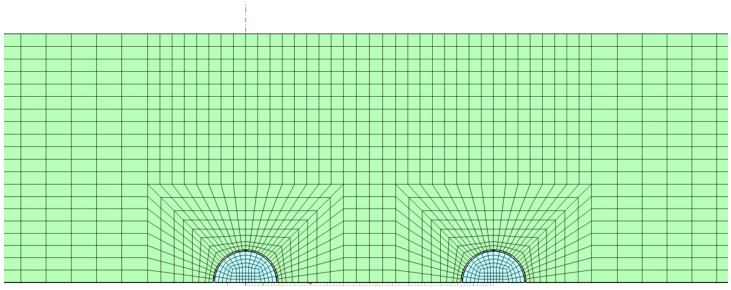
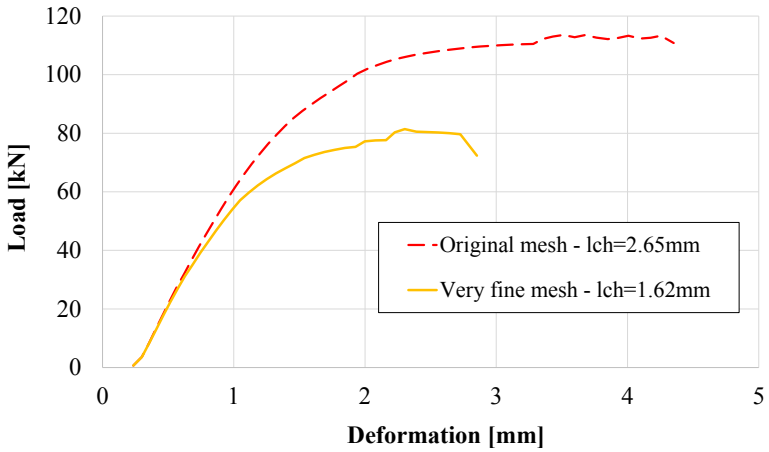


Figure 4.6: Specimen S19: Mesh sensitivity analysis.



(a) Very fine mesh geometry.



(b) Load-deformation monotonic curves.

Figure 4.7: Specimen S19: Very fine mesh of the timber zone around the dowel.

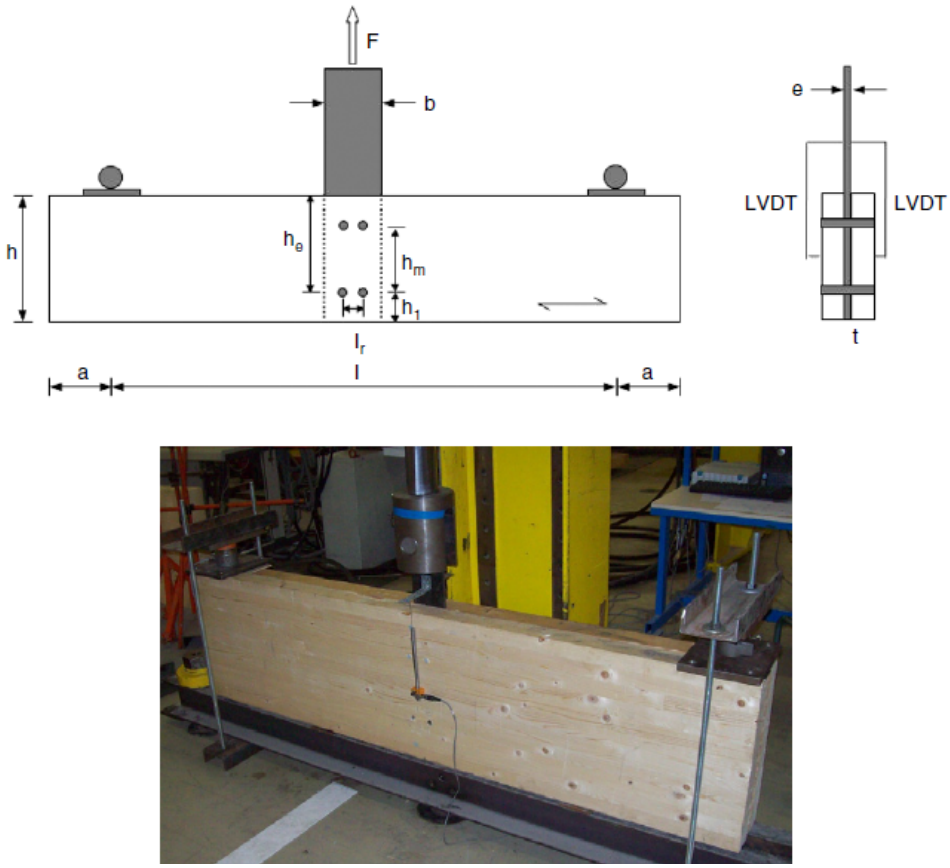


Figure 4.8: Configuration and geometric characteristics of the timber-steel connection loaded in the direction perpendicular to the grain (Figure taken from Xu et al. [185]).

Xu et al. [185] carried out an experimental and numerical study on a timber beam-steel plate dowelled connection subjected to monotonic loading in the direction perpendicular to the timber grain. This study will be used for the validation of the plasticity-damage model proposed herein. Unfortunately, the scope of this investigation was limited to monotonic loading only. The connection comprises a 1.8 m long single-span timber glulam beam with a steel plate transversally embedded in the beam at its mid-span. They are connected through 16 mm diameter steel dowels. The specimen configuration and geometric characteristics are presented in Fig 4.8 [185] and Table 4.2.

Table 4.2: Geometric dimensions (in mm) of the multi dowel timber-steel connection specimen shown in Fig. 4.8 [185]

d	**t**	**a**	**b**	$\boldsymbol{l_r}$	$\boldsymbol{h_l}$	$\boldsymbol{h_m}$	**h**	**l**	**e**
16	75	100	115	65	140	206	486	1800	8

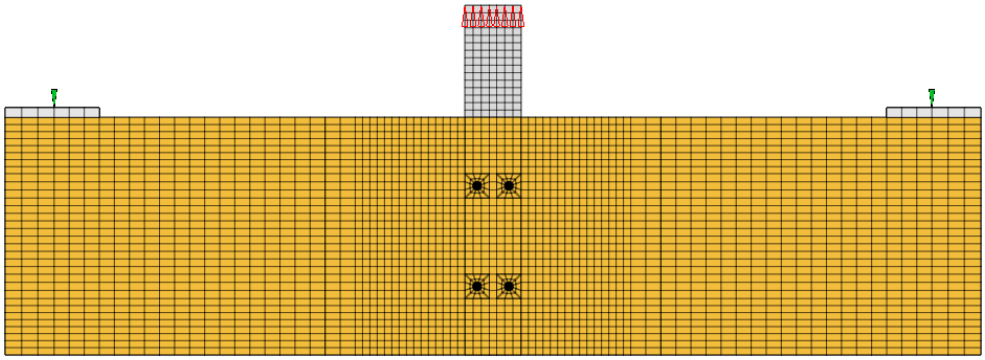


Figure 4.9: Multi dowel timber-steel connection FE model, boundary conditions (green arrows) and displacement load (red arrows).

A monotonically increasing vertical displacement is applied on the steel plate as shown in Fig. 4.8. Forces are transmitted from the steel plate to the timber beam through the four dowels. In accordance with the experimental results [185], the timber beam showed two failure modes. First, local ductile failure occurred as a consequence of wood embedment and dowel flexural yielding. Large plastic deformations of the timber around the dowels are characteristic of this type of failure. The second failure mode involved timber splitting and determined the maximum load carrying capacity of the connection. A crack along the timber grain direction appeared below the upper line of bolts [185].

4.3.1 Finite element model

The timber-steel joint specimen described above was modelled using DIANA [35]. Fig. 4.9 shows the model based on eight-node hexahedral linear solid elements with linear interpolation and an average element size of the steel-timber connection zone of around 16 mm. A static non-linear analysis was performed with monotonically increasing vertical displacement, uniformly applied to the upper part of the steel plate. The simply-supported beam boundary conditions and load application nodes are precisely indicated in Fig. 4.9. Geometric nonlinear behaviour due to large displacements and Newton-Raphson solution algorithm were considered for this analysis.

Fig. 4.10 shows the interface elements used to model the interaction between the three components of the joint: timber beam, steel plate and steel bolts. The interaction of the bolts with the surrounding timber and with the steel plate is handled by a surface inter-

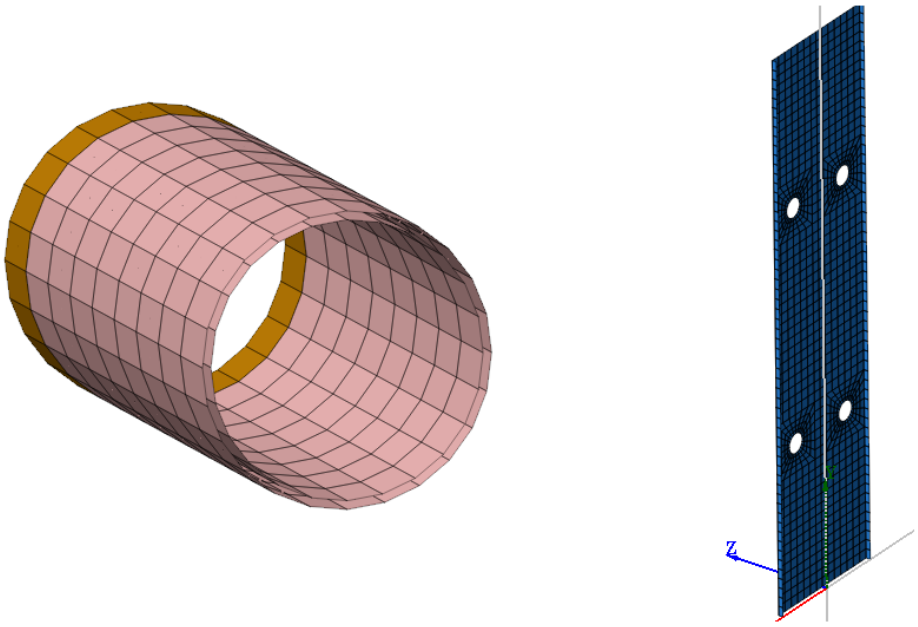


Figure 4.10: Timber-steel interface elements: Dowel-beam and dowel-plate (left side); beam-plate (right side).

face element (see left side of Fig. 4.10) which acts only when the two bounding surfaces come into contact. In such a condition, compressive and friction interaction forces are generated in the directions normal and tangential to the interface plane, respectively. On the other hand, when the boundary elements are not in contact, normal tensile stresses are not allowed. Under this condition, the normal and tangential stiffness are reduced to a value close to zero, allowing free separation and slipping between the elements located at both sides of the interface.

Likewise, the interaction between the steel plate and the timber beam along their four common vertical planes is managed by an interface element (see right side of Fig. 4.10) with a contact model similar to the one mentioned in the previous paragraph. A detailed description of the interface contact model formulation employed herein is offered in Section 6.2. Moreover, Table 4.3 presents the values of the input parameters assigned to the interface elements shown in Fig. 4.10.

The proposed plasticity-damage constitutive model was assigned to the timber beam, while a Mises associated isotropic plasticity model with linear hardening was employed for the steel plate and dowels. Tables 4.4 and 4.5 present the values of the input parameters adopted by both timber and steel material models, respectively. The values of all the mechanical and strength parameters presented in both tables were obtained from [185].

Table 4.3: Steel-timber interface elements input parameters

Parameter	**Steel Dowel-Timber Beam**	**Steel Dowel-Steel plate**	**Steel Plate-Timber Beam**
Normal stiffness [MPa/mm]	200	500	200
Shear stiffness [MPa/mm]	10	10	10
Max. allow. tensile stress [MPa]	0.1	0.1	0.1
Cohesion [MPa]	0.0	0.0	0.0
Friction coefficient	0.5	0.2	0.3

Only two modifications were needed so as to fulfil the wood transverse isotropy condition (see Section 3.2). To this end, the values of ν_{XZ} and G_{YZ} listed in Table 4.4 were updated using the expressions given in Eq. 3.6. The remaining parameters are proper to the plasticity-damage model, and therefore, they are not reported in [185]. The values of these parameters, located at the bottom half of Table 4.4, were determined following the same criteria outlined in Section 4.2.2. For this reason, the values assigned to the calibration parameters n, β and m are the same of Table 3.2. Finally, in light of the literature review in Section 2.4 and the good results obtained in Section 4.2, Hoffman orthotropic plasticity yield surface is maintained for this simulation.

A special mention should be made regarding the fracture energy density (G_f). The experimental observations [185] indicate that the local ductile failure (wood embedment plus steel dowel yielding) is followed by a brittle global splitting failure which determines the maximum load carrying capacity of the connection. As previously discussed in Section 3.8, such a brittle failure is directly linked to the fracture energy density material property, and therefore, the value assigned to this parameter has a considerable influence on the numerical prediction of the connection capacity. For this reason, a value of $G_f = 5$ was used for this case study as indicated in Table 4.4. Further discussion on the implications of the value of G_f for the numerical results is offered in the next section.

Table 4.4: Plasticity-damage material model input parameters for the timber beam

Poisson's ratios	$\nu_{XY} = 0.41$	$\nu_{YZ} = 0.41$	$\nu_{XZ} = 0.41$
Shear moduli [MPa]	$G_{XY} = 750$	$G_{YZ} = 138.3$	$G_{ZX} = 750$
Young's moduli [MPa]	$E_X = 11600$	$E_Y = 390$	$E_Z = 390$
Compressive strengths [MPa]	$f_X^- = 39$	$f_Y^- = 3.24$	$f_Z^- = 3.24$
Tensile strengths [MPa]	$f_X^+ = 19.8$	$f_Y^+ = 0.48$	$f_Z^+ = 0.48$
Shear strengths [MPa]	$f_{XY} = 3.24$	$f_{YZ} = 3.24$	$f_{ZX} = 3.24$
Fracture energy density [N/mm]	$G_f = 5$		
Characteristic length [mm]	$l_{ch} = 7.38$		
Exponential softening parameter	$n = 1$		
Hardening modulus [MPa]	$h = 13.4$		
Compressive hardening constant	$\beta = 0.85$		
Compressive hardening power	$m = 1$		
Orthotropic yield criterion	Hoffman		

4.3.2 Analysis of results

Fig. 4.11 shows the numerical and experimental [185] monotonic load-deformation curves. For comparison purposes, the numerical curve corresponding to the standard orthotropic plasticity-only model is also plotted jointly with the plasticity-damage model curve. In the elastic range, both numerical models show an accurate prediction of the joint stiffness. However, it is clear that the plasticity-only model is not able to capture the rapid stiffness degradation of the timber, resulting in a great overestimation of the connection capacity. Conversely, the plasticity-damage model proposed herein allows an early progressive stiffness reduction which results in a better match with the experimental curves and an improved estimation of the connection capacity. Moreover, the computed values presented in Table 4.6 confirm that both numerical models described above fairly predict the

Table 4.5: Plasticity material model input parameters for steel elements

Parameter	**Steel Dowel**	**Steel Plates**
Elasticity modulus [MPa]	210000	210000
Poisson's ratio	0.3	0.3
Yield stress [MPa]	366	309
Ultimate stress [MPa]	543	434
Ultimate strain	0.2	0.2
Isotropic yield criterion	Mises	Mises

elastic stiffness of the connection. Nevertheless, only the plasticity-damage model allows an accurate estimation of the maximum load and the corresponding deformation capacity.

The plasticity-damage curve in Fig. 4.11 was obtained with a value of $G_f = 5$ N/mm. Fig. 4.12, on the other hand, shows the load-deformation curves corresponding to $G_f = 1$ N/mm as well as $G_f = 10$ N/mm. It can be observed that stiffness degradation is not affected by the fracture energy density. However, for a small value like $G_f = 1$, early softening occurs immediately after the end of the stiffness degradation process. This kind of behaviour is not in agreement with the experimental evidence [185]. Conversely, higher values of G_f (e.g. 5 N/mm or 10 N/mm) result in hardening post-elastic responses that match the experimental curves. It is worth noting that, a further increment of the value of G_f does not generate a significant change on the numerical load-deformation response. Therefore, considering that for numerical reasons the value of the fracture energy density is divided over the characteristic length (l_{ch}), a geometric parameter which depends on the finite element mesh size (see Sections 3.3.3 and 3.6), a minimum value of G_f associated to a particular model mesh size should be determined for this type of problems where the main loading direction is perpendicular to the timber grain. The coarser the model, the higher the value of l_{ch}, and the higher the value of G_f required to prevent early softening in the numerical response, and *viceversa*. The mesh of the finite element model employed in this case study (Fig. 4.9) can be defined as coarse, being this the reason why a fracture energy density higher than 1 N/mm is needed to ensure a precise numerical response.

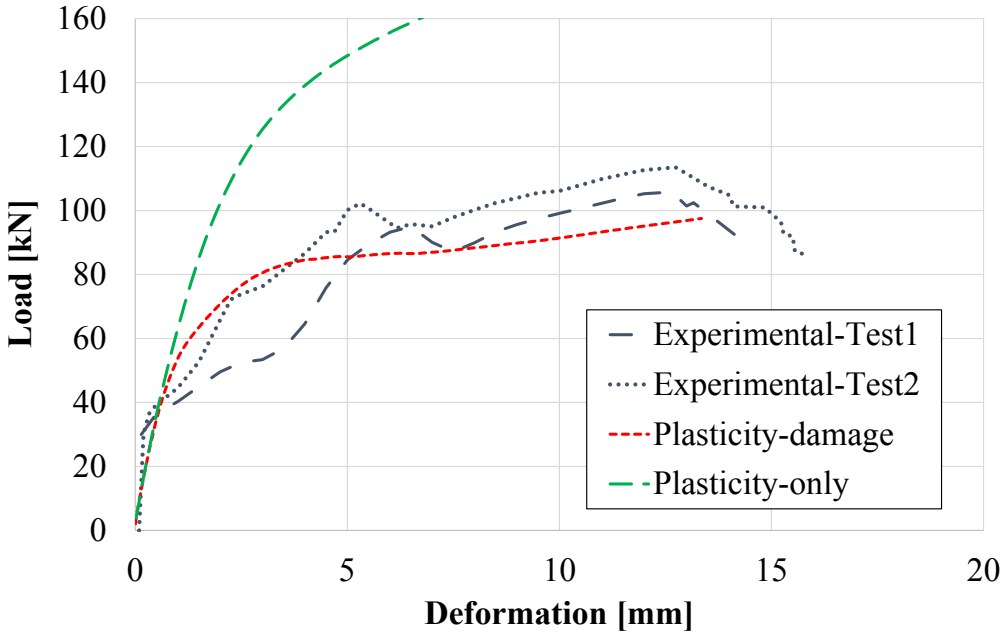


Figure 4.11: Multi dowel timber-steel connection loaded in the direction perpendicular to the grain. Comparison of experimental [185] and numerical results.

The deformed shape and the vertical displacement contour of the dowel timber-to-steel connection model is shown in Fig. 4.13 for four different stages of relative deformation (0.5 mm, 2.5 mm, 5 mm and 10 mm). Fig. 4.11 shows that the first deformation level corresponds to the linear elastic range, the second to the stiffness degradation stage, while the third and the fourth to the ultimate capacity stage with large levels of deformation. Fig. 4.13a shows that for the smaller deformation of 0.5 mm (elastic range), the vertical displacement of the beam increases uniformly from 0 mm at the supports to approximately 1.5 mm at the mid-span. Obviously, the maximum displacement zone corresponds to the steel plate where a 2 mm displacement load is imposed. In the timber beam, maximum displacements of approximately 1.8 mm (just slightly smaller than in the steel plate) are observed around the dowels.

When the applied displacement increases to 5.6 mm (Fig. 4.13b), the deformation between the timber beam and the steel plate also increases to 2.5 mm. Furthermore, the maximum vertical displacement in the timber beam is not uniformly distributed throughout the midspan any more, but only in the zone above the bottom row of dowels. A further deformation increment up to 5 mm (Fig. 4.13c) translates the peak deformation zone to the region between the upper row of dowels and the beam upper edge. Consequently, the deformation distribution is not as uniform as in the previous cases. Finally, when the

Table 4.6: Experimental and numerical load-deformation curve parameters

Test/Model	**Elastic stiffness** [kN/mm]	**Maximum load** [kN]	**Deformation at max. load** [mm]
Test 1	49	106	12.5
Test 2	67	114	12.5
Plasticity-damage model	71.7	97.5	13.35
Plasticity-only model	71.7	> 160	N.A.

applied displacement loading at the top of the steel plate is 15.5 mm (Fig. 4.13d), the corresponding relative deformation goes up to 10 mm. Here, due to large plastic deformations and the generalized damage, the maximum displacements in the central upper edge of the timber beam becomes as high as the applied vertical displacement in the steel plate.

More detailed views of the plastic deformation and extent of damage in the central zone of the timber beam, around the steel dowels, are shown in Figs. 4.14 and 4.15 for mid-span deformations of 0.5 mm, 2.5 mm, 5 mm and 10 mm. The tensile plastic strains in the horizontal direction (parallel to the grain) are displayed in the left side of Fig. 4.14, while the compressive plastic strains in the vertical direction (perpendicular to the grain) are shown on the right side. It can be noticed from Fig. 4.14 that the timber plasticity zone due to compressive stresses begins around the dowel holes and expands outwards as the applied load increases. Both types of plastic strains take place in the same region because they are linked by means of the Poisson's effect. Compressive strains in the direction perpendicular to the grain are generated by the interaction between the timber beam and the steel dowels. Consequently, tensile plastic strains are generated in the direction parallel to the grain. Given the great difference of magnitudes among the elasticity moduli in both directions, the tensile plastic strains are negligible (order of magnitude of 10^{-4}) compared to the compressive plastic strains (order of magnitude of 10^{-2}).

Similarly, the left side of Fig. 4.15 shows the contour plots of the compressive damage

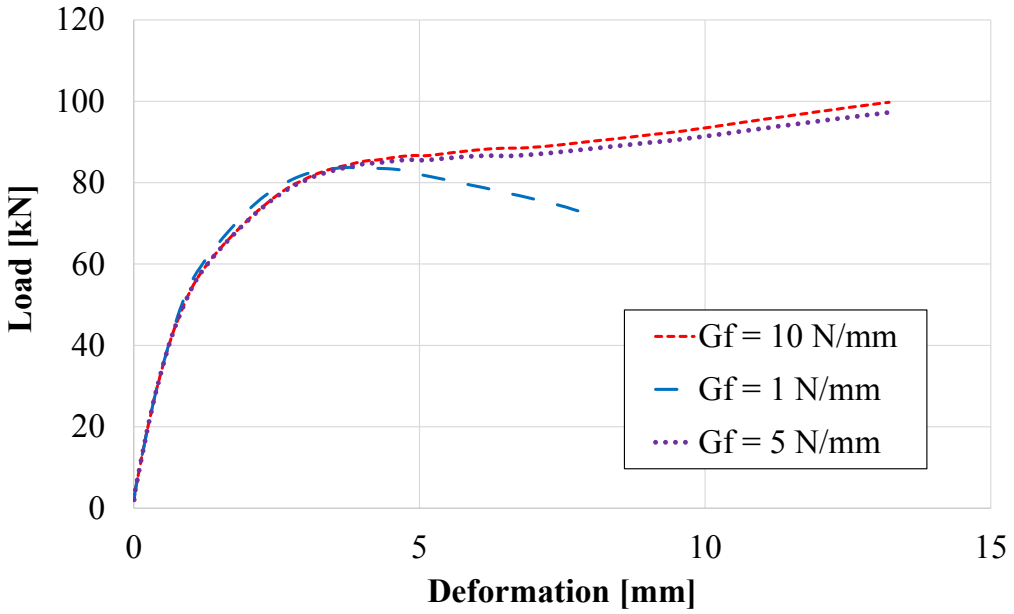
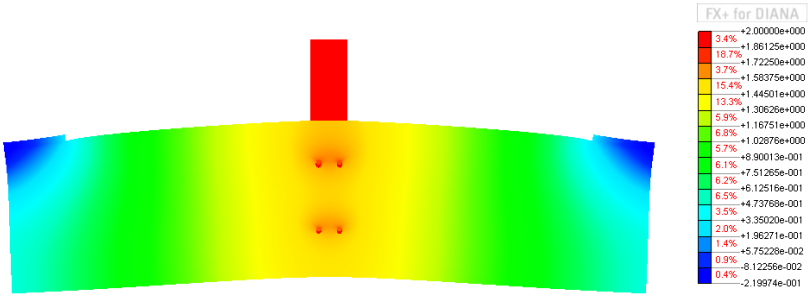


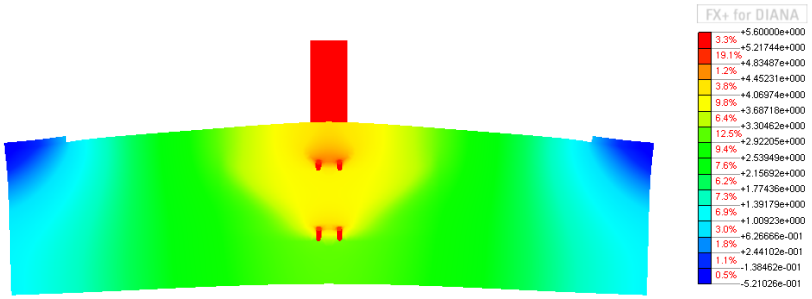
Figure 4.12: Plasticity-damage model: Influence of the fracture energy density parameter on the numerical load-deformation curve.

variable, while the right side shows the plot corresponding to the tensile damage variable. As expected, due to the simultaneous action of plasticity and damage in compression, the magnitudes and extent of compressive damage (crushing) are minor compared to tensile damage (cracking). Another evidence of such a concurrent compressive plasticity and damage phenomena is the common location of plastic strains (Fig. 4.14) and crushing (Fig. 4.15) zones.

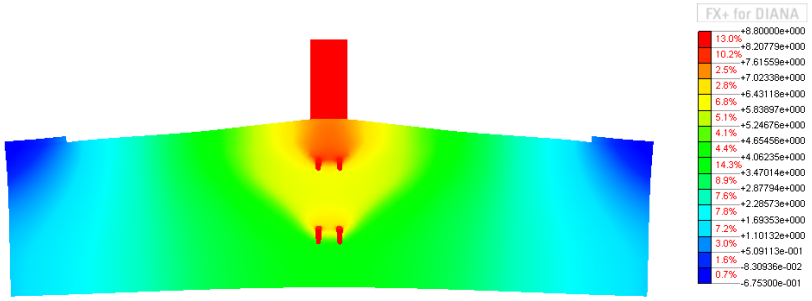
On the other hand, Fig. 4.15b draws attention to the exclusive early development of tensile damage during the initial elastic range. Later, the tensile damage zone expands towards the sides and in-between the dowel holes at a beam deformation level of 2.5 mm (Fig. 4.15d). At a beam mid-span deformation of 10 mm (Fig. 4.15f), tensile damage is also present in the central part of the timber beam upper edge. This is a consequence of timber beam bending, which generates high flexure tensile stresses in the direction parallel to the grain. At this stage, tensile damage is generalized and failure is imminent. It is important to highlight that the red zones, where the tensile damage variables reaches its maximum value equal to 1 (dowel rows and beam upper edge), configure potential regions where large cracking may take place. Based on the experimental observations reported in [185], this numerical prediction of the cracking zones locations is correct.



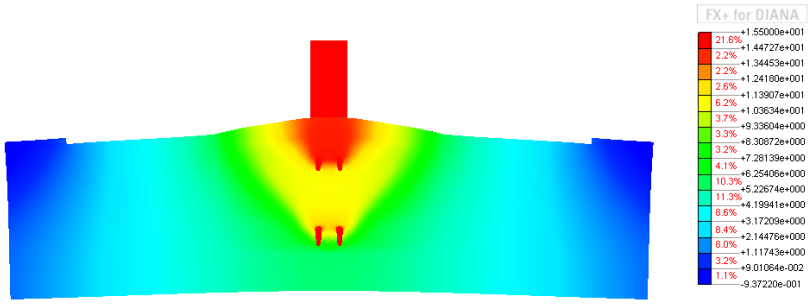
(a) Vertical deformation of 0.5 mm at mid-span



(b) Vertical deformation of 2.5 mm at mid-span

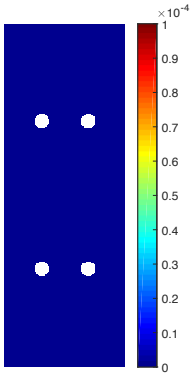


(c) Vertical deformation of 5 mm at mid-span

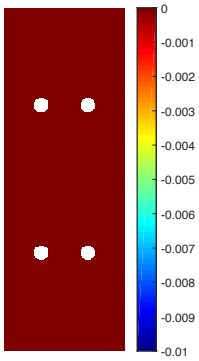


(d) Vertical deformation of 10 mm at mid-span

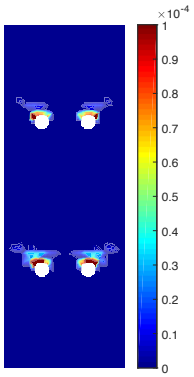
Figure 4.13: Contour of the timber-to-steel connection vertical displacement.



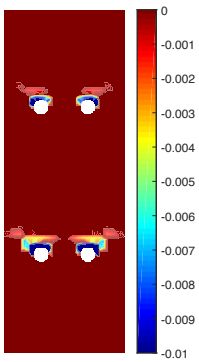
(a) ε_{pX} at 0.5 mm.



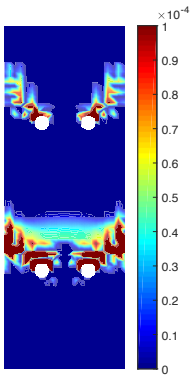
(b) ε_{pZ} at 0.5 mm.



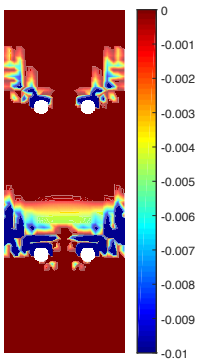
(c) ε_{pX} at 2.5 mm.



(d) ε_{pZ} at 2.5 mm.

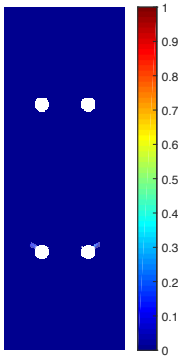


(e) ε_{pX} at 10 mm.

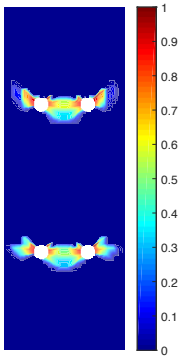


(f) ε_{pZ} at 10 mm.

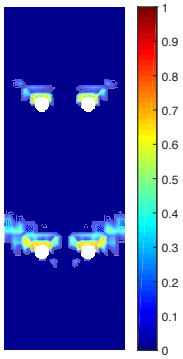
Figure 4.14: Plastic strains in the directions parallel (ε_{pX}) and perpendicular (ε_{pZ}) to the grain.



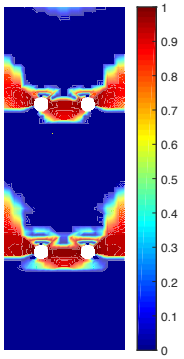
(a) ω^- at 0.5 mm.



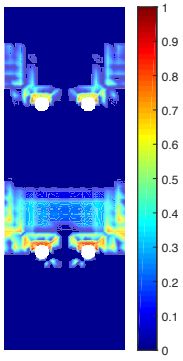
(b) ω^+ at 0.5 mm.



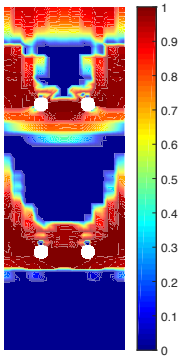
(c) ω^- at 2.5 mm.



(d) ω^+ at 2.5 mm.



(e) ω^- at 10 mm.



(f) ω^+ at 10 mm.

Figure 4.15: Compressive (ω^-) and tensile (ω^+) damage variables.

4.4 Concluding remarks

The proposed plasticity-damage model for timber structures has been validated at the component level. For this purpose, the numerical results predicted by the model were compared against the experimental data of timber-steel components reported elsewhere [135, 185]. In general, the overall nonlinear responses of timber-steel dowelled connections subjected to monotonic and cyclic loads are accurately predicted by the plasticity-damage model. A good correlation between the experimental and numerical hysteretic curves is obtained until large deformation levels. Furthermore, all the key features of the nonlinear timber behaviour were captured by the plasticity-damage model, including: tensile softening brittle failure, stiffness cyclic degradation and recovery after load-reversal, as well as compressive permanent plastic deformation due to ductile failure.

On the other hand, it has been demonstrated that plasticity-damage models are more fit for simulating the monotonic and cyclic response of timber dowelled connections than plasticity-only models. Damage mechanics allows the simulation of the progressive stiffness degradation characteristic of timber structures from early loading stages. This results in a close match of the experimental curves and an accurate estimation of the connection load capacity. By contrast, plasticity-only models produce a stiffer response that causes divergence between numerical and experimental curves, and thus, overestimation of the connection capacity. Therefore, the incorporation of continuous damage evolution is essential to capture timber stiffness degradation and to obtain a good agreement between numerical and experimental results.

A mesh-dependency analysis was carried out. Limited mesh dependency of the model was observed as a result. However, very small elements in the timber zone around the dowels should be avoided due to their potential to generate spurious stress concentrations in the contact zones, which can lead to an unrealistic underestimation of the connection maximum capacity.

Experimental studies on timber-dowelled connections show that their characteristic failure modes initiate with local ductile failure (wood embedding plus steel components yielding) and end with a global brittle failure due to wood splitting. In turn, brittle failure is directly related to the fracture energy density material property, whose magnitude has thus a considerable influence on the maximum load carrying capacity of the connection. Therefore, in order to avoid fictitious premature failure, a sensitivity analysis should be performed to determine the minimum fracture energy density value associated

to the particular mesh size of the model.

The good performance of the model for simulating the monotonic response of a timber-steel connection subjected to tension loads in the direction perpendicular to the grain [185] deserves a special mention. The brittle failure mode of this type of connection is usually difficult to simulate using numerical models. Therefore, the closer match of the experimental curves obtained with the proposed model under this particular loading condition is remarkable. Furthermore, the applicability of damage mechanics to the identification of potential cracking zones and the quantification of structural damage was demonstrated. The numerical and experimental study of similar specimens under cyclic loads is of interest, and further research work should be undertaken in this direction.

Finally, the validated constitutive model for timber structures proposed herein can now be applied to the study of other innovative (and possible more complex) structural systems or components, in combination with complementary numerical modelling techniques. To this end, experimental and numerical research carried out on an innovative timber beam-to-steel column moment connection will be presented in the following chapters.

Chapter 5

Experimental Cyclic Response of Timber-Steel Joints

5.1 Introduction

In general, there are a few reasons that justify the proposal of hybrid timber-steel structural systems in which timber beams are combined with steel columns. First of all, it has been demonstrated that most of the moment connections with timber columns suffer from severe local damage in the beam-column interface due to the accumulation of stresses perpendicular to the column axis, which is often aligned with the grain direction [78, 175, 86]. The second reason for choosing a timber beam-to-steel column moment connection is particular to seismic design considerations. Lateral forces are mainly resisted by vertical structural elements like walls and columns. The high strength of steel columns can limit the amount of plan area used by the structural elements of the lateral resisting system. Furthermore, through this chapter it is shown that the proposed beam-to-column timber-steel dowelled connection fulfils the "strong column-weak beam" seismic design principle. On the other hand, it is recognized that hybrid structures are a feasible and promising solution for the construction of high-rise buildings using mass timber in the short and medium term [166, 192]. As a consequence, pure timber structures are giving way to hybrid timber-steel, which, from an aesthetic point of view, are aligned with the current architectural trends [189].

A vast amount of experimental and numerical studies on hybrid timber-steel structures can be found in the existing literature. For instance, Tesfamariam et al. [166] studied the seismic vulnerability of a steel moment resisting frame with CLT infill walls, and found that this structural system is a feasible solution for buildings up to nine stories

height. Xu et al. [189], performed an experimental and numerical study of the nonlinear behaviour of a timber column-to-steel beam moment connection subjected to monotonic loading. Global ductile behaviour was observed for all the specimens. Later, Hassanieh et al. [67] carried out an experimental study based on a four-point bending test of a steel-timber composite floor system consisting of LVL slabs supported by steel beams. It was demonstrated that an almost full composite action between beam and slab can be achieved by joining them using glue and mechanical connectors. More recently, Zhang et al. [192] assessed the nonlinear response of a building structural system comprising a central timber core shear wall connected to a perimeter glulam frame through steel beams. A ductility reduction factor of 5 was obtained for this structural system as a consequence of the numerical analysis performed in this research work. The higher ductility of this system in comparison with timber-only structures makes it more appealing for seismic design purposes. Karagiannis et al. [86] proposed two types of hybrid timber beam-to-tubular steel moment connections whose monotonic nonlinear responses were experimentally and numerically studied. Their experimental results showed high ductility and acceptable levels of stiffness and capacity for both semi-rigid connection configurations. Finally, Andreolli et al. [1] carried out the only experimental study focused on the cyclic response of hybrid timber-steel dowelled connections. The authors studied a moment timber-steel connection which concentrates the rotations and plastic deformations in a short-length steel beam attached to the end of a glulam timber beam by means of glued-in-steel rods. The experimental results showed that high levels of ductility can be achieved with this type of connection without losing significant bending capacity.

No experimental study on hybrid timber-steel beam-to-column connections under the action of cyclic loads was found in the specialized literature. For this reason, an experimental study on the cyclic response of a hybrid timber beam-to-steel wide-flange column moment connection is presented in this chapter, building upon the previous work of Karagiannis et al. [86]. Due to its wider use in hybrid timber-steel structures, a wide-flange steel column section, instead of the tubular steel column originally employed in [86], was used herein. A particular characteristic of the hybrid timber beam-to-steel column joint proposed and studied in this chapter is the steel components employed to connect the timber beam to the steel column, namely, long bolts in combination with top and seat angles. The vertical leg of the angles is bolted to the column while the horizontal leg is connected to the timber beam via four vertical long bolts passing through the whole beam section. The steel angles and bolts are the two principal sources of ductility and energy dissipation of the connection. However, timber local failure like embedding and crushing due to compressive stresses, or cracking and plug shear due to tensile and shear

stresses, respectively, also plays an important role in the connection's cyclic non-linear behaviour. Therefore, the understanding of timber mechanics, local failure modes and non-linear response is fundamental to the design of a ductile connection with enough energy dissipation capability.

Three different specimens, each of them with a different combination of steel angle thickness and bolt diameter, were tested to analyse and compare their strengths, hysteretic responses, ductility levels, failure modes and energy dissipation capabilities. The results obtained for the three specimens allowed the identification of timber local failure types characteristic of the proposed connection, and the assessment of their influence on its global response. As a result, some basic design recommendations were drawn aimed at preventing brittle failure modes. This chapter is divided in two parts: Section 5.2 presents the test set-up, the cyclic loading protocol and the specimen geometric and material characteristics, while Section 5.3 presents the experimental results which are analysed in detail.

5.2 Experimental set-up and test specimens

5.2.1 Test set-up

A schematic representation of the test specimen is shown in Fig. 5.1. The wide-flange steel column was placed in a vertical position and steel anchors were used to rigidly attach its base to the strong floor. Upper lateral support was provided to the steel column by means of an inclined steel strut. The rectangular cross-section timber beam lay horizontally and was connected to the column via top and seat steel angles. Four long steel bolts pass through the beam section along its depth and fasten the horizontal (beam) legs of the top and seat angles. Two short bolts were employed to connect the vertical legs of the angles to the flange of the steel column. Tightening torques of 190 Nm and 100 Nm were applied to the short and long bolts, respectively.

The test set-up is shown schematically in Fig. 5.2, while Fig. 5.3 shows a picture of one of the test specimens being tested. Displacement were applied in the vertical direction through an hydraulic actuator acting on the free end of the timber beam. The actuator had a maximum loading capacity of 98 kN and a maximum stroke of $\pm$125 mm. With the objective of avoiding the application of a concentrated bending moment at the beam free end, the hydraulic actuator was connected to the beam through a double-hinged load-

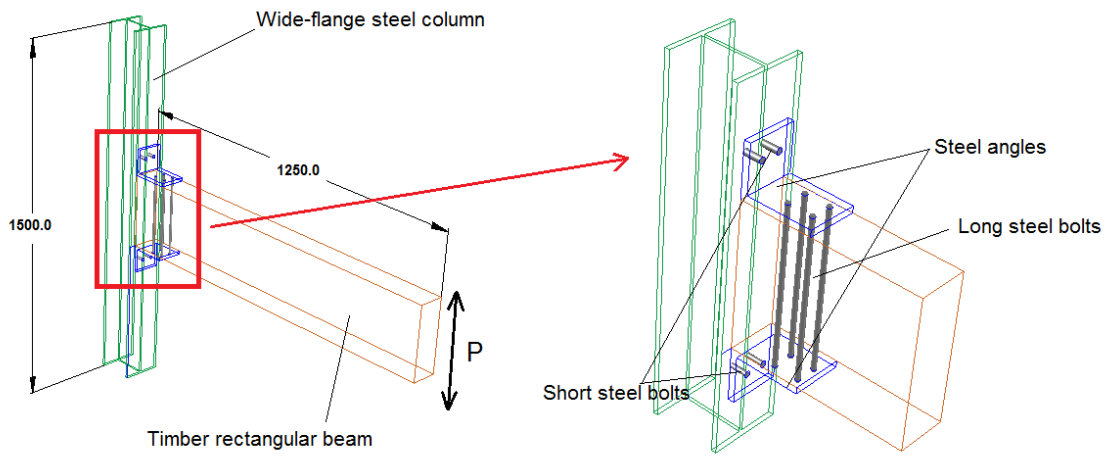


Figure 5.1: Schematic representation of specimens and set-up.

ing apparatus. Besides, in order to avoid out-of-plane movements, a frictionless lateral restraint was employed. The distance between the load application point and the beam-to-column interface is 1250 mm, while the distance between the steel column fixed base and its upper lateral support is 1500 mm. Due to the high stiffness of the wide-flange steel column, the short separation between its supports and the web stiffeners placed every 500 mm, the deformations and stress levels in the column were negligible. This was continuously monitored during testing. In this way, the behaviour of the tested moment connection was similar to a cantilever beam which maximum stresses and deformations were concentrated in the beam-to-column joint. Particularly, the steel bolts, the steel angles and the timber zones nearby were the connection components with the highest stress demands. This is consistent with the main goal of this experimental investigation, namely, studying the nonlinear response of timber-steel dowelled beam-to-column moment connections and their characteristic local and global failure modes.

Fig. 5.4 shows the geometry and dimensions (in mm) of the structural components of the hybrid timber-steel beam-to-column connection. These included a 203 x 203 x 60 kg S275 steel wide-flange column (Fig. 5.4a), 405 x 140 mm GL28 h Glulam beam with 45 mm thick lamellas (Fig. 5.4b), L 200 x 150 mm S275 steel angles (Fig. 5.4c), as well as short and long Grade 10.9 steel bolts (Fig. 5.4d). The steel angles were cut so that their width was equal to the width of the beam (140 mm). The diameter of the short bolts is 20 mm, while the diameter of the long bolts and the thickness of the angles vary for each of the three specimens tested.

The displacement transducer and the load cell incorporated within the actuator

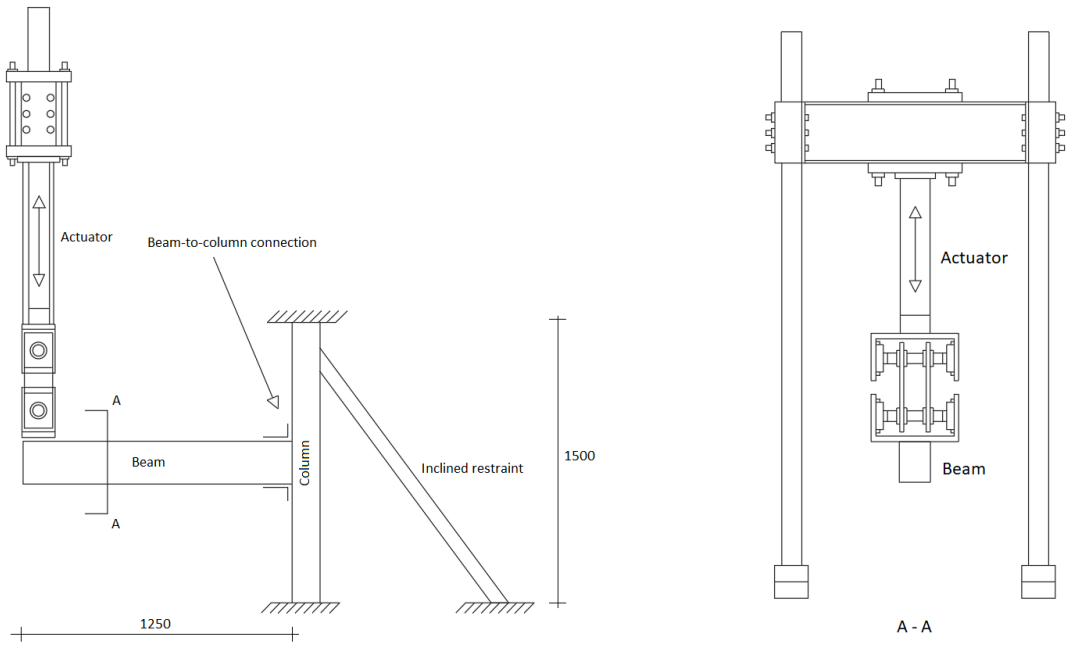


Figure 5.2: Experimental set-up.

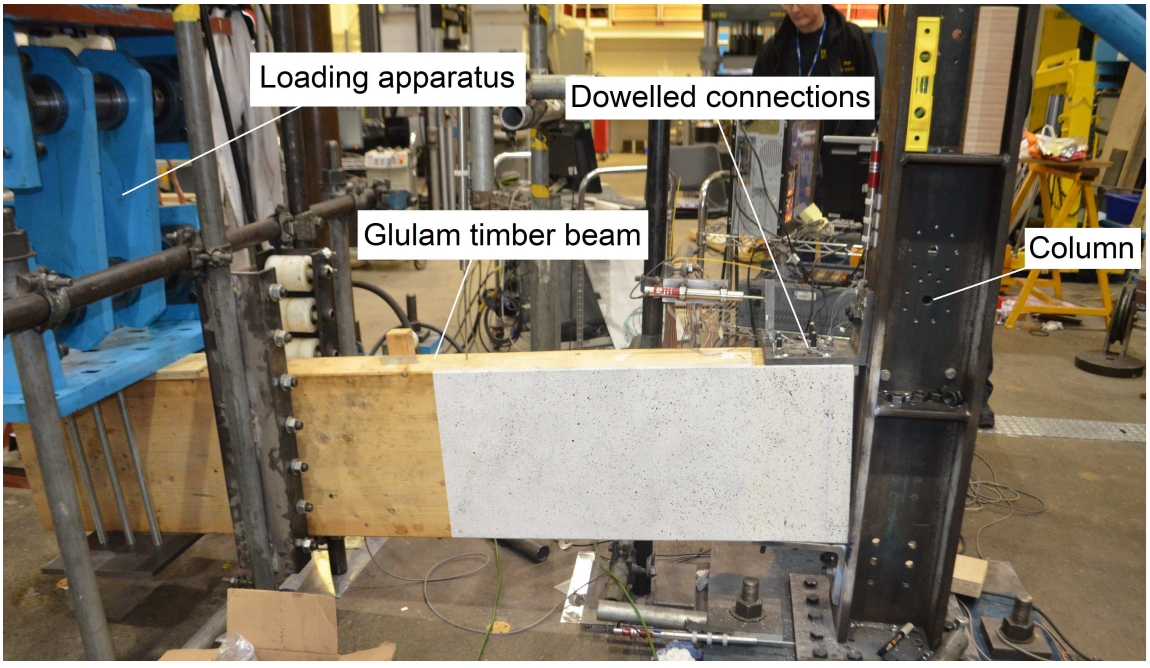
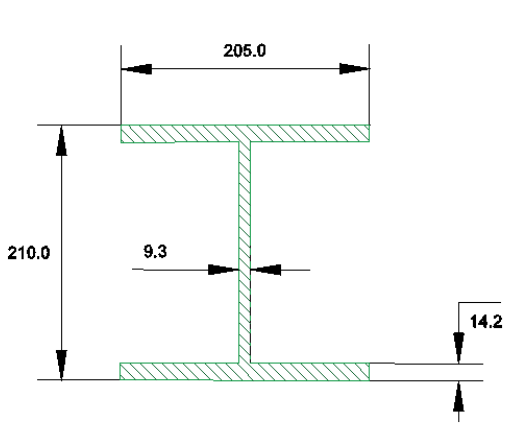
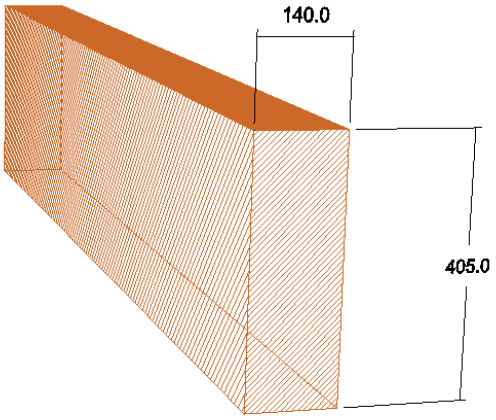


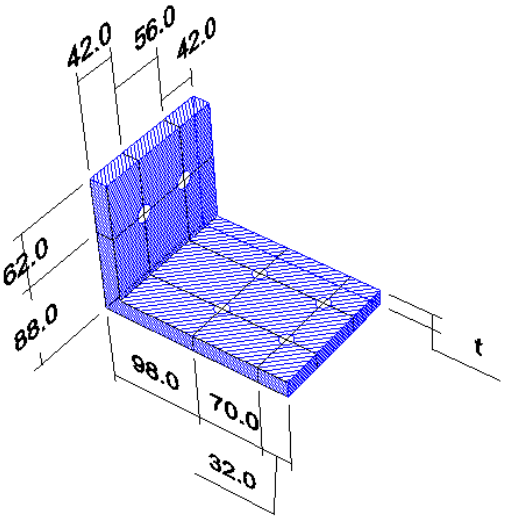
Figure 5.3: Test specimen and set-up.



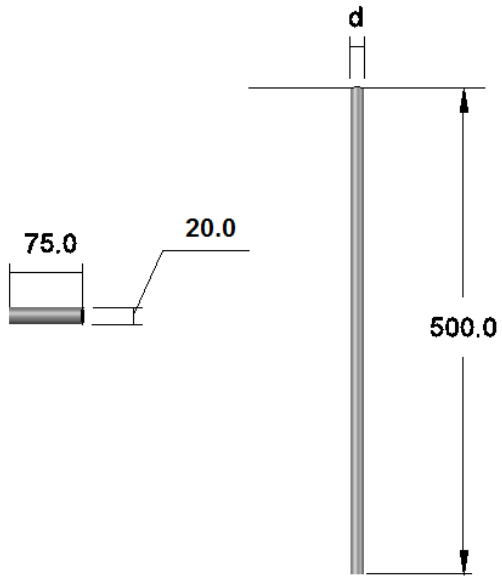
(a) Steel column cross-section



(b) Glulam beam



(c) Top and sit steel angles



(d) Short and long steel bolts

Figure 5.4: Geometry of the hybrid beam-to-column connection components.

recorded the applied vertical displacement in the beam tip and the corresponding reaction force. Besides, several transducers were employed to monitor the horizontal and vertical displacements of the top steel angle and the timber beam. An additional displacement transducer was located in the base of the column to verify that its position remained fixed with respect to the laboratory reaction floor. An inclinometer was also attached to the timber beam to measure its rotation with respect to the horizontal initial position, and to verify the displacement transducer measurements. Finally, a number of strain gauges were attached to the top steel angle and to the top and lateral faces of the timber beam.

5.2.2 Test specimens

Three specimens were tested under reversed cyclic loading. Different combinations of steel angle thickness and long bolt diameters were assigned to each specimen as indicated in Table 5.1. Depending on the size of angles and bolts, different types of behaviour and failure modes of the moment connection are expected. For instance, thick angles in combination with slender bolts concentrate the nonlinear behaviour and consequent local failure in the bolts and the timber zone surrounding them. This type of failure could be ductile or brittle, depending on the bolt slenderness and the timber mechanical properties. On the other hand, if the angle is thin a ductile failure is generated due to its own yielding, while the interaction between dowels and timber exerts minor local demands to each other.

Table 5.1: Test specimens

Specimen	**Angle thickness (t)** [mm]	**Long bolt diameter (d)** [mm]
S1-12D-12A	12	12
S2-12D-15A	15	12
S3-16D-15A	15	16

For design purposes, a ductile failure caused by yielding of the steel angles that avoids

the possibility of brittle local timber failure is desired. However, one of the main objectives of this investigation is the study of timber nonlinear behaviour when this type of hybrid timber-steel moment connections are subjected to cyclic loading. Therefore, the sizes of the angles and the long bolts in Table 5.1 were defined in light of this criterion.

In specimen S1, the strength of the steel angles and that of the timber-dowelled connection are equilibrated. Therefore, the applied loading should produce important deformations in both the angles and the bolts. However, in specimen S2 a higher demand should be imposed over the timber-dowelled connection zone due to the thicker angle, meaning that the steel bolts experience greater deformation levels. Finally, in specimen S3 the strength levels of the angles and the timber-dowelled connection are better balanced again. Nevertheless, in this case the presence of larger bolts should concentrate most of the nonlinear demand and local failure in the timber zone around them. As a consequence, the bolt holes separation indicated in Fig. 5.4c fulfils the requirements of minimum allowable bolt-to-bolt distances for timber (Table 8.4 of Eurocode 5 [14]) and steel (Table 3.3 of Eurocode 3 [15]) connections for specimens S1 and S2 only. Specimen S3 is defined not to meet these criteria with the objective of studying timber local brittle failure.

5.2.3 Cyclic loading protocol

Fig. 5.5 shows the cyclic loading protocol employed. This protocol is based on the recommendations provided by ECCS [41]. A total of 25 loading cycles of progressively increasing amplitudes were applied up to a maximum displacement of 119 mm in each direction. This is equivalent to 14 times the referential connection yield displacement of 8.5 mm, which in turn corresponds to an assumed yield rotation of 7 mrad. This is an approximate characteristic yield rotation valid for semi-rigid moment connections. The rates of displacement application were constant within each cycle and varied between 0.2 mm/s and 1.0 mm/s.

5.2.4 Material characterization

The same batch of glulam timber beams employed by Karagiannis et al. [86] was used in this study. A detailed experimental assessment (including four-point bending, compression, tension shear and embedding tests) and material characterization were performed and are reported in [87] for this batch of glulam specimens which measured density and

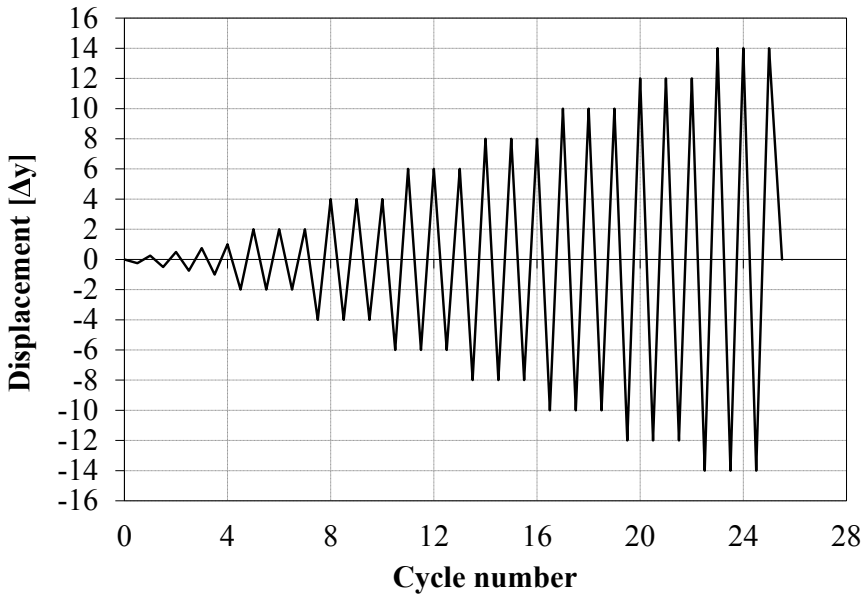


Figure 5.5: Cyclic loading protocol.

moisture content were 431 kg/m^3 and 12%, respectively. The mean values of the mechanical properties obtained from these tests are summarized in Table 5.2. The Young's modulus of the connection steel components is 200,000 MPa. For the column and angles a S275 steel grade with a yield stress of 361 MPa and an ultimate stress of 486 MPa was used. Finally, Grade 10.9 bolts were selected to attach the angles to the column and the timber beam.

5.3 Observations and analysis of experimental results

5.3.1 Moment-rotation hysteretic response

The moment-rotation hystereses response of the three specimens are shown in Fig. 5.6. During the tests, the three connections reached the maximum rotation level at ±0.10 rad, without exhibiting a global failure. What is more, after applying the specified loading protocol shown in Fig. 5.5, the three specimens were subjected to six additional cycles corresponding to the maximum amplitude of $14\Delta_y$. The purpose of this was to investigate the possibility of intensifying the strength degradation process of the connection by incrementing the number of maximum amplitude cycles, eventually leading to a global failure. However, no significant strength degradation neither global failure was observed

Table 5.2: Average values of the mechanical properties of the glulam GL28h beam in [MPa]. Adapted from Karagiannis [87].

Mechanical properties	**Parallel**	**Perpendicular**
Compressive strength	$f_{c,0} = 33.0$	$f_{c,90} = 3.6$
Tensile strength	$f_{t,0} = 36.2$	$f_{t,0} = 1.6$
Shear strength	$f_{s,0} = 5.0$	–
Young's modulus	$E_0 = 12157$	$E_{90} = 425$
Shear modulus	$G_{s,0} = 952$	–

in the hysteresis loops shown in Fig. 5.6.

It can be observed from Fig. 5.6 that the transition from the elastic to the inelastic regime is progressive and no abrupt change due to slip is appreciated. The initial loading stiffness of the three specimens remain constant at early loading stages. After moderate deformation levels, the incursion into the inelastic regime produces a progressive degradation of the loading stiffness in all specimens, although the degradation rate differs in each case. In the case of specimen S1, the loading stiffness decreases rapidly. On the other hand, the stiffness degradation in specimen S3 remains slower until the maximum moment is attained. Specimen S2 presents an intermediate degradation rate.

In general, the three moment-rotation relationships look very similar to each other in terms of shape, magnitudes of action and displacement. The bending strength capacities of the three specimens lay between 35 kN-m and 45 kN-m in the positive direction (hogging), and between -30 kN-m and -35 kN-m in the negative direction (sagging). The similar capacities exhibited by the three specimens (which major differences are constrained to the dimensions of the steel components used) is a clear indication that the maximum strength of this type of connections is governed by the capacity at the timber-dowelled connection interface, and thus less dependent on the strength of the angles.

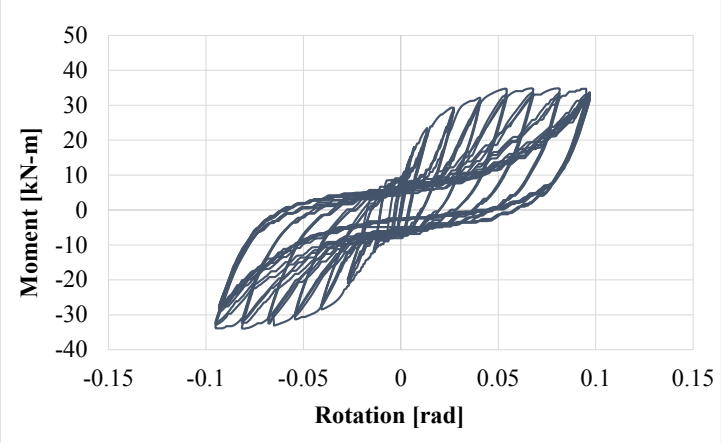
As expected, specimen S1, which combines the thinnest angle (12 mm) with the smallest bolt diameter (12 mm), presents the lowest bending capacity, the highest permanent

plastic deformations and the highest energy dissipation. Contrarily, specimen S3 has the highest capacity and shows a markedly pinching hysteretic response, which explains its lower permanent plastic deformations and energy dissipation, when compared to specimen S1. In general, the global behaviour of specimen S1 can be qualified as ductile, while in the case of specimen S3 a more brittle behaviour is appreciated. Again, specimen S2 shows a behaviour which is in-between specimens S1 and S3.

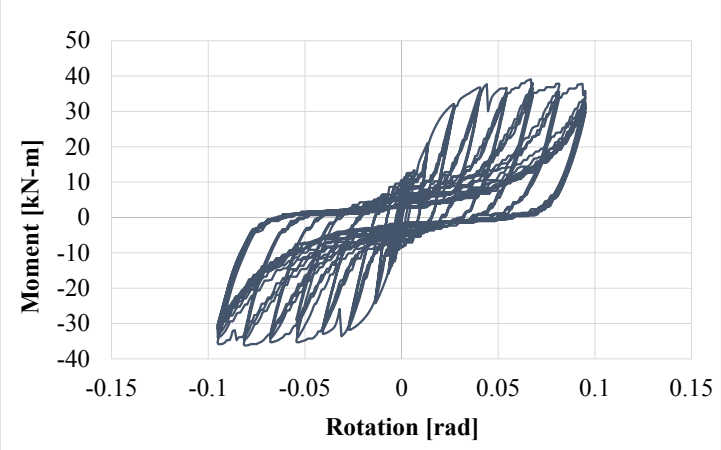
Figs. 5.7 and 5.8 show the disaggregated first and third loops of the moment-rotation hysteresis, respectively. The first hysteresis loops show that a sudden loss of strength, generally known as fracture strength degradation [32], occurs in specimens S2 (Fig. 5.7b, at cyclic amplitudes of -6.0 Dy and +8.0 Dy) and in specimen S3 (Fig. 5.7c, at cyclic amplitudes of -8.0 Dy and +12.0 Dy). This degradation occurs as a consequence of timber local failure in the dowelled connection zone. On the contrary, such a magnitude of strength loss did not happen in the specimen S1. As it can be appreciated in Fig. 5.7a, the most important advantage of a ductile connection like S1 is its ability to sustain large deformation levels without significant lost of strength. A more detailed discussion on the type of local failure witnessed during the test is developed in the next section.

Fig. 5.8 is useful to note that for the three specimens the slope of the unloading branch is almost vertical at the beginning, and that a progressive slope decline takes place when the curve is approaching the horizontal axis. This can be attributed to the enlargement of the bolt hole after wood crushing. A nearly zero stiffness is thus appreciated for the three specimens when the moment is close to zero. Nevertheless, at this stage the slope of the hysteresis loops of specimen S3 is less steep than that of specimen S1. As a consequence, the permanent deformations (residual rotation at the intersection of the hysteresis loops and the horizontal axis) in specimen S1 are larger than in specimen S3. Most of this permanent deformations comes from the plastic deformation of the connection's steel components (angles and bolts). As expected, due its more flexible steel components, specimen S1 exhibits more plasticity than the other two.

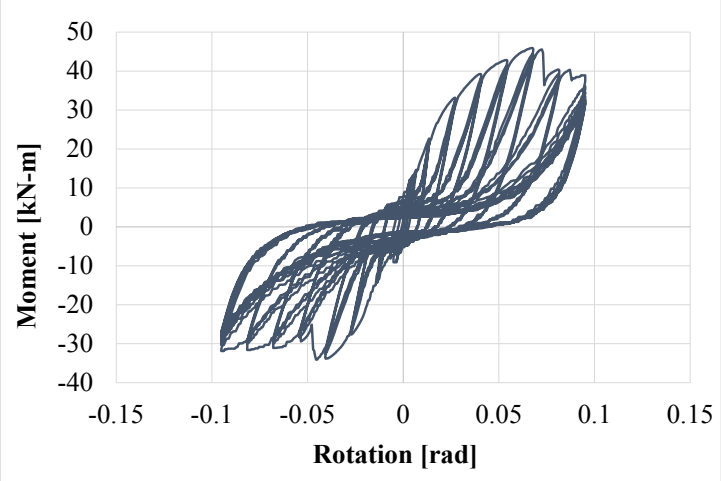
Finally, Figs. 5.7 and 5.8 show that the hysteresis loops of specimen S2 are narrower than S1 and wider than S3, which means that specimens S1 and S3 are the connections with the highest and lowest energy dissipation capacity, respectively. A more rigorous discussion involving the quantification of energy dissipation follows in Section 5.3.5.



(a) S1-12D-12A

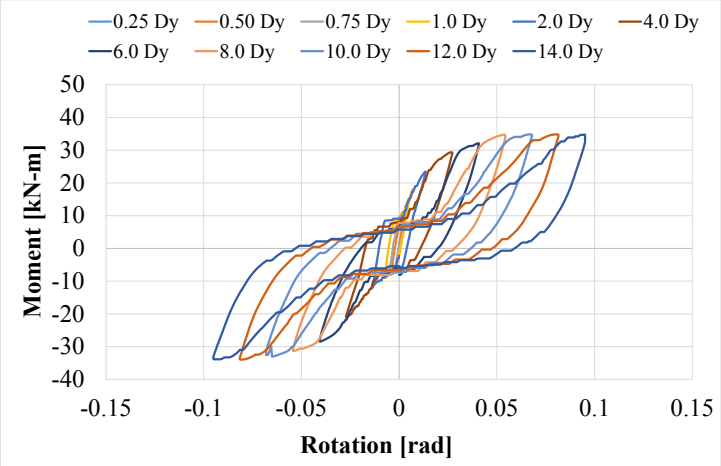


(b) S2-12D-15A

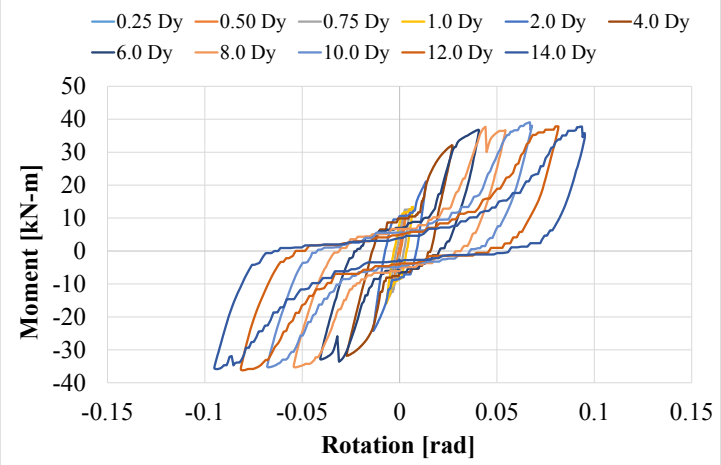


(c) S3-16D-15A

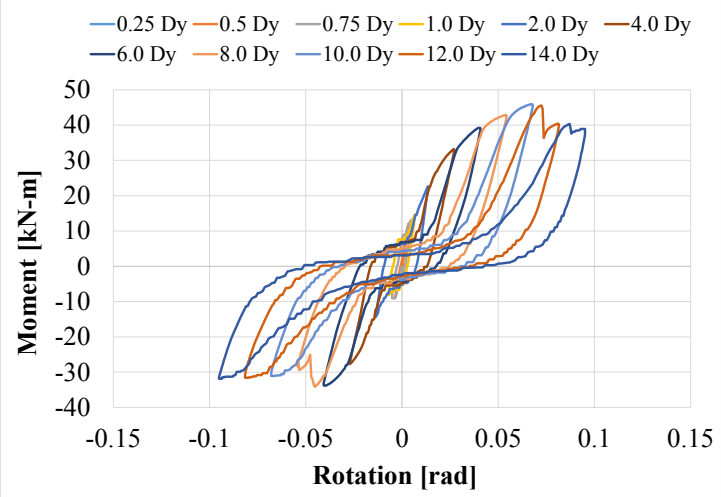
Figure 5.6: Experimental moment-rotation hysteretic responses.



(a) S1-12D-12A

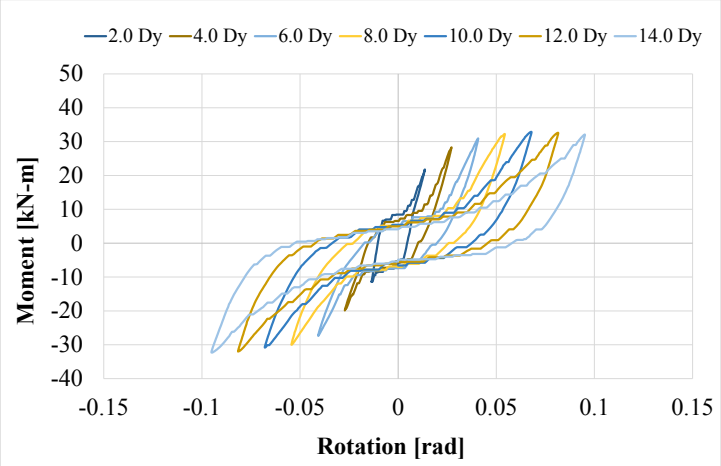


(b) S2-12D-15A

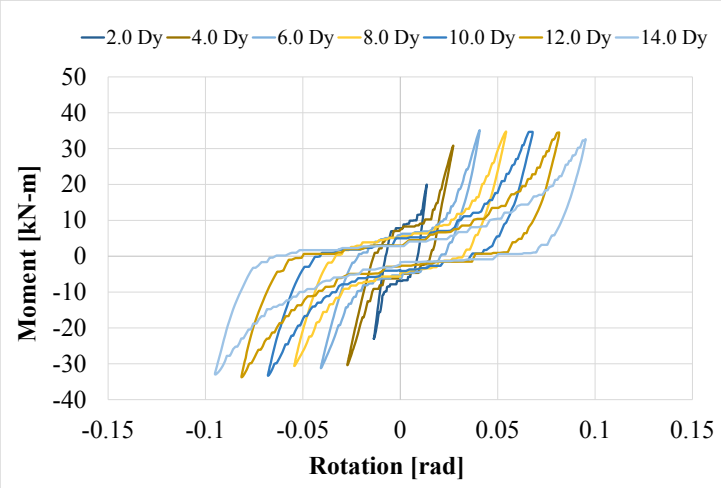


(c) S3-16D-15A

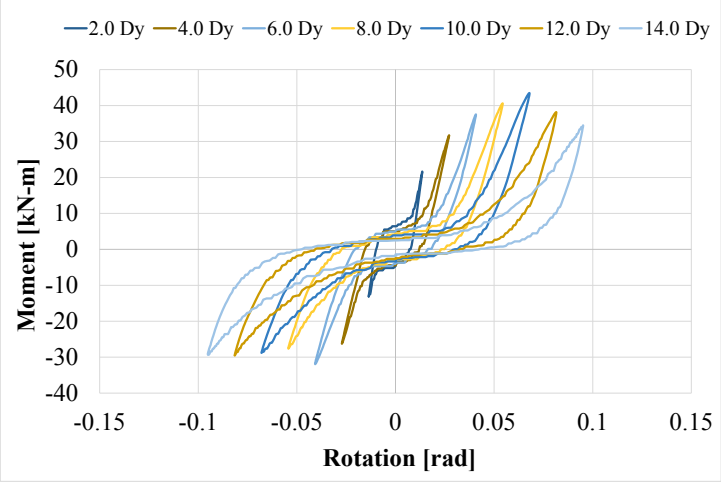
Figure 5.7: First cycle moment-rotation hysteresis loops.



(a) S1-12D-12A



(b) S2-12D-15A



(c) S3-16D-15A

Figure 5.8: Third cycle moment-rotation hysteresis loops.

5.3.2 Failure modes

Fig. 5.9 shows the state of the three specimens at the end of the test. Although, in general terms, the types of local failure modes in the timber beam were similar for the three specimens, the size of the affected zones were different. The three predominant timber failure modes were: 1) cracking and splitting along the grain due to tensile stresses perpendicular to the grain; 2) plug shear failure at the bolts row due to shear stresses parallel to the grain; and 3) embedding deformation and crushing. On the other hand, the steel components did not fracture during the test. Flexural plastic hinges formed in the angles and bolts to different extents in each of the three specimens. Similar failure modes have been reported elsewhere for other dowelled timber connections subjected to monotonic [69] and cyclic [136, 100, 101, 180] loading.

Specimen S1-12D-12A

Fig. 5.10 shows the timber local failure modes observed in specimen S1. Figs. 5.10a and 5.10d depict the cracks at the bottom and top of the beam. These cracks are a consequence of the tensile stresses perpendicular to the grain generated in the zone of the beam in contact with the steel column flange, when a bending moment is applied to the connection. Besides, plug shear was observed behind the bolts at the top and bottom due to shear stresses parallel to the grain (Figs. 5.10b and 5.10c). Under hogging moment, the seat steel angle works under high tensile stresses which, for this particular specimen, generated large deformations, as shown in Fig 5.10b. Importantly, during the test it was observed that when contact between the timber beam and the column was resumed at each cycle, the wood plugs returned to their original position, allowing the transfer of compressive stresses.

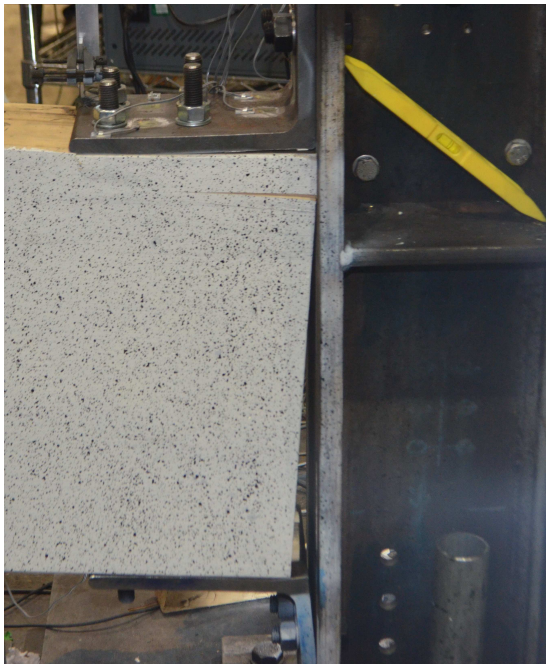
After the test was finished, the connection components were pulled apart and the timber beam was cut vertically along the bolts. Evidence of wood embedding and dowel bending deformation were observed as shown in Figs. 5.10e and 5.10f, respectively. The bolts developed two plastic hinges in both sides of the timber beam (top and bottom). One plastic hinge was located at the interfaces of the timber beam with the horizontal leg of the steel angle, while the other was located inside the timber specimen at an approximate depth of one ninth of the beam's depth.



(a) S1-12D-12A



(b) S2-12D-15A



(c) S3-16D-15A

Figure 5.9: Hybrid timber-steel moment connection specimens during testing.



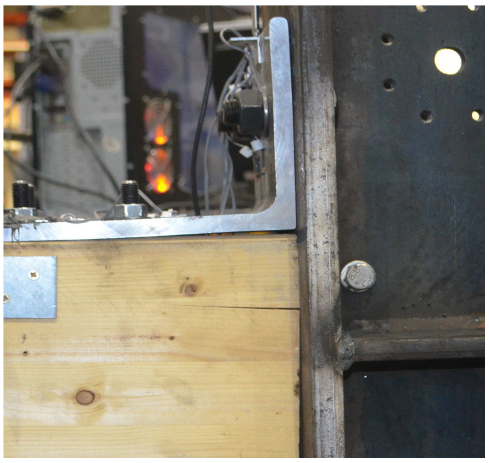
(a) Bottom crack



(b) Bottom plug shear failure



(c) Top plug shear failure



(d) Top crack



(e) Bolts embedment



(f) Transversal cut after the test

Figure 5.10: Local failure in specimen S1-12D-12A.

Specimen S2-12D-15A

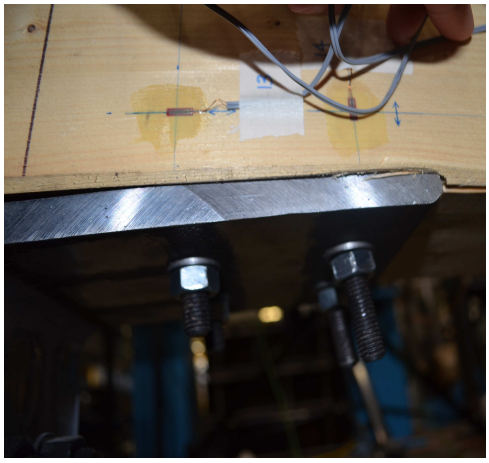
Fig. 5.11 shows the timber local failure modes observed in specimen S2. This figure shows that under sagging moment the bottom fibres of the beam experience crushing perpendicular to the grain due to bearing of the seat angle into the timber (Fig. 5.11a), while shear plug failure takes place in the upper part of the beam (Fig. 5.11e). On the contrary, when a hogging moment is applied to the connection, shear plug failure develops in the bottom fibres (Fig. 5.11b), while cracking initiates in the top part of the timber beam (Fig. 5.11d) due to the presence of tensile stresses perpendicular to the grain. Figs. 5.11b and 5.11e show that the seat and top angles experience negligible lateral deformations, which is consistent with the considerable amount of sliding shown in Fig. 5.11f. Therefore, it is verified that thicker steel angles fosters the development of embedment (Fig. 5.11c) and shear plug failure (Figs. 5.11b and 5.11e) zones.

Specimen S3-16D-15A

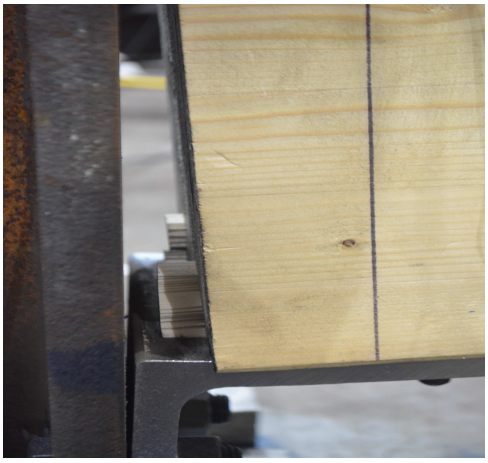
Fig. 5.12 shows the local failure modes of specimen S3. The most interesting feature of this specimen failure modes is the size of the failure zones. First of all, the width and length of the top crack shown in Fig. 5.12a are considerable larger than the corresponding cracks of specimens S1 (Fig. 5.10d) and S2 (Fig. 5.11d). Accordingly, the wood shear plugs at the bottom (Fig. 5.12b) and top (Fig. 5.12c) parts of the timber beam in specimen S3 are larger than the corresponding shear plugs in specimens S1 (Figs. 5.10b and 5.10c) and S2 (Figs. 5.11b and 5.11e). The increment of the bolts diameter from 12 mm (specimen S2) to 16 mm (specimen S3) also contributes to the development of larger embedding and shear plug failure zones. The stiffer steel components and the larger timber damaged zones are the main reasons that explain the connection's brittle behaviour and the sudden strength loss observed in its moment-rotation curves (Fig. 5.7), as discussed in the previous section.

5.3.3 Strength deterioration

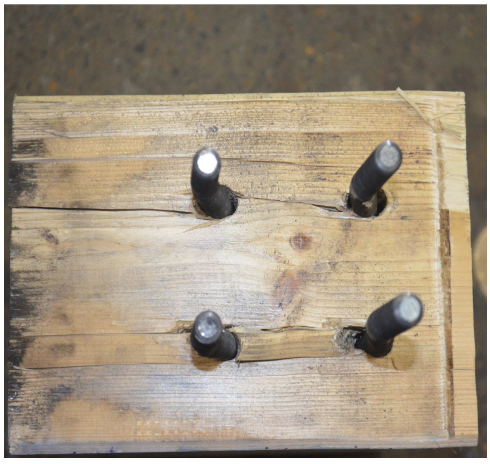
Fig. 5.13 shows the backbone envelope curves of the cyclic responses of the three specimens considered. It is worth noting that these envelope curves belong to the first cycle at a given rotation amplitude (Fig. 5.7). Therefore, both "cyclic" and "in-cycle" strength degradation can be assessed by means of Fig. 5.13. In-cycle strength degradation is associated to a sudden loss of strength that takes place within the same cyclic loop [32], and



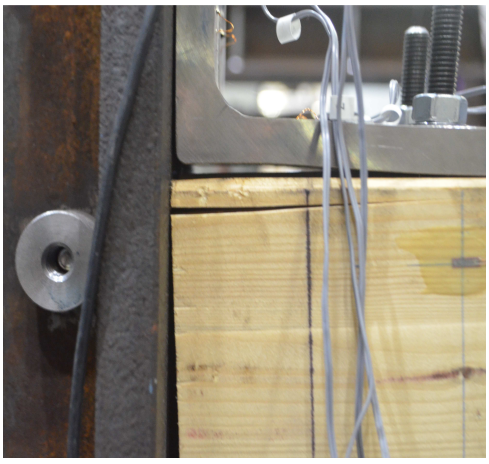
(a) Seat angle bearing



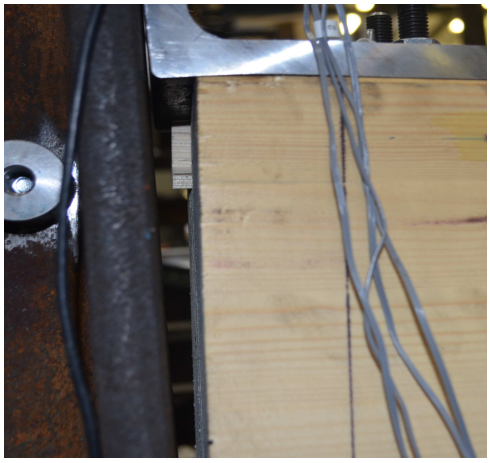
(b) Bottom plug shear failure



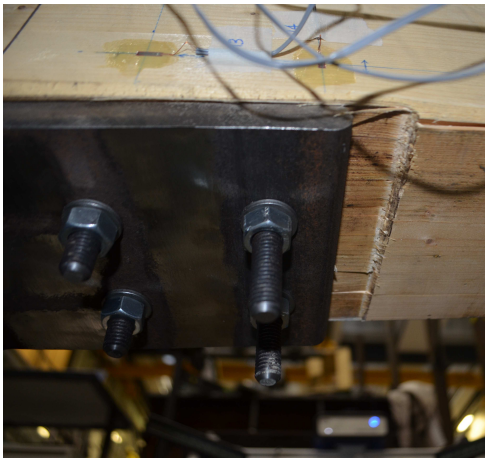
(c) Bolts embedment



(d) Top crack

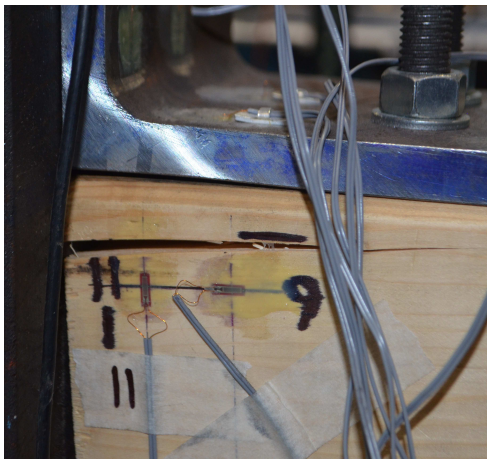


(e) Top plug shear failure



(f) Bottom shear sliding

Figure 5.11: Local failure modes in specimen S2-12D-15A.



(a) Top crack



(b) Bottom plug shear failure



(c) Top plug shear failure

Figure 5.12: Local failure modes in specimen S3-16D-15A.

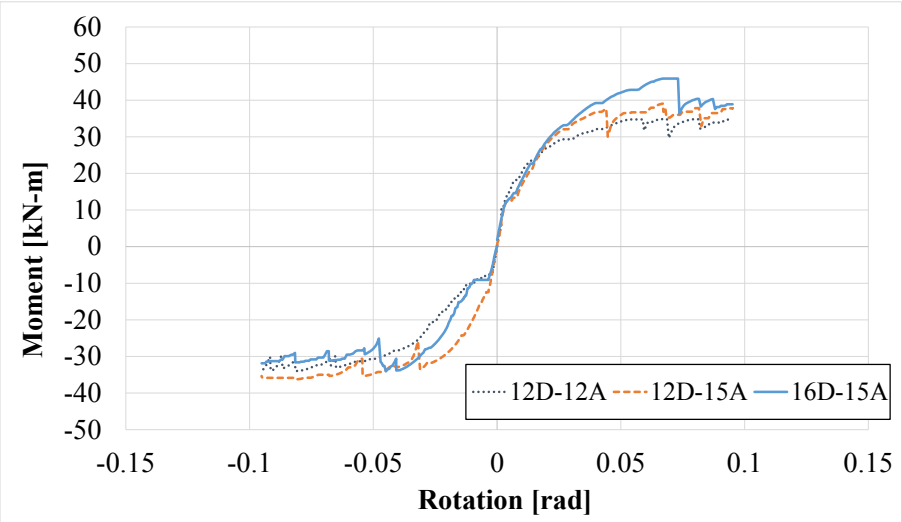


Figure 5.13: Backbone envelope curves of specimens S1-12D-12A, S2-12D-15A and S3-16D-15A.

that is caused by brittle failures like those discussed and shown in the previous section. This type of strength degradation is responsible for the largest strength drops observed in Fig. 5.13. On the other hand, the other type of strength deterioration, denominated cyclic degradation, is caused by bolt slippage each time a new cyclic amplitude is reached. Although some distinguishable strength drops in Fig. 5.13 are caused by bolt slippage, these are minor and arise only after the major in-cycle strength drop has already happened.

Fig. 5.13 suggests that strength deterioration is more critical in specimens S2 and S3 than in specimen S1. This is corroborated by the moment variations calculated in Table 5.3, where specimens S2 and S3 are associated with the greatest strength drops for both positive and negative directions. Table 5.3 indicates that for specimen S1 the maximum strength losses are in the order of -10% to -15%. On the other hand, for specimens S2 and S3, the strength losses are higher than 20%.

Several authors have defined a strength drop higher than 20% as an indicator of structural failure. For the particular case of cyclic loading, some studies have employed this definition of failure in general terms [180, 136], while others have specified that the connection resistance reduction should be measured from the first to the third loop of the same cyclic load amplitude [129, 107, 1]. Considering that in the three specimens examined herein the connection strength reduction from the first to the third cyclic loop is negligible (Fig. 5.6), it appears that the general definition of failure is more relevant to be explored herein.

Table 5.3: In-cycle strength loss variation due to local failure

Specimen	**S1-12D-12A**		**S2-12D-15A**		**S3-16D-15A**	
Displacement direction	Positive	Negative	Positive	Negative	Positive	Negative
Max Moment [kN · m]	34.83	−30.06	37.73	−25.87	45.91	−25.11
Min Moment [kN · m]	29.67	−33.86	30.04	−33.61	36.35	−31.48
Moment Var [kN · m]	−5.17	3.80	−7.69	7.74	−9.56	6.37
Strength Loss [%]	−14.8	−11.2	−20.4	−23.0	−20.8	−20.2

Based on this criterion, specimen S1 does not fail, while specimens S2 and S3 do. Fig. 5.13 shows that the first failure point of both specimens occurred during negative (sagging) deformation, at rotations equal to -0.031 rad (S2) and -0.047 rad (S3). Nevertheless, the strength is partially recovered in specimens S2 and S3 immediately after these points. What is more, when the maximum cyclic amplitude is reached, and posteriorly repeated eight additional times, a stable hysteresis loop without any further significant strength deterioration can be appreciated in Fig. 5.6 for all three specimens. For these reasons, considering a strength drop higher than 20% as an indicator of structural failure, based on the information provided by the backbone envelope curves alone, seems not to be directly applicable to the type of hybrid timber-steel dowelled connections studied herein. At least not as an indication of global structural failure. Nevertheless, the sudden strength drops of the backbone curves do provide important information about the occurrence, recurrence and magnitude of timber local brittle failure (like shear plug behind the rows of bolts or large crack formation due to tensile stresses in the direction perpendicular to the grain).

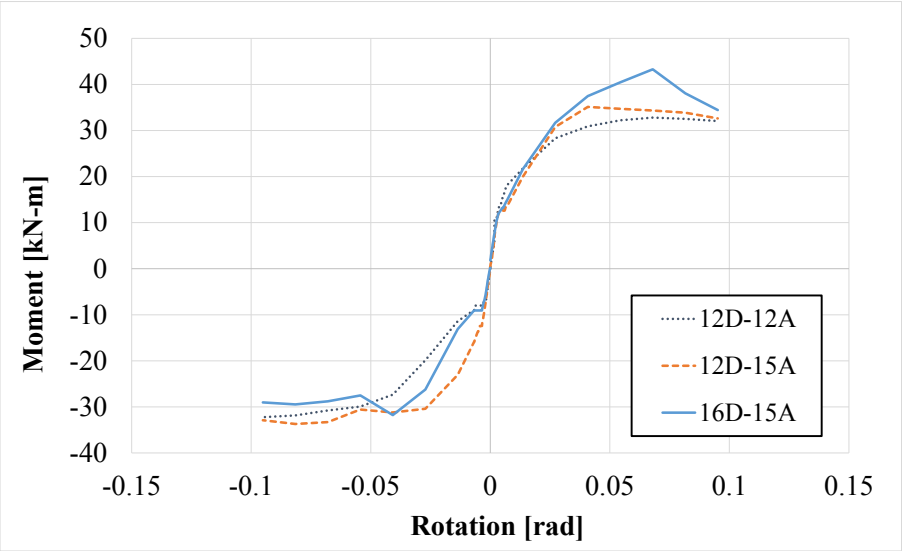


Figure 5.14: Stabilized envelope curves of specimens S1-12D-12A, S2-12D-15A and S3-16D-15A.

5.3.4 Ductility and stiffness degradation

Fig. 5.14 shows the stabilized envelope curves of specimens S1, S2 and S3. These curves were obtained by joining the peak points of the third cycle moment-rotation hysteresis loops (see Fig. 5.8). This graphic shows that both the initial stiffness and moment capacity of the three connections tested are very much alike. No initial slip is appreciated in the stabilized curves. Besides, the nonlinear responses of each of the three specimens are different in positive and negative directions. This is a consequence of the direction in which local failure occurs first.

For the three specimens examined herein, the loading protocol started pushing towards the negative direction. This is consistent with what was mentioned in the previous section about the apparent failure points of specimens S2 and S3, which appeared for the first time in the negative side of the backbone envelope curves (Fig. 5.13). For instance, the stabilized curves of specimens S1 and S3 clearly show that an early local failure occurred at a load level close to -10 kN·m. This localized failure is not appreciated in the positive side of the hysteresis.

Table 5.4 presents a summary of the connection mechanical properties corresponding to the three specimens in both loading directions. The moment and deformation at yielding were determined by fitting the elastic and tangential stiffness lines to the curves presented in Fig. 5.14. This method, which was previously used elsewhere for timber structural components under monotonic and cyclic loading [72, 101, 180], determines the

elastic stiffness by connecting the origin with the point corresponding to 40% of the maximum capacity. In turn, the tangent stiffness is defined as one sixth of the elastic value.

With the exception of the negative side of the stabilized enveloped curve of specimen S1, which does not show a clear maxima, the global maximum (peak) moment can be identified in the other five curves (see Fig. 5.14). It is worthy noting that only one of them (specimen S3, positive side) exhibits global failure, defined as a strength drop higher than 20% of the maximum capacity. Contrary to the remark in the previous section with respect to the backbone envelope curves, this definition of global failure seems to be more adequate when it is based on the information provided by the stabilized envelope curves.

Table 5.4: Connection properties from the stabilized envelope curves

Specimen	**S1-12D-12A**		**S2-12D-15A**		**S3-16D-15A**	
Displacement direction	Positive	Negative	Positive	Negative	Positive	Negative
Elastic stiff. [kN · m]	3776.83	806.98	1871.78	2726.05	1840.35	983.21
Yield rot. [rad]	0.004	−0.033	0.015	−0.008	0.017	−0.031
Yield moment [kN · m]	16.80	−27.00	27.60	−21.60	30.60	−30.60
Max. moment [kN · m]	32.80	−32.24*	35.12	−33.71	43.28	−31.78
Ultimate rot. [rad]	0.10**	−0.10**	0.10**	−0.10**	0.09	−0.10**
Ductility	> 21.39	> 2.84	> 6.45	> 12.01	5.68	> 3.06

* No peak moment attained for the specimen in the specified load direction.
** No global failure for the specimen in the specified load direction. The rotation corresponds to the maximum stroke range.

As expected from the configuration of their steel components, Table 5.4 indicates that in the positive (hogging) direction specimen S3 had a higher resistance than S2, while S2

had a higher resistance than S1. Nonetheless, this relative order of strength magnitudes is not maintained for the negative (sagging) direction. This is due to the early strength loss experienced by specimen S3.

Ductility is quantitatively defined as the ratio of the ultimate rotation (failure point) over the yield rotation. Therefore, absolute values of ductility can be calculated only for the positive (hogging) displacement direction of the specimen S3. Nevertheless, lower bounds of ductility are also presented in Table 5.4 for the other five curves. Paradoxically, the highest (21.39) and lowest (2.84) lower bound ductility values correspond to the positive (hogging) and negative (sagging) stabilized envelope curves of the same specimen, S1. Such observation can be explained by the early failure of specimen S1 at a moment around -10 kN-m, which significantly altered the position of the yielding point. On the other hand, the ductility values of specimens S2 and S3 are equal or higher than 6.45 and 3.06, respectively. This demonstrates the potential of this type of timber beam-to-steel column moment connections to sustain their bending strength after a significant number of high-amplitude cycles repetitions.

Interestingly, the good ductility exhibited by the connections under study was not significantly affected by the differences in local failure described above. Even though the larger size of the bolts used in specimen S3 resulted in a more brittle global response, its ductility ratio (equal to 5.68) is good enough for seismic design purposes. In this sense, the primary role of the steel components (particularly the steel angles) to uphold the connection's capacity without leading to global failure, even after severe local damage in the timber matrix, should be highlighted.

Finally, it is important to mention that the load-displacement (moment-rotation) curves obtained from monotonic tests of timber components predict higher capacities and ductilities than the ones obtained from stabilized envelope curves. It is thus expected that monotonic tests would generally overestimate the moment-rotation response of a connection subjected to a typical seismic action. Therefore, they are not recommended to evaluate the seismic design connection properties of timber structures [136].

5.3.5 Energy dissipation capacity

Energy dissipation capacity is one of the most important characteristics of structures subjected to strong dynamic actions like earthquakes. A structure with high energy dis-

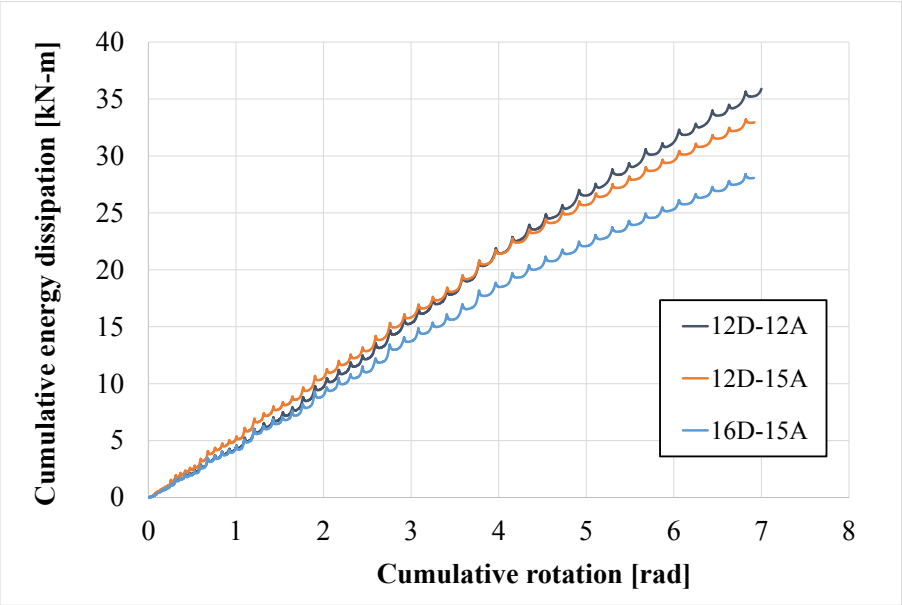


Figure 5.15: Cumulative energy dissipation of specimens S1-12D-12A, S2-12D-15A and S3-16D-15A.

sipation capacity experiences lower seismic demands and also a diminished time of free vibration. Therefore, structural systems with high energy dissipation capabilities are highly desirable for seismic design applications [136, 129, 107, 1].

Hysteretic damping, a measure of the energy dissipation capacity of a structure, is determined by calculating the area inside the moment-rotation hysteresis loops (see Figs. 5.7 and 5.8). The sum of the accumulated energy as a function of the cumulative rotation of each specimen tested is plotted in Fig. 5.15. This graphic shows that at the beginning of the test, when small amplitude loading cycles are applied, the three specimens experience the same level of energy dissipation. However, it is clear from Fig. 5.15 that the dissipation capacity of specimen S3 is between 20% and 15% lower than S1 and S2 by the end of the test.

Alternatively, Fig. 5.16 shows the amount of energy dissipated per individual cycle in the three specimens. It can be noted from this figure that for each cyclic loading amplitude the first cycle loop is wider (Fig. 5.7) and dissipates a higher amount of energy. This is followed by two narrower (second and third) cycle loops (Fig. 5.8) which energy dissipation capacity is considerably lower than during the first cycle. Moreover, during the last 9 cycles at the highest deformation amplitude, a constantly decreasing energy dissipation rate is observed in all three connections.

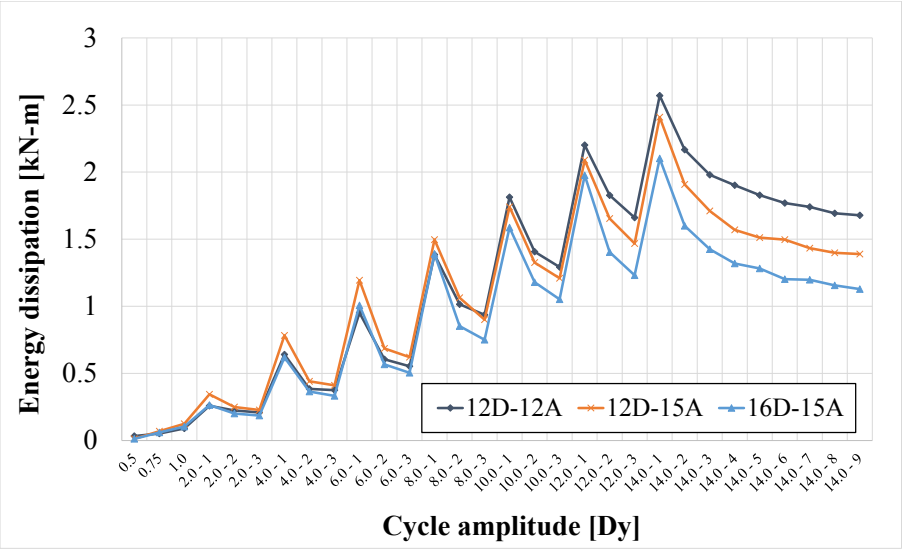


Figure 5.16: Cyclic energy dissipation of specimens S1-12D-12A, S2-12D-15A and S3-16D-15A.

Also noteworthy, specimen S2 dissipated more energy than the other two during the first testing stages. However, when the cyclic loading amplitudes increase beyond 10.0 Dy, specimen S1 exceeds the energy dissipation capacity of S2. Recalling that the only difference between specimens S1 and S2 is the steel angle thickness (see Table 5.1), it can be hypothesized that during the initial loading stage the thicker angle of specimen S2 contributed to the generation of higher plastic deformations in the steel bolts, increasing the energy dissipation of the connection as a whole. Eventually, when higher deformation amplitudes were reached, the accumulation of plastic deformations in the thin steel angle of specimen S1 overtook the dissipation capacity of S2.

5.4 Concluding remarks

An experimental study of the cyclic response of timber beam-to-steel column moment connections was performed. A total of three specimens were tested. The only difference among them was the size of the steel components (angles and bolts) employed to connect the beam to the column. At the beginning of this chapter, a detailed description of the test setup and material properties was presented. The key findings of the experimental investigation with respect to the cyclic behaviour of the connection under study are summarized below.

Similar initial stiffness and moment capacity magnitudes were observed for the three

specimens tested. This leads to the conclusion that the capacity of this type of connection is governed by the strength of the timber beam-steel angle dowelled connection. Furthermore, the three specimens showed a good capacity to sustain their bending strength without significant deterioration or global failure when subjected to large levels of deformation and several loading cycle repetitions. Accordingly, high values of ductility were calculated based on the experimental data. The primary role of the steel components (particularly the steel angles) to preserve the connection's capacity without leading to global failure, even after the occurrence of severe timber local failure, is recognized. A widespread indicator of global failure of timber structures is denoted by a post-peak strength reduction higher than 20% of the structure's capacity. Based on the analysis of the experimental results, this definition of global failure appears to be valid for the type of hybrid timber-steel dowelled connection studied herein as long as the strength reduction measurements are obtained from the stabilized envelope curves.

On the other hand, the three predominant timber local failure modes observed during and after the test were: 1) cracking and splitting along the grain due to tensile stresses perpendicular to the grain; 2) plug shear failure at the bolts row due to shear stresses parallel to the grain; and 3) embedding deformation and crushing. Although these failure modes were common to the three specimens tested, the size of the affected zones were different for each of them. It was verified that thicker steel angles and bigger bolts foster the development of larger embedding and shear plug failure zones.

By the end of the test, specimens S1 and S2 had dissipated much more energy than specimen S3. Moreover, in-cycle strength deterioration was seen to be more critical in specimens S2 and S3 than in specimen S1. The smaller steel components of specimen S1 limits the extent of timber local failure, and, as a consequence, prevent the occurrence of significant strength degradation. There is also another type of strength deterioration, denominated cyclic degradation, which is caused by bolt slippage each time a new cyclic amplitude is reached. Although some distinguishable strength drops were caused by bolt slippage, these were minor in all the specimens.

Therefore, it is concluded that the most important advantage of a ductile connection like specimen S1 is its ability to sustain large deformation levels without significant loss of strength. The design of connections like specimen S1 with small steel components and high energy dissipation capacity is recommended to prevent the occurrence of brittle failure modes.

In the next chapter, the cyclic response of the timber beam-to-steel column connections experimentally studied herein will be further investigated by means of numerical modelling. For this purpose, a finite element model that incorporates the timber material model proposed in Chapter 3 and validated in Chapter 4 will be elaborated for the three specimens tested.

Chapter 6

Numerical Modelling of Timber-Steel Joints

6.1 Introduction

In Sections 2.4, 2.3 and 2.5, the state of the art of three-dimensional finite element modelling of timber dowelled connections was presented. From the literature review, it can be concluded that the numerical simulation of timber structures' nonlinear behaviour is a challenging task with several components that need to be tackled. Among them are the proper selection of the material property values, the use of an appropriate timber failure criterion and material model, and the contact modelling between timber and steel components. Furthermore, simulating the cyclic response of timber dowelled connection using three-dimensional numerical models is a particularly complex endeavour. For this reason, up to now there is no research work which undertakes this challenge. In fact, all the related references reviewed in Section 2.5 are focused on the action of monotonic loads exclusively.

On the other hand, in Chapter 5 a experimental study was carried out on the cyclic nonlinear behaviour of timber beam-to-steel column moment connections. A complementary numerical study of the same three specimens tested will be performed in this chapter. To this end, the timber material model proposed in Chapter 6 and validated in Chapter 4 will be used. Moreover, the formulation of a timber-steel interface contact model, among other 3D finite element modelling strategies for timber-steel dowelled connections, will be presented.

The purpose of this chapter is to gain further insight into the performance of timber-

steel moment connections under the action of cyclic loads, through the application of damage mechanics concepts (see Section 2.2) and 3D finite element modelling. At a first stage, the experimental global responses of the connections will be used to further validate the proposed timber material model and the finite element modelling approach followed herein. The second stage consists on analysing the numerical output responses at the local level (strains and damage indices), which are not usually part of the experimental test data. Based on this analysis conclusions can be drawn on the applicability of damage mechanics and 3D finite element modelling to the seismic performance assessment of timber-steel dowelled connections.

In the following section the timber-steel contact interface model is formulated. Subsequently, the finite element modelling strategies employed for the elaboration of the timber beam-to-steel column joint 3D model are presented. In the next section, the calibration procedure followed to determine the values of the corresponding model parameters is outlined. Finally, the numerical global and local responses corresponding to monotonic and cyclic loading are analysed. The chapter ends with a summary of the most important concluding remarks.

6.2 Timber-steel interface contact model

The finite element modelling of bodies which can be in contact but have no physical link or attachment between them is challenging, leading to cumbersome numerical solutions and convergence problems when attempting to simulate their mutual interaction to an acceptable degree of fidelity. Unfortunately, this kind of discontinuity is frequently encountered in structural engineering applications, particularly when evaluating the response of semi-rigid connections. These complications are exacerbated in earthquake engineering due to the occurrence of cyclic load reversals which produce the alternating states of contact between structural members.

An adequate simulation of contact is particularly important in timber since most of their joints and connections employ steel fasteners that interact with the surrounding timber material. The nature of such interactions plays a fundamental role in the characteristic pinching behaviour of timber structures subjected to cyclic loading. In the particular case of timber-dowelled connections, pinching occurs as a consequence of loosening and slipping of bolts, screws and dowels [49]. When permanent plastic deformations are generated in the wood around the fasteners due to embedding and crushing,

the fastener holes become larger and a gap between them and the surrounding wood is created [71, 107, 137, 99]. During unloading, this gap causes a sudden drop in the load (steep unloading branch) which is followed by a substantial reduction of the unloading stiffness. During re-loading, contact is resumed leading to a momentary recovery from pinching. This process includes stages when the dowel fastener moves freely along the gap, where there is no contact between the fastener and the surrounding wood, and minimal strength is provided exclusively by the steel fastener [137, 99]. Pinching behaviour generates narrow hysteresis loops [138], which considerably reduce the energy dissipation capacity of the system [71, 107].

Depending on the specific characteristics of the structural system, the pinching stage when the sudden slope reduction begins during the unloading process can take place before or after attaining zero load [49]. Besides, the degree of pinching (quantified by the magnitude of stiffness reduction) is related to the amount of permanent plastic deformations, not only in the timber, but also in the steel components of the connection. In this regard, Fig. 5.6a showed that specimen S1 (specimen with the most flexible steel components and the highest permanent plastic deformations) has milder unloading stiffness, wider hystersis loops, and therefore, a lower degree of pinching behaviour in comparison with the other two specimens, S2 and S3. On the contrary, specimen S3 (specimen with the stiffest steel components and the smallest permanent plastic deformations) has steep unloading stiffness and narrower hysteresis loops, which lead to a higher degree of pinching.

In finite element modelling, timber-steel interaction can be simulated by means of interface elements. The element shown in Fig. 6.1 [35] is a plane quadrilateral interface for 3D models which can be located in-between the surfaces of two solid elements. To this end, two vector variables are employed to describe the interface behaviour, namely, relative displacement, $\Delta \boldsymbol{u}$, and stress, $\boldsymbol{t}$. Each of them has three components corresponding to one normal (n) and two tangential ($s1$, $s2$) directions relative to the interface plane (see Fig. 6.1) such that:

$$\boldsymbol{t} = \begin{bmatrix} t_n & t_{s1} & t_{s2} \end{bmatrix}^T \tag{6.1}$$

$$\Delta \boldsymbol{u} = \begin{bmatrix} \Delta u_n & \Delta u_{s1} & \Delta u_{s2} \end{bmatrix}^T \tag{6.2}$$

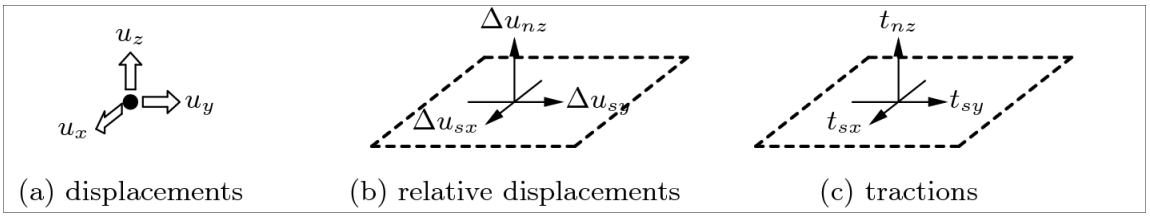


Figure 6.1: Two-dimensional interface element for timber-steel contact modelling (Figure taken from DIANA User's manual [35]).

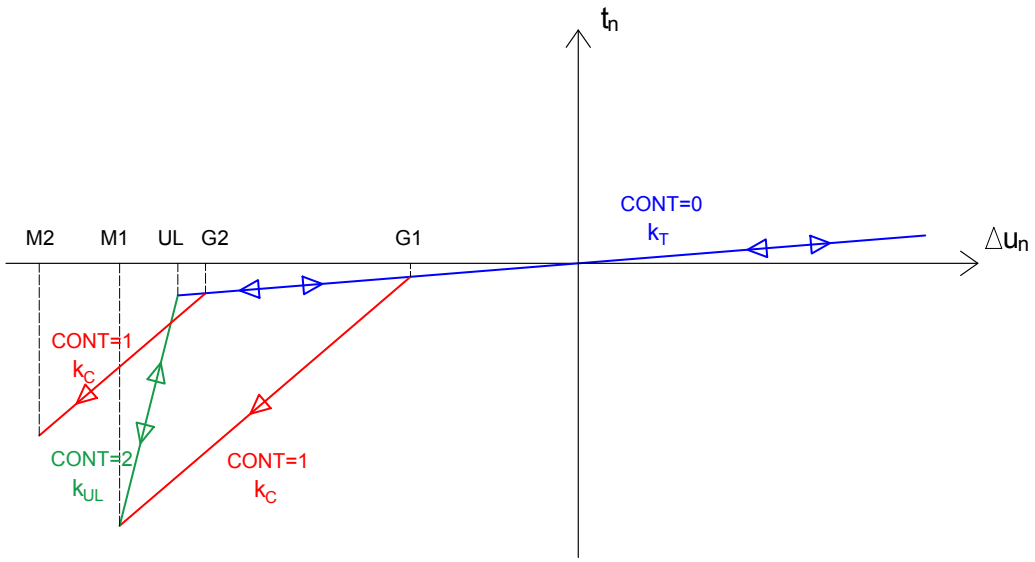


Figure 6.2: Timber-steel contact hysteretic model in the normal direction to the interface plane.

6.2.1 Interface contact model in the normal direction

Given the relative displacement vector, the stress vector is obtained herein by means of a timber-steel interface contact model. Accordingly, a simplified nonlinear hysteretic model was developed to simulate the cyclic contact behaviour of the connection's timber-steel components. The hysteretic model for the interface normal stress and relative displacement is graphically described in Fig. 6.2. Three contact states are defined as:

- No contact: Steel and timber components are separated (CONT=0)
- Contact: Steel and timber components are pressing onto each other (CONT=1)
- Unloading: After being in contact, steel and timber components are moving apart but are not totally separated yet (CONT=2)

It can be noticed from Fig. 6.2 that different magnitudes of stiffness that relates the increment rate of the normal relative displacement to the increment rate of the normal

stress are defined for each contact state. The "no contact" (CONT=0) stiffness value (k_T) is very small (close to zero) because large positive or negative relative displacements may occur without generating any significant traction or compression stresses. On the contrary, the "contact" (CONT=1) stiffness (k_C) should be high enough to prevent unrealistic overlaps between the bodies, and yet, not excessively high to generate numerical convergence issues [146]. Within these upper and lower boundaries a wide range of stiffness values is possible. Therefore, the final value of k_C should be determined via a calibration process. A new yet simplified procedure for performing such a calibration is outlined in Section 6.4. Finally, since only a small positive (separation) relative displacement is enough to uncouple the bodies in contact, and consequently, to generate a sudden loss of normal stresses between their surfaces, the "unloading" (CONT=2) stiffness (k_{UL}) should be considerably higher than the"contact" stiffness. Such a fast separation during unloading is achieved by assigning a value of k_{UL} that is a number of times higher than k_C. In order to successfully model pinching in timber dowelled connections, both plastic permanent deformations (wood constitutive model) and fast unloading separation (interface contact model) should be incorporated.

Finally, in addition to the contact state integer variable, CONT, the contact model requires the definition of three additional normal relative displacement state variables:

- Gap relative displacement ($\Delta u_{n,G}$): Negative normal relative displacement which determines the pass from CONT=0 to CONT=1. If the negative normal relative displacement is less than $\Delta u_{n,G}$, then contact takes place. Otherwise, the "no contact" state is maintained.

- Minimum relative displacement ($\Delta u_{n,M}$): Keeps track of the historic minimum negative normal relative displacement corresponding to the last maximum compressive stress due to contact. This state variable is updated every time a new compressive loading step takes place during the CONT=1 state.

- Total unloading relative displacement ($\Delta u_{n,UL}$): Negative normal relative displacement which determines the switch from CONT=2 to CONT=0. A positive (separation) normal relative displacement automatically changes the state from "contact" (CONT=1) to "unloading" (CONT=2), and the value of $\Delta u_{n,UL}$ is calculated at that point. If during the "unloading" state, the negative normal relative displacement is higher than $\Delta u_{n,UL}$, total separation occurs and the "no contact" state begins. Otherwise, the unloading process continues.

6.2.2 Interface friction model in the tangential direction

A kind of stick-slip friction model [36, 146, 144, 187] is formulated herein to determine the interface shear stresses (t_{s1}, t_{s2}) induced by the associated tangential relative displacements (Δu_{s1}, Δu_{s2}) (See Fig. 6.1). Similarly to the contact model in the normal direction, the stick-slip friction model includes three states, namely: "no contact", "stick" and "slip". Therefore, in addition to the natural dependency on the tangential relative displacements, the shear stresses also depend on the contact state variable (CONT) and the normal stress magnitude (t_n).

The timber-steel interface friction model for the two tangential directions is depicted in Fig. 6.3. When there is no contact (CONT=0), the shear stiffness, which relates the rate of shear stress to the rate of tangential relative displacement, is almost zero. Therefore, in order to avoid numerical instability, a very small shear stiffness value (k_T) is assigned (blue line in Fig. 6.3a). Alternatively, when full (CONT=1) or partial (CONT=2) contact takes place, either "stick" or "slip" states can be activated (red lines in Fig. 6.3a), depending on the value of the total shear stress (τ) compared to the maximum friction stress (τ_{max}). The Coulomb friction law (see Fig 6.3b) is used to determine the maximum friction stress, τ_{max}, such that:

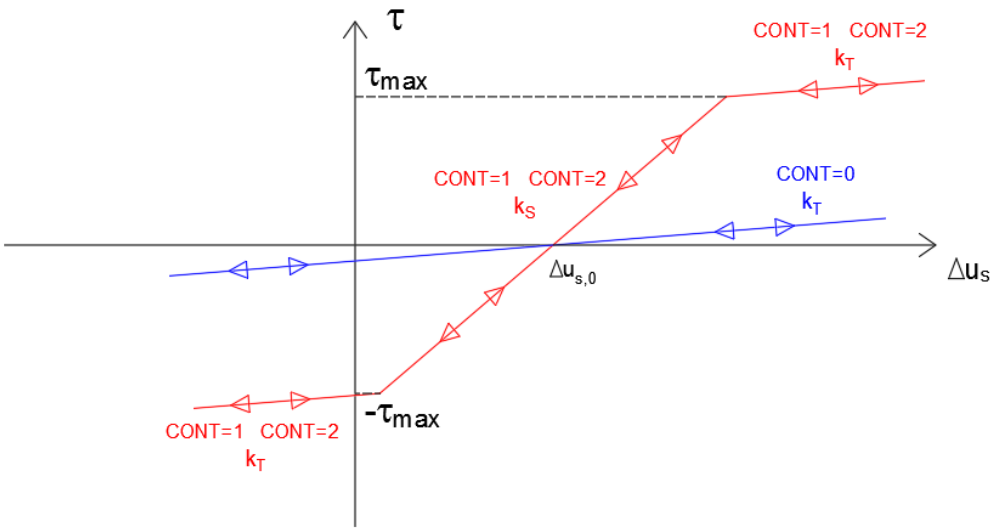
$$\tau_{max} = c - \mu t_n \tag{6.3}$$

where c and μ are the cohesion and the friction coefficient between the timber and steel surfaces, respectively. On the other hand, the total shear stress, τ, is calculated as:

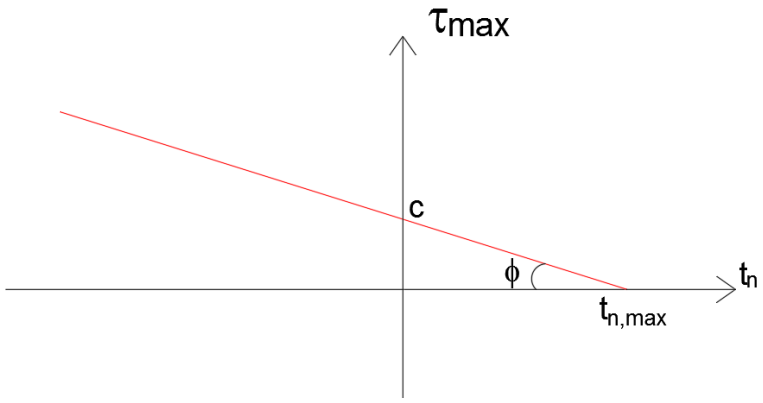
$$\tau = \sqrt{(t_{s1})^2 + (t_{s2})^2} \tag{6.4}$$

If $\tau < \tau_{max}$ the "stick" state prevails and the tangential relative displacement is restricted and controlled by the shear stiffness k_S. On the other hand, if the total shear stress exceeds the maximum friction stress, "slip" or sliding between the two surfaces in contact is allowed, and consequently, the shear stiffness is reduced to k_T.

To compute the shear stresses (t_{s1}, t_{s2}) it is necessary to calculate the variation of relative tangential displacements between the current load step and the load step corresponding to the last contact initiation (load step switching from CONT=0 to CONT=1). Therefore, two state variables (one per each tangential direction) are used to keep track of the relative tangential displacement corresponding to the last contact initiation (Δu_{s10} and Δu_{s20}). With these considerations in mind, the layout of the timber-steel contact



(a) Stick-slip friction model: shear stress-tangential relative displacement relation.



(b) Coulomb friction law.

Figure 6.3: Timber-steel friction nonlinear model in the direction tangential to the interface plane.

model algorithm for the calculation of the normal and tangential stresses is shown in Tables 6.1 and 6.2, respectively.

6.2.3 Tangent stiffness matrix

The tangent stiffness matrix of the interface element, $\boldsymbol{D}^t$, relates the increment of the stress vector to the increment of the relative displacement vector, such that:

$$\dot{\boldsymbol{t}} = \boldsymbol{D}^t \Delta \dot{\boldsymbol{u}} \tag{6.5}$$

where $\boldsymbol{D}^t$ is a 3 by 3 matrix defined as:

$$\boldsymbol{D}^t = \begin{bmatrix} \frac{\mathrm{d}t_n}{\mathrm{d}\Delta u_n} & 0 & 0 \\ \frac{\mathrm{d}t_{s1}}{\mathrm{d}\Delta u_n} & \frac{\mathrm{d}t_{s1}}{\mathrm{d}\Delta u_{s1}} & \frac{\mathrm{d}t_{s1}}{\mathrm{d}\Delta u_{s2}} \\ \frac{\mathrm{d}t_{s2}}{\mathrm{d}\Delta u_n} & \frac{\mathrm{d}t_{s2}}{\mathrm{d}\Delta u_{s1}} & \frac{\mathrm{d}t_{s2}}{\mathrm{d}\Delta u_{s2}} \end{bmatrix} \tag{6.6}$$

For simplicity, and in order to keep the symmetry of the global tangent stiffness matrix, it is assumed that the shear stress components are independent of the normal relative displacement. This assumption is exact in all cases except for the "slip" state. In this state the Coulomb friction law introduces an indirect dependency between shear stresses and normal relative displacement through the maximum friction stress, which in turn is formulated in terms of the normal stress (Eq. 6.3). Therefore, the expressions to calculate the tangent matrix coefficients defined in Eq. 6.6 are provided in Eqs. 6.7 to 6.11:

$$\frac{\mathrm{d}t_n}{\mathrm{d}\Delta u_n} = \begin{cases} k_T & \text{IF} \quad \text{CONT} = 0 \\ k_C & \text{IF} \quad \text{CONT} = 1 \\ k_{UL} & \text{IF} \quad \text{CONT} = 2 \end{cases} \tag{6.7}$$

$$\frac{\mathrm{d}t_{s1}}{\mathrm{d}\Delta u_n} = \frac{\mathrm{d}t_{s2}}{\mathrm{d}\Delta u_n} = 0 \tag{6.8}$$

$$\frac{\mathrm{d}t_{s1}}{\mathrm{d}\Delta u_{s1}} = \begin{cases} k_T & \text{IF} \quad \text{CONT} = 0 \\ k_S & \text{IF} \quad \text{STICK} \\ k_T + \frac{\tau_{max}}{\tau}(k_S - k_T)[1 - (\frac{k_S(u_{s1} - u_{s10})}{\tau})^2] & \text{IF} \quad \text{SLIP} \end{cases} \tag{6.9}$$

$$\frac{\mathrm{d}t_{s2}}{\mathrm{d}\Delta u_{s2}} = \begin{cases} k_T & \text{IF} \quad \text{CONT} = 0 \\ k_S & \text{IF} \quad \text{STICK} \\ k_T + \frac{\tau_{max}}{\tau}(k_S - k_T)[1 - (\frac{k_S(u_{s2} - u_{s20})}{\tau})^2] & \text{IF} \quad \text{SLIP} \end{cases} \tag{6.10}$$

$$\frac{\mathrm{d}t_{s2}}{\mathrm{d}\Delta u_{s1}} = \frac{\mathrm{d}t_{s1}}{\mathrm{d}\Delta u_{s2}} = \begin{cases} 0 & \text{IF} \quad \text{CONT} = 0 \\ 0 & \text{IF} \quad \text{STICK} \\ -\frac{\tau_{max}}{\tau^3}(k_S - k_T)[k_S(u_{s1} - u_{s10})][k_S(u_{s2} - u_{s20})] & \text{IF} \quad \text{SLIP} \end{cases} \tag{6.11}$$

As previously mentioned in Section 3.5.3 in relation to the wood plasticity-damage model, $\boldsymbol{D}^t$ is required for the calculation of the global structural tangent stiffness matrix, which in turn is used by the Newton-Raphson iterative procedure to determine the global displacement vector corresponding to the next iteration. The newly proposed timber-steel interface contact model was coded in FORTRAN and implemented in the finite element software DIANA [35] by means of a user-supplied subroutine (USS).

6.3 Finite element modelling of timber-steel dowelled connection

Three-dimensional continuum finite element modelling of timber-dowelled connections is a challenging task. An accurate numerical simulation of the nonlinear cyclic behaviour of timber-steel beam-to-column joints requires proper modelling, not only of the connection components, but also of their interaction mechanisms. For this reason, the development of both, the wood plasticity-damage constitutive model described in Chapter 3 and the timber-steel contact model presented in Section 6.2, are fundamental steps towards a realistic numerical simulation of dowelled timber-steel joints.

The details of the strategies followed to model the test specimens studied in Chapter 5 are exposed below. First, the modelling approach for each joint component is presented, followed by a description of the interface elements used to model their interaction. Besides, some guidelines for an efficient definition of the mesh geometry and size are provided. Finally, the criteria followed for the determination of input values for the parameters of the contact and material models are explained.

6.3.1 Finite element model description

Three FE models were elaborated for each of the three specimens (S1, S2 and S3) described in Chapter 5. Their geometric characteristics are given in Figs. 5.1 to 5.4 and in Table 5.1. Fig. 6.4 shows the three-dimensional finite element model developed in DIANA FE software for the specimen S3 for illustration purposes. All the solid elements employed in the model were eight-nodes hexahedral with linear interpolation. Only one half of the specimens was considered in the model due to its symmetry with respect to the XZ plane. First, an initial prestress force equivalent to 5 MPa was applied along the long bolts to simulate the tightening torque. The bolts prestressing force ensures the development of initial contact between the timber beam and the horizontal leg of the steel angle [68]. Then, the self-weight gravity load is applied to the specimens. Finally, a displacement-control vertical load was imposed as represented in Fig. 6.4 by the red arrow at the beam free end. The fixed boundary condition in the steel column base is also indicated by the green arrows in Fig. 6.4. The same cyclic loading protocol used in the laboratory test (see Fig. 5.5) was applied. Geometric nonlinear behaviour due to large displacements and Newton-Raphson solution algorithm were considered in the analysis.

Table 6.1: Timber-steel interface contact model algorithm in the normal direction

Initial values: $\Delta u_{n,G,0}$; $\Delta u_{n,M,0}$; $\Delta u_{n,UL,0}$; $\Delta u_{s10,0}$; $\Delta u_{s20,0}$; $\text{CONT}_0 = 0$

Load step input parameters: $\Delta u_{n,j+1}$, $\Delta u_{s1,j+1}$, $\Delta u_{s2,j+1}$, $\Delta u_{n,G,j}$, $\Delta u_{n,M,j}$, $\Delta u_{n,UL,j}$, $\Delta u_{s10,j}$, $\Delta u_{s20,j}$, $CONT_j$

- No contact (CONT=0)

  IF $\Delta u_n > \Delta u_{n,G}$ THEN

  $$t_n = k_T \Delta u_n$$

  ELSE

  $$\text{CONT} = 1$$

  $$\Delta u_{s10} = \Delta u_{s1}$$

  $$\Delta u_{s20} = \Delta u_{s2}$$

  END IF

- Contact (CONT=1)

  IF $\Delta u_n \leq \Delta u_{n,M}$ THEN

  $$t_n = k_T \Delta u_{n,G} + k_C \left(\Delta u_n - \Delta u_{n,G}\right)$$

  $$\Delta u_{n,M} = \Delta u_n$$

  ELSE

  $$\text{CONT} = 2$$

  END IF

- Unloading (CONT=2)

  IF $\Delta u_{n,M} \leq \Delta u_n \leq \Delta u_{n,UL}$ THEN

  $$t_n = k_T \Delta u_{n,UL} + k_{UL} \left(\Delta u_n - \Delta u_{n,UL}\right)$$

  ELSE IF $\Delta u_n > \Delta u_{n,UL}$ THEN

  $$\text{CONT} = 0$$

  $$\Delta u_{n,G} = \Delta u_n$$

  ELSE

  $$\text{CONT} = 1$$

  END IF

Output parameters: $t_{n,j+1}$, $\Delta u_{n,G,j+1}$, $\Delta u_{n,M,j+1}$, $\Delta u_{n,UL,j+1}$, CONT_{j+1}, $\Delta u_{s10,j+1}$, $\Delta u_{s20,j+1}$

Table 6.2: Timber-steel interface friction model algorithm in the tangential direction

Load step input parameters: $\Delta u_{s1,j+1}$, $\Delta u_{s2,j+1}$, $t_{n,j+1}$, $\Delta u_{s10,j+1}$, $\Delta u_{s20,j+1}$, $CONT_{j+1}$

- No contact (CONT=0)

$$t_{s1} = k_T \left(\Delta u_{s1} - \Delta u_{s10}\right)$$

$$t_{s2} = k_T \left(\Delta u_{s2} - \Delta u_{s20}\right)$$

- Contact (CONT=1) or Unloading (CONT=2)

$$t_{s1} = k_S \left(\Delta u_{s1} - \Delta u_{s10}\right)$$

$$t_{s2} = k_S \left(\Delta u_{s2} - \Delta u_{s20}\right)$$

$$\tau = \sqrt{(t_{s1})^2 + (t_{s2})^2}$$

IF $\tau < \tau_{max}$ THEN

STICK

ELSE

SLIP

$$\tau_{max} = c - \mu t_n$$

$$F = [(1 - \frac{k_T}{k_S})\frac{\tau_{max}}{\tau}] + \frac{k_T}{k_S}$$

$$t_{s1} = F t_{s1}$$

$$t_{s2} = F t_{s2}$$

END IF

Output parameters: $t_{s1,j+1}$, $t_{s2,j+1}$

Fig. 6.4 shows that the glulam beam model is divided in two parts: 1) the beam section adjacent to the column, connected to it via the angles and the dowels; and 2) the cantilevering part of the beam, at which end the actuator imposes the vertical displacements. During the test, most of the nonlinear behaviour was concentrated at the beam-to-column joint, where the timber beam interacts with the steel bolts and angles. For this reason, a continuum modelling approach, comprising eight-nodes hexahedral solid elements in combination with the plasticity-damage wood constitutive model proposed in Chapter 3, was followed for this part of the beam. Conversely, a linear elastic behaviour is expected for the second portion of the beam, which main function is the transmission of flexure and shear stresses to the joint zone. Therefore, a Timoshenko beam element with linear elastic behaviour was used for this region.

All the steel components (column, angle and bolts) modelled by means of hexahedral solid elements are shown in Fig. 6.5. The 20 mm diameter short bolts (Fig. 6.5d) connect the angle vertical leg to the column flange, while the long bolts (Fig. 6.5b) pass through the timber beam along its height and connect it to the horizontal legs of the angles (Fig. 6.5c). Following experimental observation, plastic deformations are expected to occur in the angles and in the long bolts. The column (Fig. 6.5a) is very stiff and for that reason its response was limited to the linear elastic range during testing. Therefore, a standard Mises plasticity model was assigned to the long bolts and the angles only, whereas a linear elastic model was considered for the column and the short bolts.

The interaction between the timber beam and the steel components was modelled for any shared surface where contact is feasible. In this sense, Fig. 6.6a, which shows the front view of the steel connection components exclusively, is helpful to identify four interaction surfaces for which bi-dimensional interface elements were defined. Three of them connect the timber beam with the long bolts (Fig. 6.6c), the angles horizontal legs (Fig. 6.6d) and the column flange (Fig. 6.6b). The fourth interface element connects the angles vertical legs to the column flange (Fig. 6.6e). Furthermore, Fig. 6.7 indicates two additional bi-dimensional interface elements required to simulate the contact interaction between steel bolts, angles and column. The interfaces which connect the short bolts with the angles vertical legs and the column flange are shown in Fig. 6.7b, while the interfaces that connect the long bolts with the angles horizontal legs are shown in Fig. 6.7c.

Four different constitutive models were assigned to the six types of interface elements previously mentioned, and shown in Figs. 6.6 and 6.7. First, the contact model formulated in Section 6.2 was assigned to the three timber-steel interface elements (Figs. 6.6b,

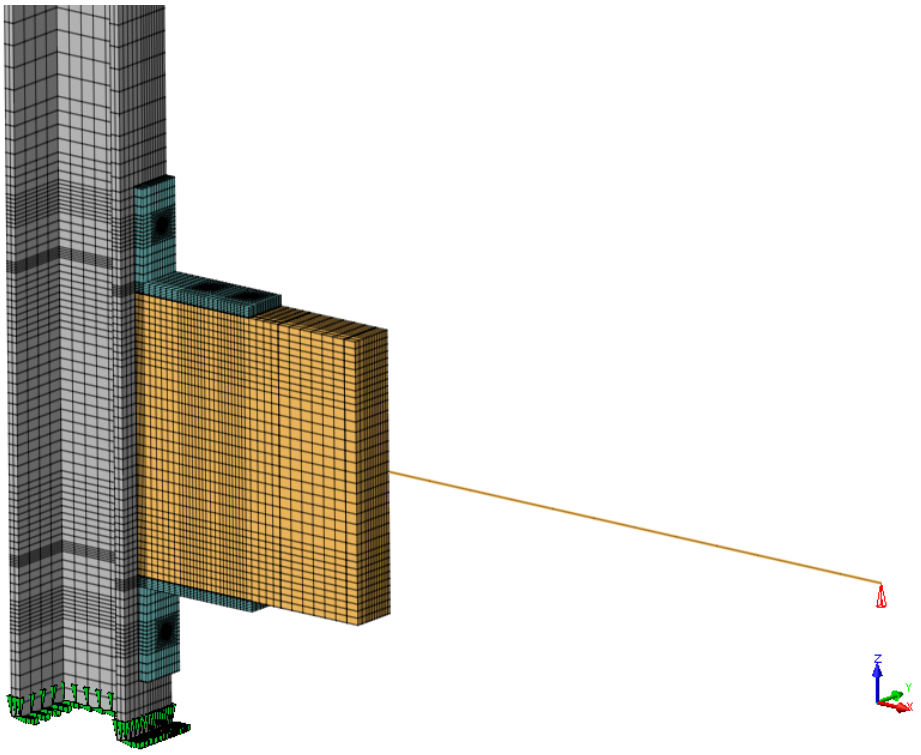
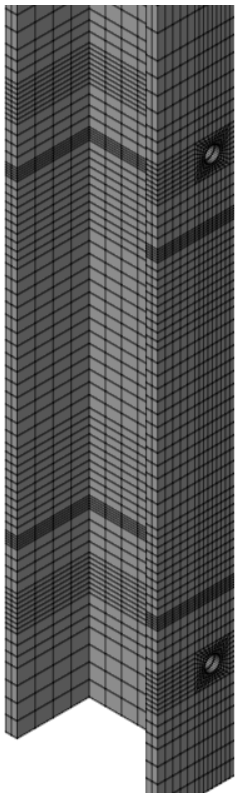


Figure 6.4: FE model 3D view of the timber beam-to-steel column dowelled connection (Specimen S3-16D-15A).

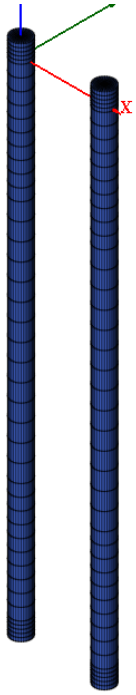
6.6c and 6.6d). Second, considering that the yield stresses of the steel components are high and that their elastic moduli are the same, a simpler no-tension nonlinear elastic model in the normal direction combined with coulomb friction model in the tangential direction was assigned to the angle-column interface element (Fig. 6.6e). Third, a similar no-tension model in the normal direction but this time combined with a linear elastic model in the tangential direction was assigned to the long bolt-angle interface (Fig. 6.7c). Finally, the simplest linear elastic model in both normal and tangential directions was assigned to the short bolt-column and short bolt-angle interface elements (Fig. 6.7b). It will be explained in Section 6.3.2 that even using the same interface constitutive model, different behaviours can be achieved based on the values assigned to its input parameters.

Timber dowelled connection mesh geometry

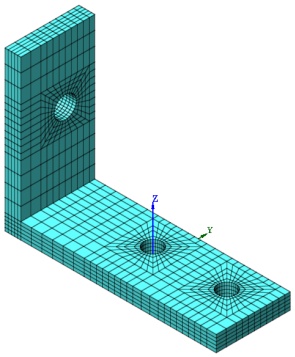
Guidelines to build the mesh of timber dowelled connections are proposed in Fig. 6.8. The proportions given in Fig. 6.8 and expressed in terms of the bolt radius, r, are useful for a proper definition of the mesh size and geometry of both the bolt and the surrounding timber. These configurations were obtained from careful and extensive sensitivity analyses.



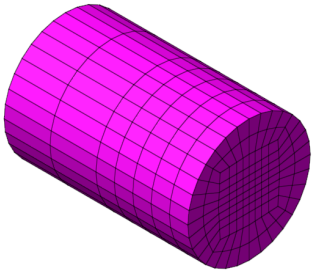
(a) Column



(b) Long bolts

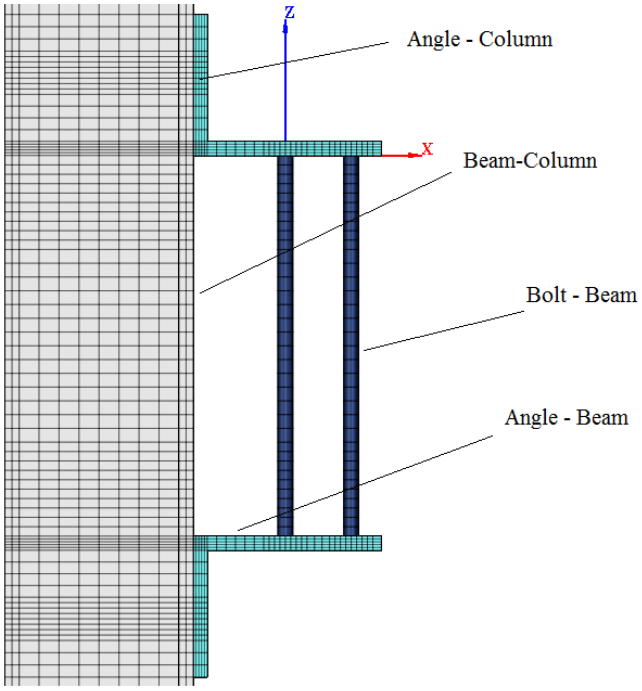


(c) Angle

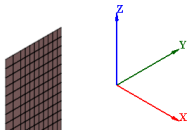


(d) Short bolts

Figure 6.5: Steel components of the FE model (Specimen S3-16D-15A).



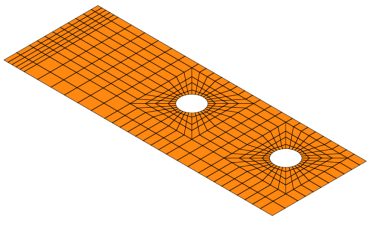
(a) Interaction surfaces



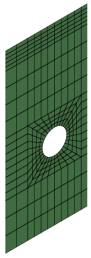
(b) Beam-Column



(c) Bolt-Beam

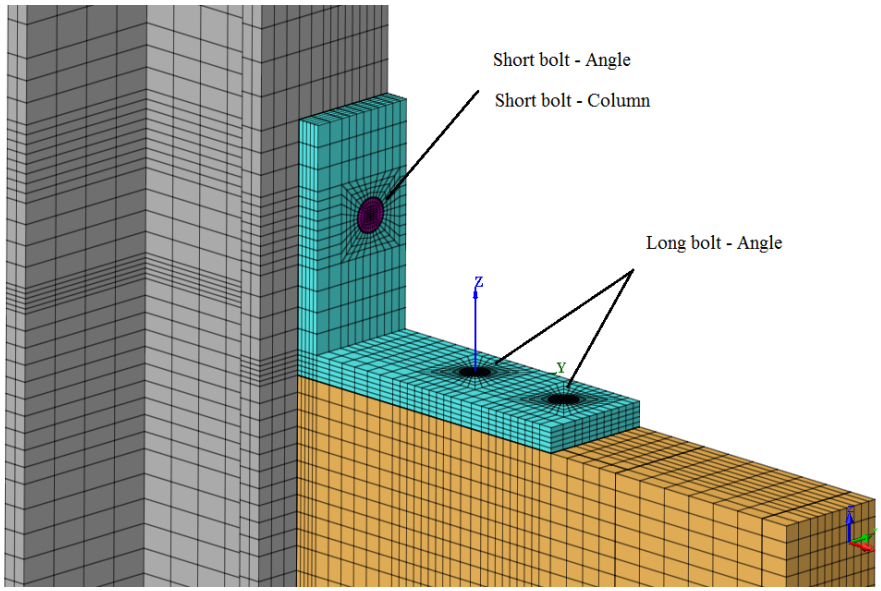


(d) Angle-Beam

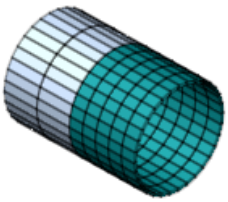


(e) Angle-Column

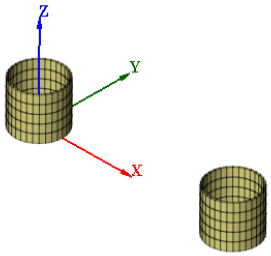
Figure 6.6: Interface elements (Specimen S3-16D-15A).



(a) Location



(b) Short Bolt - Column and Short Bolt - Angle interface elements



(c) Long Bolt - Angle interface element

Figure 6.7: Bolts interface elements (Specimen S3-16D-15A).

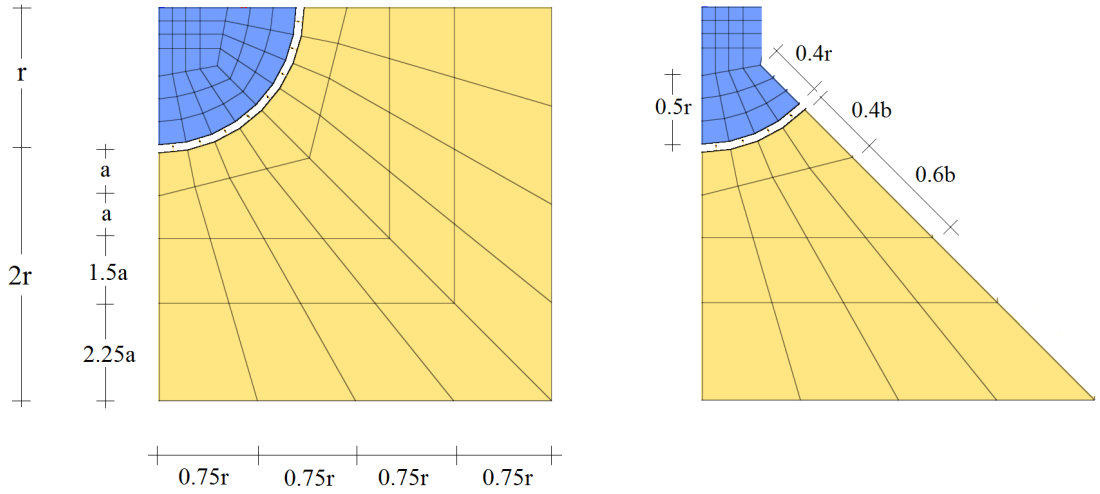
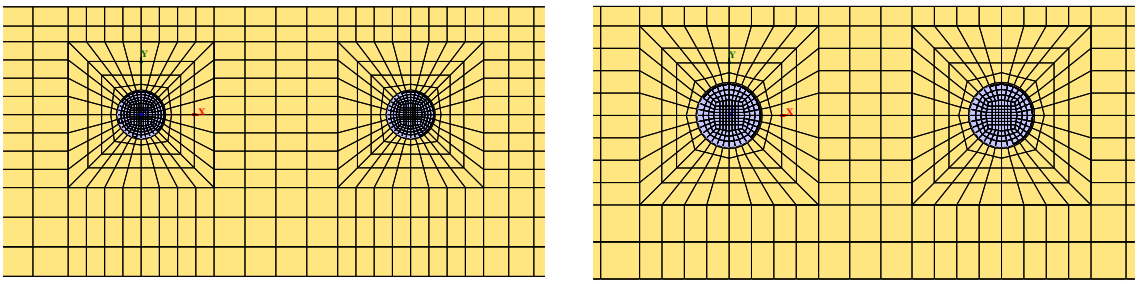


Figure 6.8: Guidelines for the definition of the dowelled connection zone mesh geometry in terms of the bolt radius length.



(a) Specimens S1-12D-12A and S2-12D-15A (12 mm long bolt diameter)

(b) Specimen S3-16D-15A (16 mm long bolt diameter)

Figure 6.9: Finite element mesh geometry of the steel dowel and the timber beam.

Accordingly, Fig. 6.9 shows the finite element mesh geometry of bolt and timber which results from the application of the proposed guidelines to the specimens under consideration. As previously demonstrated in Section 4.2.5, more precise numerical results are obtained when the smallest elements in the timber zone are larger than any of the dowel elements. In such a way, strain localization problems in the zones around the dowels can be neutralized. This type of numerical issue is common and well-known in nonlinear finite element models with softening behaviour and is responsible for hindering the stress transfer and leading to an unrealistic reduction of the predicted maximum deformation and capacity [82, 118, 31, 28, 105]. Finally, a clearance gap of 0.5 mm is left between the bolt and the hole in the timber beam (see Fig. 6.8) based on recommendations from previous studies [145].

6.3.2 Material models and input parameters selection

Figs. 6.4 to 6.7 have shown all the element types which compose the timber beam-to-steel column joint FE model. These elements are classified in three groups: timber elements, steel elements and interface elements. A detailed description of the reasoning behind the material model and input parameters selection corresponding to each element type is provided in the following sections.

Timber elements

As previously mentioned in Section 6.3.1, the wood plasticity-damage model developed in this thesis is assigned to the timber beam. The complete list of the constitutive model input parameter values (excepting the calibration parameters to be determined in Section 6.4) used for the simulation of the timber beam-to-steel column joint cyclic response is presented in Table 6.3.

It is important to note that a unique set of parameter values is used for modelling the three specimens S1, S2 and S3. This is consistent with the micro model approach at the material level followed herein, for which the parameter values definition and calibration processes are required to be performed only once for each material type. Conversely, this is not the case for the more commonly used component-based macro models, for which calibration is more intensive and needs to be repeated for each different type of specimen to be analysed, even in the case that all of them are made of the same material batch.

The wood plasticity-damage model was founded on the assumption of a symmetric elastic stiffness matrix and the transverse isotropy hypothesis (see Section 3.2). Therefore, only five of the nine elastic mechanic parameters (3 Young moduli, 3 Shear moduli and 3 Poisson's ratios) are needed as input parameters, namely, E_X, E_Z, G_{ZX}, ν_{XZ} and ν_{YZ}. The other four properties (E_Y, G_{XY}, G_{YZ} and ν_{XY}) are calculated from Eqs. 3.5 and 3.6. It is important to recall that X denotes the longitudinal direction parallel to the grain, while Y and Z denote the transversal directions perpendicular to the grain.

The first parameter shown in Table 6.3 is the Poisson's ratio corresponding to the longitudinal planes, ν_{XY} and ν_{XZ}. An average of the values reported in [87] for the same batch of timber material was assigned to this parameter, resulting in $\nu_{XY} = \nu_{XZ} = 0.42$. The second input parameter is the Poisson's ratio corresponding to the isotropic transverse plane, for which a value of $\nu_{YZ} = 0.435$ was assigned based on the experimental results also reported in [87]. These Poissons's ratios are in the same range of magnitude

of those employed in [189]. However, higher Poisson's ratios have been used elsewhere [146, 163]. Other studies [68, 162, 8] have used higher values of ν_{XY} and ν_{XZ}, and considerable lower values of ν_{YZ}. On the other hand, some researchers have found that the magnitudes of Poisson's ratios have almost no influence on the predicted global response [36]. Nevertheless, Poisson's ratios actually have a direct impact at the local level. The lateral tensile strains produced mainly in the zones subjected to high levels of compression depend on their magnitude. Furthermore, it was mentioned in Section 3.3 that the potential degradation of Poisson's ratio is not taken into account by the wood constitutive model previously proposed. Therefore, in order to avoid large artificial lateral plastic strains, the use of Poisson ratios around (or lower than) 0.4 is highly recommended. An alternative modelling strategy would be to define two sets of Poisson's ratios. The first set of standard values could be assigned to all timber elements in general, whereas values of half the nominal Poison's ratio could be assigned to the critical timber zones subjected to high levels of damage [144] (e.g. timber zone around the dowels). In this way, the degradation in the Poisson's ratios would be approximately taken into account.

The third and fourth input parameters required are the elastic moduli in the directions parallel (E_X) and perpendicular (E_Y, E_Z) to the grain. A value of $E_X = 12157$ MPa was obtained from [87], while a value of $E_Y = E_Z = 425$ MPa was indirectly obtained using the following approximate expression:

$$E_Y = E_Z = 0.035 E_X \tag{6.12}$$

Eq. 6.12 arises from a series of preliminary numerical analyses and is considered valid for most standard cases. The fifth and last elastic property input parameter is the shear modulus in the planes parallel to the grain. The value of $G_{ZX} = G_{XY} = 952$ MPa reported in [87] was used for the simulation presented later in this chapter. Moreover, Eq. 3.6 was employed to obtain a value of the shear modulus in the transversal plane perpendicular to the grain equal to $G_{YZ} = 148$ Mpa. Coincidentally, the elastic and shear moduli magnitudes listed in Table 6.3 are very similar to the ones experimentally obtained by van Beerschoten et al. [8] for Radiata Pine LVL.

The following nine parameters listed in Table 6.3 are the timber normal compressive (f_X^-, f_Y^-, f_Z^-), normal tensile (f_X^+, f_Y^+, f_Z^+) and shear (f_XY, f_YZ, f_ZX) strengths. The values assigned to all of them, except f_YZ, were experimentally obtained by Karagiannis

[87] for the same wood batch used in this thesis. Conversely, the value of the shear strength in the plane perpendicular to the grain, $f_{YZ} = 1$ MPa, also known as rolling shear strength, was analytically derived under the assumption that the ratio of shear modulus to shear strength in the longitudinal planes parallel to the grain is similar to the corresponding ratio in the transversal plane perpendicular to the grain:

$$\frac{f_{XY}}{G_{XY}} \approx \frac{f_{YZ}}{G_{YZ}} \tag{6.13}$$

For the interested reader, reference values of most of the wood mechanical properties required as input parameters of constitutive models can be found in the Wood Handbook [50].

The next input parameter to be specified is the mixed-mode fracture energy density. A suitable value of $G_f = 1$ was chosen after consulting several references on the topic [80, 154, 7, 149, 53, 123]. This is the same fracture energy density magnitude used for modelling the timber brace-steel plate dowelled connection studied in Section 4.2. Moreover, the discussion in Section 4.3.2, about the influence of the mesh size of the timber elements on the minimum value of G_f, was taken into account to avoid spurious numerical early brittle failure.

The characteristic length, l_{ch}, depends on the size of the finite element discretization (see Section 3.5.1). In timber dowelled connections the size of the finite element mesh is usually directly linked to the bolt diameter. This is clearly appreciated in Fig. 6.9. Therefore, the values of l_{ch} shown in Table 6.3 were calculated as the cubic roots of the volume of the smallest timber finite elements located around the steel dowels, where high nonlinear behaviour and first cracks appearance are expected. Given that the bolt diameter in specimens S1 and S2 is 12 mm, while in specimen S3 is 16 mm, two different characteristic lengths (2.81 mm and 3.47 mm) were determined.

Four additional calibration parameters are required by the proposed wood constitutive model. Nevertheless, only two of them, the hardening modulus (h) and the compressive hardening constant (β) were obtained by means of the calibration process depicted in Section 6.4. Default values of $n = 1$ and $m = 1$ were assumed for the exponential softening parameter and the compressive hardening power parameter, respectively. The reasoning behind the selection of these default values is explained in Section 6.4. Finally, based on the observations and conclusions drawn from the literature review carried out in Section 2.4, the Hoffman criterion [75] was selected as an appropriate plasticity yield

surface for the timber beam.

Table 6.3: Timber beam plasticity-damage constitutive model input parameters values

Poisson's ratios	$\nu_{XY} = 0.42$	$\nu_{YZ} = 0.435$	$\nu_{XZ} = 0.42$
Shear moduli [MPa]	$G_{XY} = 952$	$G_{YZ} = 148$	$G_{ZX} = 952$
Young's moduli [MPa]	$E_X = 12157$	$E_Y = 425$	$E_Z = 425$
Compressive strengths [MPa]	$f_X^- = 33$	$f_Y^- = 3.6$	$f_Z^- = 3.6$
Tensile strengths [MPa]	$f_X^+ = 36.2$	$f_Y^+ = 1.6$	$f_Z^+ = 1.6$
Shear strengths [MPa]	$f_{XY} = 5$	$f_{YZ} = 1$	$f_{ZX} = 5$
Fracture energy density [N/mm]		$G_f = 1$	
Characteristic length [mm]	$l_{ch,S1} = 2.81$	$l_{ch,S2} = 2.81$	$l_{ch,S3} = 3.47$
Exponential softening parameter		$n = 1$	
Hardening modulus [MPa]		Calibration parameter (see Section 6.4.2)	
Compressive hardening constant		Calibration parameter (see Section 6.4.2)	
Compressive hardening power		$m = 1$	
Orthotropic yield criterion		Hoffman	

Steel elements

The four steel components of the connection FE model shown in Fig. 6.5 share the same elastic mechanical properties, namely, a Young's modulus of 200000 MPa and a Poisson's ratio equal to 0.3. As mentioned in Section 6.3.1, plasticity is only modelled in the angles and the long bolts. The column and short bolts are assumed to work within the elastic range.

The nonlinear behaviour of the angles and the long bolts is modelled using a standard

Mises plasticity yield criteria with isotropic hardening. Furthermore, a trilinear stress-strain law [67, 68, 36], which considers three different phases (elasticity, hardening and yielding), is employed for steel components. In consequence, three additional steel material input parameters values are required: yield strength, ultimate strength and ultimate strain. The parameter values assigned assumed are shown in Table 6.4. The yield and ultimate strength of the angles were obtained from coupon tests [86], while Grade 10.9 steel nominal yield and ultimate strength values were assumed for the long bolts. Finally, referential values found in [67, 68, 36] were assumed for the ultimate strain of both steel components.

Table 6.4: Steel plasticity model input parameters values

Parameter	**Angles**	**Long bolts**
Yield strength [MPa]	361	1040
Ultimate strength [MPa]	486	1350
Ultimate strain	0.2	0.1

Interface elements

As mentioned in Section 6.3.1 four different constitutive models were assigned to the interface elements shown in Figs. 6.6 and 6.7. The first of them corresponds to the contact model developed in Section 6.2 and was used to simulate the timber-steel interaction surfaces shown in Fig. 6.6, namely, the beam-column interface (Fig. 6.6b), the angle-beam interface (Fig. 6.6d) and the bolt-beam interface (Fig. 6.6c). The input parameter values assumed for the different interface models are presented in Table 6.5. Two important facts should be highlighted from the information provided in this table. First, given their similar nature, the beam-column and the angle-beam interfaces share the same set of input values. However, in the case of the bolt-beam interface, where embedment is expected to govern, three of the six input parameter values are not assumed *a priori* but obtained via a calibration process which is explained in detail in Section 6.4.2. The different nature and higher relevance of this timber-steel interface, in comparison with the other two, makes it reasonable to seek higher precision in the calibration of those

parameters which link to physical properties is more difficult.

For the beam-column and angle-beam interface elements, a normal compressive stiffness of $k_C = 100$ MPa/mm is assumed based on the magnitude of the wood bulk modulus (see Section 6.4.2 for further explanation). Moreover, a negligible default value of $k_T = 0.01$ MPa/mm is always assigned to the normal stiffness tension parameter. A higher value equivalent to 10% of k_C, and thus equal to $k_S = 10$ MPa/mm, is assigned to the shear stiffness corresponding to the"stick" state of the friction model proposed in Section 6.2.2. Similarly, a default value of the unloading stiffness equivalent to five times the normal stiffness in compression was assumed. Therefore, $k_{UL} = 5k_C = 500$ MPa/mm. Finally, a comprehensive literature review [186, 67, 68, 141, 36, 145, 39, 144, 38] was carried out to determine realistic values of both cohesion and friction coefficient input parameters. In all cases, a null value was assumed for cohesion ($c = 0$ MPa) due to the lack of physical evidence in support of the development of a friction resistance between the timber and steel surfaces when there is no normal compressive force acting in the normal direction. On the other hand, a high variability of friction coefficients (from 0.1 to 0.7) was employed by different researchers [38]. For this reason, a value of $\mu = 0.35$ was considered an appropriate mean value for modelling friction between the beam-column and angle-beam interface elements.

In the case of the short steel bolt-timber beam interface, the same criteria and values mentioned above were assigned to k_T and c. Nevertheless, a higher value of friction coefficient equal to $\mu = 0.5$ [141, 36, 145, 39, 144] was assigned due to the higher roughness of the bolt surface in comparison with the steel column flange or angle leg. The other three interface parameters in Table 6.5 are determined via the calibration process described in Section 6.4.

The second interface constitutive model considered refers to the steel angle-steel column interface element. The input parameters values required for this no-tension model in the normal direction combined with a coulomb friction model in the tangential direction are provided in the second column of Table 6.6. Due to the higher stiffness of steel compared to wood, a normal stiffness equal to five times the normal stiffness assigned to the timber-steel interfaces is assumed ($k_N = 5 \cdot 100 = 500$ MPa/mm). On the other hand, the same "stick" state shear stiffness defined for the beam-column or angle-beam interfaces, and equal to $k_S = 10$ MPa/mm, is assumed for the angle-column interface. By default, a maximum tensile stress equal to $f_{t,max} = 0.1$ MPa is assigned as input parameter of the no-tension model. This means that every time the normal stress in

Table 6.5: Timber-steel interface model input parameters values

Parameter	**Beam-Column / Angle-Beam**	**Bolt-Beam**
Normal stiffness in compression (k_C) [MPa/mm]	100	Calibration parameter (see Section 6.4.2)
Normal stiffness in tension (k_T) [MPa/mm]	0.01	0.01
Shear stiffness (k_S) [MPa/mm]	10	Calibration parameter (see Section 6.4.2)
Unloading stiffness (k_{UL}) [MPa/mm]	500	Calibration parameter (see Section 6.4.2)
Friction coefficient (μ)	0.35	0.5
Cohesion (c) [MPa]	0	0

the interface element exceeds 0.1 MPa the normal stiffness is automatically reduced to a very small value close to zero. In this way, no further tension is allowed and opening can occur freely. Finally, a theoretical value of the friction coefficient for two steel surfaces in contact equal to $\mu = 0.3$ is considered. Accordingly, a theoretical value of the cohesion parameter is determined as the multiplication of the maximum tensile stress times the friction coefficient ($c = f_{t,max} \cdot \mu = 0.03$ MPa).

The third interface constitutive model simulates the interaction between the long bolts and the angle legs. In this case, the nonlinear elastic no-tension model in the normal direction is combined with a linear elastic model in the tangential direction. Taking into account that this is also a steel-steel interface element, the same normal stiffness ($k_N = 500$ MPa/mm) and maximum tensile strength ($f_{t,max} = 0.1$ MPa) parameters values previously assigned to the angle-column interface are used. On the contrary, a very high shear stiffness value ($k_S = 250$ MPa/mm) is employed to prevent sliding. This is consistent with the restriction imposed by the nut on the tangential relative displacement between the bolts and the angle. All the parameter values corresponding to this interface are listed in the fourth column of Table 6.6.

Finally, the third column of Table 6.6 contains the parameters values of the linear elastic model employed for the short bolt-angle and short bolt-column interface elements. These short bolts joint tightly together the angle vertical leg to the column flange, only allowing minor relative displacements in both normal and tangential directions. Therefore, a simple linear elastic model with the same normal and shear stiffness values assigned to the long bolt-angle interface is used to simulate the interaction between these steel components.

Table 6.6: Steel-steel interface models input parameters values

Parameter	**Angle-Column**	**Short Bolt-Angle / Short Bolt-Column**	**Long Bolt-Angle**
Normal stiffness (k_N) [MPa/mm]	500	500	500
Shear stiffness (k_S) [MPa/mm]	10	250	250
Max. tensile stress ($f_{t,max}$) [MPa]	0.1	N.A.	0.1
Friction coefficient (μ)	0.3	N.A.	N.A.
Cohesion (c) [MPa]	0.03	N.A.	N.A.

Table 6.3 indicates that two parameters of the wood constitutive model need to be calibrated. Similarly, the three calibration parameters of the steel bolt-timber beam interface constitutive model are indicated in Table 6.5. A procedure to calibrate these five parameters based on embedding tests is described in detail in the following section.

6.4 Calibration procedure using embedment tests

The wood constitutive model formulated in Chapter 3 requires four parameters which cannot be directly obtained from commercially available timber material specifications.

Therefore, a calibration process based on simple material characterization tests needs to be performed to determine their values. The four calibration parameters under consideration are: β and m (that defines compressive damage evolution law), n (that affects tensile damage evolution law), and the compressive plasticity hardening modulus, h. The values of m and n are mainly related to the qualitative characteristics of the post-elastic stress-strain curves under compression and tension, respectively. Therefore, values equal to $m = 1$ (corresponding to linear hardening under compression) and $n = 1$ (corresponding to an asymptotic exponential softening without residual strength under tension) are assigned to these two parameters. The chosen post-elastic behaviours are based on the experimental uniaxial stress-strain curves obtained by Karagiannis et al. [85] for the same batch of timber material employed herein, the numerical results shown in Figs. 3.11 and 3.9, and the discussion provided in Sections 3.8.1 and 4.2.2.

On the other hand, the input stiffness parameters values of the timber-steel contact model proposed and formulated in Section 6.2 (e.g. normal compressive stiffness, k_C, shear stiffness, k_S, or unloading stiffness, k_{UL}) are difficult to derive experimentally or analytically. For this reason, the input parameters of this type of interface elements are generally defined based on numerical considerations and analyst experience [146]. However, it was noticed that the compressive normal stiffness, k_C, has a considerable influence on the global initial linear elastic stiffness of the connection, whereas the shear stiffness under the "stick" state (before the friction force is exceeded and sliding initiates), k_S, contributes to the capacity increment of a dowelled connection. Moreover, as explained in Section 6.2, a proper value of the unloading stiffness, k_{UL}, is important for modelling pinching behaviour. Therefore, it is proposed that these three stiffness parameters be obtained by means of a calibration process. In summary, a total of five parameters need to be calibrated, two from the wood constitutive model (h and β) and three from the timber-steel interface contact model (k_C, k_S and k_{UL}).

The maximum capacity of a timber dowelled connection is strongly influenced by both compressive hardening parameters (h and β). More specifically, the hardening modulus, h, determines the extent of plastic deformation due to compressive stresses, while the parameter β controls the maximum level of stiffness degradation in compression. However, the experimental determination of plastic deformations is complex and rare. Similarly, cyclic tests on timber specimens at the material level that would be useful to determine the extent of stiffness degradation due to tensile or compressive loading are also unusual. To overcome these issues, a simplified calibration process based on simple embedment curves in the directions parallel and perpendicular to the grain is proposed in this the-

sis. This kind of tests are easy to perform and usual in timber engineering practice. In fact, the design expressions given in Chapter 8.2.3 of Eurocode 5 [14] to determine the load-carrying capacity of timber dowelled connections are formulated in terms of the embedding strength of wood.

6.4.1 Embedment tests

The embedment tests carried out by Karagiannis et al. [85] on the same batch of glulam beams employed in this thesis were used in the calibration process that follows. It is well-known that the embedment initial stiffness and strength are mainly affected by the wood density and the dowel size [22, 151]. For this reason, four embedment tests, corresponding to two different bolt diameters (12 mm and 16 mm) for each loading direction (parallel and perpendicular to the grain), were considered in [85]. Coincidently, these are the same diameters of the long bolts used in the beam-to-column connection specimens described in Chapter 5. All these observations support the relevance and validity of the results to be obtained from this calibration process.

Fig. 6.10 shows a typical 12 mm bolt diameter embedment specimen examined in [85]. The details of the test set-up and the specimens geometric characteristics are reported in [85]. Between 8 and 12 embedment tests were conducted for each of the four configurations, making a total of 37 specimens. The corresponding four sets of embedment force-displacement curves are reproduced in Fig. 6.11 [85].

6.4.2 Calibration methodology

The idea behind the methodology proposed is to find a unique set of parameter values (k_C, k_S, k_{UL}, h, β) that results in four numerical embedment force-displacement curves which lie within the bounds of the experimental curves shown in Fig. 6.11. The first step consists on the identification of the "primary" direction of analysis (parallel or perpendicular to the grain) based on the purpose of the calibration. Priority should be given to the set of calibrated parameters which results on a better numerical fitting of the experimental results along the primary direction of analysis. For instance, in the beam-to-column connections studied in Chapter 5, the interaction between the steel bolt and the timber beam due to the application of a cyclic loading produces stresses in the direction parallel to the grain. Therefore, in this case the primary direction of analysis is parallel to the grain, and thus, for this particular calibration process, the numerical fitting of the

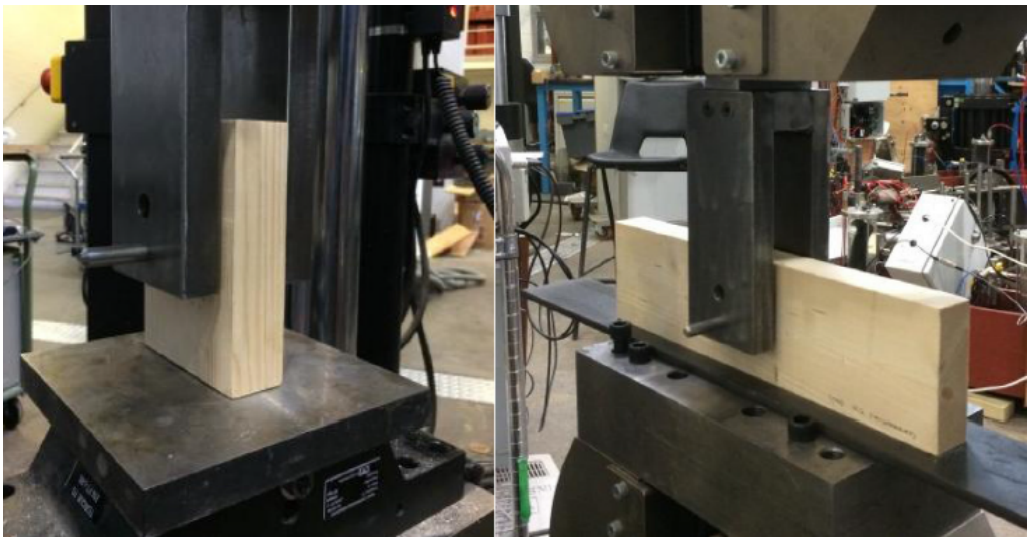
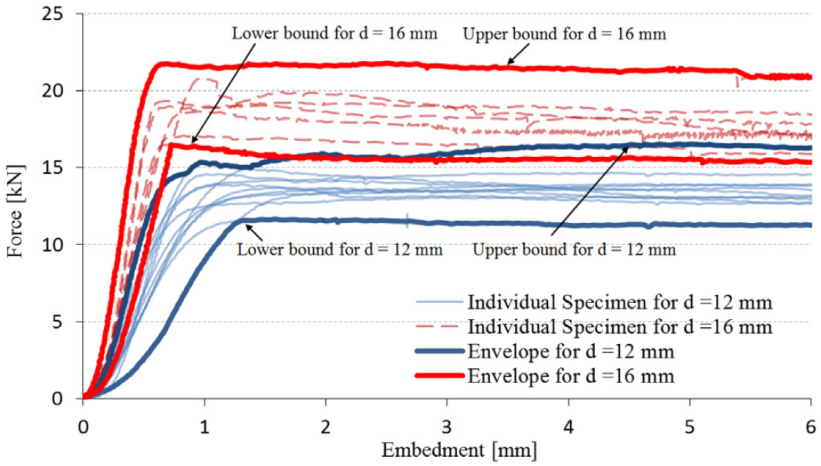


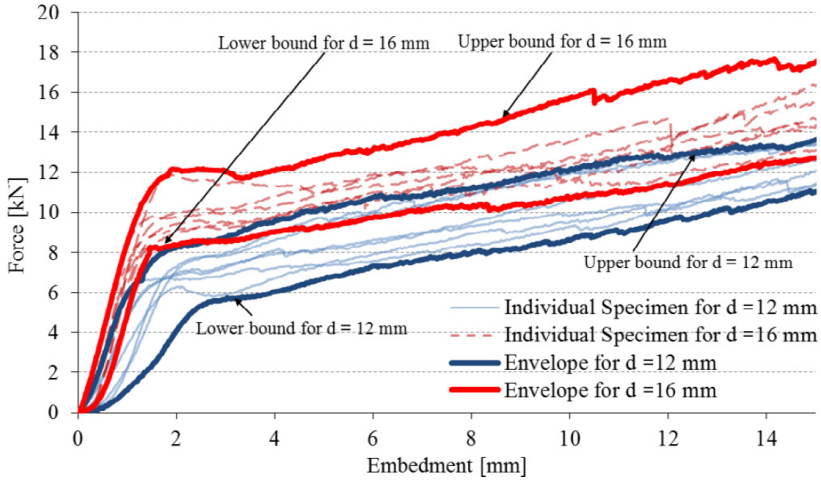
Figure 6.10: Embedment test experimental set-up for 12 mm bolt diameter specimens: parallel (left) and perpendicular (right) to the grain (Figure taken from Karagiannis et al. [85]).

experimental embedding curves in Fig. 6.11a is more important than for the curves in Fig. 6.11b. If there were more than one zone with different primary directions, then, different sets of calibrated parameters could be determined for each zone, if necessary.

Based on the guidelines developed in Section 6.3, four FE models were elaborated, one per each of the four embedment specimens described in Section 6.4.1. Two of these models, corresponding to 12 mm bolt diameter specimens loaded in the directions parallel and perpendicular to the grain, are displayed in Fig. 6.12. The red arrows indicate the direction of the displacement control load applied at the ends of the steel bolts. Likewise, two additional models were elaborated for the corresponding 16 mm bolt diameter specimens. All the input parameter values of the wood material model and the timber beam-steel bolt interface contact model, except the five parameters to be calibrated, were obtained from Tables 6.3 and 6.5, respectively. Furthermore, a set of initial values should be assigned to the five calibration parameters. Based on the author's experience, the following set of default values can be regarded as a good starting point: $k_C = 100$ MPa/mm, $k_S = 10$ MPa/mm, $k_{UL} = 450$ MPa/mm, $h = 40.9$ MPa, $\beta = 0.9$. On the basis of these initial values, each of the five parameters were calibrated one by one. A detailed explanation of the calibration procedure follows below.

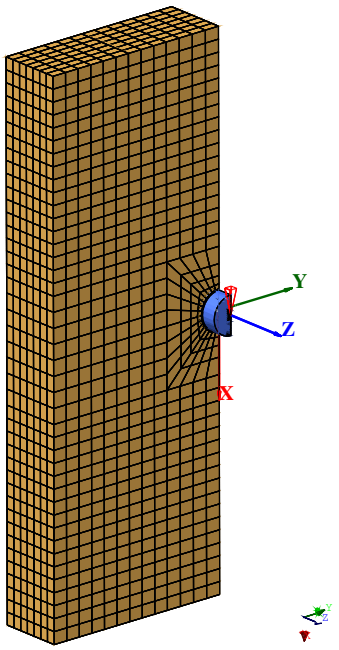


(a) Parallel to the grain

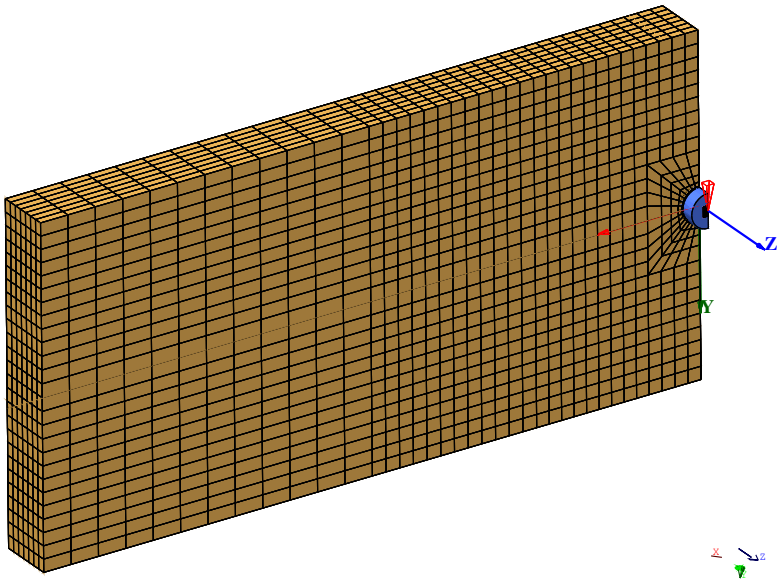


(b) Perpendicular to the grain

Figure 6.11: Experimental embedment curves for 12 mm and 16 mm bolt diameter specimens (Figures taken from Karagiannis et al. [85]).



(a) Parallel to the grain



(b) Perpendicular to the grain

Figure 6.12: FE models of the 12 mm bolt diameter embedment test specimens.

Interface normal stiffness in compression

The first parameter to be calibrated is the compressive normal stiffness of the timber beam-steel bolt interface (k_C). For this purpose, the objective is to obtain a good fitting of the initial elastic part of the embedment force-displacement curve only, where timber non-linear behaviour does not play a significant role [146]. A relation can be established between k_C and the timber bulk modulus, K. More precisely, a first approximation of the value of k_C can be calculated as a fraction of K [145]. The bulk or compression modulus is defined as the ratio of the hydrostatic pressure, p, to the volumetric strain, ϵ_{vol}, [29] such that:

$$K = \frac{p}{\epsilon_{vol}} \tag{6.14}$$

For orthotropic materials, the bulk modulus can be calculated using the compliance matrix, $\boldsymbol{C}^e$, previously defined in Eq. 3.2, as follows:

$$\begin{bmatrix} \epsilon_{XX} \\ \epsilon_{YY} \\ \epsilon_{ZZ} \\ 0 \\ 0 \\ 0 \end{bmatrix} = \begin{bmatrix} \frac{1}{E_X} & -\frac{\nu_{YX}}{E_Y} & -\frac{\nu_{ZX}}{E_Z} & 0 & 0 & 0 \\ -\frac{\nu_{XY}}{E_X} & \frac{1}{E_Y} & -\frac{\nu_{ZY}}{E_Z} & 0 & 0 & 0 \\ -\frac{\nu_{XZ}}{E_X} & -\frac{\nu_{YZ}}{E_Y} & \frac{1}{E_Z} & 0 & 0 & 0 \\ 0 & 0 & 0 & \frac{1}{G_{XY}} & 0 & 0 \\ 0 & 0 & 0 & 0 & \frac{1}{G_{YZ}} & 0 \\ 0 & 0 & 0 & 0 & 0 & \frac{1}{G_{ZX}} \end{bmatrix} \begin{bmatrix} p \\ p \\ p \\ 0 \\ 0 \\ 0 \end{bmatrix} \tag{6.15}$$

$$\epsilon_{vol} = \epsilon_{XX} + \epsilon_{YY} + \epsilon_{ZZ} \tag{6.16}$$

From Eqs. 6.14 to 6.16, and under the hypothesis of transverse isotropy, the expression for calculating the timber bulk modulus is obtained as:

$$\frac{1}{K} = \frac{1}{E_X} + \frac{1}{E_Y} + \frac{1}{E_Z} - 2\left(\frac{\nu_{XY}}{E_X} + \frac{\nu_{XZ}}{E_X} + \frac{\nu_{YZ}}{E_Y}\right) \tag{6.17}$$

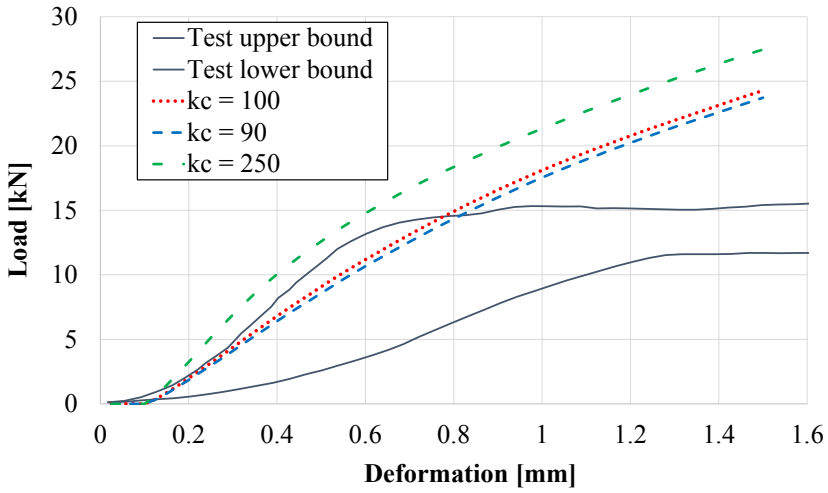
The substitution of the elasticity moduli and Poisson's ratios given in Table 6.3 into Eq. 6.17 results in a Bulk modulus equal to $K = 384$ MPa. Therefore, an initial value of $k_C = 100$ MPa/mm, which is approximately the result of multiplying the bulk modulus by a penalty factor of 0.25 ($k_C \approx 0.25 \cdot K$), is employed. Once the value of k_C is set and the initial elastic embedment response is reasonably reproduced, the other four parameters are calibrated based on the non-linear inelastic part of the embedment force-

displacement curves. In general, it can be stated that the final value of k_C at the end of the calibration process falls between 50 Mpa/mm and 500 MPa/mm.

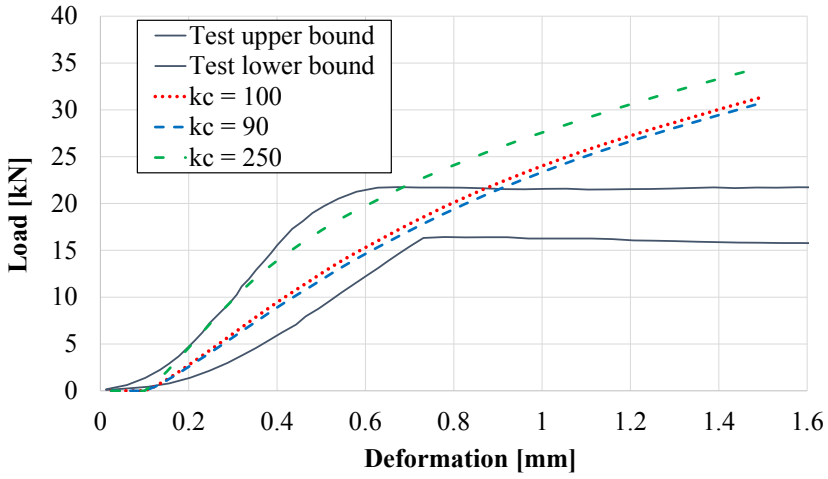
Figs. 6.13 and 6.14 show the numerical embedment load-displacement curves corresponding to the calibration process of k_C, together with the upper and lower bound experimental curves for the four specimens tested. The numerical results obtained with $k_C = 100$ MPa/mm indicate that a good approximation of the experimental bounds is achieved in the direction parallel to the grain for both bolt diameters. Nevertheless, in the direction perpendicular to the grain the predicted initial stiffness is slightly higher than the experimental upper bound curve. Therefore, in order to explore the possibility of getting a better estimate of the initial stiffness, a second set of analysis using $k_C = 90$ MPa/mm was carried out. Even though the reduction of the initial stiffness is not significant compared to the initial assumption, the final results obtained were considered satisfactory, specially in the direction parallel to the grain, which for this case study is the primary direction of analysis (see Section 6.4.2). Consequently, a calibrated value of $k_C = 90$ MPa/mm is selected for the numerical modelling of the timber-steel beam-to-column connection, and henceforth this value will be used for the calibration of the other four parameters. It can be noticed in Figs. 6.13 and 6.14 that the post-elastic part of the curve is not calibrated yet, and that the current set of parameters values lead to a high embedding strength prediction, particularly in the direction parallel to the grain. Finally, in order to assess the influence of a higher value of the normal contact stiffness on the numerical response, a third set of analysis with $k_C = 250$ MPa/mm was also performed for illustration purposes only.

Compressive hardening constant

The second parameter to be calibrated is the compressive hardening constant β. Recalling the discussion in Section 3.3.3 and the results obtained from the sensitivity analysis performed in Section 3.8.1 (see Fig. 3.10), it is clear that β limits the maximum level of compressive damage, and therefore, has an important influence on the post-elastic hardening level and the maximum compressive strength. The calibrated value of β should lie between 0 (no damage at all) and 1 (fully damaged). A value of $\beta = 0.9$ was selected for the beginning of the calibration process. The calibrated parameter value $k_C = 90$ MPa/mm was employed, while the default initial values were assigned to the other three parameters (i.e. $h = 40.9$ MPa, $k_S = 10$ MPa/mm and $k_{UL} = 450$ MPa/mm).

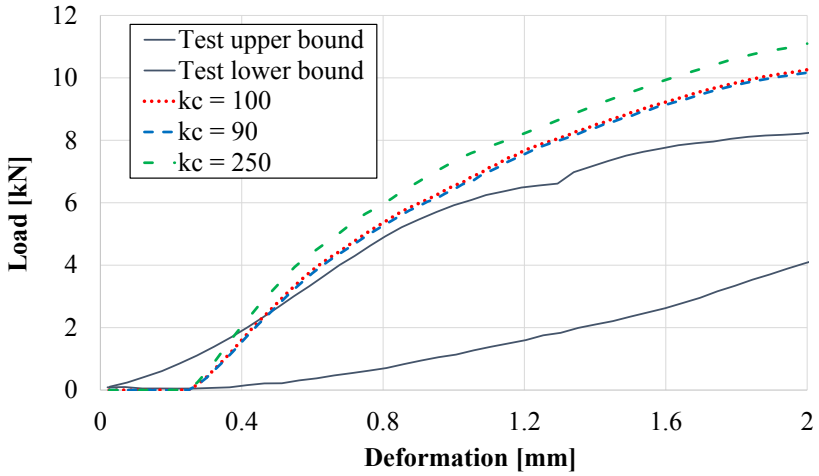


(a) 12 mm dowel diameter

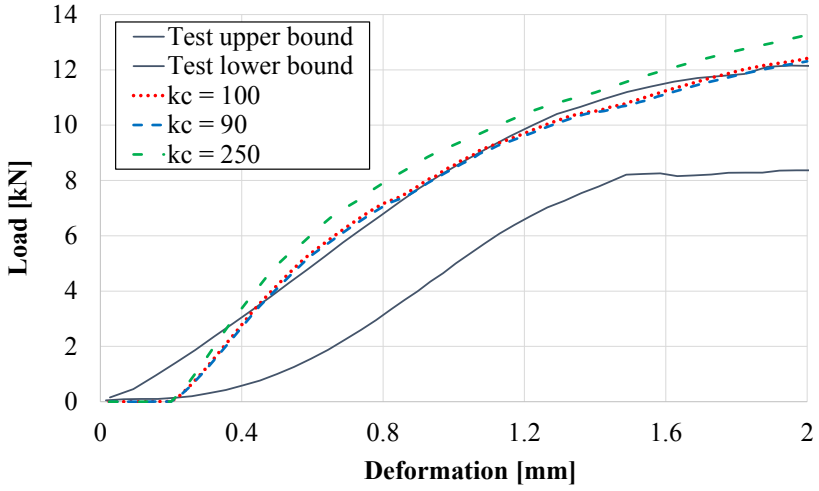


(b) 16 mm dowel diameter

Figure 6.13: Calibration of k_C based on the experimental embedment curves [85] in the direction parallel to the grain.



(a) 12 mm dowel diameter



(b) 16 mm dowel diameter

Figure 6.14: Calibration of k_C based on the experimental embedment curves [85] in the direction perpendicular to the grain.

Additional analyses were carried out for higher values, $\beta = 0.95$ and $\beta = 0.995$. The comparison of the three sets of numerical embedment curves against the corresponding experimental bounds is shown in Figs. 6.15 and 6.16. It can be appreciated from these figures that the strength and hardening reduction obtained with $\beta = 0.95$ is insufficient. A better match between experimental and numerical results is, however, achieved by using $\beta = 0.995$. Despite the fact that only the curves in the direction perpendicular to the grain (see Fig. 6.16) lie between the experimental upper and lower bounds curve, a substantial improvement is also obtained for the numerical prediction in the direction parallel to the grain (see Figs. 6.15). Furthermore, no significant differences were encountered when using the maximum value $\beta = 1$. On the contrary, convergence instability and numerical issues may arise if this value is chosen. Therefore, $\beta = 0.995$ is selected as the final calibrated parameter value to be used hereafter.

Plasticity hardening modulus

The initial value for the calibration of the plasticity hardening modulus, h, can be analytically derived from Eqs. 3.46 and 3.47 such that:

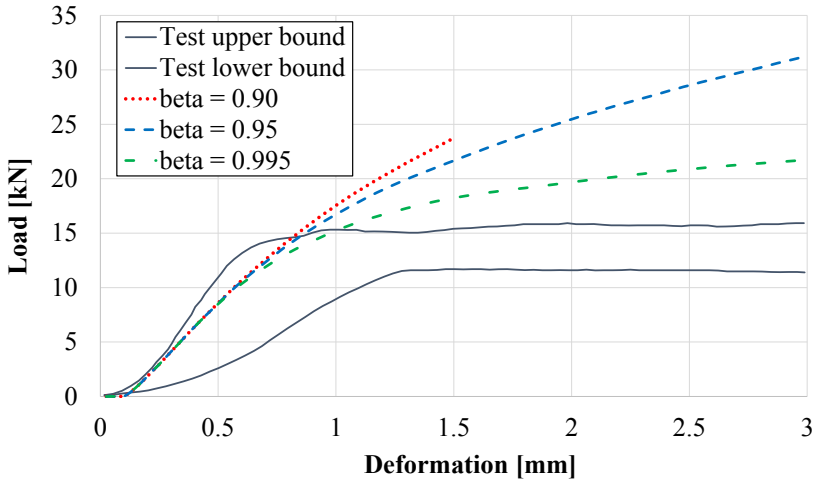
$$h = \frac{\alpha_Z}{1 - \alpha_Z} \frac{E_Z}{f_Z^-} \tag{6.18}$$

where E_Z and f_Z^- are the elasticity modulus and the compressive strength, respectively, in the direction perpendicular to the grain, while $\alpha_Z = \frac{T_Z}{E_Z}$ is the ratio of tangent plastic to elastic moduli. Following the procedure outlined in Section 3.4.3, an analogous expression can also be obtained for a load direction parallel to the grain:

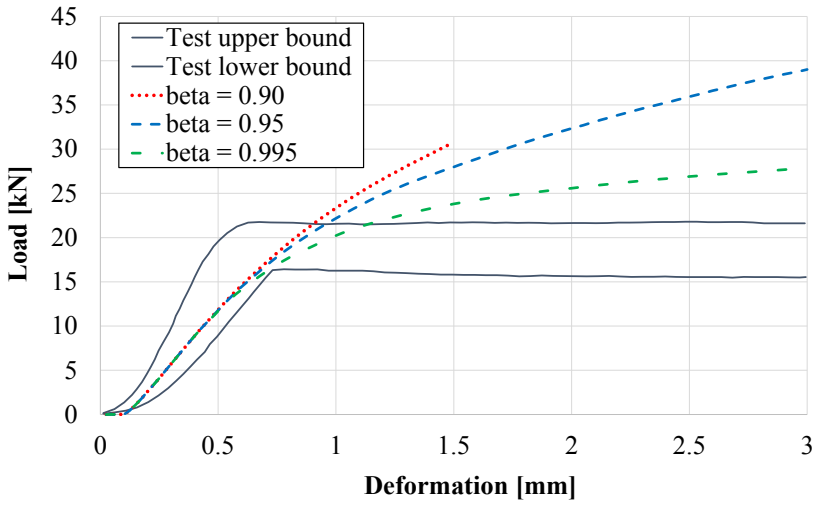
$$h = \frac{\alpha_X}{1 - \alpha_X} \frac{E_X}{f_X^-} \tag{6.19}$$

where E_X, f_X^- and $\alpha_X = \frac{T_X}{E_X}$ are the parameters corresponding to that direction.

Consequently, two alternative initial values of h can be obtained from Eqs. 6.18 and 6.19. The glulam elasticity moduli (E_X, E_Z) and compressive strengths (f_X^-, f_Z^-) values are taken from Table 6.3. On the other hand, the ratio of tangent plastic to elastic moduli in the direction perpendicular to the grain can be assumed as $\alpha_Z = 0.1$ [187]. Considering that hardening in the direction parallel to the grain is less pronounced, it would be reasonable to assume that a lower value should be assigned to α_X. However, in a plasticity-damage model the post-elastic hardening response in compression does not depend on plasticity only, but also on damage, which further reduces the level of

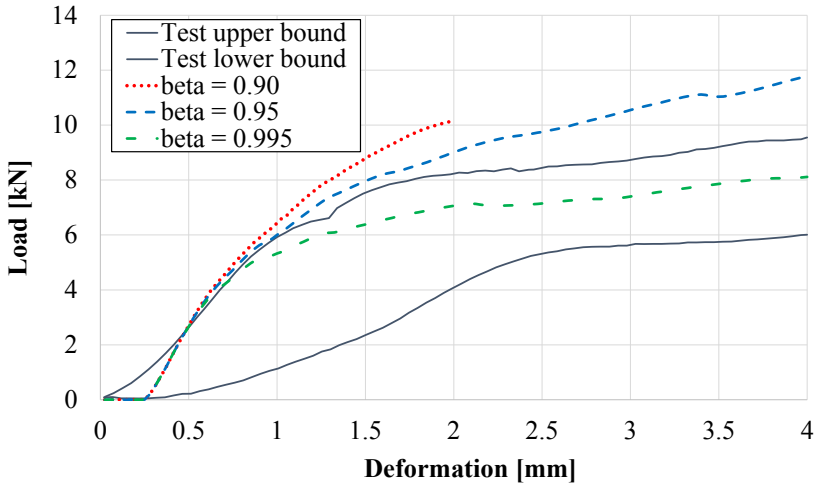


(a) 12 mm dowel diameter

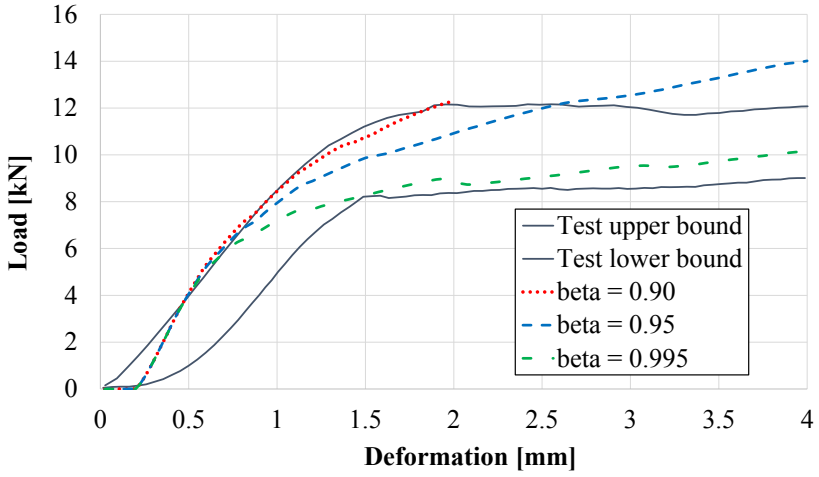


(b) 16 mm dowel diameter

Figure 6.15: Calibration of β based on the experimental embedment curves [85] in the direction parallel to the grain.



(a) 12 mm dowel diameter



(b) 16 mm dowel diameter

Figure 6.16: Calibration of β based on the experimental embedment curves [85] in the direction perpendicular to the grain.

hardening through the parameter β, as previously discussed in Sections 3.3.3 and 3.8.1. Therefore, the same value is assumed for the ratio of tangent plastic to elastic moduli in both directions ($\alpha_X = \alpha_Z = 0.1$).

With these considerations in mind, the two initial plasticity hardening moduli obtained from Eqs. 6.18 and 6.19 for calibration purposes are $h = 13.1$ MPa and $h = 40.9$ MPa, respectively. It was mentioned above that for this particular case study the primary direction of analysis is parallel to the grain. For this reason, $h = 40.9$ MPa was selected as the initial value. However, in order to asses the influence of this parameter on the embedment nonlinear response, a second set of analysis was carried out for a value of $h = 13.1$ MPa as well. It is important to bear in mind that $h = 40.9$ MPa and $h = 13.1$ MPa correspond to $\alpha_X = 0.1$ and $\alpha_X = 0.03$, respectively, in the direction parallel to the grain. By contrast, in the direction perpendicular to the grain, $h = 13.1$ MPa corresponds to $\alpha_Z = 0.1$, while $h = 40.9$ MPa corresponds to $\alpha_Z = 0.26$.

Figs. 6.17 and 6.18 show the numerical embedment curves obtained for both values of h and the experimental upper and lower bound curves. The numerical unloading branch is also plotted with the objective of quantitatively assess the influence of h on the level of plastic deformations, stiffness degradation and pinching (see Section 6.2). For both loading directions and bolt diameters, the influence of the plasticity hardening modulus parameter on the loading branch of the embedment curves is negligible. The unloading branches, however, show different responses for each value of h.

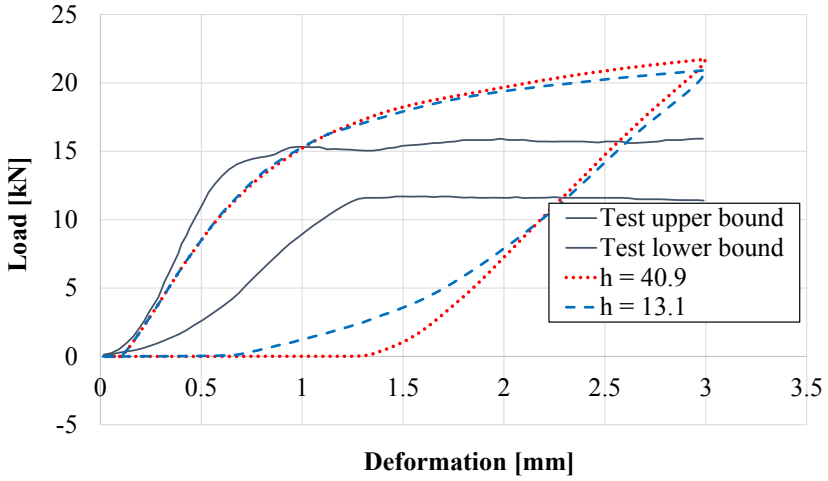
In the direction parallel to the grain (Fig. 6.17) similar unloading stiffness can be noticed at the beginning for both magnitudes of plasticity hardening moduli. Moreover, the slope of the unloading branch is similar to that of the elastic loading branch, meaning that minor stiffness degradation is experienced in both cases. On the other hand, the higher timber plastic deformations associated to $h = 13.1$ ($\alpha_X = 0.03$) explain the gradual unloading stiffness reduction observed in Fig. 6.17, which starts in the point where the elastic strains are fully recovered (deformation around 2 mm) and finishes when the bolt and the timber are completely separated (zero load). For $h = 40.9$ ($\alpha_X = 0.1$) the plastic deformations are minor, and therefore, the elastic unloading stiffness remains constant until a sudden change of slope occurs as a consequence of bolt and timber separation, just before reaching zero load. Accordingly, the use of $h = 40.9$ results in a more pronounced pinching behaviour. Most of the characteristics described above are also valid for $h = 13.1$ and $h = 40.9$ in the direction perpendicular to the grain (Fig. 6.18). Nevertheless, considerably higher levels of stiffness degradation (unloading stiffness lower than

loading elastic stiffness) are observed in the direction perpendicular to the grain for a hardening modulus of $h = 40.9$ ($\alpha_Z = 0.26$).

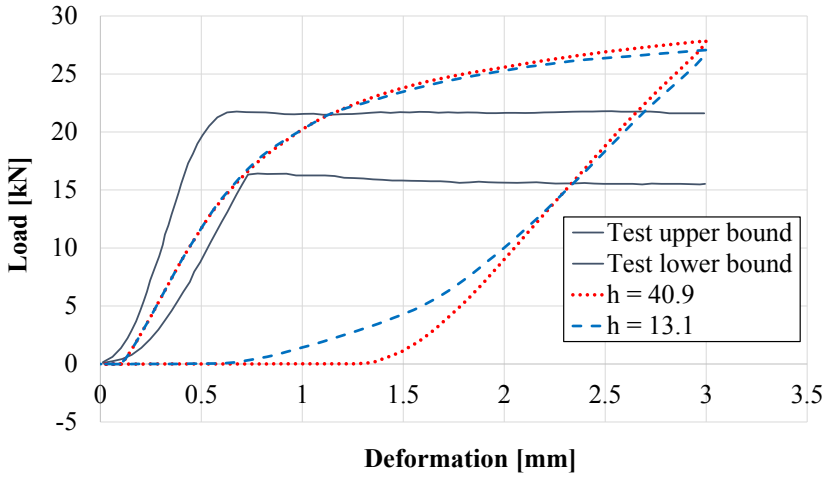
Based on these observations, the plasticity hardening modulus calculated for $\alpha_X = 0.1$ ($h = 40.9$ MPa) is selected as the final calibrated parameter value to be used hereafter. Moreover, in the author's experience, the definition of h taking into account the loading direction is fundamental to adequately transfer the stresses from the wood to the dowel, and also to avoid convergence issues during the analysis. It is also important to mention that, although wood incurs in plastic deformations (which magnitudes are directly related to the value of h), residual permanent deformations are not observed in the loading-unloading embedment curves (see Figs. 6.17 and 6.18). The reason for this is that, during unloading, the load becomes zero immediately after the bolt and the surrounding wood separate. Considering that at this point the bolt begins to freely translate along the gap (which is a consequence of wood plastic deformation), and that a displacement control is applied to the bolts in the FE model (see Section 6.4.2), the zero load remains until the curve goes back to the origin. Nevertheless, the experimental evidence shows that additional permanent plastic deformations may arise in the wood as a consequence of the ovalization of the bolt holes. Therefore, in those cases an additional load in the opposite direction (residual strength) would need to be applied after unloading in order to go back to zero deformation. This effect can be included in the timber-steel interface contact model, however, there is lack of experimental verification and quantification of this phenomenon because embedment tests do not comprise the unloading stage. For that reason, it was decided to stay in the safe side by not incorporating the residual strength in the interface contact model formulation.

Interface normal unloading stiffness

The unloading stiffness parameter should also be calibrated based on the unloading branch of a experimental curve. However, this kind of information is only available for cyclic loading tests on dowelled connections, which are scarce (see Section 5.1). Thus, similarly to h, the calibration of k_{UL} will be based on qualitative criteria, taking as reference the characteristic pinching hysteretic behaviour observed in Section 5.3.1. The initial value of k_{UL} is 450 MPa/mm. Two more values are evaluated ($k_{UL} = 90$ MPa/mm and $k_{UL} = 900$ MPa/mm) in Figs. 6.19 and 6.20. It should be noted that the first value is equal to the loading compressive stiffness k_C, while the latter is equal to twice the initial value.

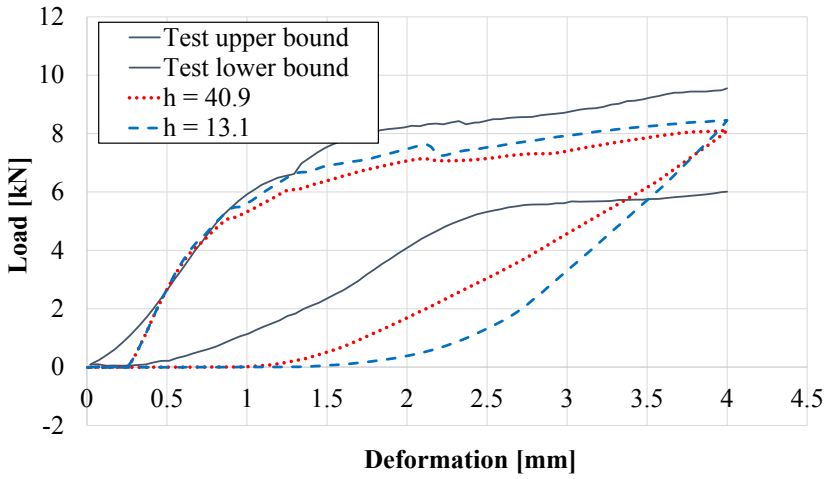


(a) 12 mm dowel diameter

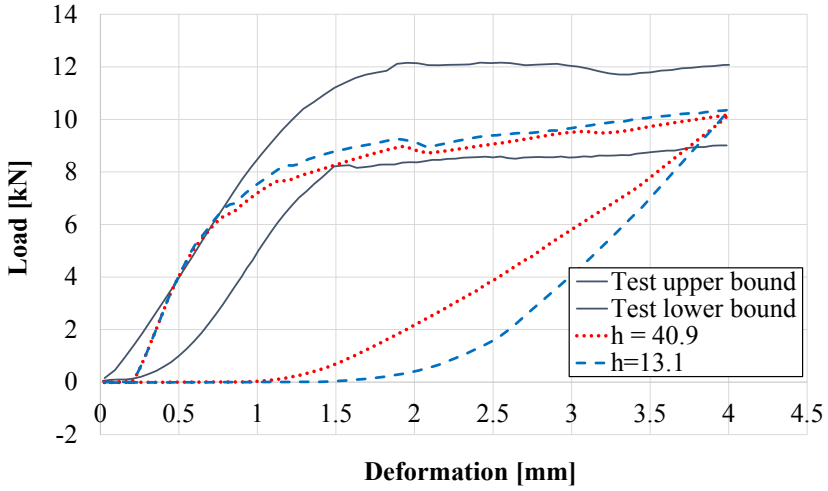


(b) 16 mm dowel diameter

Figure 6.17: Calibration of h based on the experimental embedment curves [85] in the direction parallel to the grain.



(a) 12 mm dowel diameter



(b) 16 mm dowel diameter

Figure 6.18: Calibration of h based on the experimental embedment curves [85] in the direction perpendicular to the grain.

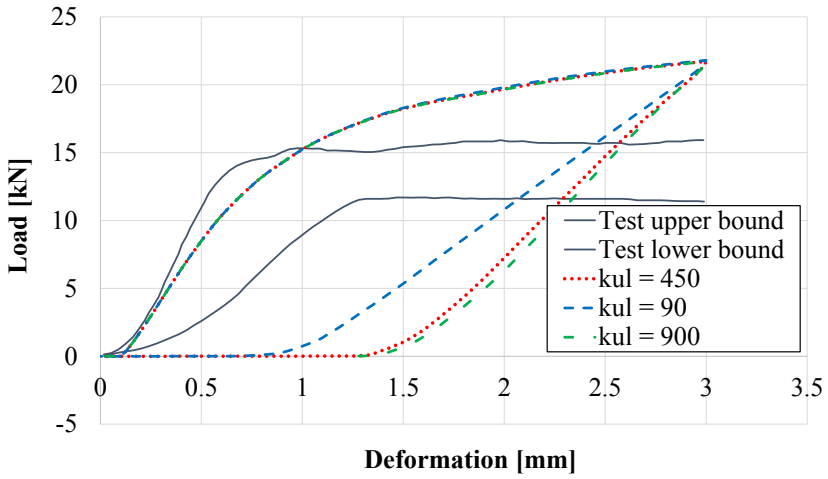
Figs. 6.19 and 6.20 show the numerical curves corresponding to each of the three values of k_{UL} jointly with the experimental upper and lower bounds for both bolts diameters in the directions parallel and perpendicular to the grain, respectively. In the direction parallel to the grain, the increment of the unloading stiffness when passing from $k_{UL} =$ 90 MPa/mm to $k_{UL} = 450$ MPa/mm is significant. However, almost no difference is encountered between the unloading branches corresponding to $k_{UL} = 450$ MPa/mm and $k_{UL} = 900$ MPa/mm. Therefore, it is concluded that a value of $k_{UL} = 450$ MPa/mm (equivalent to five times the value of k_C) is high enough to obtain a steep unloading branch characteristic of pinching systems. On the other hand, in the direction perpendicular to the grain no substantial difference is appreciated among the three curves. Thus, the influence of this parameter is very limited for this loading direction.

Interface shear stiffness

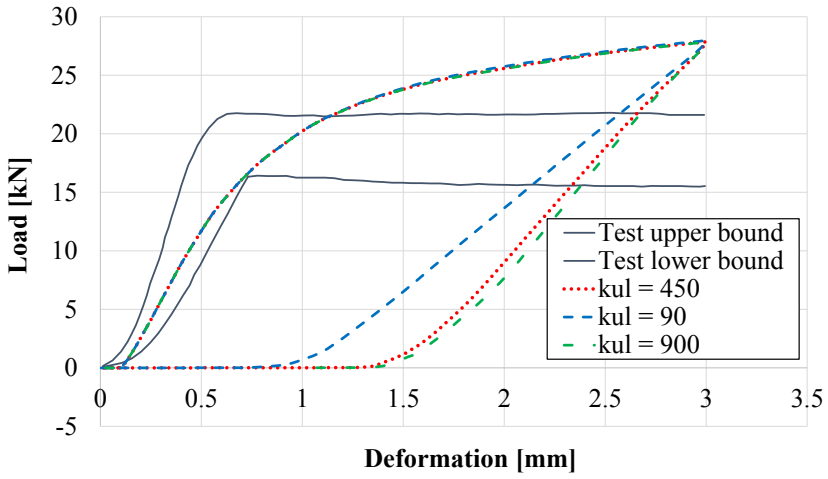
The interface shear stiffness is the last parameter to be calibrated. It is known that for dowelled connections a higher timber-bolt friction coefficient results in a higher connection capacity [80, 38, 189]. Therefore, based on the friction model formulation developed in Section 6.2.2, it can be concluded that the interface shear stiffness corresponding to the "stick" state also influences the capacity of the connection.

Up to now, the calibrated embedment curves were obtained using the default interface shear stiffness value of $k_S = 10$ MPa/mm. However, a higher capacity than the experimental upper bound curve in the direction parallel to the grain has been numerically obtained in all cases. Conversely, in the direction perpendicular to the grain the numerical predicted capacity is within the experimental bounds. Therefore, in order to obtain a better numerical prediction of the connection embedding strength in the direction parallel to the grain, a second set of analysis using a reduced value of the interface shear stiffness equal to $k_S = 1$ MPa/mm is carried out.

The numerical embedment curves for $k_S = 10$ MPa/mm and $k_S = 1$ MPa/mm are plotted and compared against the experimental lower and upper bounds in Figs. 6.21 and 6.22. In the direction parallel to the grain (see Fig. 6.21), a better prediction of the embedding capacity is achieved when $k_S = 1$ MPa/mm is used. What is more, for large deformation levels, the numerical curve matches well with the experimental upper bound curve. On the contrary, Fig. 6.22 demonstrates the variation of k_S has a minor influence on the load-deformation response in the direction perpendicular to the grain.

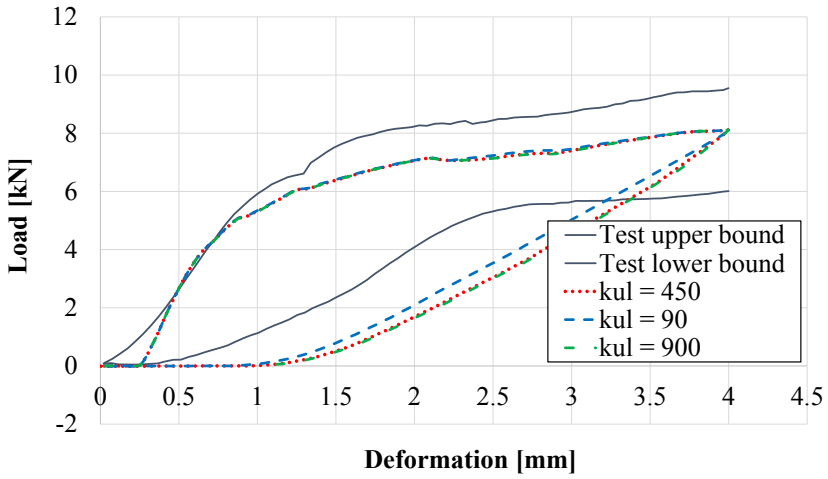


(a) 12 mm dowel diameter

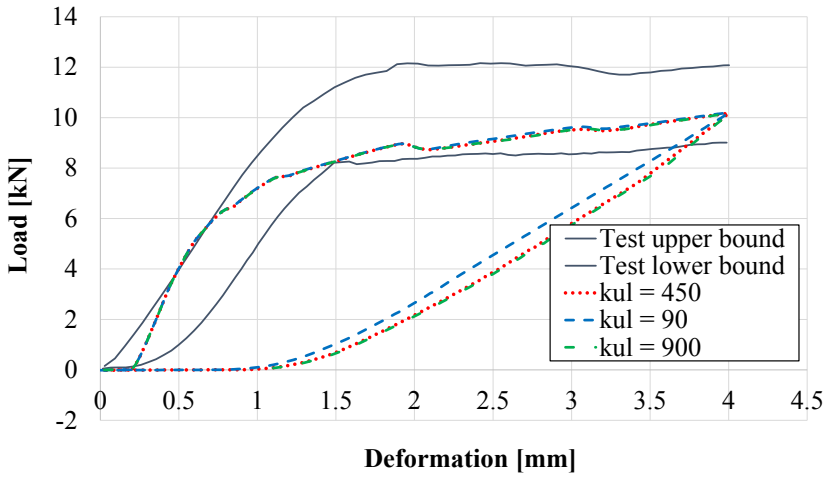


(b) 16 mm dowel diameter

Figure 6.19: Calibration of k_{UL} based on the experimental embedment curves [85] in the direction parallel to the grain.

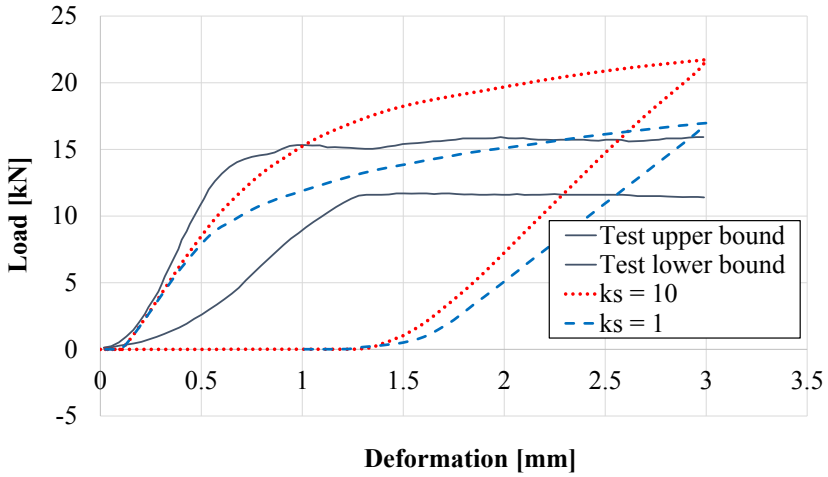


(a) 12 mm dowel diameter

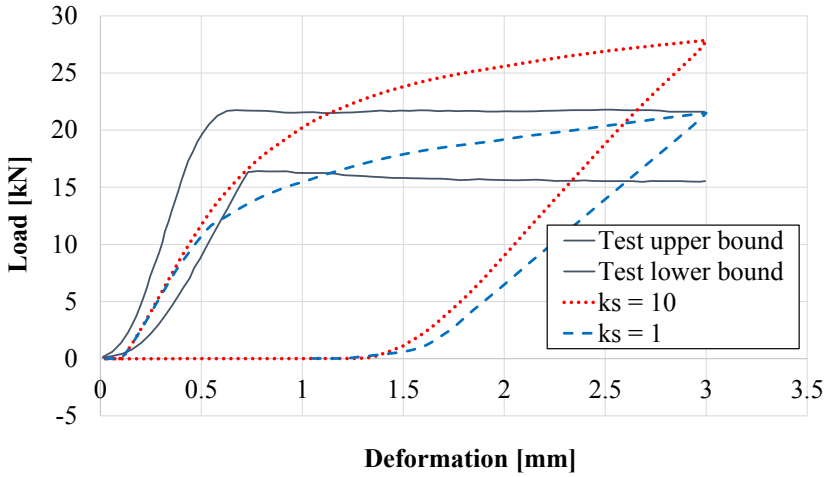


(b) 16 mm dowel diameter

Figure 6.20: Calibration of k_{UL} based on the experimental embedment curves [85] in the direction perpendicular to the grain.



(a) 12 mm dowel diameter



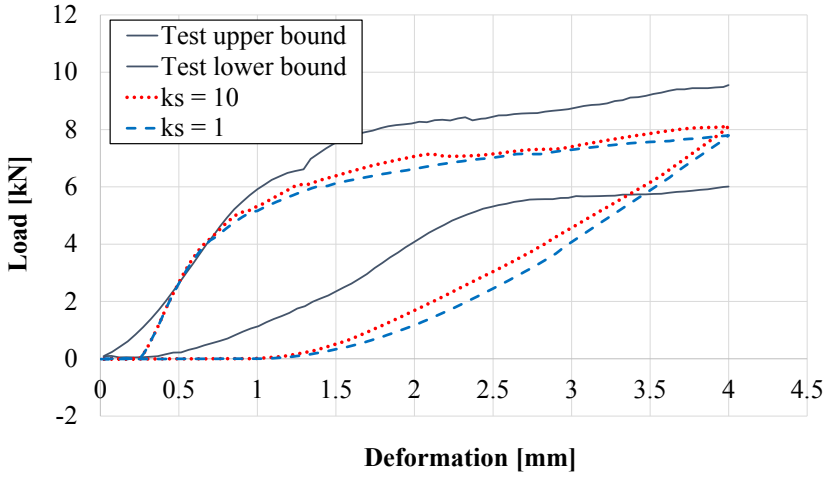
(b) 16 mm dowel diameter

Figure 6.21: Calibration of k_S based on the experimental embedment curves [85] in the direction parallel to the grain.

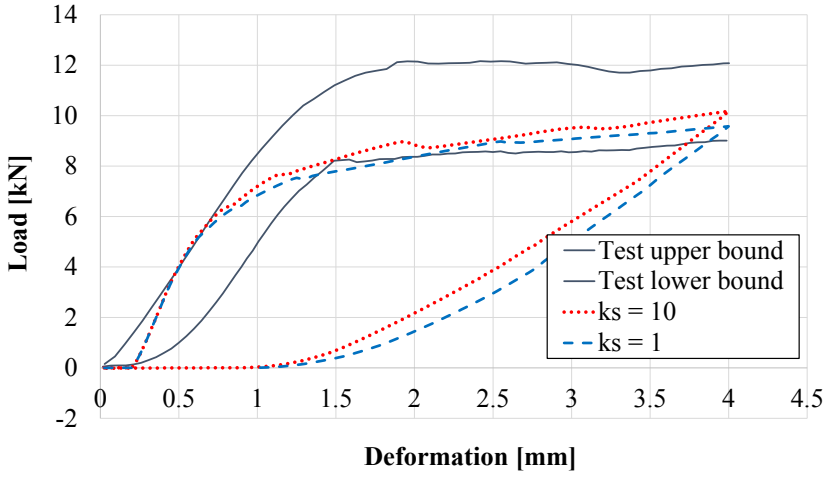
This is good for calibration purposes since the numerical response in this direction shows already a good agreement with the experimental curves. In summary, $k_S = 1$ MPa/mm is kept as the final calibrated value of the interface shear stiffness.

Summary of the calibrated parameter values

Fig. 6.23 shows the numerical curves obtained with the final values of the five calibrated parameters, compared against the upper and lower bound experimental curves. The calibrated parameter values are: $k_C = 90$ MPa/mm, $h = 10$ and $\beta = 0.995$, $k_{UL} = 450$ MPa/mm, $k_S = 1$ MPa/mm. A good numerical fitting of the experimental

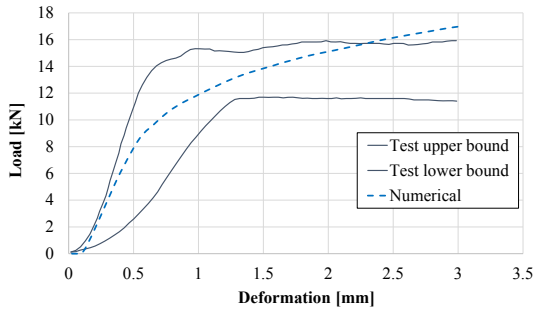


(a) 12 mm dowel diameter

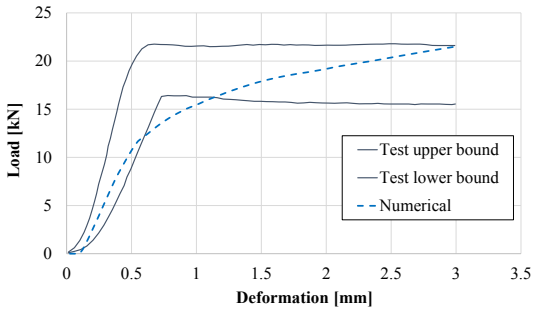


(b) 16 mm dowel diameter

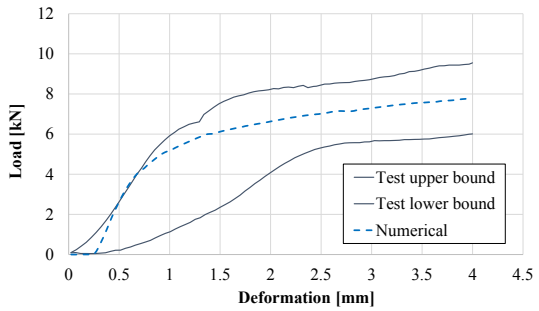
Figure 6.22: Calibration of k_S based on the experimental embedment curves [85] in the direction perpendicular to the grain.



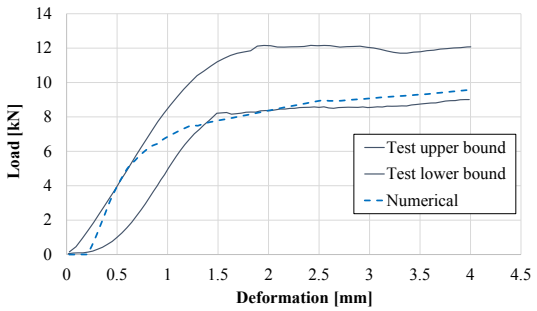
(a) 12 mm dowel diameter paralell to grain



(b) 16 mm dowel diameter paralell to grain



(c) 12 mm dowel diameter perpendicular to grain



(d) 16 mm dowel diameter perpendicular to grain

Figure 6.23: Numerical calibrated against experimental [85] embedment curves.

embedment curves is appreciated for both 12 mm and 16 mm dowel diameter specimens in both parallel and perpendicular loading directions. Therefore, the calibration process of the five parameters summarized in Table 6.7 is considered successful, and and the models are ready to perform the finite element simulation that follows in the next section.

6.5 Analysis of numerical results and comparison against experimental data

In this section, the efficiency of the modelling strategies developed in chapters 3, 4 and 6 is evaluated against the results of monotonic and cyclic tests in dowelled timber beam-to-steel column connections. The monotonic tests results come from [87] and are presented first, followed by a comparison against the cyclic test performed as part of this thesis and presented in Chapter 5.

Table 6.7: Calibration parameters values

	k_C MPa/mm	β	h Mpa	k_{UL} MPa/mm	k_S MPa/mm
Initial	250	0.90	40.9	450	10
1^{st} Variation	100	0.95	13.1	90	1
2^{nd} Variation	90	0.995	–	900	–
Final	**90**	**0.995**	**40.9**	**450**	**1**

6.5.1 Monotonic loading

The numerical moment-rotation response obtained with the FE model described in Section 6.3 is compared against:

- The positive and negative stabilized envelope curves derived from the experimental hysteretic response shown previously in Fig. 5.14.
- The experimental monotonic response obtained by Karagiannis [87] for similar specimens (available for specimens S1 and S2 only).

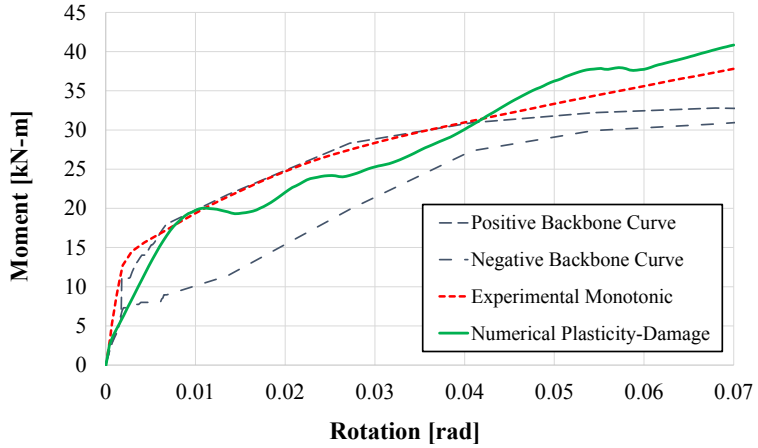
As described in Section 6.3.1, an initial prestressing force simulating the bolts tightening torque was applied first. The model was then subjected to the action of self-weight gravity loads, before the application of vertical displacements of monotonically increasing magnitudes, as indicated by the red arrow in Fig. 6.4. 350 load steps of 0.25 mm each made a total maximum applied displacement of 87.5 mm, which is approximately equivalent to a total joint rotation of 70 mrad. The monotonic global and local results obtained for the hybrid timber beam-to-steel column dowelled connections are presented and analysed below.

Global response

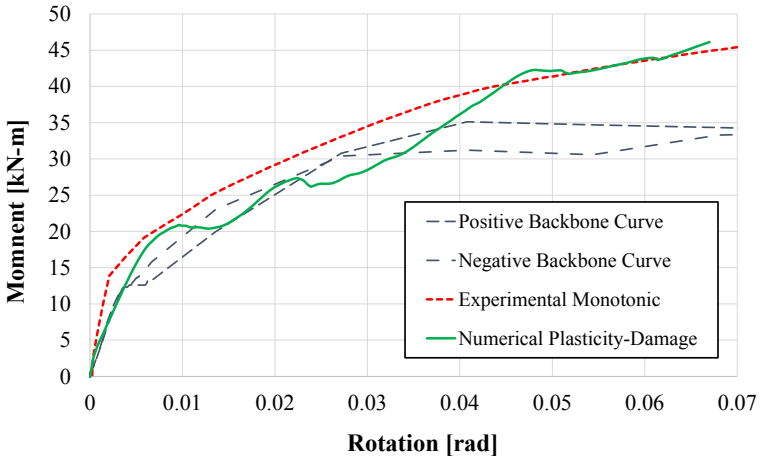
Fig. 6.24 shows the numerical and experimental monotonic moment-rotation curves of the three specimens under study: S1, S2 and S3. Both the positive and negative sides of the stabilized envelope curves previously presented in Fig. 5.14 are plotted here, both in the positive quadrant. The characteristics of the stabilized envelope curves were discussed in detail in Section 5.3.4. On the other hand, Karagiannis [87] carried out an experimental study of two specimens similar to S1 and S2 under the action of monotonic loads. The corresponding curves were also plotted in Figs. 6.24a and 6.24b for reference. Lastly, Fig. 6.24 presents the numerical curves obtained by means of the FE model described in Section 6.3. The plasticity-damage wood constitutive model formulated in Chapter 3 and the timber-steel contact model developed in Section 6.2 were employed.

It is clear from Fig. 6.24 that the numerical results are in good agreement with the experiments. For specimens S1 and S2, where monotonic experimental curves are available, a better correspondence can be noticed among these monotonic curves and the stabilized envelope curves (positive) up to a rotation of 40 mrad. For larger deformation levels, the strength increment of the monotonic curves continues, while in the case of the stabilized envelope curves, the maximum strength is reached followed by a plateau. Naturally, under the action of monotonic loads, the numerical curves resemble the experimental curves obtained by Karagiannis [87]. A precise prediction of the moment connection strength is obtained even for large deformation levels higher than 50 mrad. For specimen S3, a good agreement is also found among the monotonic numerical curve and the experimental positive stabilized envelope curve up to a joint rotation of 40 mrad. As in specimens S1 and S2, for greater deformation levels the capacity predicted by the monotonic numerical curve is higher than that of the cyclic stabilized envelope. This is expected given the significantly higher damage accumulation experienced during cyclic action.

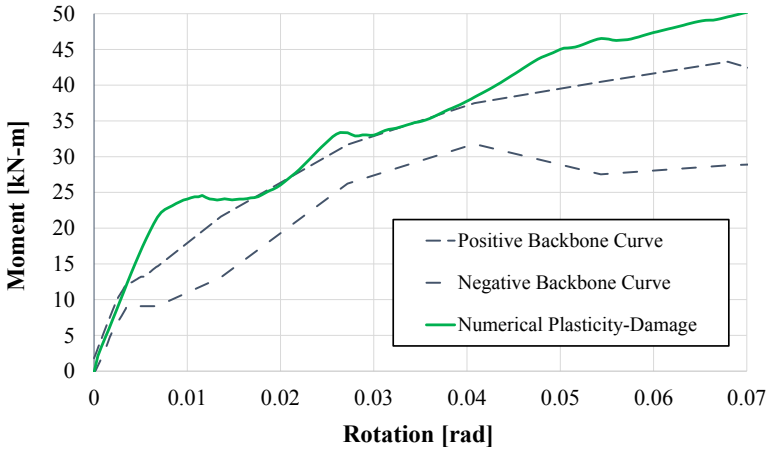
The three monotonic numerical curves reproduced in Fig. 6.24 show flat zones where the force remains constant for increasing ranges of deformation. These plateauing zones are a consequence of timber local failure around the bolt holes followed by slip between the timber-steel contact surfaces. Therefore, this phenomena is simulated by both, the plasticity-damage wood constitutive model and the timber-steel contact model. These graphs demonstrate that it is possible to simulate the behaviour of this type of highly non-linear structural components and reproduce their experimentally observed interactions.



(a) Specimen S1-12D-12A



(b) Specimen S2-12D-15A



(c) Specimen S3-16D-15A

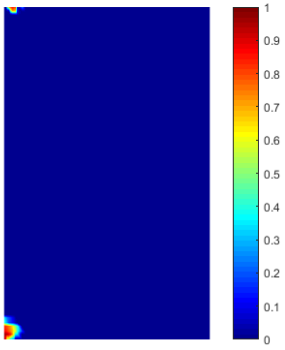
Figure 6.24: Comparison between numerical and experimental monotonic [87] and cyclic stabilized envelope curves.

Local response

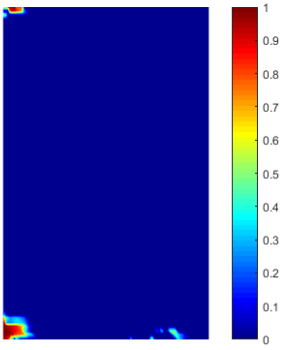
The local response of the timber beam and the steel components in terms of damage accumulation and plastic strains is discussed below. With respect to the timber beam, the analysis is focused on the top and lateral faces, in the close proximity to the column. Fig. 6.25 shows the tensile damage variable contour plot in the lateral face of the timber beam for the three specimens and for two levels of deformation, namely, 40 mrad and 70 mrad. Fig. 6.25 indicates that the zone with the highest potential for crack formation is around the bottom left corner, where this part of the timber beam is pressed against the steel column, while it separates from the bottom steel angle. This mechanism produces high tensile stresses in the direction perpendicular to the grain that eventually lead to the development of cracks. Furthermore, two other potential cracking zones are also predicted by the numerical results for specimens S2 and S3. The first of them is located at the bottom of the timber beam, around the zone in contact with the horizontal leg of the angle. The second zone of potential cracking is located at the top, near to the upper left corner (see Figs. 6.25d and 6.25f). These two cracking zones are the result of transversal expansion caused by high compressive stresses in the direction perpendicular to the grain. The horizontal legs of the top and bottom steel angles exert pressure on the timber beam top and bottom fibres, and as a consequence, the splitting tensile stresses generated in the transversal direction produce timber cracking. This type of cracking, however, cannot be easily seen from the outside.

Fig. 6.26 presents the compressive damage contour for the same timber beam zone selected in Fig. 6.25. This plot shows the crushing zones in the lateral face of the timber beam generated by the action of the high compressive stresses mentioned in the previous paragraph. Therefore, these zones are located in the same positions of the cracking zones produced by lateral expansion. The extent of crushing due to compressive damage in specimen S3 is considerably higher than in the other two specimens (See Figs. 6.26e and 6.26f). Moreover, the compressive damage growth from a joint rotation of 40 mrad to 70 mrad is substantial, particularly in specimens S2 and S3.

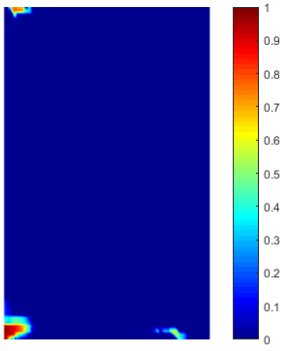
On the other hand, Fig. 6.27 shows the location and magnitude of the compressive plastic strains in the vertical direction, perpendicular to the timber grain. Large plastic strains higher than 1% can be appreciated in the same zones of the timber beam where crushing occurs (see Fig. 6.26). The extent of the area where the greatest plastic strains are concentrated in specimens S2 and S3 is considerably larger than in specimen S1. This means that for this type of connections, the angle thickness has an important influence on



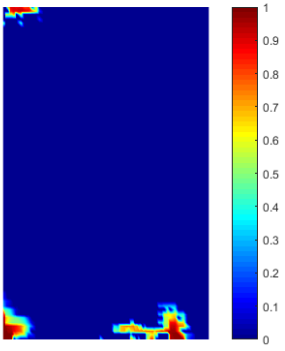
(a) Specimen S1-12D-12A - 40 mrad



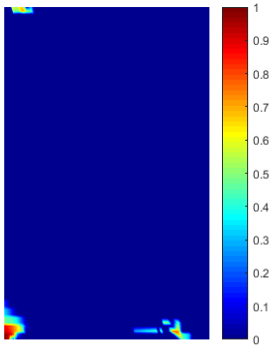
(b) Specimen S1-12D-12A - 70 mrad



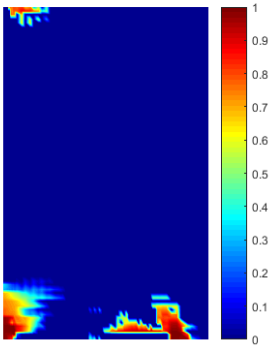
(c) Specimen S2-12D-15A - 40 mrad



(d) Specimen S2-12D-15A - 70 mrad

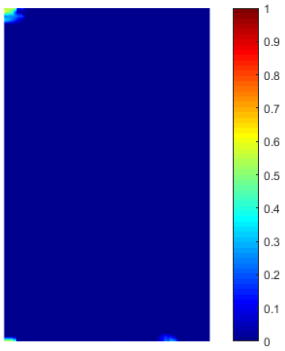


(e) Specimen S3-16D-15A - 40 mrad

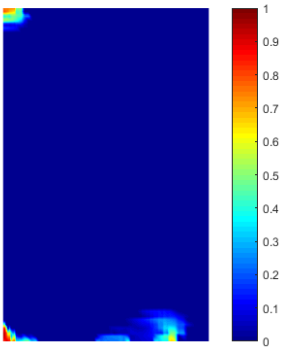


(f) Specimen S3-16D-15A - 70 mrad

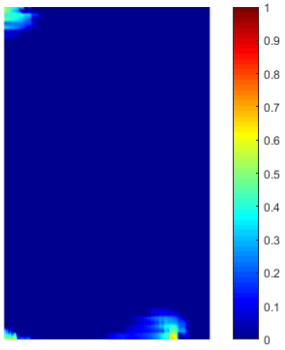
Figure 6.25: Timber beam lateral face tensile damage contour plot under monotonic load.



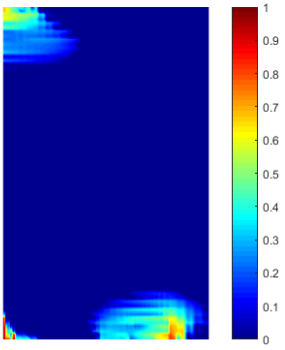
(a) Specimen S1-12D-12A - 40 mrad



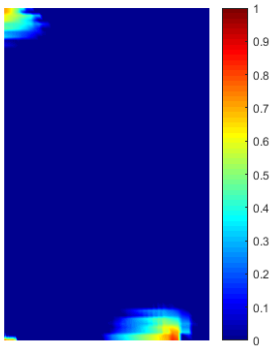
(b) Specimen S1-12D-12A - 70 mrad



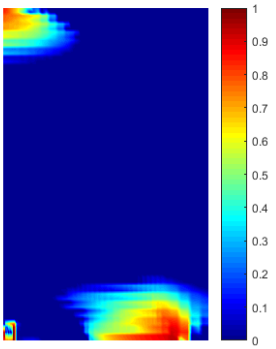
(c) Specimen S2-12D-15A - 40 mrad



(d) Specimen S2-12D-15A - 70 mrad



(e) Specimen S3-16D-15A - 40 mrad



(f) Specimen S3-16D-15A - 70 mrad

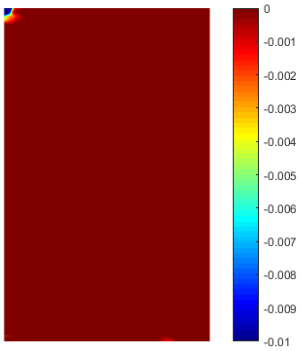
Figure 6.26: Timber beam lateral face compressive damage contour plot under monotonic load.

the amount of plasticity generated by compressive stresses in the direction perpendicular to the grain.

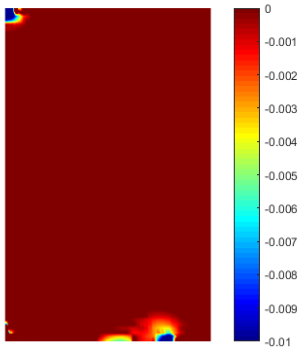
Fig. 6.28 shows the tensile damage zones and their corresponding intensities in the beam's top face. More precisely, Fig. 6.28 shows the rectangular area with two bolt holes corresponding to half the timber beam top face that is covered by the steel angle horizontal leg. Symmetry was assumed, and thus, only one half of the specimen including two bolt holes was modelled (see Section 6.3.1). For a joint rotation of 40 mrad, the cracking zone is mainly located around the bolt holes. When the deformation level increases up to a joint rotation of 70 mrad, the cracking zone is extended. Fig. 6.28b shows that in the case of specimen S1, the zone with the highest tensile damage, besides the area around the bolts, is the transversal strip near to the beam-column interface. In this region, high compressive stresses are generated due to the interaction between the timber beam and the steel angles. Therefore, it can be concluded that in this zone cracking is also produced as a consequence of lateral expansion. On the other hand, Fig. 6.28f shows that for specimen S3 the extended tensile damage zone is not located in the transversal strip previously identified for specimen S1, but in the larger area limited by the bolt holes on the right and the beam-angle contact zone on the left. Finally, specimen S2 (Fig. 6.28d) can be considered as an intermediate case between S1 and S3. It is important to mention that, in addition to tensile stresses in the direction perpendicular to the grain, the generalized cracking zones predicted for specimens S2 and S3 are also the consequence of shear stresses in the direction parallel to the grain. Shear local failure typically occurs behind the bolts rows, as depicted in Figs. 6.28d and 6.28f. Similarly, Fig. 6.29 shows the crushing zones of the timber beam top face in terms of the compressive damage variable. The crushing zones are consistently located around the bolts and along the transversal strip zone where the steel angle and the wood are pressed one against the other. It is clear from Fig. 6.29 that the damaged area due to crushing expands in direct proportion to the increment of the joint rotation magnitude and the size of the steel components.

Finally, the concentration zones of compressive plastic strains in the longitudinal direction (parallel to the grain) is shown in Fig. 6.30. As expected, the zones of large plastic strains higher than 1% coincide with the crushing zones around the bolt holes. Since the compressive damage transversal strip zones shown in Fig. 6.29 are not present in Fig. 6.30, it can be concluded that they result from contact compressive stresses exerted by the angles in the direction perpendicular to the grain.

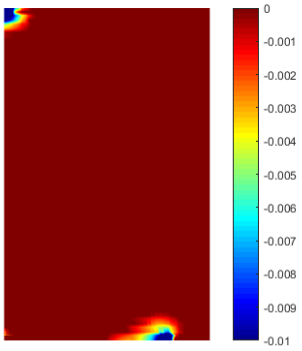
It should be recalled that the only difference among the three specimens (S1, S2 and



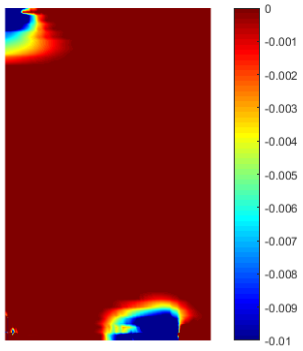
(a) Specimen S1-12D-12A - 40 mrad



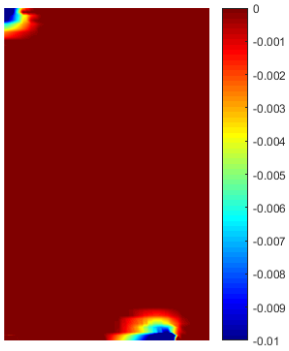
(b) Specimen S1-12D-12A - 70 mrad



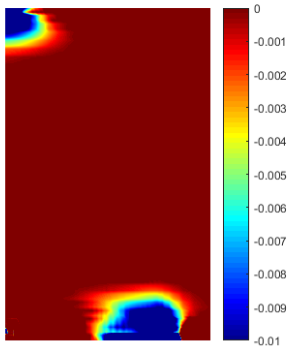
(c) Specimen S2-12D-15A - 40 mrad



(d) Specimen S2-12D-15A - 70 mrad

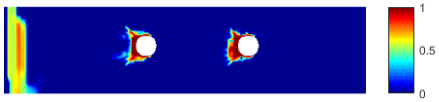


(e) Specimen S3-16D-15A - 40 mrad

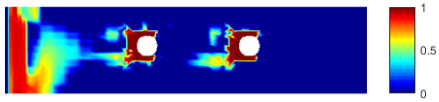


(f) Specimen S3-16D-15A - 70 mrad

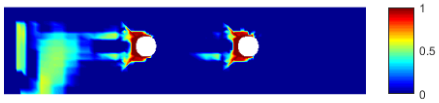
Figure 6.27: Timber beam lateral face compressive plastic strain in the vertical direction (perpendicular to the grain) contour plot under monotonic load.



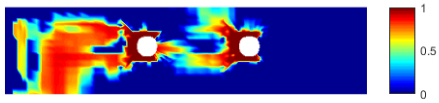
(a) Specimen S1-12D-12A - 40 mrad



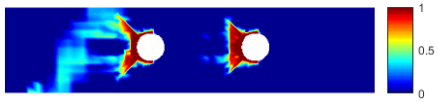
(b) Specimen S1-12D-12A - 70 mrad



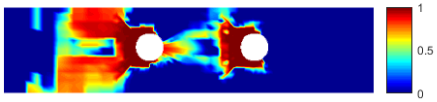
(c) Specimen S2-12D-15A - 40 mrad



(d) Specimen S2-12D-15A - 70 mrad

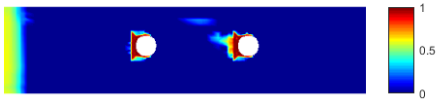


(e) Specimen S3-16D-15A - 40 mrad

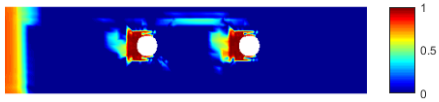


(f) Specimen S3-16D-15A - 70 mrad

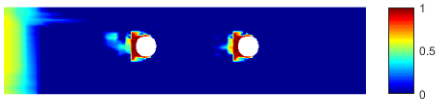
Figure 6.28: Timber beam top face tensile damage contour plot under monotonic load.



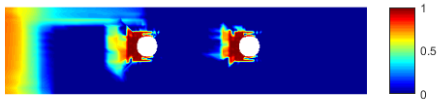
(a) Specimen S1-12D-12A - 40 mrad



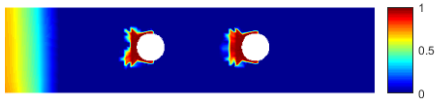
(b) Specimen S1-12D-12A - 70 mrad



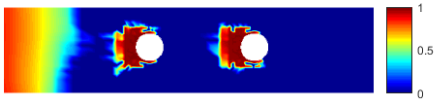
(c) Specimen S2-12D-15A - 40 mrad



(d) Specimen S2-12D-15A - 70 mrad



(e) Specimen S3-16D-15A - 40 mrad

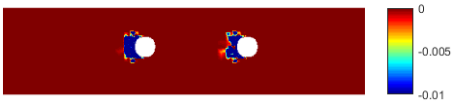


(f) Specimen S3-16D-15A - 70 mrad

Figure 6.29: Timber beam top face compressive damage contour plot under monotonic load.



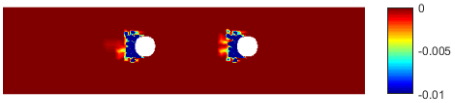
(a) Specimen S1-12D-12A - 40 mrad



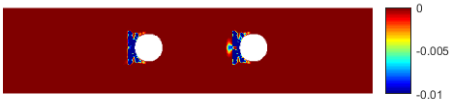
(b) Specimen S1-12D-12A - 70 mrad



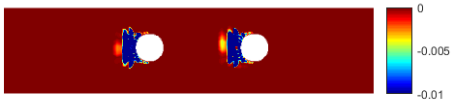
(c) Specimen S2-12D-15A - 40 mrad



(d) Specimen S2-12D-15A - 70 mrad



(e) Specimen S3-16D-15A - 40 mrad



(f) Specimen S3-16D-15A - 70 mrad

Figure 6.30: Timber beam top face plastic strain in the longitudinal (parallel to the grain) contour plot under monotonic load.

S3) resides in the combination of bolts and angles sizes employed by them. To analyze their effects, Figs. 6.31 and 6.32 show the magnitude and location of tensile principal plastic strains in the long bolts and the top angle, respectively. The same two stages of global joint rotation previously used are represented in both figures. Fig. 6.31 shows that the application of a downwards displacement produces a plastic hinge in the upper fourth of the bolt length. Specimens S1 and S2 have the smaller bolt diameter of 12 mm, while specimen S3 uses a 16 mm bolt diameter. As expected, specimens S1 and S2 experience the highest bolt tensile plastic strain magnitudes of 0.5% (see Figs. 6.31a and 6.31c) and 1% (see Figs. 6.31b and 6.31d), associated to joint rotations of 40 mrad and 70 mrad, respectively. On the contrary, the larger bolts of specimen S3 experience negligible levels of plasticity (see Figs. 6.31e and 6.31f). It is worth noting that in specimen S2 high tensile plastic strains are also concentrated in the top end of the long bolts (see Fig. 6.31d), more precisely, in the part which passes through the holes of the top steel angle horizontal leg. This is clearly a consequence of the particular characteristic of specimen S2, which incorporates a thick steel angle (15 mm) in combination with a small bolt diameter (12 mm).

Similarly, Fig. 6.32 shows that for the three specimens the tensile plastic strains of

the steel angle are concentrated in the horizontal leg, near to the intersection zone with the vertical leg. The thinner angle of 12 mm which belongs to specimen S1 experiences high tensile principal plastic strains magnitudes up to 2% for a joint rotation of 70 mrad. These strain levels are equivalent to twice the plastic strain magnitude found in the long bolts (see Fig. 6.31b). Moreover, the larger deformation levels incurred by the angles of specimen S1 produce a concentration of high stresses in the vertical leg, around the hole of the short bolt that fastens the angle to the column. Eventually, high tensile plastic strains are also developed in this zone, as shown in Fig. 6.32b. Lastly, specimens S2 and S3 have thicker steel angles of 15 mm. Their maximum tensile plastic strains are approximately 1% and 0.5%, respectively. Even though the plastic strain magnitudes of specimens S2 and S3 are similar, it can be concluded based on the observations reported in this section, that the nonlinear response of specimen S3 is defined by wood local failure (e.g. cracking, plasticity, crushing), while in the case of specimen S2 the contribution of the steel components plasticity is more influential.

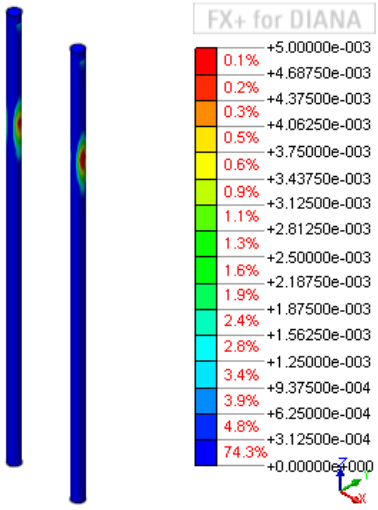
6.5.2 Cyclic loading

In this section the performance of the proposed numerical model is evaluated under cyclic loading conditions. The same cyclic loading protocol used in the laboratory test (see Fig. 5.5) was applied. Furthermore, the definition of the displacement-control load in the FE model is as described in Section 6.5.1 for monotonic loading. Different load step sizes ranging between 0.0625 mm (for the first shortest cyclic amplitude) and 0.5 mm (for the last longest cyclic amplitudes) were employed through all the analysis.

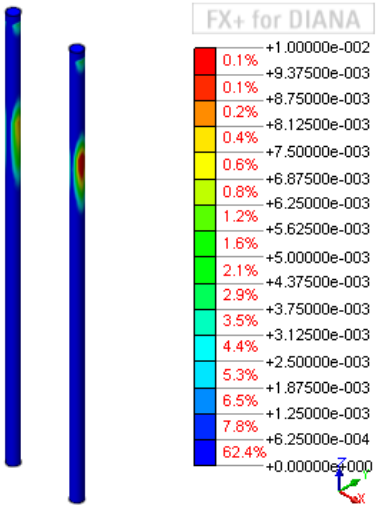
The local response of the timber beam and steel components was obtained from the FE analysis output, and reported for the two maximum joint rotation cyclic amplitudes (40 mrad and 54 mrad) in both positive and negative directions. Finally, Digital Image Correlation (DIC) technique was employed to obtain the strain fields on the timber beam for specimen S3. This information was used to assess the quality of the quantitative and qualitative results provided by the numerical model with respect to the experimental response.

Global response

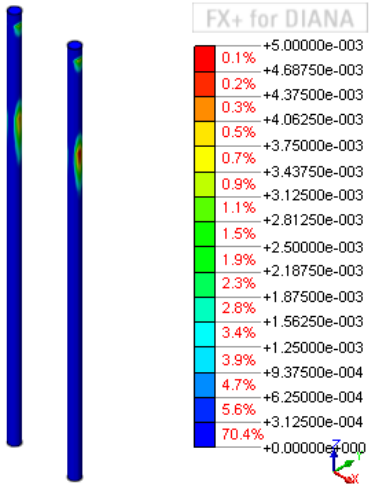
Fig. 6.33 shows both the experimental and numerical hysteretic moment-rotation responses for specimens S1, S2 and S3. A good agreement between numerical and ex-



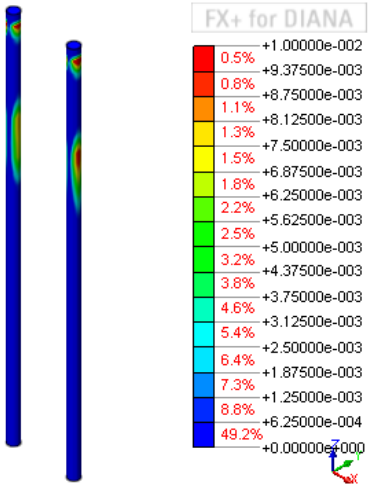
(a) Specimen S1-12D-12A - 40 mrad



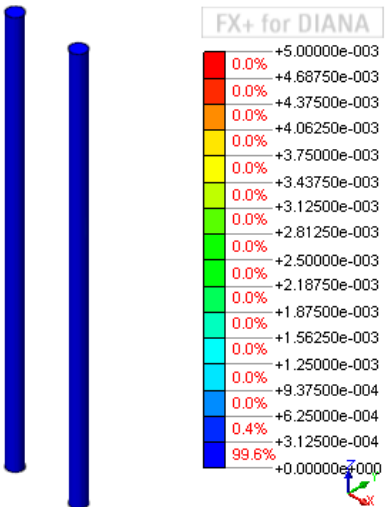
(b) Specimen S1-12D-12A - 70 mrad



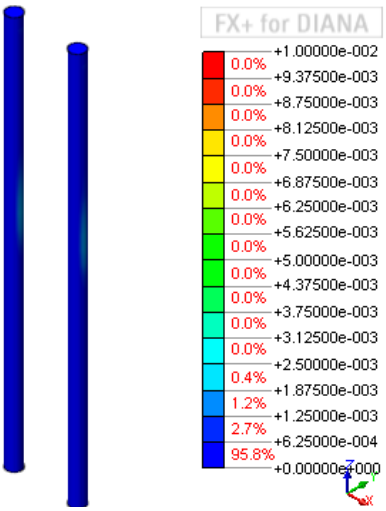
(c) Specimen S2-12D-15A - 40 mrad



(d) Specimen S2-12D-15A - 70 mrad

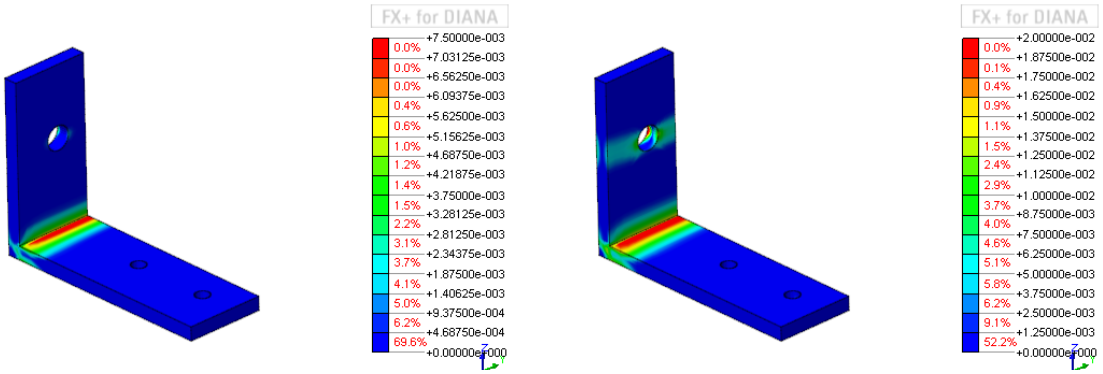


(e) Specimen S3-16D-15A - 40 mrad



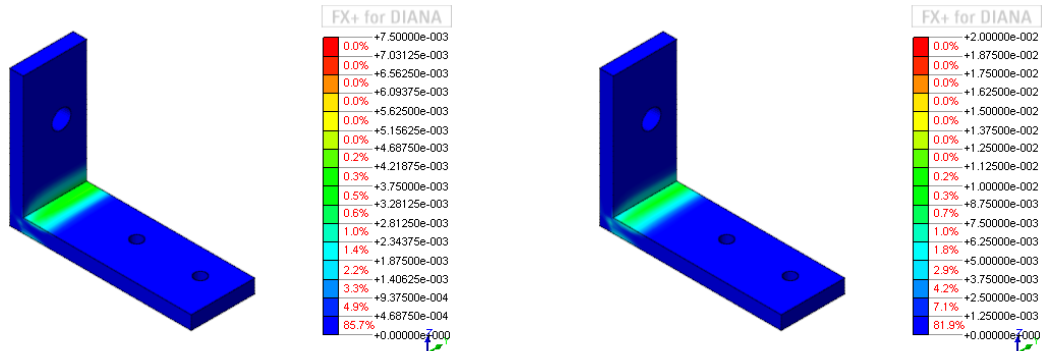
(f) Specimen S3-16D-15A - 70 mrad

Figure 6.31: Steel long bolt principal tensile plastic strain contour plot under monotonic load.



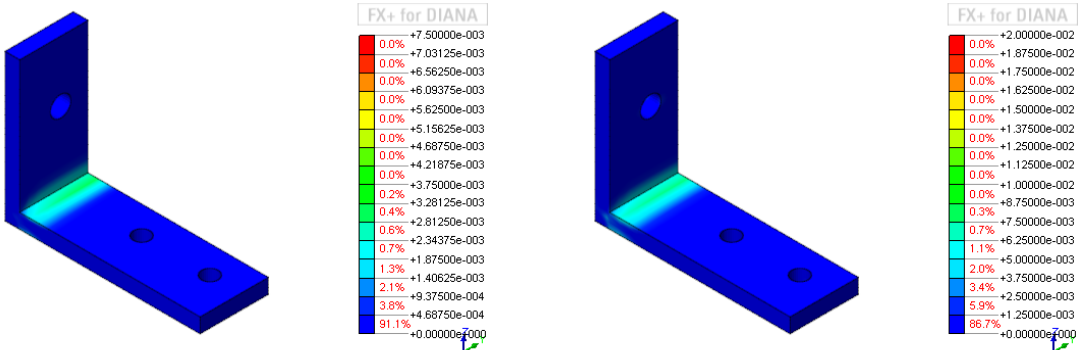
(a) Specimen S1-12D-12A - 40 mrad

(b) Specimen S1-12D-12A - 70 mrad



(c) Specimen S2-12D-15A - 40 mrad

(d) Specimen S2-12D-15A - 70 mrad



(e) Specimen S3-16D-15A - 40 mrad

(f) Specimen S3-16D-15A - 70 mrad

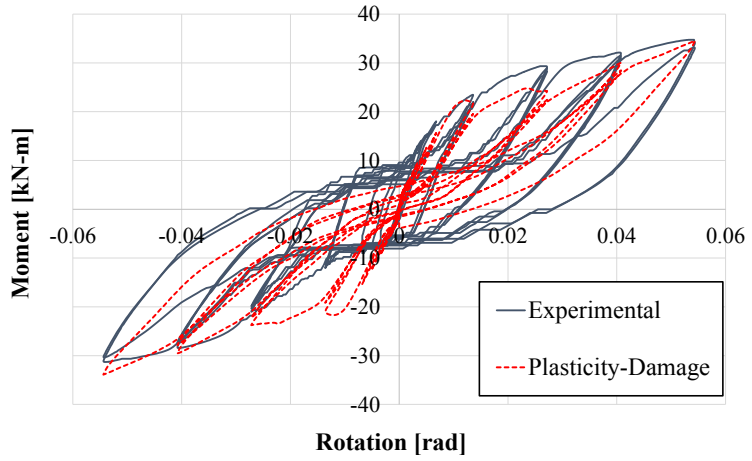
Figure 6.32: Top steel angle principal tensile plastic strain contour plot under monotonic load.

perimental results can be appreciated for the three specimens. In general, the maximum connection capacity and stiffness degradation for each cyclic loop are well captured. Nevertheless, although the experimental pinching behaviour of the connection is clearly reproduced by the numerical model, the permanent residual deformations are underestimated. Considering that the greatest permanent residual deformation contribution is provided by the steel components (angles and bolts), the employment of a more elaborated steel constitutive model could significantly improve the precision of the numerical results. However, the ability of the proposed wood constitutive model to accurately predict the maximum capacity of such a complex timber beam-to-steel column connection for different levels of deformation is confirmed.

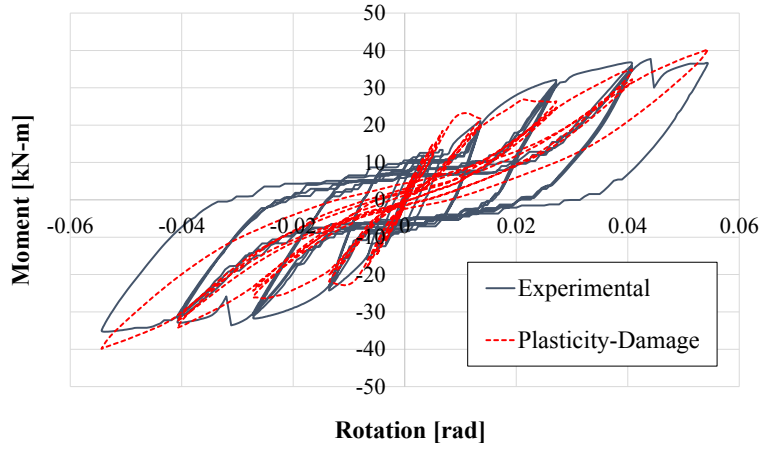
Fig. 6.33 also shows that the experimental hysteresis is not symmetric. However, despite not being identical, the shapes of both negative and positive branches of the numerical hysteresis are similar to each other. The main reason for the asymmetry observed in experimental hysteresis is the lack of homogeneity in the timber specimens. This is exacerbated by the weaker zones that are randomly distributed within the wood matrix, and therefore, not possible to be explicitly included in the idealized model. This asymmetry is also the expression of an asymmetric load where one side experiences always the first excursions at a given deformation level leading to an unbalance of the damage concentration. It is important to note that the purpose of the model presented herein is to offer an accurate numerical tool for the assessment of timber structures maximum capacity under cyclic loads at large deformation levels. Therefore, the evaluation of the influence of timber material heterogeneity or knots on the global cyclic structural response is beyond the scope of this thesis.

Local response

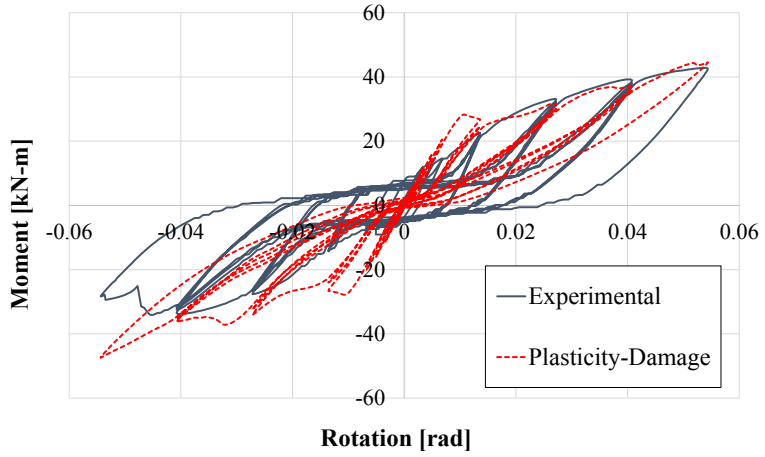
Fig. 6.34 shows the tensile damage contour plots corresponding to the lateral face of the timber beam for a joint rotation of ±54 mrad. It can be appreciated from this figure that the potential cracking zones (where the tensile damage variable adopt high values up to 1) are concentrated in the left top and left bottom corners of the beam lateral face in all three specimens. Two additional smaller cracking zones located near the right top and right bottom corners are also present in specimens S2 and S3 (see Figs. 6.34d and 6.34f). Moreover, considering that the cyclic load is first applied downwards, the damaged areas corresponding to positive (hogging) joint rotations (on the right-hand column) in Fig. 6.34 are larger than their negative (sagging) rotation counterparts (on the left-hand



(a) Specimen S1-12D-12A



(b) Specimen S2-12D-15A



(c) Specimen S3-16D-15A

Figure 6.33: Comparison between numerical and experimental hysteretic curves.

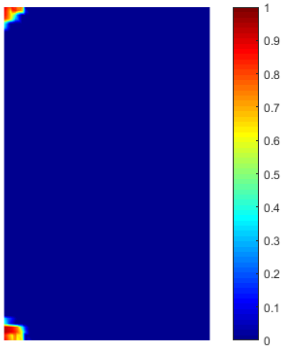
column). Finally, based on the extent and intensities of tensile damage, larger and more cracks are expected to occur in specimen S3 than in the other two.

Fig. 6.35 shows the compressive damage contour plots corresponding to the lateral face of the timber beam for a joint rotation of ±54 mrad. Compressive damage in specimen S1 is minor. Its potential crushing zones are small and the highest values of the compressive damage variable do not exceed 0.6 (see Fig. 6.35b). By contrast, four large crushing zones (one per each corner) with high damage intensities are shown in Fig. 6.35 for specimens S2 and S3. Therefore, it can be concluded that the locations of both critical tensile and compressive damaged zones in specimens S2 and S3 are defined by the interaction between the timber beam and the steel angles. All the observations and conclusions above, based on the analysis of Figs. 6.34f and 6.35f, were corroborated by the experimental results previously presented in Chapter 5.

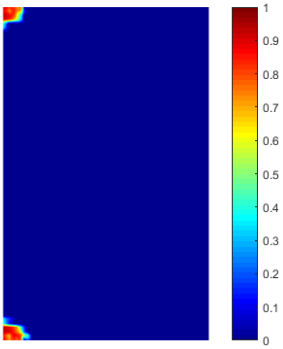
Fig. 6.36 shows the tensile damage variable contour plot in the top (sagging) and bottom (hogging) faces of the timber beam for a joint rotation amplitude of 40 mrad. Due to symmetry conditions, only one half of the timber beam including two bolt holes (instead of four) is presented. It can be seen that damage due to tensile stresses is concentrated around the bolt holes and in the transversal strip where the timber beam interacts with the column and the angle. Fig. 6.36f shows that in the bottom face of specimen S3, tensile damage reaches the zone behind the bolts row and the strip in contact with the tip of the seat angle horizontal leg.

Fig. 6.37 displays the same information provided by Fig. 6.36 for a larger joint rotation amplitude of 54 mrad. For specimen S1, tensile damage growths in the zone behind the bolts row. For specimen S3, tensile damage is generalized almost through all the area covered but the steel angle horizontal leg. Nonetheless, the higher tensile damage growth occurs along the bolts row and in the transversal strips defined by the interaction of the timber beam with the horizontal leg of the steel angle. It is also important to mention that Figs. 6.36 and 6.37 show that for all the three specimens tensile damage in the timber beam bottom face (right column) is more widespread than in the top face (left column). This might be related to the to the fact that the reversed cyclic load is applied first in the negative direction. Thus, the bottom face shows the additional damage accumulated along the loading path from the negative (sagging) to the positive (hogging) cyclic amplitudes.

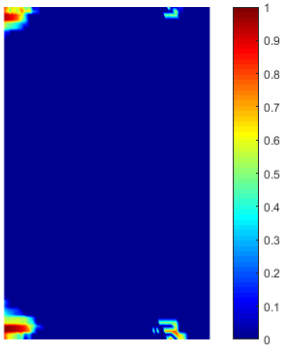
In the same way, Figs. 6.38 and 6.39 show the corresponding compressive damage



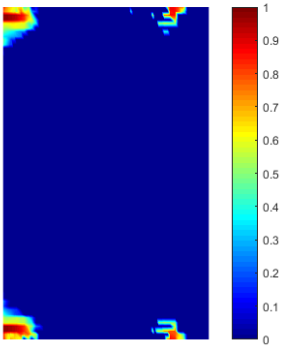
(a) Specimen S1-12D-12A - Negative Rotation



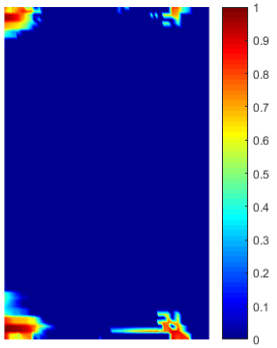
(b) Specimen S1-12D-12A - Positive Rotation



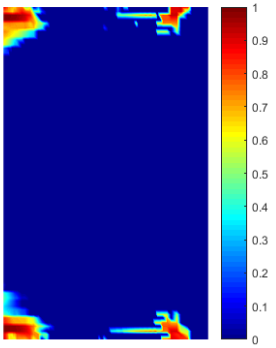
(c) Specimen S2-12D-15A - Negative Rotation



(d) Specimen S2-12D-15A - Positive Rotation

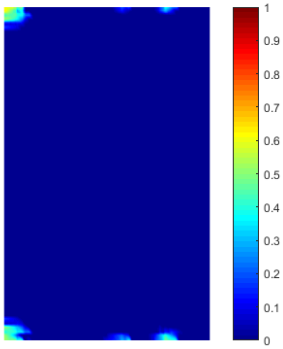


(e) Specimen S3-16D-15A - Negative Rotation

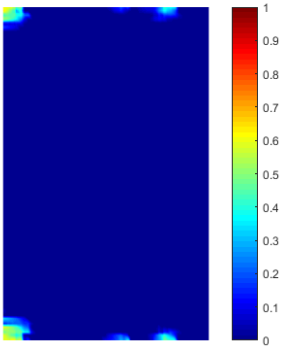


(f) Specimen S3-16D-15A - Positive Rotation

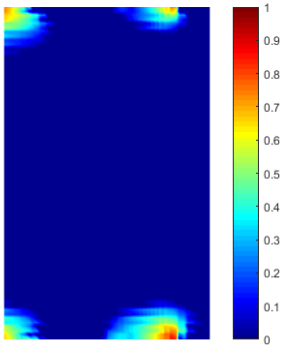
Figure 6.34: Timber beam lateral face tensile damage contour plot corresponding to a cyclic joint rotation amplitude of 54 mrad.



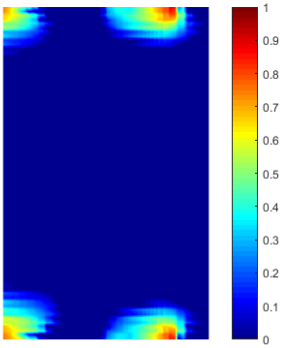
(a) Specimen S1-12D-12A - Negative Rotation



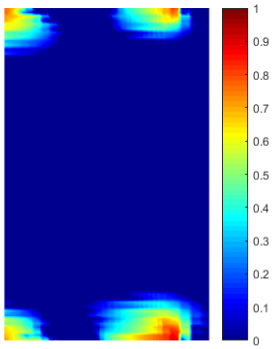
(b) Specimen S1-12D-12A - Positive Rotation



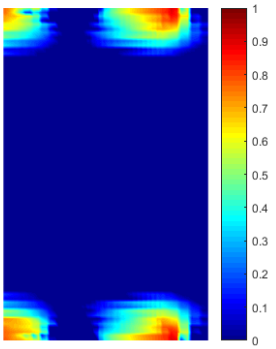
(c) Specimen S2-12D-15A - Negative Rotation



(d) Specimen S2-12D-15A - Positive Rotation

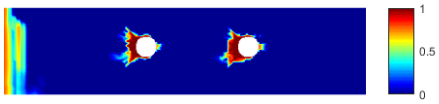


(e) Specimen S3-16D-15A - Negative Rotation

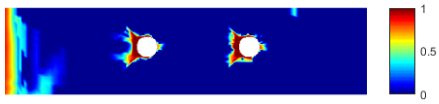


(f) Specimen S3-16D-15A - Positive Rotation

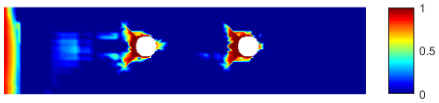
Figure 6.35: Timber beam lateral face compressive damage contour plot corresponding to a cyclic joint rotation amplitude of 54 mrad.



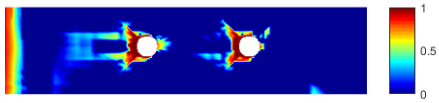
(a) Specimen S1-12D-12A - Top Face



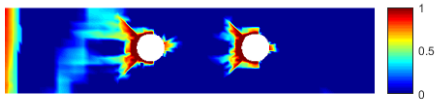
(b) Specimen S1-12D-12A - Bottom Face



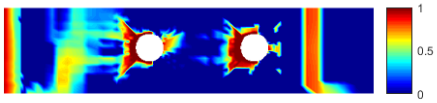
(c) Specimen S2-12D-15A - Top Face



(d) Specimen S2-12D-15A - Bottom Face



(e) Specimen S3-16D-15A - Top Face

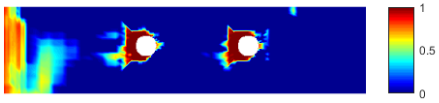


(f) Specimen S3-16D-15A - Bottom Face

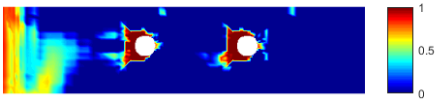
Figure 6.36: Tensile damage contour plot in timber beam top and bottom faces for a joint rotation cyclic amplitude of 40 mrad.

zones for joint rotation magnitudes of 40 mrad and 54 mrad, respectively. It is evident from these figures that in the case of specimen S1, compressive damage is more pronounced than tensile damage in the zone around the bolt hole that is further from the beam end. Moreover, in the case of specimen S3, crushing occurs in the zone that is in contact with the horizontal leg of the steel angle, more precisely, in the zones below the two ends of the angle horizontal leg, where higher contact pressure arises as a consequence of the joint rotation. Contrarily to tensile damage, no compressive damage takes place along the bolts row. Therefore, compressive damage in the top and bottom faces of the timber beam appears to be a consequence of the angle bearing that produces high compressive stresses in the direction perpendicular to the grain. On the other hand, Fig. 6.39 shows that for a larger rotation magnitude of 54 mrad, the original compressive damage areas expand, although no new damage locations appear.

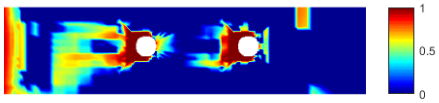
With respect to the principal tensile plastic strains contour plots in the bolts and in the top angle, no significant differences were found with respect to those obtained for the monotonic load case (see Figs. 6.31 and 6.32).



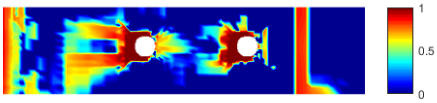
(a) Specimen S1-12D-12A - Top Face



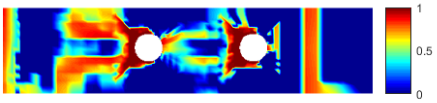
(b) Specimen S1-12D-12A - Bottom Face



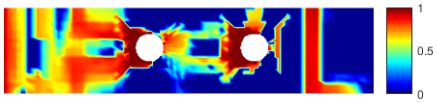
(c) Specimen S2-12D-15A - Top Face



(d) Specimen S2-12D-15A - Bottom Face



(e) Specimen S3-16D-15A - Top Face

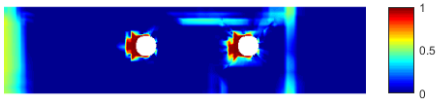


(f) Specimen S3-16D-15A - Bottom Face

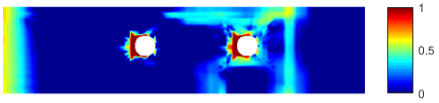
Figure 6.37: Tensile damage contour plot in timber beam top and bottom faces for a joint rotation cyclic amplitude of 54 mrad.

Comparison between Digital Image Correlation (DIC) and FE results for specimen S3-16D-15A

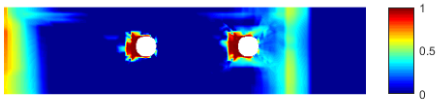
Non-contact strain field measurements were carried out during the laboratory test of specimen S3. For this purpose, a LaVision [103] Digital Image Correlation (DIC) system was employed. DIC is an image processing technique which allows the estimation of displacement and strain fields on the surface of an specimen. It works by taking a number of pictures of the region of interest during the testing period and performing statistical correlation between consecutive images [8]. Over the last years, DIC has gained interest among timber structures and material researchers. For instance, Sjödin et al. [161] carried out an experimental study on steel-to-timber dowelled joints subjected to tension loads. Shear and normal tensile strain fields (in both directions parallel and perpendicular to the grain) were obtained using DIC, and their relation with cracking and with particular types of failure modes was discussed. A similar approach was followed by Sjödin et al. [162] to determine appropriate values of friction coefficients at the timber-steel bolt interface using DIC and FE strain contour plots. Schoenmakers and Svensson [152] used the DIC to obtain the strains field in the direction perpendicular to the grain of a single-fastener timber connection with the objective of studying its embedding behaviour. Interesting



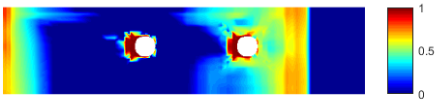
(a) Specimen S1-12D-12A - Top Face



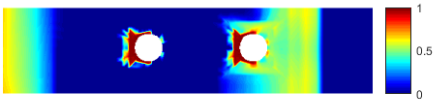
(b) Specimen S1-12D-12A - Bottom Face



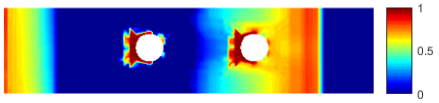
(c) Specimen S2-12D-15A - Top Face



(d) Specimen S2-12D-15A - Bottom Face



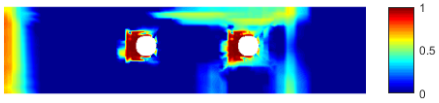
(e) Specimen S3-16D-15A - Top Face



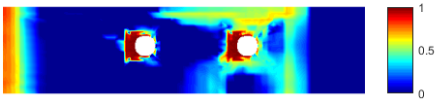
(f) Specimen S3-16D-15A - Bottom Face

Figure 6.38: Compressive damage contour plot in timber beam top and bottom faces for a joint rotation cyclic amplitude of 40 mrad.

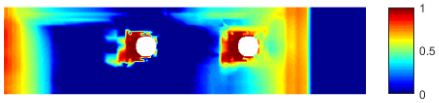
findings were presented on the limitations of both DIC and FE models to obtain precise strain fields of the surrounding wood underneath the bolt, not only due to the high levels of strain concentration, but also due to the large strain gradients within a relative small zone. On the other hand, van Beerschoten et al. [8] used DIC to measure timber Poisson's ratios and compare these values against the theoretical estimations. Bader et al. [2] used the DIC technique to obtain the shear and normal strain fields in the directions parallel and perpendicular to the grain in a multi-dowel LVL moment connection. Reynolds et al. [139] performed tension tests on single-fastener timber and bamboo connections. Crack locations were determined based on the maximum principal tensile strain fields obtained from DIC. Moreover, interesting observations were made related to the DIC capability to capture asymmetric strain distributions due to the heterogeneous nature of timber material, which in general cannot be obtained from FE models contour plots. Lastly, Hochreiner et al. [74] used DIC strain fields to identify the cracking sequence around the bolts for timber-steel dowelled connections. Shear and normal strain fields were obtained for this purpose, and some frequently encountered problems associated to DIC were addressed.



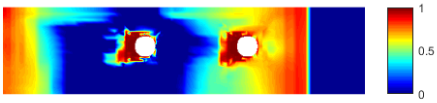
(a) Specimen S1-12D-12A - Top Face



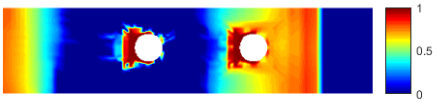
(b) Specimen S1-12D-12A - Bottom Face



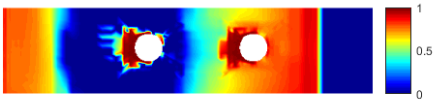
(c) Specimen S2-12D-15A - Top Face



(d) Specimen S2-12D-15A - Bottom Face



(e) Specimen S3-16D-15A - Top Face



(f) Specimen S3-16D-15A - Bottom Face

Figure 6.39: Compressive damage contour plot in timber beam top and bottom faces for a joint rotation cyclic amplitude of 54 mrad.

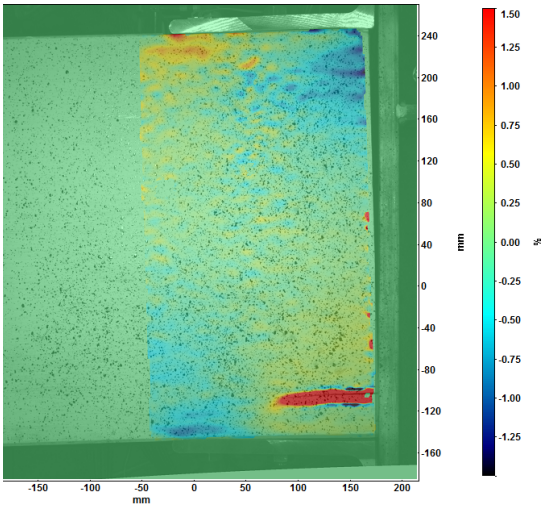
The same DIC set-up configuration and calibration protocol used by Karagiannnis et al. [86] were followed herein. Accordingly, pictures of the lateral face of the timber beam were taken by two high-resolution cameras through the duration of the test. Fig. 6.40 compares the vertical strain fields (perpendicular to the grain) of the timber beam lateral face of specimen S3 obtained with the DIC and with the FE model for a joint rotation amplitude of 40 mrad. Figs. 6.40a and 6.40c on the left show the DIC results for negative (sagging) and positive (hogging) rotation directions, respectively, while Figs. 6.40b and 6.40d on the right show the corresponding FE model numerical results. All these figures show the deformed shape of the connection and share the same maximum and minimum strain limits of the contour plot legend. A maximum tensile strain limit equal to +1.5% is shown in red, while minimum compressive strains of -1.5% are presented in blue.

For a rotation of -40 mrad, a good agreement is observed between DIC and FE results with respect to the locations of the maximum tensile and compressive strain concentration zones. The maximum tensile strains occur along an horizontal crack at the right bottom corner (next to the beam-column interface). On the other hand, the maximum vertical compressive strains occur in the right top corner and in the left bottom corner,

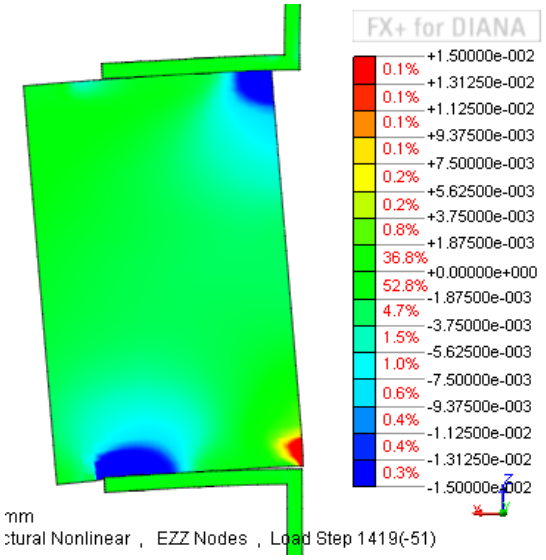
where contact between the timber beam and the top and seat angles develops. It is worth noting that the DIC results in Fig. 6.40a suggest that the magnitude of maximum tensile strains is higher than the magnitude of maximum compressive strains. This is not the case, however, for the FE predictions in Fig. 6.40b, which maximum tensile and compressive strain magnitudes are similar. Besides, a minor concentration of vertical tensile strains at the left top corner, just below the tip of the top angle horizontal leg, can be noticed in the DIC contour plot in Fig. 6.40a. Such a tensile strain zone, which cannot be straightforwardly related to the joint rotation mechanics, is not captured by the FE model strain contour plot in Fig. 6.40b.

When a joint rotation of +40 mrad is applied, the tensile and compressive strain concentration zones swap their positions. The maximum tensile strains in the direction perpendicular to the grain moves to the upper right corner, where a horizontal crack appears (see Fig. 6.40c). Accordingly, the maximum compressive strain zones translate to the left top corner and to the right bottom corner. These strain concentration zones are well reproduced by the FE model contour plot in Fig. 6.40d. Likewise, Fig. 6.40c shows that for a hogging (positive) rotation similar magnitudes of maximum tensile and compressive strains are found. Finally, the FE contour plot in Fig. 6.40d reproduces a third minor compressive strain concentration zone located in the left bottom corner, which is not present in the DIC contour plot. This minor compressive strain zone results from the plastic strains calculated by the FE model during the joint rotation in the negative (sagging) direction. When the joint rotation is reversed the elastic strains disappear, while the plastic strains remain permanently there. The fact that the DIC results do not identify such a permanent deformation possibly means that a higher plasticity hardening modulus should be employed in future FE simulations of this type of timber beams.

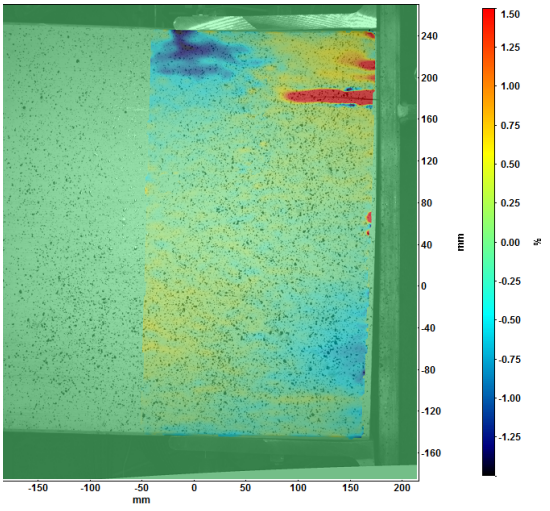
Fig. 6.41 displays the same information of Fig 6.40 for a larger joint rotation cyclic amplitude of 54 mrad. Consequently, the maximum and minimum strain limits of the contour plot legend increase to +2% and -2%, respectively. For a rotation in the negative direction, the DIC strain field in Fig.6.41a is similar to that obtained for a joint rotation amplitude of 40 mrad in Fig. 6.40a. However, there are some minor differences that should be mentioned. First, in Fig.6.41a the compressive strains in the right top corner are higher than those in the left bottom corner. Second, in Fig.6.41a the crack in the right bottom corner is longer than in Fig. 6.40a. The FE model results reproduced in Fig. 6.41b are consistent with the increment of the maximum tensile strain zone in the left bottom corner. Nevertheless, contrary to DIC results, the maximum compressive strain zone in the left bottom corner is larger than the corresponding zone in the right



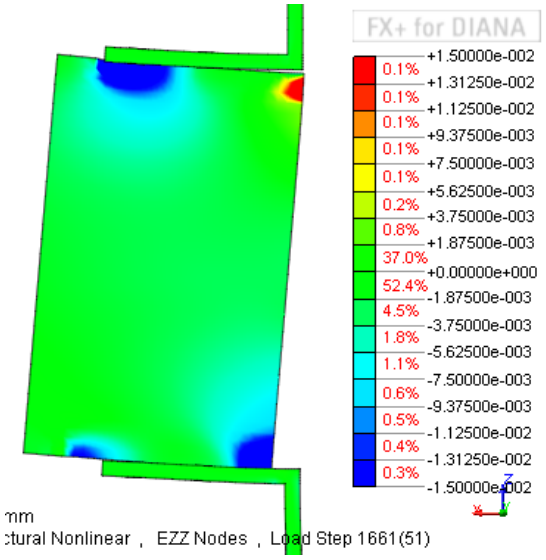
(a) DIC - Negative Rotation



(b) Numerical - Negative Rotation



(c) DIC - Positive Rotation



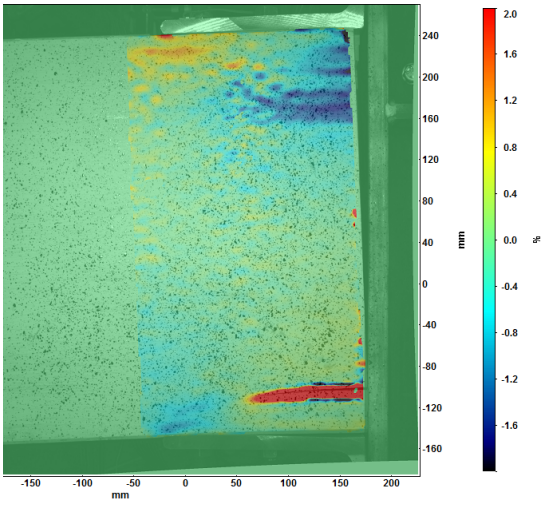
(d) Numerical - Positive Rotation

Figure 6.40: Comparison between DIC and FE vertical strain contour plots in specimen S3-16D-15A for a joint rotation amplitude of 40 mrad.

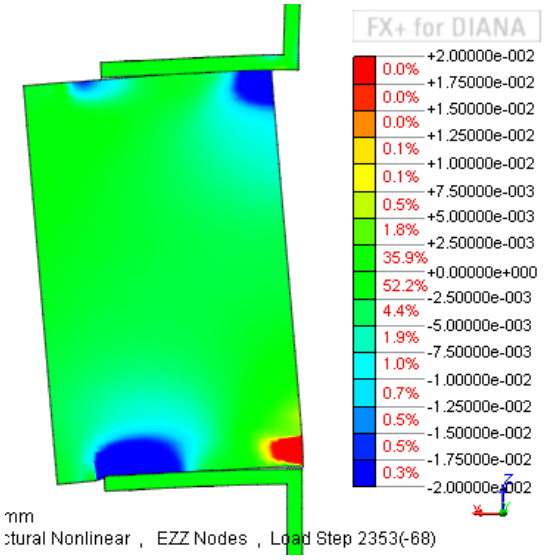
top corner. Permanent plastic compressive strains are also captured by the numerical model and graphically represented in the left top corner of Fig. 6.41b. For a rotation in the positive direction, the DIC strain contour plot presented in Fig. 6.41c is also similar to that of Fig. 6.40c, with the only difference that in the right upper corner a second crack longer than the first one appears. Both of them are located in the same maximum tensile strain zone. The FE model numerical results in Fig. 6.41d consistently show the size increment of the maximum tensile and compressive strain zones in the right and left upper corners. Furthermore, the previously mentioned permanent plastic strain zone in the left bottom corner shows an increment of size and magnitude.

In order to assess the ability of the proposed constitutive model to identify the potential crack formation zones, Fig. 6.42 presents a comparison between the DIC principal tensile strain contour plot and the FE model tensile damage variable contour plot for joint rotation amplitudes of 40 mrad and 54 mrad. Although the nature of these response parameters (principal tensile strain and tensile damage variable) is different, both of them are able to identify the zones where the greatest deformation levels due to tensile stresses occur. For a joint rotation amplitude of 40 mrad, Figs. 6.42a and 6.42b highlight in red colour the zones where the highest tensile strain magnitudes up to 7% take place for sagging and hogging rotations, respectively. These red zones indicate the position and orientation of the largest open cracks. For this particular case, the cracks orientation turned out to be horizontal, and therefore, these DIC contour plots do not provide any additional information on this matter than that obtained from the vertical strain contour plots in Figs. 6.40 and 6.41. However, this is not always the case. More complex three-dimensional stress states can lead to the appearance of inclined cracks which location and orientation cannot completely be determined by means of the vertical tensile strain contour plot only.

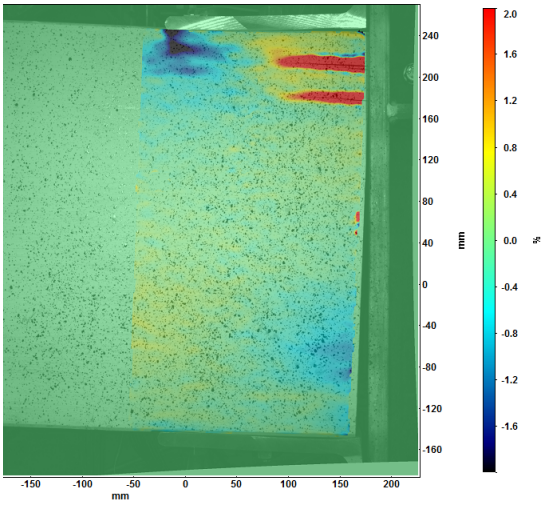
On the other hand, in Fig. 6.42c the tensile damage variable contour plot is employed as a numerical indicator of the cracking zones locations. Some interesting observations with respect to Fig. 6.42c are possible. First, the zones in red correspond to the maximum value of the damage variable equal to 1, which means that the upper and lower right corners are identified as the zones where cracking is more likely to occur. The information provided by the DIC contour plots proves the correctness of the numerical prediction of the crack locations using the tensile damage variable as indicator. Second, neither the orientation nor the status (closed or open) of cracks can be determined based on the tensile damage variable indicator. For this reason, the shapes of the zones with higher values of tensile damage variable do not reflect the geometry of the actual cracks. What



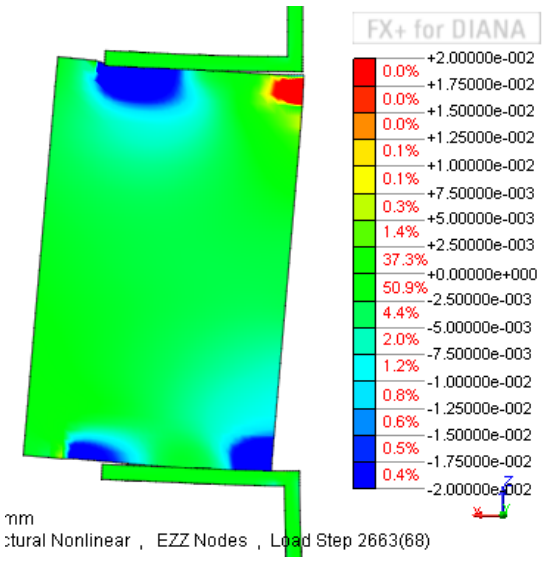
(a) DIC - Negative Rotation



(b) Numerical - Negative Rotation



(c) DIC - Positive Rotation



(d) Numerical - Positive Rotation

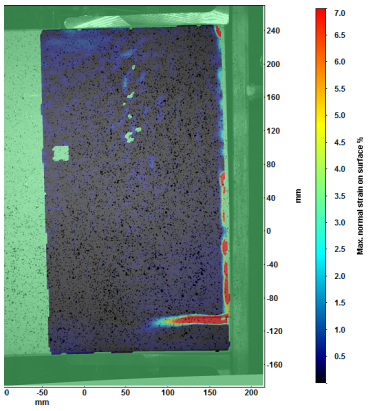
Figure 6.41: Comparison between DIC and FE vertical strain contour plots in specimen S3-16D-15A for a joint rotation amplitude of 54 mrad.

is more, considering that the damage variables increase monotonically, both upper and lower corners crack zones are always shown, regardless of whether they are open or closed.

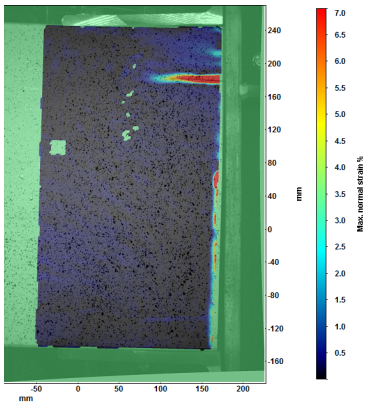
Figs. 6.42d and 6.42e show the same DIC contour plots discussed above for a joint rotation amplitude of 54 mrad. Besides the appearance of the second crack in the upper right corner mentioned above, there are no significant differences between the DIC contour plots corresponding to joint rotation amplitudes of 40 mrad and those of 54 mrad. The numerical contour plot of the tensile damage variable in Fig. 6.42f shows the expansion of the tensile damage zone in the upper and lower right corners. Furthermore, two new smaller crack zones appear in the left upper and lower corners, where bearing between the timber beam and the horizontal legs of the angles occurs. These new cracking zones, not identified by the DIC contour plots in Figs. 6.42d and 6.42e, are a consequence of lateral expansion due to high compressive stresses. Although it is possible to obtain 3D principal strain fields using DIC, the contour plots shown herein only take into account a 2D strain state of the beam lateral surface. As a consequence, the DIC principal stain contour plots in Fig. 6.42 do not take into account the out-of-plane tensile strains. On the contrary, the tensile damage variable is calculated taking into account the complete 3D strain state. Thus, the new potential cracking zones in the left upper and lower corners of Fig. 6.42f are related to minor local wood splitting caused by compression stresses perpendicular to the grain that has little influence on the global nonlinear response of the connection. Moreover, it is important to bear in mind that Poisson's ratios play a fundamental role in the magnitude of lateral expansion. As a consequence, the magnitude of the tensile damage variable in zones subjected to high compressive stresses is highly influenced by the values of the Poisson's ratios. Too high Poisson's ratios can lead to mistaken numerical predictions and fictitious cracking zone locations.

6.6 Concluding remarks

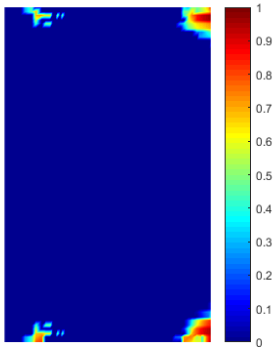
In this chapter a comprehensive guide for the elaboration of three-dimensional finite element models of timber beam-to-steel column moment connections was developed. To this end, several essential topics and strategies for a successful modelling of this type of connections were covered. First of all, the formulation of a timber-steel interface contact model for the simulation of the interaction between the bolts and the surrounding timber was proposed. Then, some guidelines for the definition of the model mesh size and geometry were presented. The criteria followed for selecting the input parameter values of the timber and steel material models employed were also provided. Moreover,



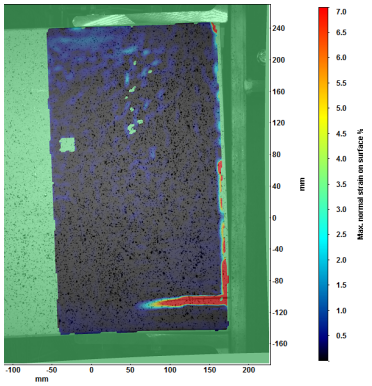
(a) DIC - Principal tensile strain (-40 mrad)



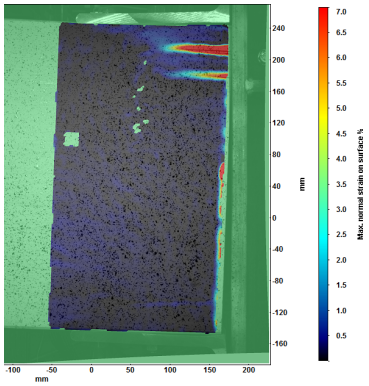
(b) DIC - Principal tensile strain (+40 mrad)



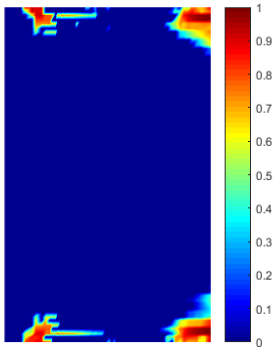
(c) Numerical - Tensile damage variable (+40 mrad)



(d) DIC - Principal tensile strain (-54 mrad)



(e) DIC - Principal tensile strain (+54 mrad)



(f) Numerical - Tensile damage variable (+54 mrad)

Figure 6.42: Numerical prediction of crack locations in specimen S3-16D-15A.

a methodology to determine the values of the calibration parameters of the timber material and the timber-steel interface models was developed and presented in detail. Finally, the analysis of the results obtained from the timber beam-to-steel connection FE model under the action of monotonic and cyclic loads was performed. These numerical results were compared against the experimental results previously presented in Chapter 5 and elsewhere [87].

From the results obtained in this chapter, it is concluded that an appropriate modelling of the timber-steel contact mechanism is fundamental to obtain a good prediction of the hysteretic response of timber dowelled connections with pinching behaviour. Therefore, the timber-steel interface model formulated in this chapter is a contribution in this direction. Besides, the guidelines depicted in Fig. 6.8 for the definition of the mesh size and geometry of timber dowelled connection models proved sufficient to successfully avoid strain localization problems. On the other hand, although the influence of the plasticity yield criteria on the model performance is beyond the scope of this thesis, the author thinks that this is a research topic worthy to be undertaken in the future.

The proposed parameter calibration procedure based on embedment tests has demonstrated to be feasible, efficient and precise. Preliminary sensitivity analyses were conducted as part of this calibration method. The results obtained from these analyses demonstrated the reliability of the global numerical response when the values of any of these parameters are slightly modified.

With respect to the timber material model parameters, it can be concluded that the maximum capacity of a timber dowelled connection is strongly influenced by the compressive damage hardening constant (β). The parameter β controls the maximum level of stiffness degradation in compression, and therefore, has an important influence on the post-elastic hardening level and the maximum compressive strength. The second calibration parameter is the plasticity hardening modulus (h). It is concluded that the influence of h on the slope of the embedment curves loading branch is negligible. By contrast, h has a significant effect on the extent of plastic deformation and stiffness degradation due to compressive stresses, and consequently, on the unloading branch slope of the embedment curves. An analytical expression for the estimation of h was derived based on the timber material properties in the loading direction (parallel or perpendicular to the grain). In dowelled connections, the estimation h taking into account the loading direction is fundamental to adequately transfer the stresses from the wood to the dowel, and also to avoid convergence issues during the analysis.

The three calibration parameters of the timber-steel interface contact model are the following: compressive normal stiffness (k_C), shear stiffness (k_S) and unloading stiffness (k_{UL}). The compressive normal stiffness has a considerable influence on the global initial linear elastic stiffness of the connection, whereas the shear stiffness has a significant influence on its predicted embedding strength. Moreover, the unloading stiffness is important for modelling pinching behaviour. One fourth of the timber bulk modulus has demonstrated to be a good approximation for the initial value of k_C. An expression to determine the bulk modulus for orthotropic materials was also presented in this chapter. On the other hand, a value of $k_S = 1$ MPa/mm (around $0.01 \cdot k_C$) resulted from the calibration process, while $k_{UL} = 450$ MPa/mm (around $5 \cdot k_C$) is a high enough value to obtain a steep unloading branch characteristic of pinching systems. Finally, it is concluded that it is more efficient to perform the calibration process of each of these parameters in the following order: k_C, k_S, β, h, k_{UL}.

The numerical predictions of the monotonic response of the timber beam-to-steel connection specimens S1, S2 and S3 are in good agreement with the experimental results. Furthermore, precise predictions of the specimen capacities were obtained even for large deformation levels higher than 50 mrad. On the other hand, it was concluded that for this type of connection the angle thickness has an important influence on the amount of crushing and plasticity generated in the timber beam due to compressive stresses in the direction perpendicular to the grain. The crushing zones were consistently located around the bolts and along the transversal strip zones where the steel angle and the wood are pressed one against the other. The pressure exerted by the horizontal legs of the top and seat angles causes splitting tensile stresses in the transversal direction (lateral expansion), and consequently, timber cracking. It is important to mention that, in addition to tension and compression, cracking zones are also the consequence of shear stresses in the direction parallel to the grain. Shear local failure typically occurs behind the bolt rows. All these cracking zones could be captured by the FE model through the tensile damage variable contour plots. Moreover, it was observed from the model results that tensile plastic strains in the steel angle are concentrated in the horizontal leg, near to the intersection zone with the vertical leg. The 12 mm thickness angles which belongs to specimen S1 experience high tensile principal plastic strain magnitudes equivalent to twice the plastic strain magnitudes found in the long bolts. A comparison of the FE model local response obtained for each specimen leaded to the conclusion that the nonlinear response of specimen S3 is defined by wood local failure (e.g. cracking, plasticity, crushing), while in the case of specimens S1 and S2 the contribution of the steel components plasticity is also important.

A good agreement between the numerical and experimental results was also appreciated for the three specimens when subjected to cyclic loading. In general, the maximum connection capacity and cyclic stiffness degradation are well captured. Nevertheless, although the experimental pinching behaviour of the connection is clearly reproduced by the numerical model, the permanent residual deformations are underestimated. Additional permanent plastic deformations in the model may arise in the wood as a consequence of the ovalization of the bolt holes. This effect was not incorporated in the proposed model due to lack of experimental verification and quantification of this phenomenon. Moreover, another potential reason for the underestimation of permanent deformations is that the Mises plasticity model is not suited to properly quantify the plastic strain accumulation in the connection's steel components under the action of cyclic loads.

Vertical strain (perpendicular to the grain) and tensile damage variable contour plots obtained from the FE model were compared against the experimentally measured Digital Image Correlation (DIC) strain fields. The information provided by the DIC proves the correctness of the crack location numerical prediction, using the tensile damage variable as indicator. However, neither the orientation nor the status (closed or open) of cracks can be determined based on the tensile damage variables. On the other hand, minor compressive plastic strain concentration zones not present in the DIC contour plot are predicted by the FE models. The fact that the DIC results do not identify those permanent deformation zones possibly means that a higher plasticity hardening modulus, equivalent to a post-elastic stiffness ratio (α_X) higher than 0.1 (value of α_X used in the analysis), should be employed in future FE simulations of this type of timber beams. Moreover, it is concluded that the magnitude of the tensile damage variable in zones subjected to high compressive stresses is highly influenced by the values of the Poisson's ratios. Too high Poisson's ratio values can lead to mistaken numerical predictions and fictitious cracking zone locations.

To sum up, the results obtained in this chapter demonstrate the ability of the proposed finite element model to simulate the behaviour and to accurately predict the maximum capacity of complex timber beam-to-steel column connections for different levels of deformation. Furthermore, the application of damage mechanics concepts on the prediction of crack zones location in timber structures under the action of cyclic loads has been proved. On the other hand, the simulation of such highly nonlinear structural systems by means of the finite element model described in this chapter, including continuous plasticity-damage and contact modelling, requires very small load steps in order to obtain convergence and

acceptable numerical precision. For instance, for the moment connection studied herein under the action of monotonic loads, a total of 350 steps of 0.25mm were employed to apply a total displacement-control of the load of 87.5mm.

Chapter 7

Simplified Component-Based Model

7.1 Introduction

Through all this work the importance of using detailed three-dimensional continuous finite element models for a proper prediction and understanding of the nonlinear behaviour of timber structures has been illustrated. Moreover, the original plasticity-damage constitutive model for wood proposed in this thesis has been proved to accurately capture the most important features of timber dowelled connections subjected to the action of cyclic loads. Nevertheless, there are a number of situations in seismic analysis and design that demand extensive series of runs to be performed for which simpler macro models (that can be realistically employed in the engineering professional practice) should be developed. In general, such models can be empirical and mechanically-based (i.e. each main component of the structural system or sub-assembly is represented by a particular element). Furthermore, such models should strive to reduce the computational elaboration and running time, without losing prediction accuracy.

The most basic macro models define the hysteretic response of each component utilizing single degree of freedom systems [155]. Alternatively, more elaborated macro models use beam elements for the steel bolts or nails, while the embedding and friction mechanisms generated by the dowel-wood interaction are modelled by means of spring elements [21]. In this section, a new macro model that is strongly influenced by the basic principles of the continuous three-dimensional model described in Chapter 6 is presented. As a result, a synergistic version of a continuous micro model combined with a component-based macro model is proposed and its performance is assessed.

The macro model of the beam-to-column moment connections studied in Chapters 5

and 6 can be used as a basis for the formulation of two-dimensional global models of hybrid timber-steel lateral-resisting joints. In this way, the effects of several aspects such as gravity loading, slab diaphragm force transfer, shear walls, foundation supports can be studied. Moreover, parametric analysis of the seismic performance of innovative structural lateral-resisting systems can be carried out. These are particularly relevant for the development of fragility curves and the collapse capacity assessment of such earthquake-resistant systems. In order to reach this ambitious objective, the proposed component-based macro model should be comprehensive, which means capable of accurately simulating its non-linear hysteretic response up to large deformation levels, taking due account of the underlying damage accumulation.

One of the most innovative and promising damage-avoidance structural systems is the self-centring (SC) post-tensioned (PT) frames. For this reason, the cyclic behaviour of a SC-PT timber beam-to-steel column joint will be used as a case study in this chapter to assess the performance of the proposed component-based macro model. In this case, in addition to energy dissipation, pinching and cyclic degradation characteristics, the component-based model should be able to reproduce the self-centring nature of the hysteretic response for large lateral deformation levels. Therefore, the proposed model should take into account the combined contribution of the following joint sources of nonlinearity: 1) interface gap opening and friction mechanisms; 2) post-tensioning bar; 3) steel dissipation angles; 4) steel bolt bending and yielding; and 5) timber beam plasticity and damage. Other nonlinear response sources are related to the steel column plasticity and panel zone shear deformation. Even though the proposed component based model is able of simulating them, the study of their influence is out of the scope of this chapter.

In the following section the components of the proposed two-dimensional macro model are described in detail. Then, the monotonic and cyclic responses of the timber beam-to-steel column sub-assembly examined in Chapters 5 and 6 are compared with the predictions obtained using the proposed component based model. The influence of the timber beam element thickness in the joint zone and the wood nonlinear material model employed is assessed in this section. Based on these results, a set of guidelines to build component based models of timber-steel dowelled connections is drawn. Finally, the application of the component based model to the study of a SC-PT timber beam-to-steel column moment connection is presented.

7.2 Description of the component based model

7.2.1 General aspects

The component based model proposed herein is obtained by reducing the full three-dimensional continuous model described in Chapter 6 to its plane stress two-dimensional version. In order to perform this reduction, all the 3D solid elements are replaced by beam and shell elements, while the surface plane interfaces described in Section 6.2 are reduced to linear interfaces with only one tangential relative displacement direction instead of two. A faithful simulation of the interaction between the steel bolt and the surrounding wood is achieved by modelling a portion of the timber beam with two-dimensional continuous shell elements.

Timoshenko beam

Quadratic (or higher order) beam elements based on the Timoshenko theory, and therefore, accounting for shear deformations [16, 11, 109, 47], are proposed to be employed for all the timber and steel connection components. These type of elements, named "Class-III" beams in DIANA FE software and shown in Fig. 7.1, "are numerically integrated over their cross-section and along their axis" [35]. This means that they are similar to the so-called fibre beam elements that are usually applied for the seismic analysis of concrete and steel structures, and that are able to incorporate both uniaxial [105, 119, 108, 13] and three-dimensional [131, 109, 47] constitutive models that were originally developed for solid continuous elements. Therefore, this kind of beam elements are ideal for the proposed component-based model, given their natural suitability to be connected to continuous elements like solids or shells.

In fact, the wood constitutive model described in Chapter 3 can also be used in combination with the Timoshenko beam element to study the global nonlinear response of timber beams, columns or frames. This can be achieved by incorporating a condensation local algorithm to the user-supplied subroutine at the material level developed herein. This is done with the objective of imposing the "zero-stress" or "plane stress" condition characteristic of beam elements for some of their three-dimensional stress components. In the case of the component-based model proposed herein, the nonlinear behaviour is concentrated in the shell elements next to the steel bolts. Therefore, there is no need to incorporate the wood nonlinearity into the beam element for this particular component-based model. Nevertheless, further research on the performance of this technique applied

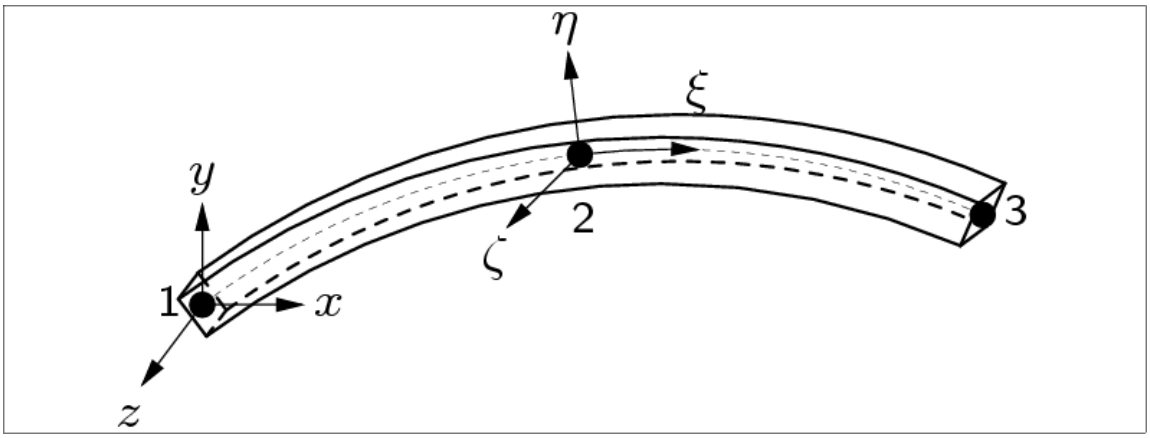


Figure 7.1: Class-III Timoshenko beam element (Figure taken from DIANA User's manual [35]).

to the nonlinear seismic analysis of timber structures is worth to be carried out in the future. A detailed description of the previously mentioned condensation algorithm can be found in [95, 147].

Isoparametric shell element

The shell element employed to model the area of wood affected by its interaction with the steel bolts is based on an isoparametric degenerated-solid approach [3] with drilling rotational degrees of freedom. Fig. 7.2 shows an example of this kind of isoparametric shell elements [35]. The element formulation is obtained from the assumptions corresponding to a continuum element (e.g. solid) [40] "which fully three-dimensional stress and strain conditions are degenerated to shell behavior" [4], this being the reason behind its denomination as "degenerated-solid" shell element. Similarly to the case of the Class-III Timoshenko beams described above, the main motivation for selecting this particular type of shell element for the component-based model is its straightforward compatibility with the wood plasticity-damage constitutive model developed in Chapter 3 of this thesis. No modification of the previously mentioned user-supplied subroutine is required [4].

In this type of shell elements the lateral edges in the thickness direction "are assumed to remain straight, but not necessarily normal to the reference surface. Transverse shear deformation is included according to the Mindlin-Reissner theory" [35]. Moreover, one of the most relevant characteristic of the isoparametric shell elements employed herein is that the normal stresses perpendicular to the shell tangent planes are forced to be equal to zero (plane stress condition). In-plane strains (normal and shear) vary linearly

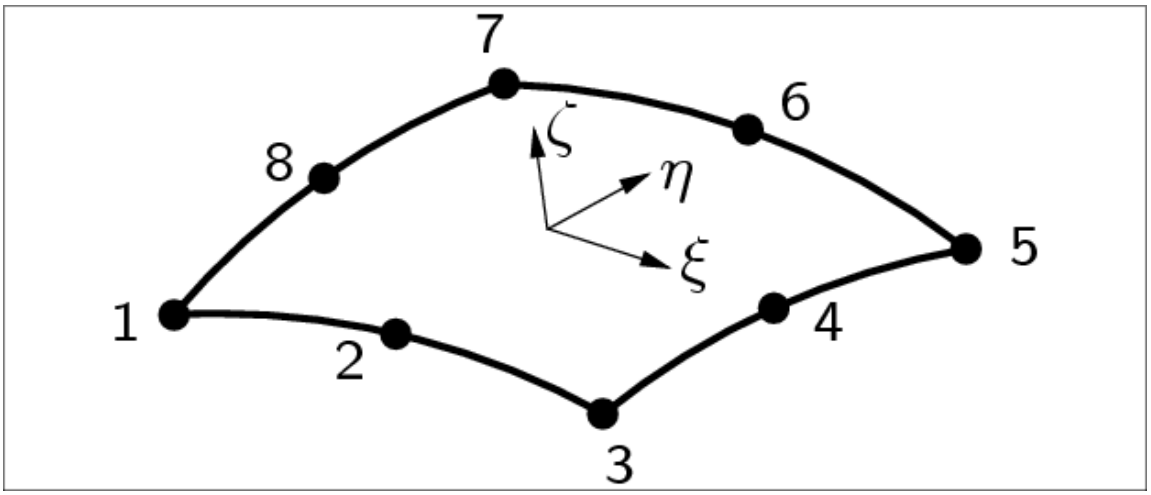


Figure 7.2: Quadrilateral isoparametric shell element (Figure taken from DIANA User's manual [35]).

in the thickness direction, while transverse shear strains are approximately represented by a constant (instead of a parabolic) distribution [35].

The regular isoparametric shell element has five degrees of freedom per node, three displacements and two rotations around the two orthogonal axes which are coplanar with the tangent plane to the shell mid-surface. In the case of flat elements like the ones employed in the component-based model described herein, these two orthogonal axes lie in the element plane and have the same directions for all element nodes. However, the full set of six degrees of freedom per node, including the third fictitious rotation around the normal axis to the shell element plane, called "drilling rotation", is required for isoparametric shell elements that are expected to interact with Timoshenko beams (isoparametric shell elements are not compatible with Bernoulli beams) by sharing the same group of nodes [40]. This is the case for the proposed component-based model. Furthermore, the inclusion of the drilling rotation in the shell element formulation improves its numerical performance, especially when the element nodes are co-planar [35].

A frequently encountered problem in isoparametric shell elements is shear locking. With the objective of satisfying the zero shear strain condition in thin shell elements, some degrees of freedom are artificially "locked" by setting their displacement magnitudes to zero [4]. An important undesired effect of this numerical phenomena, which is totally related to the nature of the element formulation, is the artificial stiffening of the structural response. A well-known technique to avoid shear locking is the use of reduced integration schemes. Nevertheless, this technique usually produces spurious zero-energy

modes associated to rigid body motions [40, 3, 4]. Therefore, an appropriate integration scheme is fundamental for isoparametric shell elements. High order (quadratic or cubic) Lagrangian elements are recommended for undistorted and moderately thick shell elements to avoid shear locking [4]. Moreover, for nonlinear analysis applications the definition of more than 2 integration points in the thickness direction is recommended [4].

Generally, shear locking problems are restricted to thin (and critical for very thin) isoparametric shell elements [4]. Conversely, for thick shell elements like the timber beam modelled herein, shear locking is seldom an issue. However, by definition, shells can only accurately represent thin and moderately thick (not very thick) elements. This can be a problem if the whole timber beam width were to be modelled by the shell element. For this reason, among others, modelling a single portion, instead of the whole width, of the timber beam is consistent with the shell element nature and is the approach followed herein.

Finally, some relevant characteristics of the performance of shell elements in nonlinear analysis should be highlighted. By definition, plasticity spread through their thickness is possible to be calculated when using isoparametric shell elements [4]. High accuracy is thus ensured for material nonlinear analysis. Contrarily, when geometric nonlinear analysis is performed, only the position of the nodal points and normal vectors directions are updated, while the shell thickness remains constant. Therefore, the formulation of this element provides precise solutions for small strains only[4]. On this matter the solid elements will show a superior performance, given their ability to take into account thickness variations.

7.2.2 Detailed description

A general view of the proposed component-based model that shows a complete set of its components is provided in Fig. 7.3. This model simulates the timber beam-to-steel column connections studied in previous parts of this thesis. As previously mentioned, despite the component-based nature of this simplified macro model, there is a close conceptual resemblance between it and the detailed three-dimensional continuous model developed in Chapter 3. Fig. 7.4 shows a detailed view of the model and indicates the position of all its components. A brief description of their characteristics and functions follows below:

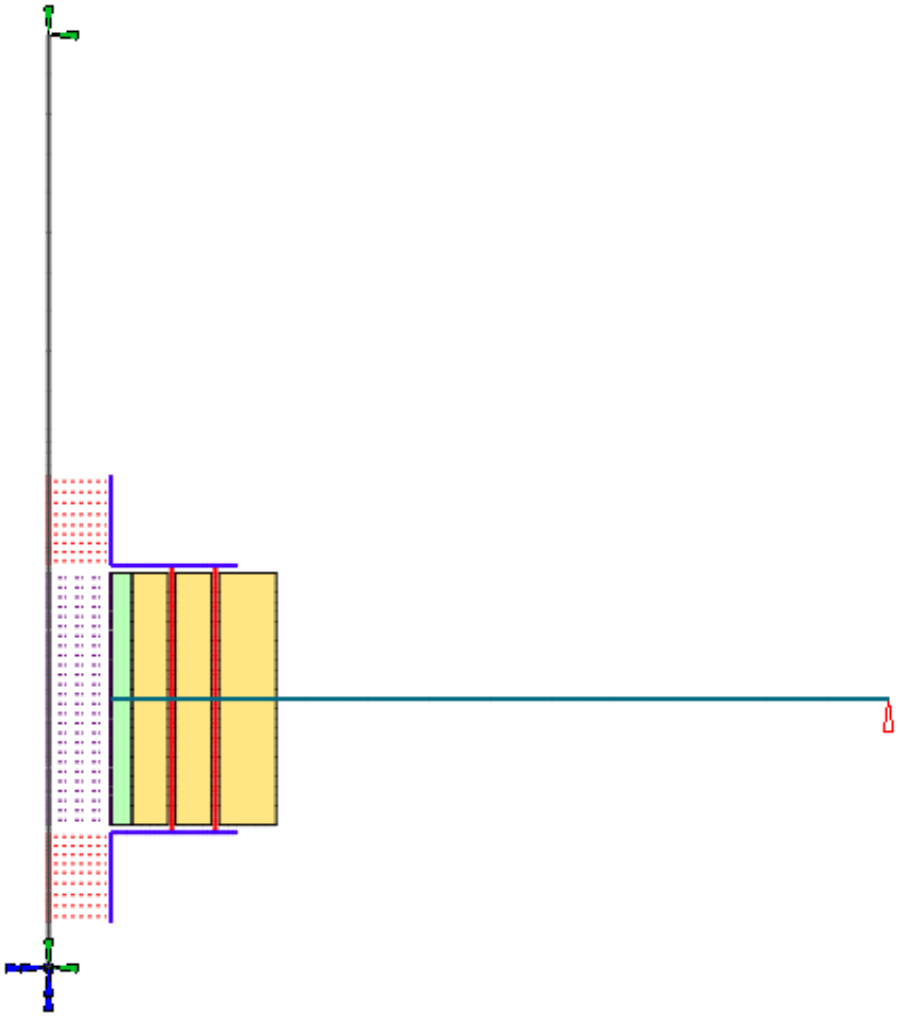


Figure 7.3: General view of the component-based model proposed for timber beam-to-steel column dowelled connections.

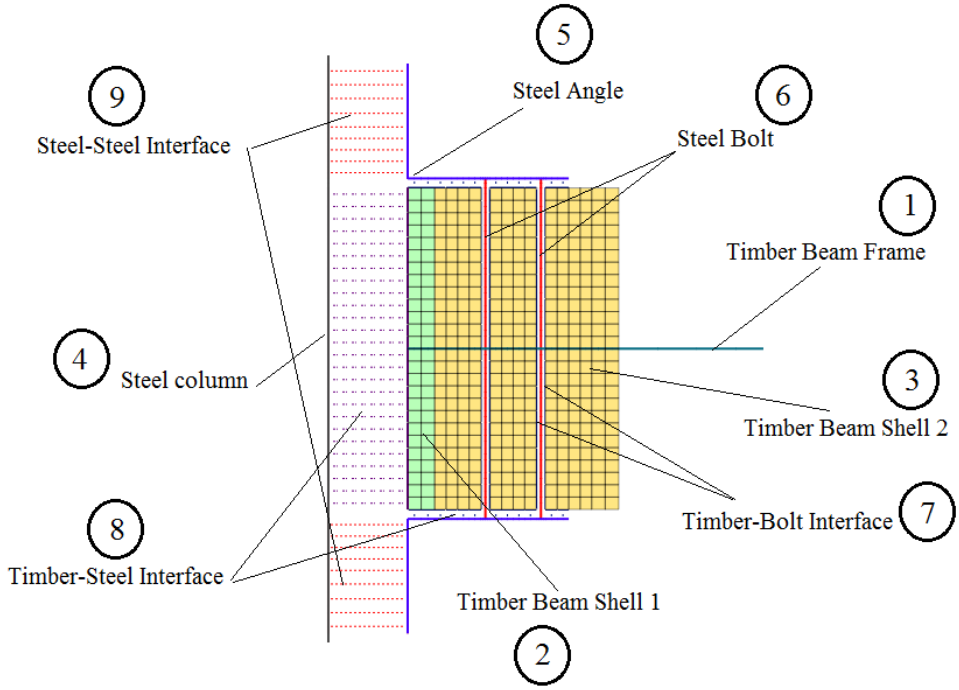


Figure 7.4: Detailed view of the complete set of elements that make up the component-based model proposed for timber beam-to-steel column dowelled connections.

1. **Timber Beam Frame**

   The timber beam is modelled by three elements. The first one is a Timoshenko beam element with linear elastic material properties. This element's function is to transfer the stresses, displacements and rotations generated by the vertical displacement load applied at the tip of the beam to the beam-to-column joint zone. A rectangular cross-section with the actual dimensions of the timber beam is assigned to the Timoshenko beam element.

2. **Timber Beam Shell 1**

   A small portion of the timber beam adjacent to the column and interacting with it is modelled by isoparametric shell elements. The purpose of using shell instead of beam elements in this zone is to simulate the contact compression stresses generated by bearing of the beam at the beam-column interface when a bending moment is transferred to the joint. Therefore, at the beam-column interface the beam element hypothesis that cross-sections remain perpendicular to the beam axis does not hold, and the use of continuous elements like shells is required. The thickness assigned to this group of shell elements is equal to the beam width that is in full contact with

the column flange.

3. **Timber Beam Shell 2**

   With the objective of modelling the interaction of the steel bolts with the surrounding wood, a second group of shell elements is defined at the joint connection zone. Only a well-defined zone of the timber beam is directly affected by the interaction with the steel bolts. For this reason, a reduced equivalent thickness is assigned to this group of shell elements. It is important to bear in mind that one of the greatest sources of nonlinear response comes from this part of the model. Therefore, the performance of this group of shell elements is crucial for the model's prediction accuracy. The equivalent thickness for this group of shell elements is determined based on the results obtained in Section 7.3.1.

   Shell 1 and Shell 2 elements described above and shown in Fig. 7.4 employ four-node quadrilateral isoparametric shell elements based on linear interpolation and 2 x 2 Gauss integration scheme over the element area. The plasticity-damage model developed in Chapter 3 is assigned to both groups of shell elements. With the objective of obtaining the best possible performance from the wood material model, a 7-point Simpson integration scheme is used in the thickness direction [35]. Furthermore, to avoid the the shear locking problem described above, the DIANA FE software capability of automatically modifying the transverse shear strain fields [35] was utilized.

4. **Steel Column**

   Fig. 7.4 shows the steel column component that is modelled by means of a Timoshenko beam element in combination with a steel linear elastic material model. The corresponding wide-flange steel cross-section is assigned to this element. Moreover, in a similar way to the beam element used to model the timber beam, the steel column element has a minor influence on the component-based model global response. Its main function is to reproduce the boundary conditions of the joints studied previously in this thesis. This is not always the case, however. In real hybrid timber-steel building frames, the steel column may play a fundamental role in the seismic response of the structure. In those cases, the same Timoshenko beam approach can be successfully applied provided that a suitable plasticity steel material model is assigned or a concentrated plasticity approach is followed.

5. **Top and Seat Steel Angles**

   Timoshenko beam elements of rectangular cross-section are also employed to model the top and seat steel angle legs as shown in Fig. 7.4. Furthermore, a von Mises plasticity model is assigned to the steel angles. The influence of these components on the global nonlinear response of the joint macro model is important, as discussed in previous chapters.

6. **Long steel Bolts**

   The long bolts connecting the steel angles with the timber beam are modelled using Timoshenko beam elements. Similarly to the steel angle elements, a von Mises plasticity material model is assigned to the bolts, while a circular geometry is assigned to their cross-section. A correct simulation of the interaction of these elements with the timber beam is crucial for obtaining a faithful description of the structure nonlinear response, particularly for large deformation levels when plasticity develops in the bolts.

7. **Timber-Bolt Interface**

   The nonlinear interaction between the steel bolts and the surrounding wood (timber beam shell 2) is modelled through interface elements as shown in Fig. 7.4. Their main function is to simulate the friction in the tangential direction and the contact in the normal direction. For this purpose, the quadrilateral 3D interface constitutive model developed in Section 6.2 was reduced to its linear bidimensional version by eliminating one of the two tangential components. Therefore, a similar performance of the interface element described and analysed in detail in Chapter 6 is also obtained for this simplified model. Given its bidimensional configuration, it is necessary to define a thickness magnitude along the direction perpendicular to the plane, which should be defined based on the bolt diameter.

8. **Timber-Steel Interface**

   Fig. 7.4 shows two additional interface elements which connect the timber beam with the steel column and the steel angles, respectively. Although these interfaces behave in a similar way to the timber-bolt interface described above and employ the same user-defined material model subroutine, the input values assigned to them are different. Moreover, for compatibility reasons, the thickness of the beam-column

and beam-angle interfaces are equivalent to those of the timber Shell 1 and Shell 2 elements, respectively. The main function of the timber-steel interface element is to model the gap opening mechanism and to transfer the bearing compressive stresses from the steel components to the wood.

9. **Steel-Steel Interface**

   Finally, a simple nonlinear elastic compression-only and friction constitutive model is assigned to the linear bidimensional interfaces that simulate the gap opening mechanism and the contact interaction between the steel column and the vertical leg of the steel angle.

Besides the elements typology, the constitutive material models and the general arrangement of the model components described above, an adequate definition of the constraints and tyings is fundamental for the successful performance of a component-based model. Constraints are mathematical expressions that eliminate some selected nodal degrees of freedom by relating their displacements or rotations to those of other degrees of freedom. The latter are called "master" nodes, while the former are called "slave" nodes. There are many types of constraints according to their purpose. For instance, the most basic constraint, known as "Equal", assigns the same displacement of the master node to the slave nodes. Fig. 7.5 shows the three types of constraints that were defined to achieve the desired performance in the models under consideration. A brief description of each of them follows below:

- **Rigid body motion**

  This constraint solves the problem of connecting the timber frame to the Timber Shells 1 and 2 (see Fig. 7.4) and of transferring the kinematics of a discrete element to a continuous element, like solids or shells. This constraint should be defined for all the shell nodes along the imaginary vertical line which defines the location of the beam cross-section. The master node is located in the middle of the cross section, at the intersection of the timber beam axis with the shell elements. The two translations (Tx and Ty) and the rotation (Rz) in the plane of the nodes along the cross-section vertical line are fully dependent on the master node's translations and rotations, and on their relative position with respect to it. A rigid body motion is enforced along this line.

The purpose of this modelling decision is to transfer the Timoshenko beam hypothesis that "cross-section planes remain straight" to the shell elements. Therefore, this constraint must be defined in those particular zones where no major local deformations is expected (i.e. zones not in contact with the steel bolts or column). The three black lines in Fig. 7.5 indicate the three sections where this constraint was assigned. The selection of these locations responds to the need of unifying the three zones of timber shell elements divided by the steel bolts, and thus, provide continuity to the component-based model. Notice that no local deformation due to the interaction with the steel bolts or the steel column occurs in the vicinity of the three cross-section planes.

- **Releases**

  The bolted connection constraints the translations of the long bolts and the steel angle plate. However, their in-plane rotations are not tied, and thus, independent from each other. To simulate this behaviour, two different nodes were defined at the same location, one belonging to the steel angle element and the other to the steel bolt. Then, all the degrees of freedom of both nodes, except the in-plane rotation (Rz), were tied with an "Equal" constraint. In this way, a hinged connection between these components is simulated.

- **Rigid links**

  As previously mentioned, the steel column and the steel angles are modelled with linear frame elements. Considering that there is a distance between the axis of the column and of the angle elements, a virtual rigid link connecting them must be defined. This was done through the definition of a "rigid link" constraint of the translational degrees of freedom in the plane (Tx and Ty).

The three types of constraints defined above ensure the complete interconnection of all the model components. Subsequently, the boundary conditions are the only characteristics missing to conclude with the model definition. Fig. 7.3 shows that boundary conditions are assigned to both ends of the column and to the tip of the beam. The three translations and the three rotations are restrained at the base of the column to simulate a clamped connection. On the other hand, only the translations are restrained at the column top end. Finally, the vertical translation of the tip of the beam is automatically

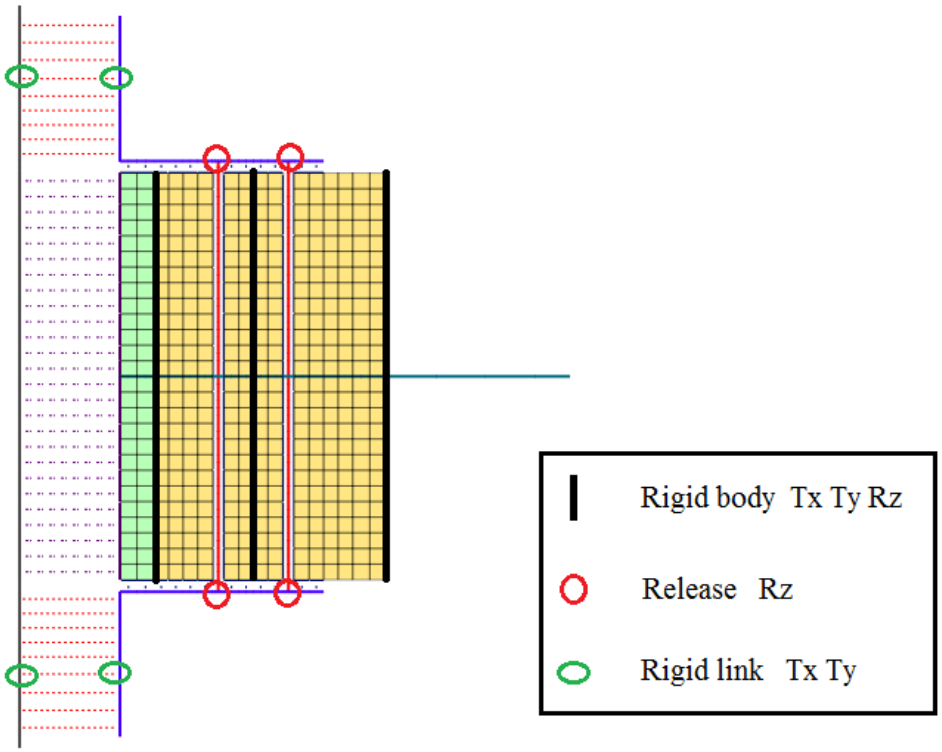


Figure 7.5: Tyings and constraints of the component-based model proposed for timber beam-to-steel column dowelled connections.

restrained due to the application of a predefined vertical displacement.

7.3 Model validation

In this section a validation of the simplified component-based model is carried out using the timber beam-to-steel column dowelled specimens studied in Chapters 5 and 6. First, the influence that "Shell 2" elements thickness magnitude and timber material nonlinear behaviour have on the monotonic moment-rotation response obtained with the component-based model is investigated. Then, the thickness magnitudes of "Shell 2" is empirically determined based on the analysis of the monotonic curves previously obtained. Finally, the experimental moment-rotation hysteretic curves are compared against the prediction of the component-based models.

7.3.1 Influence of "Shell 2" thickness magnitude and timber material nonlinear behaviour

Figs. 7.6 to 7.8 show a suit of monotonic moment-rotation curves corresponding to specimens S1, S2 and S3. These relationships were obtained with the component-based model using different values of "Shell 2" thickness and two different timber material models: linear and nonlinear (plasticity-damage model). The experimental and the numerical three-dimensional plasticity-damage model monotonic curves previously presented in Chapters 5 and 6 are also reproduced in Figs. 7.6 to 7.8 for referential purposes. A fair reproduction of the experimental monotonic moment-rotation curve is achieved by the component-based model in all cases. Given the simplified character of the model and the complexity of the beam-to-column joint mechanics, the precision of the model's global response prediction is very good. Nevertheless, the ability of the model to capture local failure and to quantify its influence on the global monotonic response is limited. Nevertheless, the purpose of this type of simplified macro models is not to identify the occurrence of local damage but to predict its influence on the global strength of the structure to an acceptable precision. This objective is clearly fulfilled by the proposed model. The simplified model shows better precision for specimens S1 and S2 (Figs. 7.6 to 7.7) than for specimen S3 (Fig. 7.8). This is due to the highly localized damage concentration in specimen S3.

Figs. 7.6 to 7.8 also show the influence that the thickness of "Shell 2" elements has

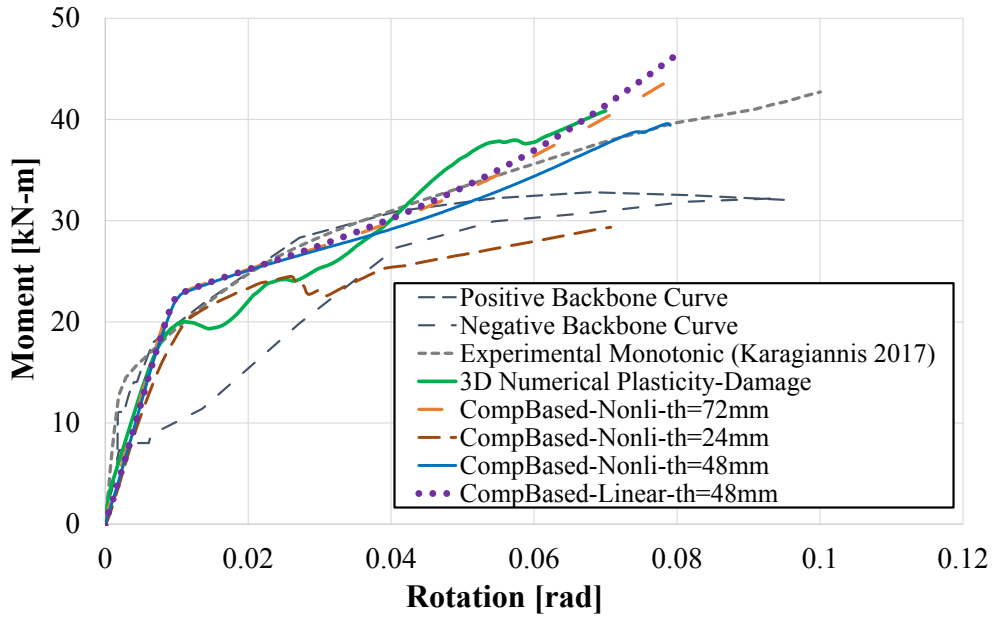


Figure 7.6: Specimen S1 monotonic curves: component-based model predictions compared against experimental test and 3D continuous model estimations.

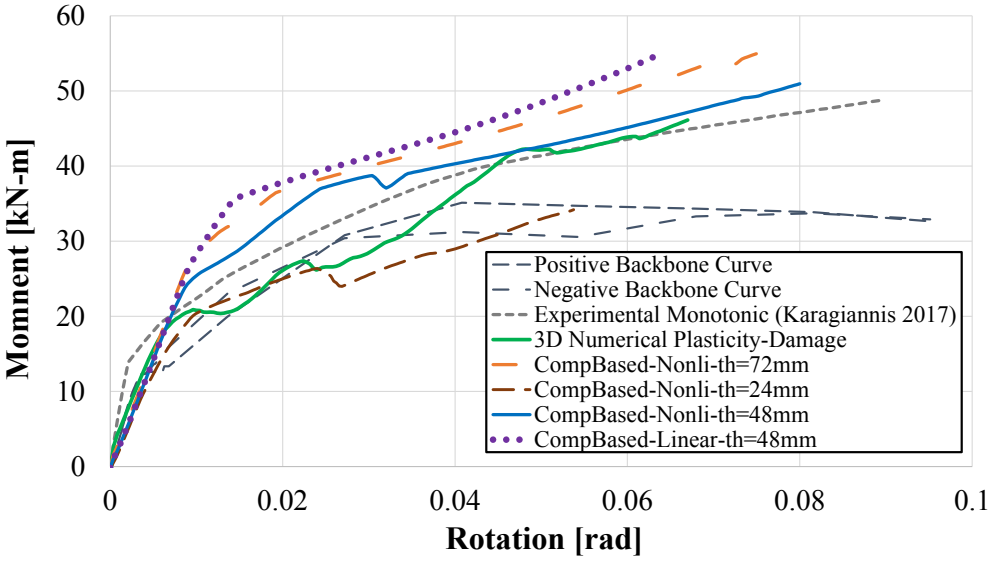


Figure 7.7: Specimen S2 monotonic curves: component-based model predictions compared against experimental test and 3D continuous model estimations.

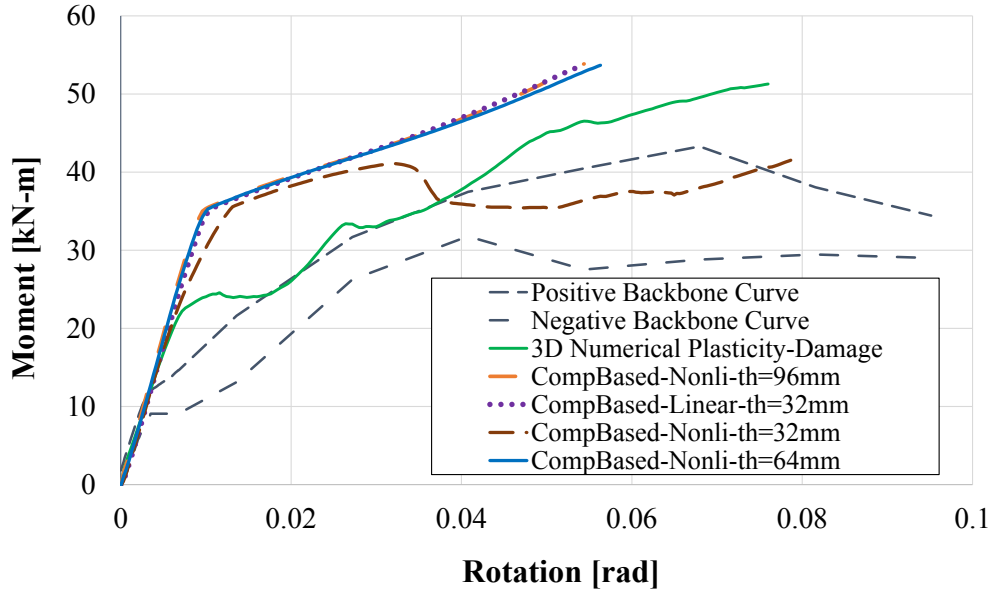


Figure 7.8: Specimen S3 monotonic curves: component-based model predictions compared against experimental test and 3D continuous model estimations.

on the component-based model predictions. It should be recalled that "Shell 2" elements fulfil the function of interacting with the steel bolts. Therefore, the thickness of "Shell 2" elements is equivalent to the width of the timber beam portion damaged by the bolts. Hence, the equivalent shell thickness (th) is proposed to be calculated as a function of the number and size of long steel bolts employed, such that:

$$th = C \cdot n \cdot d \tag{7.1}$$

where n is the number of bolts per row in the direction perpendicular to the plane, d is the bolt diameter, and C is a constant to be empirically determined. To this end, the results for C equal to 1, 2 and 3 are presented in Figs. 7.6 to 7.8.

In the case of specimens S1 and S2 (Figs. 7.6 and 7.7), the results obtained for $C = 1$ ($th = 24$ mm) are unstable and predict an unrealistic premature failure which leads to an under estimation of the connection's capacity. On the contrary, when a factor of $C = 3$ ($th = 72$ mm) is employed, the connection strengths of specimens S1 and S2 are overestimated, particularly for large levels of deformation. Therefore, an intermediate value of $C = 2$ ($th = 48$ mm) seems to provide a better prediction of the connection's global behaviour. In the case of specimen S3 (Figs. 7.8), however, there is almost no difference between the results obtained when using $C = 2$ ($th = 64$ mm) or $C = 3$ ($th = 96$ mm). A significant connection's capacity overestimation is obtained for both values of C. On the

other hand, more precise results are obtained for specimen S3 when a reduced equivalent shell thickness corresponding to $C = 1$ ($th = 32$ mm) is employed.

The influence of timber material nonlinear behaviour on the component-based model performance can also be assessed with reference to Figs. 7.6 to 7.8. For this purpose, additional curves for $C = 2$ (specimens S1 and S2) or $C = 1$ (specimen S3) employing a linear elastic orthotropic (instead of plasticity-damage) timber material model are also depicted in theses figures. For specimens S1 and S2, the monotonic curves corresponding to a linear elastic (Linear-th=48mm) and a plasticity-damage (Nonli-th=48mm) models diverge with increasing rotations. This makes sense considering that timber nonlinear behaviour plays a more important role when deformations are large. It is worth noting that for these two specimens the curves corresponding to a linear elastic material model and $C = 2$ show higher strength than the curves corresponding to a plasticity-damage material model and $C = 3$. On the other hand, for specimen S3 (Fig. 7.8) the influence of timber material nonlinear modelling is considerably higher. The linear elastic (Linear-th=32mm) and plasticity-damage (Nonli-th=32mm) monotonic curves are completely different. Moreover, the curve obtained using a linear elastic model and $C = 1$ is similar to the curves obtained using a plasticity-damage model with $C = 2$ or $C = 3$. Therefore, it can be concluded that modelling timber nonlinear behaviour, even in a simplified component-based model like the one proposed herein, is essential for a correct prediction of the structural response. Based on these results, a timber plasticity-damage model with $C = 2$ (specimens S1 and S2) and $C = 1$ (specimen S3) are used for the simulations that follow.

7.3.2 Cyclic response

Figs. 7.9 to 7.11 show the moment-rotation hysteretic curves obtained with the component-based model for specimens S1, S2 and S3. These curves are compared against the experimental results presented in Chapter 5. A remarkable match of the experimental hysteretic response of specimen S1 is achieved by the simplified model in terms of strength, loading and unloading stiffness, permanent deformations and energy dissipation. The good performance of the component-based model under cyclic loads is also related to the adequate modelling of timber-bolt contact and friction through the interface element. Similarly, an acceptable level of precision can be appreciated for specimen S2. Although there is minor over-prediction of the connection capacity (less than 20%), the other characteristics of the experimental moment-rotation hysteretic curve are well captured.

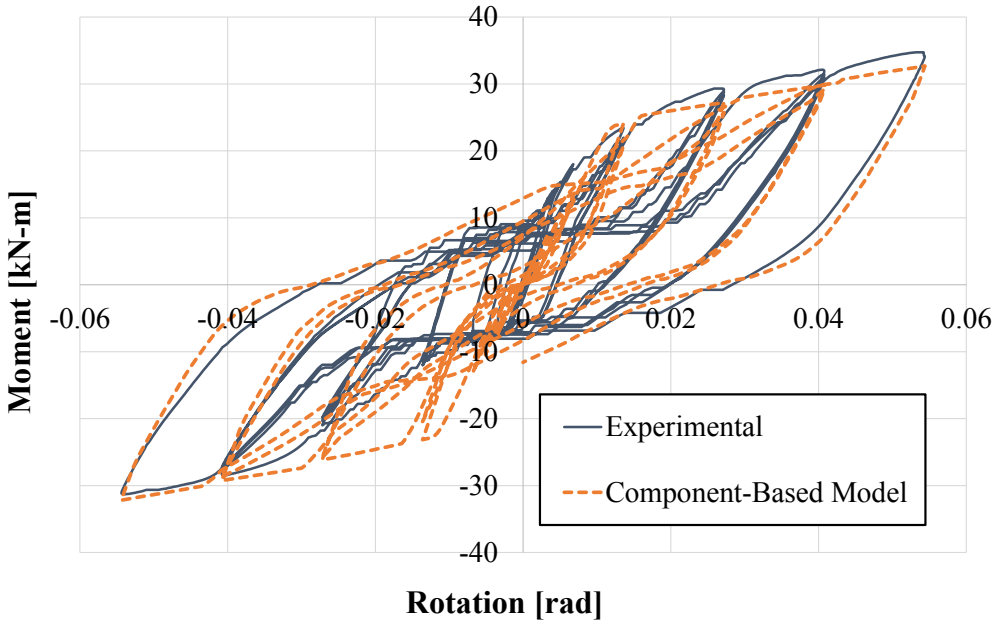


Figure 7.9: Specimen S1 hysteretic curves: component-based model compared against experimental test.

Even though the capability of the component-based model to match the experimental hysteretic response of specimen S3 is not as good as for specimens S1 and S2, a fair prediction of the connection capacity, permanent deformations, pinching behaviour and stiffness and strength degradation was obtained for large deformation levels. The simplified model's difficulty to capture the early timber local brittle failure, which occurs as a consequence of the high strength of the large steel components (bolts and angles) of specimen S3, explains the delay in the initiation of the post-elastic phase. On the other hand, the ability of the component-based model to simulate the highly nonlinear pinching behaviour of timber structures under large deformations is remarkable.

7.4 Case study: Post-tensioned timber beam-to-steel column joint

Due to the great potential of hybrid timber-steel structures, the study of damage-avoidance self-centring systems based on this kind of hybrid structures is interesting and novel. However, at the moment there are not many published references dealing with the seismic behaviour of self-centring hybrid timber-steel structures. Therefore, in this section the proposed component-based model will be used to simulate the monotonic and cyclic re-

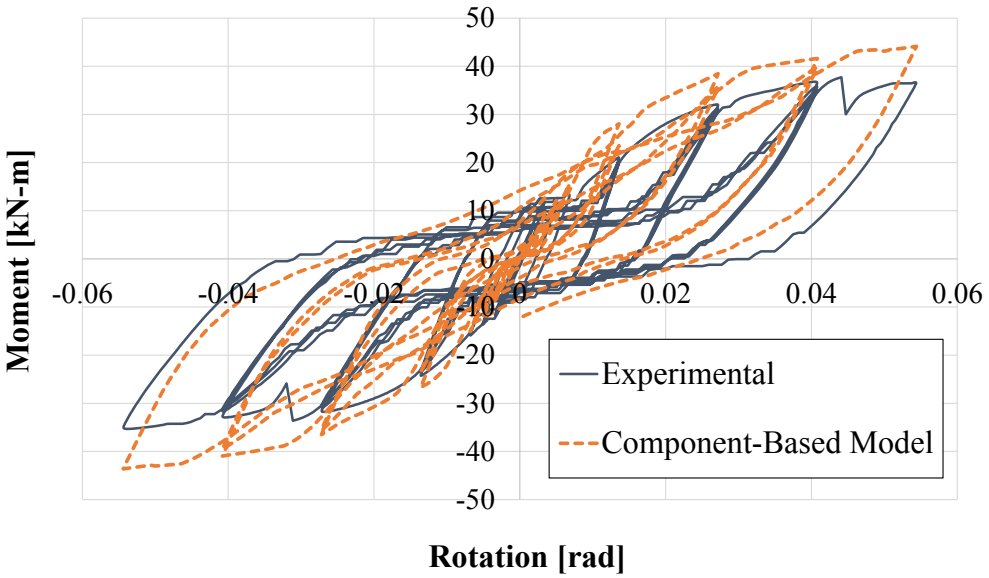


Figure 7.10: Specimen S2 hysteretic curves: component-based model compared against experimental test.

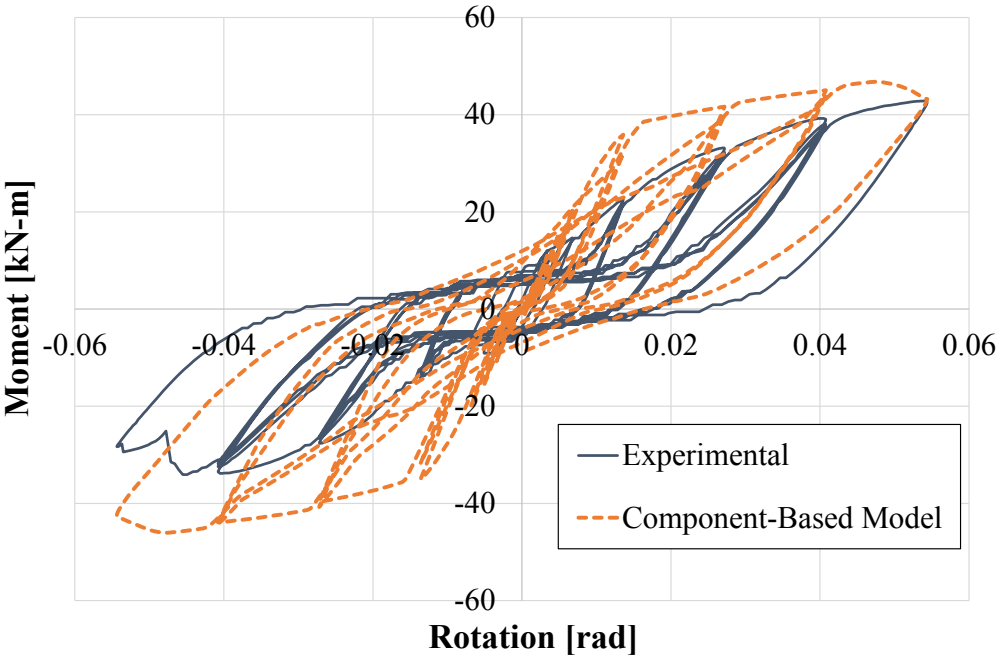


Figure 7.11: Specimen S3 hysteretic curves: component-based model compared against experimental test.

sponse of a self-centring post-tensioned timber beam-to-steel column connection.

The purpose of self-centring is to avoid or reduce damage. The proposed component-based model not only incorporates plasticity but is also capable to quantify damage levels in the timber components using a continuous approach. To this end, the tensile and compressive damage variables can be used as indices of material damage (see Section 2.2 for theoretical background and Figs. 4.15, 6.37 and 6.42 for examples of such an assessment). Thus, this model is particularly suitable for the evaluation of the efficiency of damage-avoidance structural systems like the one proposed herein. A brief literature review of a few studies on steel-only and timber-only self-centring post-tensioned systems follows below.

Ricles et al. [140] investigated the seismic response of a six-storey post-tensioned steel frame. Top and seat angles were added to the system as energy dissipation devices in which all the structural damage was concentrated. The campaign of experimental tests showed that high post-tensioning (PT) forces not only increase the moment capacity of the section but can also speed-up the steel beam flange compression yielding due to bearing stresses at the column interface. As a result, permanent damage was generated and some loss of self-centring (SC) capability was observed. The comparison between post-tensioned and typical welded moment resistant frames leaded to the conclusion that the maximum responses of both systems are similar. Then, the main advantages of post-tensioned steel frames rely on its self-centring capacity and its lower level of structural damage after an earthquake. Nevertheless, the numerical studies showed that residual deformations can also occur in post-tensioned steel frames, especially when plastic hinges are formed at the base of the columns.

Christopoulos et al. [19] studied a post-tensioned moment connection for wide flange steel frames. However, PT bars instead of strands, and energy-dissipating (ED) bars instead of angles, were employed in this investigation. The ED bars were inserted into steel cylinders to allow yielding in compression without buckling. An initial PT force of 1310 kN (655 kN per each bar) was applied to the connection. The initial PT force controls the magnitude of the decompression moment. Once this moment has been exceeded, the gap opening is generated and the rotational stiffness of the connection is provided by a combination of the elastic stiffness of the post-tensioned bars and the post-yielding stiffness of the ED bars [19]. After a cyclic loading test up to a maximum drift of 4%, full self-centring and no damage was observed in the beam-to-column connection specimen. Nevertheless, unloading stiffness degradation was observed for drifts higher than 2% [19].

Garlock et al. [55] performed experimental studies of six full-scale PT steel connection with bolted top and seat angles subjected to cyclic loading. The vertical shear in the connection was resisted by both, the top and seat angles and the friction generated by the compression force in the beam-column interface. It is important to note that a mechanism formed by the three plastic hinges was generated in the tension angle, whereas only one plastic hinge was formed in the compression angle. Garlock et al. [55] analysed the cyclic variation of the PT tendon force in function of the connection moment-beam plastic moment ratio. After decompression moment, a fast increase of the PT force was observed. The authors stated that using many strands or large bars has the following two advantages: 1) a larger connection stiffness is achieved after decompression; 2) a greater deformation capacity is obtained since the initial PT force is smaller [55]. On the other hand, beam local buckling caused loss of self-centring capacity and beam shortening. In turn, this leaded to loss of PT force, diminish of connection strength, and eventually, loss of the PT connection capability to resist gravity loads (global instability).

Kim and Christopoulos [94] presented three levels of numerical modelling techniques to study the seismic response of post-tensioned self-centring steel frames. First, a sectional analysis [19] was developed to capture the monotonic response of the PT connection for lateral deformation levels within the SC range (lateral drift less than 4%). Good results are obtained when compared with experimental results, and for this reason, it was expected that this procedure be useful as a design tool. Second, an enhanced component-based spring model of the PT connection is incorporated into a frame model to capture its cyclic response for a maximum lateral deformation within the SC range. Third, a refined non-linear FE model capable to predict the ultimate response of a SC-PT steel frame beyond its self-centring limit state is presented and described in detail.

Dimopoulos et al. [37] designed, modelled and assessed a SC steel PT connection with web hourglass shape pins (WHPs) energy dissipation devices. A simplified component-based model of the PT connection consisting of fibre beam-column elements, hysteretic and contact springs was employed in the seismic analysis of the SC lateral-resisting system. The design procedure of the SC lateral-resisting system followed the criteria developed in [56], for which an energy dissipation ratio (β) equal to 0.31 was employed. Based on the definition given in [20], β is defined as:

$$\beta = \frac{M_s}{M} \tag{7.2}$$

where M is the total moment strength of the beam-to-column joint, and M_s is the moment strength provided by the energy dissipation devices exclusively.

Finally, Guo et al. [62] conducted a seismic fragility analysis of a self-centring moment resistant frame (SC-MRF) with web friction ED devices. The need of a comprehensive numerical model for collapse and fragility analysis was emphasised. Such a model should be capable to simulate special features of the structure's behaviour, like strength cyclic degradation. The authors stated that the seismic fragility of this type of novel systems subjected to random ground motions has been barely studied, and that this type of analysis is crucial for the development of a reliability-based design method.

Among the studies on timber-only self-centring systems, Palermo et al. [130] presented a post-tensioned timber frame based on laminated veneer lumber (LVL) material as an advantageous alternative for low-rise multi-storey buildings due to its low mass, good seismic performance, flexibility of design and reduced construction time. The seismic performance of an innovative type of ductile beam-to-column connection assembled by means of unbonded post-tensioning techniques were experimentally investigated through quasi-static cyclic tests of exterior beam-to-column joint sub-assemblies. Similarly than in the case of steel self-centring moment resisting frames, the seismic performance target of post-tensioned timber frames is the achievement of large inelastic deformations, low-damage levels and full re-centring capacity after an earthquake. Contrarily to the traditional timber connections, the inelastic demand in post-tensioned connections is taken by the gap opening mechanism, while the damage is concentrated on the internal energy dissipation yielding devices. Due to the joint rocking motion, contact bearing stresses loaded the column in the direction perpendicular to the grain, leading to some degree of timber material non-linear behaviour. The authors claimed that, for moderate levels of seismic intensity, properly designed connections do not experience LVL crushing at the beam-column interface. However, it was also recognized that the low strength and stiffness in the direction perpendicular to the grain characteristic of timber-based materials is a major disadvantage for its use as columns.

Newcombe et al. [124] undertook a complete treatment of the mechanics of post-tensioned ductile timber connections with internal and external energy dissipation epoxied mild-steel rods. This was complemented with an extensive experimental testing on beam-to-column, wall-foundation and column-foundation LVL timber sub-assemblies. As a consequence, a simplified section analysis of PT timber joints, similar to the previously described in [19], was adapted from the existing methodology originally developed for

precast concrete ductile connections. The simplified model was calibrated against the experimental results and its accuracy was verified using a numerical model. The authors stated that in post-tensioned connections the occurrence of plastic deformation is expected, and as a consequence, it needs to be considered and modelled for design purposes. The presence of timber plastic deformation in the direction perpendicular to the grain was identified as one of the main reasons for the diminish of self-centring capacity. Finally, significant differences between the experimental and the numerical responses were encountered. It was concluded that one of the most important reasons for this discrepancy was the lack of timber plastic behaviour modelling. Besides, the importance of numerical modelling capability to take into account the loss of post-tensioning force due to elastic shortening was also pointed out [124].

Iqbal et al. [78] conducted experimental tests on both interior and exterior post-tensioned LVL beam-to-column connections. The authors concluded that local material non-linear behaviour of LVL at the beam-column interface due to contact compression stresses was responsible for the loss of PT force and for the occurrence pf minor hysteretic energy dissipation. For the prediction of the cyclic behaviour of the specimens with ED devices, two types of numerical models were elaborated: 1) Lumped plasticity model; and 2) Multi-spring model. From the obtained results it can be concluded that the lumped plasticity model shows difficulties to capture the position of the yielding point and to trace the unloading path of the hysteresis. On the other hand, the more refined component-based multi-spring model represented with higher precision the influence of both, the gap-opening mechanism and the energy dissipation yielding devices, on the hysteretic behaviour of the connection. In similar fashion to the component-based models described above for steel SC-PT systems, this type of models allows a better prediction of the stress and strain distributions at the beam-column interface, the yielding point, the unloading stiffness, the residual deformations, the neutral axis position, and the PT force variation as a consequence of the gap opening and the beam axial deformation [78].

Lastly, Valipour et al. [175] developed a 2D continuum FE model for the analysis of post-tensioned Laminated Veneer Lumber (LVL) timber frames subjected to cyclic lateral loading. The strategy followed to model the timber non-linear behaviour consisted on the superposition of two element types: an isotropic continuum matrix and smeared uniaxial reinforcing fibres in the direction parallel to the grain. The combination of both types allows to simulate timber orthotropy in a plane stress state. This modelling technique was applied to the study of the cyclic behaviour of post-tensioned timber-concrete composite (TCC) structures. In this particular case, the TCC building consisted on tim-

ber frames (beams and columns) and concrete slabs. It is mentioned that, in general, one-dimensional beam elements rely on component-based lumped models which require previous calibration every time a new specimen is analysed. For this reason, the popularity of continuum FE models is continuously raising [175]. Continuum models are less dependent on calibration because they rely on basic properties at the material level, like stress-strain curves. In this study, the level of damage in the timber column is assessed through the contour plots of the normal stress in the direction perpendicular to the grain. The beam-column interface was identified as the zone of highest damage for this type of structural systems [175]. In any case, continuum FE models do not always provide an accurate prediction of the global response. For instance, the comparison between the experimental and numerical lateral load-deformation hysteresis of a three-storey post-tensioned timber frame showed that the model failed to reproduce energy dissipation [175]. Finally, despite of being limited to bidimensional plane stress models only, it is noteworthy that this is the only reference found that makes use of continuum FE models to assess the cyclic response of post-tensioned timber frames. Unfortunately, no reference dealing with three-dimensional non-linear FE models of post-tensioned timber frames was spotted.

The mechanics and seismic resistant properties of self-centring post-tensioned beam-to-column joints were briefly reviewed above. Besides, modelling techniques with different levels of complexity that has been employed for analysing these structural systems were summarized. Both timber and steel self-centring post-tensioned structures were considered, and the lack of studies that combine both materials in hybrid systems is striking. Despite component-based models are generally used for assessing the response of SC-PT structural systems, only one reference [175] employed bidimensional continuum elements to model timber components. Moreover, component-based models of SC-PT structures that incorporate plasticity-damage constitutive models to simulate wood nonlinear behaviour have not been used yet. For these reasons, the applicability of the proposed component-based model on the numerical study of the seismic response of this kind of high performance structural hybrid timber-steel system is of interest.

7.4.1 Model description

The same timber beam-to-steel column sub-assembly examined through all this thesis is employed in this section for the study of post-tensioned connections. For this purpose, steel bars are added to the numerical model and post-tensioning forces are applied. The

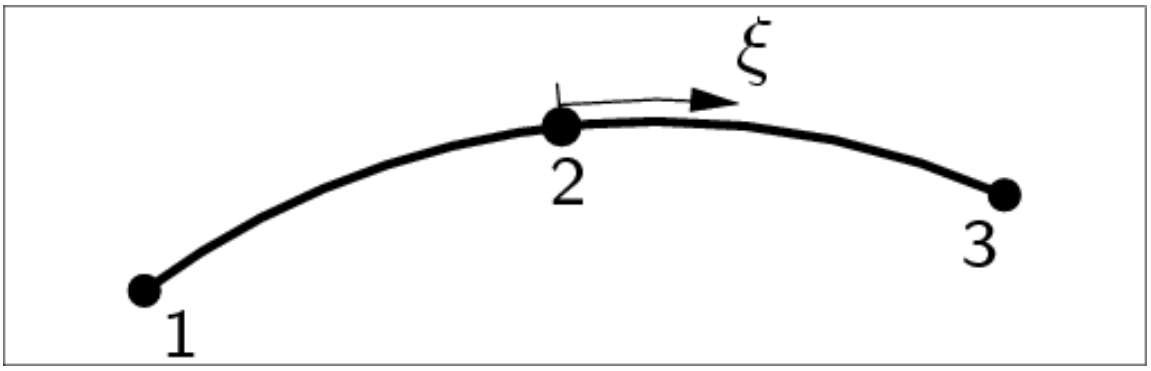


Figure 7.12: Cable element used for modelling the post-tensioned steel bar (Figure taken from DIANA User's manual [35]).

steel bars are represented in the model by horizontal cable elements with three nodes and three degrees of freedom per node. These elements are connected to the column and to the beam free end. Fig. 7.12 shows an example of this kind of cable elements [35]. Therefore, the post-tensioned bars pass next to the beam lateral sides, parallel to the beam longitudinal axis. Fig. 7.13 shows a lateral view of the component-based model including the post-tensioned bars.

7.4.2 Post-tensioning force

The design verification example outlined here uses the energy dissipation ratio, β [20], as a design parameter. This is necessary for the determination of the required post-tensioning force and the size and quantity of the dissipative steel components [164]. The top and seat steel angles of specimens S1, S2 and S3 are used as energy dissipation devices. The required post-tensioning force magnitude (F_{pt}) can hence be determined from the definition of the energy dissipation ratio (β) in Eq. 7.2 as follows:

$$M_{pt} = \frac{1-\beta}{\beta} M_s \tag{7.3}$$

$$F_{pt} = \frac{M_{pt}}{h} \tag{7.4}$$

where M_s is the bending moment strength provided the steel angles, M_{pt} is the bending moment strength provided by the post-tensioning steel bar, and h is the timber beam depth.

The size and quantity of the post-tensioning steel bars or cables depend on their yield

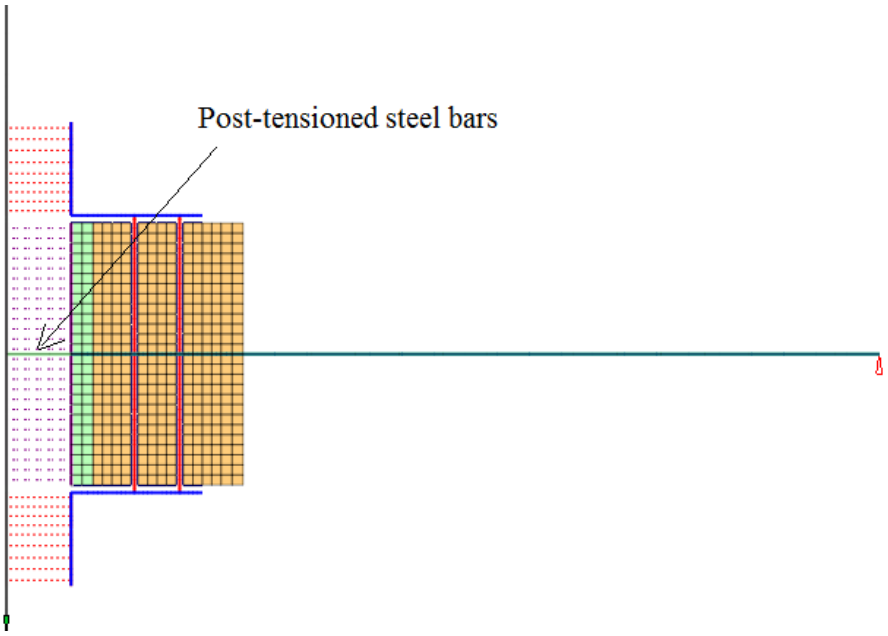


Figure 7.13: Lateral view of the component-based model including the post-tensioned steel bars.

strength and on the magnitude of the post-tensioning force to be applied. High-strength (1050 MPa yield strength) steel bars of 25 mm diameter are employed. Design information related to the post-tensioning force magnitude, the number of steel bars, the total post-tensioning steel area and the initial pre-stress to be directly applied to the bars is provided in Table 7.1 for specimens S1, S2 and S3, and for three values of energy dissipation ratios (β = 0.3, 0.5 and 0.75).

A value of $\beta = 0.3$ is commonly used for the design of PT steel frames [56, 37]. Nevertheless, the consequences of a reduction in post-tensioning forces on the decrease of the joint capacity, loss of self-centring capabilities, increment of energy dissipation, and strength and stiffness degradation are worthy to be numerically investigated by means of a powerful numerical tool like the component-based model proposed herein. For this reason, case studies including values of $\beta \geq 0.3$ are incorporated into the analysis. It should be noted that the required post-tensioning force magnitude is lower for higher values of β. Besides, the multiplication of the total cross-sectional area of the post-tensioning steel bars times the initial applied pre-stress should be equal to the required design post-tensioning force. The numerical monotonic and cyclic responses obtained for the cases outlined in Table 7.1 are presented and discussed in the following sections.

Table 7.1: Case studies: Post-tensioned timber beam-to-steel column joint

β	**Specimen**	**PT force** [kN]	**No. bars**	**Steel area** [mm^2]	**Initial PT** [MPa]
0.3	S1 or S2	289	2	982	295
0.3	S3	446	2	982	455
0.5	S1 or S2	124	2	982	127
0.5	S3	191	2	982	195
0.75	S1 or S2	41	2	982	43
0.75	S3	64	2	982	65

7.4.3 Monotonic response

Figs. 7.14 to 7.16 show the numerical moment-rotation monotonic curves obtained for specimens S1 to S3, with and without post-tensioning. A total of four curves are shown in each graphic. The monotonic response without post-tensioning force is also shown in these figures. The other curves correspond to post-tensioned connections with three different values of energy dissipation ratios (β= 0.3, 0.5 and 0.75).

The first important difference between the case studies with and without post-tensioning is that the former show a considerable increase in its initial stiffness. This observation is valid for the three specimens. As expected, due to the fixed amount and size of the steel dissipative angles corresponding to each specimen, the lower the value of β, the higher the post-tensioning force, and thus, the higher the moment capacity of the connection. The capacity of the connections with post-tensioning is more than twice the capacity of the connection without post-tensioning for the three specimens. On the other hand, global yielding occurs at a rotation of around 0.01 rad in all the cases, including that without post-tensioning. Even though a higher value of post-tensioning force produces a slight increment of the yielding rotation, its effect is very small in comparison with the magnitude of the post-tensioning force increment.

It is worth noting that, despite their higher strength, the monotonic curves of post-tensioned cases show a maximum capacity point followed by a gradual strength degradation for higher levels of deformation. This strength reduction is associated with the

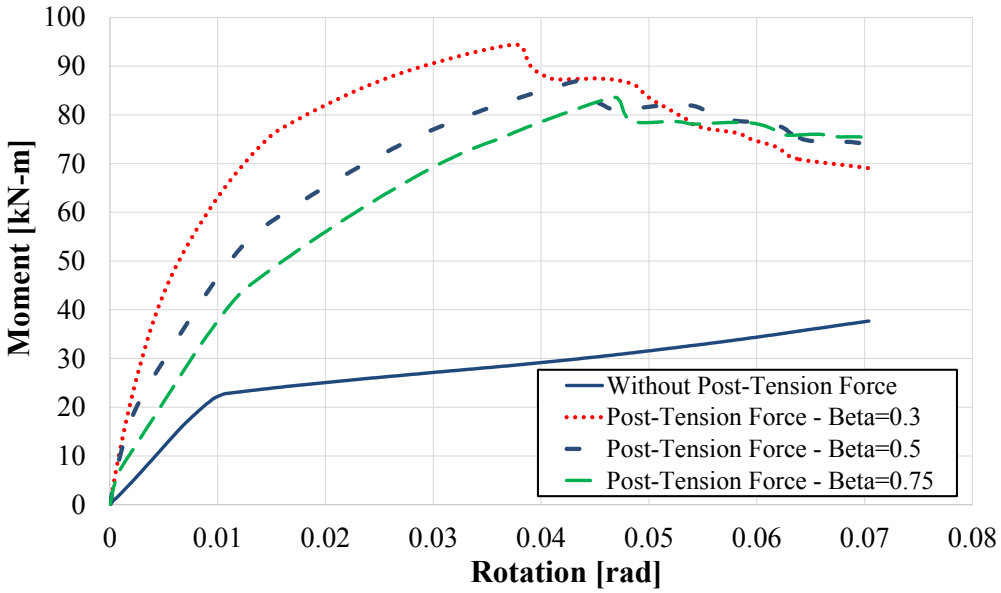


Figure 7.14: Moment-rotation monotonic curves of specimen S1 with post-tensioning.

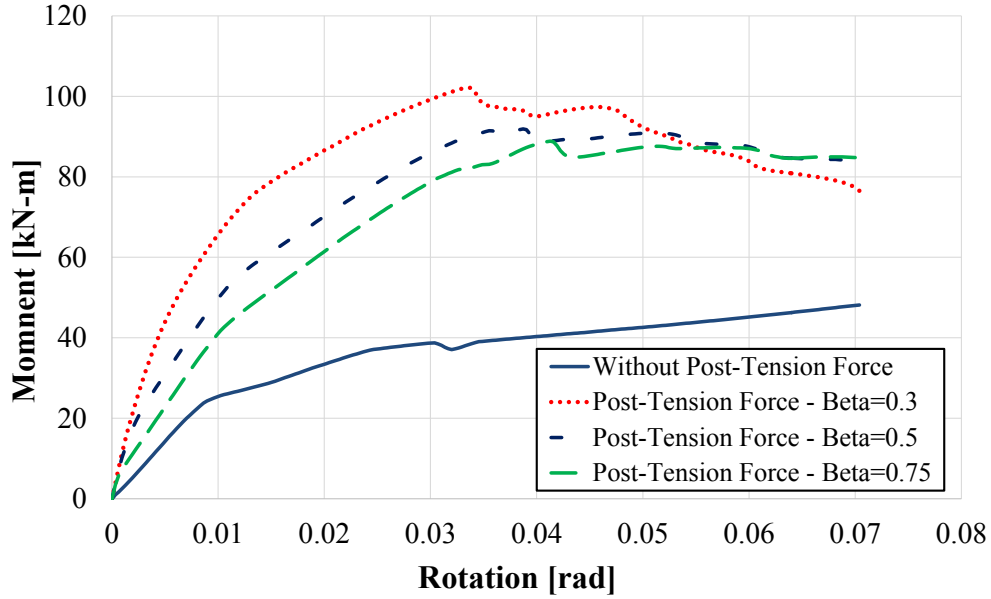


Figure 7.15: Moment-rotation monotonic curves of specimen S2 with post-tensioning.

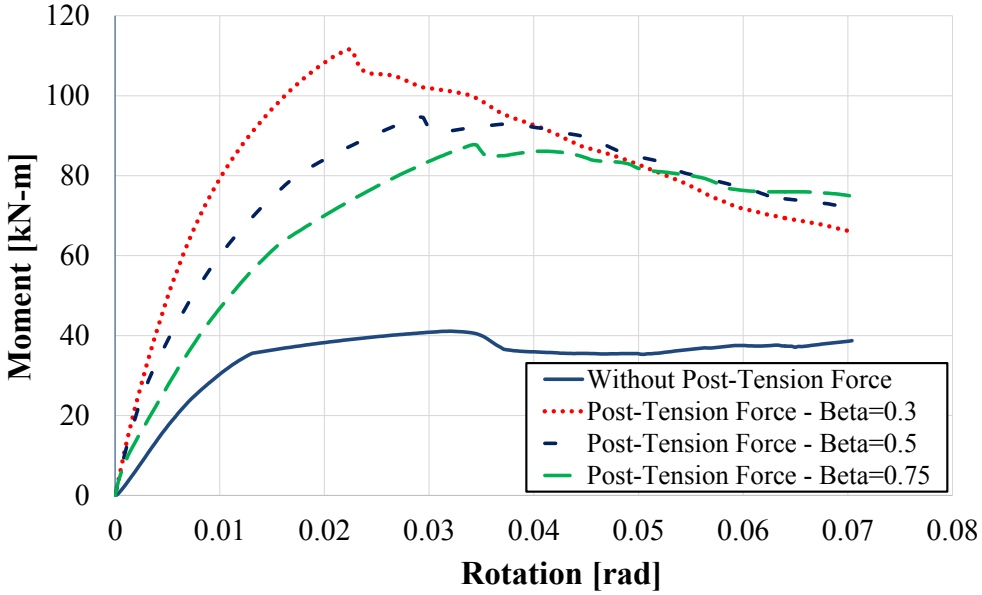


Figure 7.16: Moment-rotation monotonic curves of specimen S3 with post-tensioning.

loss of pre-stress as a consequence of local timber failure around the steel bolts [55, 78]. Therefore, Figs. 7.14 to 7.16 show that the ductility of the post-tensioned connections is limited in comparison to that of the connection without post-tensioning. A ductility value of around 3 is obtained in all the post-tensioned connections. Slightly higher ductility values are obtained for the cases with higher values of β (lower post-tensioning force). This is not the case for connections without post-tensioning, which show a sustained mild hardening response after yielding, and therefore, no clear maximum capacity.

Finally, it is interesting to note that after reaching their maximum capacity, all moment-rotation curves concur to the same residual bending moment magnitude, irrespective of the value of β. This residual moment strength is related to the new equilibrium post-tensioning stress in the steel bar, after wood failure has occurred. This is a characteristic property of well-designed post-tensioned structural systems (i.e. enough post-tensioning steel area is provided not to reach the yield strength even at large deformation levels) which makes them safe and reliable even after reaching their maximum capacity.

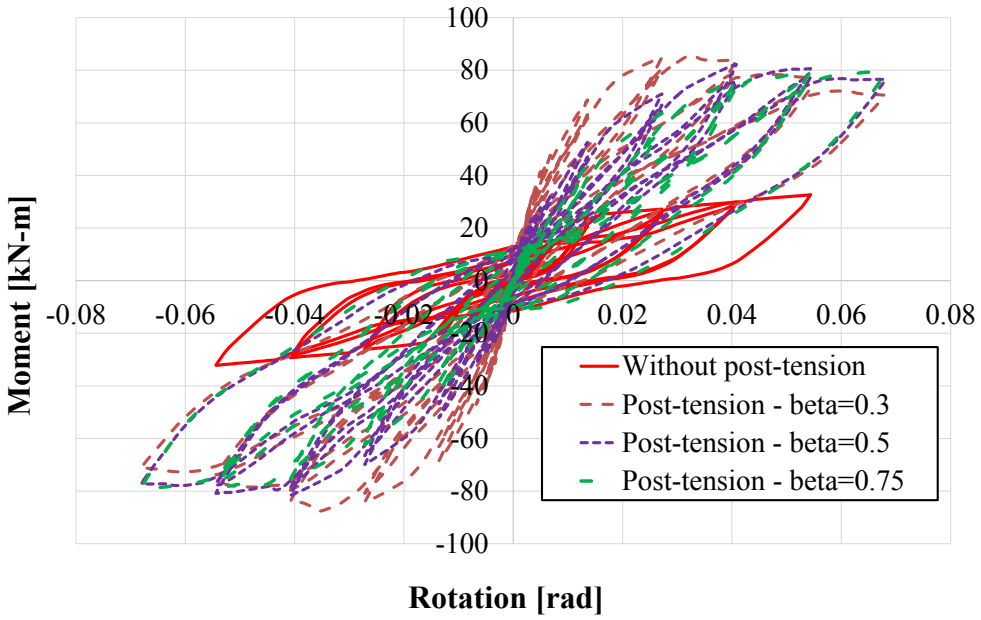


Figure 7.17: Specimen S1 hysteretic curves with and without post-tensioning.

7.4.4 Cyclic response

In the experimental study carried out in Section 5.3 specimen S1 showed a better seismic performance than specimens S2 and S3. Therefore, from a seismic design point of view, future hybrid timber-steel buildings are expected to incorporate connections similar to specimen S1. Furthermore, the precision of the component-based model to predict the hysteretic response of specimen S1 is better than for the other specimens (see Section 7.3.2). For conciseness, only the cyclic response of specimen S1 with post-tensioning will be discussed in this section. In this way, the discussion can be focused on the influence of β on the hysteretic response of this type of post-tensioned connections.

Fig. 7.17 shows the moment-rotation hysteretic curves corresponding to specimen S1 with and without post-tensioning. β values equal to 0.3, 0.5 and 0.75 were considered. At first glance, Fig 7.17 confirms the higher capacity brought about by the post-tensioning. The three post-tensioned case studies show a maximum strength of approximately 2.5 times the strength of that without post-tensioning. Furthermore, the permanent deformation magnitudes are clearly smaller when post-tensioning is applied (self-centring). On the other hand, no significant differences are encountered between the energy dissipation capacities of the four hysteretic curves. This was expected considering that the sizes of the steel components are the same for the four case studies.

Fig 7.17 highlights the influence of β on the initial stiffness of the connections. The hysteresis loops of β=0.3 (with the highest initial post-tensioning force) show that an early timber local failure occurs at a rotation magnitude around 0.035 rad due to its high initial stiffness and strength. It is interesting to note that after this point the size and shape of the hysteresis loops corresponding to the following cyclic amplitude (equal to 0.057 rad) are similar for the three cases, irrespective of the value of β. Such a similar behaviour for large deformation levels confirms the observation made in the previous section regarding their monotonic response. After local timber failure around the steel bolts occur in the curve corresponding to β=0.3, a reduction of the post-tensioning force takes place before reaching a new equilibrium state. This force reduction seems to be independent of the initial value of the post-tensioning force, being this the reason why the hysteretic curves of the three case studies coincide at this particular cyclic amplitude.

On the other hand, a noticeable self-centring capability is appreciated for the three post-tensioning case studies. As expected, less permanent rotations are obtained for the case study with the highest initial post-tensioning force (β=0.3). Nevertheless, the hysteresis loops corresponding to a cyclic amplitude of 0.068 rad clearly show that a higher initial post-tensioning force also implies a more accelerated cyclic strength and stiffness degradation. This together with the early local timber failure noted above, support the conclusion that a high post-tensioning force corresponding to β=0.3 does not result in a good seismic performance. Instead, lower post-tensioning forces (e.g. $\beta = 0.5$ or $\beta = 0.75$) are able to provide a significant increment of strength with respect to the case without post-tensioning, avoid timber local failure, increase ductility and diminish the cyclic degradation of strength and stiffness.

7.5 Concluding remarks

The proposed model is an original mixed version of a three-dimensional continuous model combined with a component-based macro model, which brings together the advantages of both approaches. Accordingly, Timoshenko beam elements and isoparametric shell elements are used for modelling the timber beam, instead of the more expensive solid elements used in 3D models. In addition to their efficient formulation, the main advantages of the beam elements employed in the proposed component-based model are their capability to take into account the influence of shear deformations and to directly interact with continuous isotropic 3D constitutive material models. Therefore, beam elements are ideal for modelling steel components like bolts and angles. On the other hand, contin-

uous shell elements are capable to incorporate orthotropic constitutive material models like the one developed in this thesis (Chapter 3). Thus, shell elements are particularly suited for simulating timber local deformation as a consequence of its interaction with the steel bolts. Moreover, a bidimensional timber-steel interface element, which simulates contact and friction between the two bodies, completes the set of primary elements of the component-based model.

The foundation basis of the proposed simplified component-based macro model is composed of the three element types described above, in addition to the wood constitutive model developed and formulated in Chapter 3. This means that both plasticity and damage are taken into account for simulating wood material nonlinear behaviour. Therefore, in spite of being a simplified model, it keeps the most relevant advantages of the 3D continuous modelling approach developed in Chapter 6. This original feature, not previously incorporated in other component-based models for timber structures, is fundamental for capturing pinching behaviour and matching the experimental load-deformation curves.

The proposed component-based model demonstrates a remarkable precision for simulating the global monotonic and hysteretic behaviour of the timber beam-to-steel column joint studied herein, in terms of connection capacity, stiffness and strength degradation, permanent deformations and energy dissipation. In this way, the importance of an adequate modelling of timber material nonlinear response, even in the case of simplified component-based models, is demonstrated.

The component-based model performance is not uniform for all the specimen types. The best performance is obtained for those timber dowelled structures with small steel components, which better comply with the seismic design philosophy. On the contrary, the response of systems which experience early timber local failure and high pinching behaviour is more difficult to simulate using a simplified macro model.

The capability of the proposed simplified model to capture the global hysteretic response of self-centring post-tensioned timber-steel beam-to-column joints was demonstrated in this chapter. Once the component-based model is elaborated, it is relatively easy to introduce post-tensioning into the analysis. Only a geometric non-linear cable element representing the steel bars should be added to the model together with an initial pre-stress. Besides, a straight-forward methodology is used to determine the magnitude of the post-tensioning force as a function of the energy dissipation ratio and the size of the top and seat steel angles.

The component-based model was totally capable of reproducing the self-centring behaviour characteristic of post-tensioned structures (i.e. flag-shape hysteresis loops and reduced permanent deformations). The monotonic results obtained shows that both the initial stiffness and the maximum capacity of the connection with post-tensioning are considerable higher than those of the connection without post-tensioning. For instance, the maximum strength of a connection with post-tensioning can be as high as twice the capacity corresponding to the same connection without post-tensioning. Furthermore, strength degradation and limited ductility was observed for the cases with post-tensioning force. Finally, it is concluded that higher initial post-tensioning forces not always lead to a good seismic performance. Contrarily, early local timber failure, cyclic strength and stiffness degradation, and the connection's ductility reduction can be generated as a consequence.

The component-based model can be built in a simple way and has a good numerical performance in terms of computational cost. Given its smaller size and the less expensive types of elements employed, the running time is negligible compared to a full 3D continuous model. For instance, the monotonic analysis of specimens S1 to S3 using the 3D continuous model took an average of ten to twelve hours, while the same analysis was completed in less than 1 hour with the component-based model. An efficiency increment of more than 90% can be obtained without loosing significant precision at the global level.

For all the reasons mentioned above, the component-based model can be perfectly implemented in the engineering professional practice, particularly when timber dowelled connection nonlinear behaviour needs to be assessed for design purposes. Moreover, its applicability as a numerical tool for advanced numerical assessment of the seismic performance of innovative timber post-tensioned structures is also promising. Taking into account its capability to accurately simulate the nonlinear hysteretic response of timber structures and the low computational cost associated, the component-based model can be used as an advanced numerical tool for further research on the calculation of seismic fragility curves and collapse capacities of innovative damage-avoidance timber-steel frame structural systems.

Chapter 8

Conclusions

This chapter summarizes the findings of the thesis. Additionally, as a result of the contributions made in this thesis, new fields of research have been found and are also presented below.

8.1 General conclusions

In general, continuum 3D FE models are an important tool for acquiring a better understanding of wood's nonlinear behaviour, especially when dealing with highly localized nonlinearities. Furthermore, when properly defined, continuum 3D FE models can provide accurate predictions of the seismic response of structures up to ultimate deformation levels leading to collapse, a particularly challenging task that is required by state-of-the-art Performance-Based Seismic Design and Assessment (PBSDA) methodologies. For timber structures, in particular, continuum 3D FE modelling is especially suited because it is the only consistent numerical approach that can: 1) predict the location and size of potential cracking zones; and 2) enable an assesment of the influence of local damage and plastic deformations on the global response of the structure. In this regard, it can be said that 3D FE modelling is the only numerical approach that is a realistic alternative to experimental investigations.

Society's interest on expanding the boundaries of timber structures is growing faster than the progress made in the development of advanced numerical tools with comparable levels of accuracy to those already available for more traditional materials like concrete or steel. To overcome this gap, this thesis advances a complete three-dimensional plasticity-damage constitutive model for timber. The model's conceptual development, its mathe-

matical formulation, numerical coding and implementation have been documented in the previous chapters of this thesis. The model has been incorporated in the FE software DIANA under the framework of a user-supplied subroutine (USS). However, enough information, including its algorithmic design, is provided to allow its implementation in any other FE software. It has been demonstrated that this material model captures the key features of wood cyclic nonlinear behaviour at the material and component levels, including: i) cyclic stiffness and strength degradation, ii) brittle local failure due to tensile and shear stresses, iii) ductile local failure due to compressive stress, iv) stiffness recovery after load reversal (crack opening and closing), and v) permanent plastic deformation due to compressive stress. To the author's knowledge, this is the first timber constitutive model tailored to the reproduction of the cyclic response of wood, expected during earthquake action.

The conceptual core of the material model formulation is based on three theoretical components: continuum damage mechanics (CDM), orthotropic plasticity theory and spectral decomposition. Each of them accomplishes key functions that, joined together, build up the model's overall performance. CDM is responsible for the incorporation of brittle failure, stiffness degradation and the identification of crack formation zones. Plasticity, on the other hand, allows the modelling of ductile failure and the quantification of permanent plastic deformations due to compressive stresses. Finally, spectral decomposition enables the definition of different independent post-elastic responses for tensile and compressive failures. This approach made possible the definition of a "compression-only" plasticity formulation, which is grounded on the typical wood post-elastic behaviour. This is an original characteristic of the plasticity-damage model proposed herein.

The material model has been validated at the component level by comparing the numerical results obtained against experimental data corresponding to three types of timber-steel connections:

- Timber brace-steel plate connection subjected to axial monotonic and cyclic loading (Chapter 4).
- Timber beam-steel plate connection subjected to mid-point transversal monotonic loading (Chapter 4).
- Timber beam-to-steel column moment connection subjected to monotonic and cyclic bending moments (Chapter 6).

In general, it is concluded that the overall nonlinear responses of timber-steel dowelled connections subjected to monotonic and cyclic loads are accurately predicted by the proposed plasticity-damage model. Both the maximum connection capacity and the cyclic stiffness degradation are well captured. Moreover, in the particular case of cyclic loading, a good correlation was found between the experimental and numerical hysteretic curves until large deformation demands.

On the other hand, it is proved that CDM offers a fair combination of accuracy and versatility, making it the most efficient approach for capturing both global and local nonlinear behaviour, particularly when dealing with cyclic loading conditions. Furthermore, plasticity-damage models are demonstrated to be more fit for simulating the monotonic and cyclic response of timber dowelled connections than plasticity-only models. To this end, damage mechanics allows the simulation of progressive stiffness degradation characteristic of timber structures since early loading stages, and for that reason, achieves a close match with the experimental curves and an accurate estimation of the connection load capacity. By contrast, plasticity-only models produce stiffer responses that cause divergence between numerical and experimental curves, and thus, overestimation of the connection capacity. Therefore, it is concluded that the incorporation of continuous damage evolution is essential to capture timber stiffness degradation, and consequently, to obtain a good agreement between numerical and experimental global responses.

At the local level, this thesis demonstrates the applicability of damage mechanics to the identification of potential cracking zones and the quantification of structural damage in timber structures due to the action of cyclic loads. Strains in the direction perpendicular to the grain and tensile damage variable contour plots obtained from the FE model were compared against the experimentally measured Digital Image Correlation (DIC) strain fields. The information provided by the DIC proves that the tensile damage variable is a good indicator of crack zones locations. However, neither the orientation nor the status (closed or open) of cracks can be determined based on the tensile damage variables.

It is also concluded that, especially in timber structures, the use of an appropriate contact model which simulates the interaction between the steel fasteners and the surrounding wood is as important as a suitable wood constitutive model. An accurate description of this interaction is required to reproduce the pinching behaviour characteristic of timber dowelled structures, to capture the large localized plastic deformations around the fastener holes, and to accurately quantify the frictional forces generated in the interface. For this reason, this thesis has proposed, formulated and implemented an

interface contact model tailored to the simulation of timber-steel fastener interaction.

Finally, it was demonstrated that embedment tests are useful for the investigation of the local nonlinear behaviour of wood under the action of concentrated stresses generated by the steel fasteners. Moreover, they are relatively simple to implement for monotonic loading, and are generally employed for material characterization in timber engineering practice. For these reasons, a feasible, efficient and precise procedure based on embedment test load-deformation curves is proposed in this thesis for the calibration of the wood material model and the interface contact model.

Overall, the ability of the proposed finite element model, including continuous plasticity-damage and contact modelling, to simulate the behaviour of complex timber beam-to-steel column connections for different levels of deformation has been demonstrated. The proposed plasticity-damage constitutive model for wood under cyclic loads relies on an efficient and reliable algorithm which implementation in a widely-used FE software opens the door for realistic simulations to be performed by the broader structural engineering community. Therefore, this thesis represents a fundamental first step towards a faithful estimation of the ultimate capacity of timber structures subjected to extreme loads such as earthquakes and, as a consequence, a more genuine assessment of their performance.

8.2 Specific findings

8.2.1 Performance of the wood constitutive model at the material point level

The plasticity-damage constitutive model was successfully tested at the material level by means of several simple case studies corresponding to different stress states (tension, compression, shear, uniaxial, biaxial and triaxial), loading conditions (monotonic and cyclic) and directions with respect to the grain alignment (0°, 45° and 90°). The stiffness degradation that occurs in timber under the action of tensile stresses is considerably higher than under the action of compressive stresses. The mixed normal-shear stress state generated by a load at 45° introduces a mixed hardening-softening post-elastic response that is consistent with the simultaneous presence of compressive and tensile stresses acting in different directions. It has been demonstrated that the combined brittle-ductile failure mode associated with this stress-state is well represented by the model under both monotonic and cyclic loads.

Besides, it has also been shown that strain localizations produce mesh dependency. Although the crack band method can efficiently avoid it, a prior mesh refinement analysis is required to determine the appropriate mesh size. However, for timber dowelled connections very small elements in the zone around the dowels should be avoided due to their potential to generate spurious stress concentrations in the contact zones, which can lead to an unrealistic underestimation of the connection maximum capacity.

8.2.2 Plasticity-damage model

In addition to the standard input parameters of classical orthotropic plasticity models, the proposed plasticity-damage model requires a total of six additional parameters, namely: mixed-mode fracture energy density (G_f), characteristic length (l_{ch}), exponential softening constant (n), plasticity hardening modulus (h), compressive damage hardening constant (β) and compressive hardening power (m). The characteristic length is a geometric parameter defined as the cubic root of the volume of the smallest timber element. Furthermore, $n = 1$ and $m = 1$ have been successfully employed in all the simulations performed in this thesis.

Experimental studies on timber-dowelled connections show that their characteristic failure modes initiate with local ductile failure (wood embedding plus steel components yielding) and end with a global brittle failure due to wood splitting. In turn, brittle failure is directly related to G_f, and its magnitude has a considerable effect on the maximum load carrying capacity of the connection. Therefore, in order to avoid fictitious premature failure, a sensitivity analysis should be carried out to determine an appropriate value of G_f which is associated to the particular model mesh size. An initial referential value of $G_f = 1$ MPa can be used.

h and β are calibration parameters that can be determined following a procedure based on embedment test load-deformation curves, as suggested in this thesis. The maximum capacity of a timber dowelled connection is strongly influenced by the compressive damage hardening constant (β). The influence of h on the slope of the embedment curve loading branch is negligible. By contrast, h has a significant effect on the extent of plastic deformation and stiffness degradation due to compressive stresses, and consequently, on the unloading branch slope of the numerical embedment curves. In dowelled connections, the estimation of h accounting for the loading direction (parallel or perpendicular to the

grain) is fundamental to adequately transfer the stresses from the wood to the dowel, and also to avoid convergence issues during the analysis. Accordingly, an analytical expression for the estimation of h has been derived based on the timber material properties corresponding to the loading direction.

8.2.3 Contact interface model

The three calibration parameters of the timber-steel interface contact model are the following: compressive normal stiffness (k_C), shear stiffness (k_S) and unloading stiffness (k_{UL}). The compressive normal stiffness has a considerable influence on the global initial linear elastic stiffness of the connection, whereas the shear stiffness has a significant influence on its predicted embedding strength. In turn, the unloading stiffness is important for modelling pinching behaviour. It was demonstrated that one fourth of the timber bulk modulus is a good approximation for the initial value of k_C. An expression to determine the bulk modulus for orthotropic materials was also presented in this thesis. On the other hand, a value of $k_S = 1$ MPa/mm (around $0.01 \cdot k_C$) resulted from the calibration process, while $k_{UL} = 450$ MPa/mm (around $5 \cdot k_C$) is a high enough value to obtain a steep unloading branch characteristic of pinching systems.

8.2.4 Experimental response of timber beam-to-steel column connections

An experimental study of the cyclic response of timber beam-to-steel column moment connections was carried out as part of this thesis. The use of steel columns in combination with timber beams is attractive for multi-storey construction given the low strength of timber in the direction perpendicular to the grain. A total of three specimens with different sizes of steel components (angles and bolts) were tested.

The proposed connection details showed high levels of ductility that allowed it to sustain its load-carrying capacity without significant strength deterioration or global failure up to large levels of deformation and after several cycles of loading. Moreover, the experimental results obtained also demonstrated that the capacity of this type of connection is governed by the strength of the timber beam-steel angle dowelled connection. Complementarily, the primary role of the steel components (particularly the steel angles) is to yield first and preserve the connection's capacity without leading to global failure, even

after the occurrence of severe timber local failure.

Three predominant timber local failure modes were observed: 1) cracking and splitting along the grain due to tensile stresses perpendicular to the grain; 2) plug shear failure at the bolt rows due to shear stresses parallel to the grain; and 3) embedding deformation and crushing. Although these failure modes were common to the three specimens tested, the size of the affected zones were different for each of them. It was verified that thicker steel angles and bigger bolts foster the development of larger embedding and shear plug failure zones. Moreover, the test results showed that for this particular type of hybrid timber-steel moment connection, smaller steel components (angles and bolts) augment the energy dissipation capacity and diminish the strength deterioration of the structure. Therefore, it is concluded that the most important advantages of ductile connections with small steel components is their ability to reduce the extent of timber local failure, and sustain large deformation levels without significant loss of strength. A design including these characteristics is recommended to prevent the occurrence of brittle failure modes under the action of earthquake loading.

8.2.5 Simplified component-based model

An original mixed version of a degenerated three-dimensional continuous model combined with a component-based macro model, which brings together the advantages of both approaches, has been proposed in this thesis. Accordingly, Timoshenko beam elements and isoparametric shell elements, instead of the more expensive solid elements, are used for modelling the timber beam. In addition to its efficient formulation, the main advantage of the beam elements employed in the component-based model is their capability to consider the influence of shear deformations and to directly interact with continuous isotropic 3D constitutive material models. On the other hand, continuous shell elements can incorporate timber orthotropic 3D constitutive material models and are the natural option for simulating timber local deformation and its interaction with the steel bolts.

The foundational basis of the proposed simplified component-based macro model are the element types described above jointly with the wood constitutive model developed and formulated in this thesis. It is demonstrated that the proposed component-based model can achieve a remarkable precision for simulating the global monotonic and hysteretic behaviour of the timber beam-to-steel column joints studied experimentally and numerically herein. Good estimates of strength, loading and unloading stiffness, permanent

deformations and energy dissipation have been obtained. Besides, this new model can be built in a simple way and has a good numerical performance in terms of computational cost. However, it has been observed that the best performance of the component-based model is obtained for those timber dowelled structures with small steel components, which comply better with the current seismic design philosophy.

On the other hand, the component-based model was fully capable of reproducing the self-centring behaviour characteristic of post-tensioned structures, namely, their flag-shape hysteresis loop and reduced permanent deformations. Nevertheless, the numerical results showed that too high initial post-tensioning forces do not necessary lead to a good seismic performance. On the contrary, high post-tensioning forces can produce early local timber failure, and consequently, foster cyclic strength and stiffness degradation, and hinder the connection's ductility capacity.

It is concluded that the component-based model can be further developed and implemented in the engineering professional practice, particularly when timber dowelled connection nonlinear behaviour needs to be assessed for design purposes. In particular, its improved computational cost coupled with its ability to output damage variable indicators constitutes an asset for assessing the structural response at highly damaged performance levels required by current practice. Moreover, its applicability as a numerical tool for advanced numerical assessment of the seismic performance of innovative timber post-tensioned structures is also promising.

8.3 Suggestions for future work

A number of interesting related topics for future research have been highlighted as a result of the findings of this thesis. This section summarizes and briefly describes them. The undertaking of further work in these directions is recommended.

- **Numerical study of the nonlinear behaviour of timber dowelled structures**

  The validated FE modelling approach proposed herein for timber structures (wood constitutive model and timber-steel interface contact model) can be applied to the study of other types of structural systems or connections. For instance, the numerical study of the cyclic response of timber dowelled structures loaded in the direction

perpendicular to the grain is of interest, and further research work should be undertaken in this direction. Moreover, other important issues like the influence of the Poisson's ratio values on the predicted tensile strains and cracking zone locations generated by high compressive stress can be investigated by means of the proposed constitutive model.

To this end, the model code is open and available to be programmed in any FE platform under the framework of a user-supplied subroutine (USS). In case of using DIANA FE software, a .dll extension file for the model's direct use as coded for this thesis is also available on request.

- **Wood failure criteria**

  It was noted that no general consensus exists to date on which failure surface provides the best description of the timber elastic boundary when subjected to generic loading. It is recommended that the proposed constitutive model be employed for the purpose of studying the influence of the plasticity yield criterion on the global and local numerical response. The constitutive model code, in its current configuration, allows the use of Hill, Hoffman and the more general Tsai-Wu criteria. In order to explore the Tsai-Wu criterion with different interaction factors small modifications are required in the user-supplied material model subroutine. On the other hand, other compressive or tensile damage criteria different to Hill can be defined by modifying a few lines of the USS. The USS will be made open-source in due course.

- **Constitutive model for wood under cyclic loads**

  The literature review conducted revealed the lack of detailed numerical studies on the cyclic response of timber structures. Therefore, it is expected that this first attempt of advanced modelling of wood cyclic response might encourage the development of many more new constitutive models using different approaches and theoretical frameworks. In fact, enhanced versions of the constitutive model proposed herein could be obtained by modifying specific parts of the USS. For instance, code modifications can be implemented with the objective of defining a unique failure surface for tensile and compressive damage, as well as for the plasticity yielding surface. Or alternatively, viscous stabilization could be included.

- **Plasticity-damage constitutive model for Timoshenko beam elements**

  The wood constitutive model proposed in this thesis can also be modified to be used in combination with the Timoshenko beam elements to study the global nonlinear response of timber beams, columns or frames. This can be achieved by incorporating a simple condensation local algorithm in the USS to impose the "zero-stress" or "plane stress" condition characteristic of beam elements. A detailed description of the previously mentioned condensation algorithm to be implemented can be found in [95, 147].

- **Plasticity-damage consistent tangent stiffness matrix**

  In this thesis a thorough mathematical expression to calculate the plasticity-damage consistent tangent stiffness matrix was derived. However, some numerical instabilities which led to divergence were encountered when analysing large and complex models at the component level. The investigation of more efficient formulations for the consistent tangent stiffness matrix is suggested.

- **Timber-steel interface contact model**

  The enhancement of the timber-steel contact model here developed is recommended with the objective of incorporating the additional permanent plastic deformations that may arise in the wood as a consequence of the bolt hole ovalization. This can allow a better capture of the permanent deformations observed in the experimental hysteretic response of timber dowelled connections. The contact model algorithm will also be released open-source in due course.

- **Component based model**

  Given its capability to accurately simulate the nonlinear hysteretic response of timber structures and the low computational cost entailed, the component-based model proposed in this thesis can be used as an advanced numerical tool for further research on the calculation of fragility curves and seismic performance assessment of innovative hybrid timber-steel structural systems. Furthermore, the functionality of this simplified model could be considerably improved if further research is carried out to determine a methodology to define the equivalent thickness of the timber shell elements and the cross-section geometry of the steel dowels.

Bibliography

[1] M. Andreolli, M. Piazza, R. Tomasi, R. Zandonini, Ductile moment-resistant steel–timber connections, Proceedings of the Institution of Civil Engineers: Structures and Buildings, 164(SB2) (2011) 65-–78. 171, 190, 195

[2] T.K. Bader, M. Schweigler, G. Hochreiner, E. Serrano, B. Enquist, M. Dorn, Dowel deformations in multi-dowel LVL-connections under moment loading, Wood Material Science and Engineering, 10(3) (2015) 216–231. 267

[3] K.J. Bathe, S. Bolourchi, A geometric and material nonlinear plate and shell element, Computers and Structures, 11 (1980) 23–48. 282, 284

[4] K.J. Bathe, E. Dvorkin, L.W. Ho, Our Discrete-Kirchhoff and Isoparametric Shell Elements for Nonlinear Analysis-An Assessment, Computers and Structures, 16 (1983) 89–98. 282, 283, 284

[5] Z.P. Bazant, B.H. Oh, Crack band theory for fracture of concrete, Materials and Structures, 16(3) (1983) 155–177. 90, 100

[6] BBC News, Plans drawn up for world's tallest wooden skyscraper, (2018). Available online from: http://www.bbc.co.uk/news/technology-42839463/ Last access date: February 23, 2018. 33

[7] C. Bedon, M. Fragiacomo, FE Modelling of Notched Connections for Timber-Concrete Composite Structures, World Conference on Timber Engineering (2016) Vienna, Austria. 19, 66, 67, 117, 219

[8] W.A. van Beerschoten, D.M. Carradine, A. Carr, Development of constitutive model for laminated veneer lumber using digital image correlation technique, Wood Science and Technology, 48 (2014) 755–772. 218, 266, 267

[9] R. Bilham, The seismic future of cities,Bulletin of Earthquake Engineering, 7 (2009) 839–887. 33

[10] H. Blaβ, P. Schadle, Ductility aspects of reinforced and non-reinforced timber joints, Engineering Structures, 33 (2011) 3018–3026. 70

[11] N. Bui, M. Ngo, M. Nikolic, D. Brancherie, A. Ibrahimbegovic, Enriched timoshenko beam finite element for modeling bending and shear failure of reinforced concrete frames, Computers and Structures, 143 (2014) 9–18. 281

[12] J.M. Cabrero, C. Blanco, K.G. Gebremedhin, A. Martin-Meizoso, Assessment of phenomenological failure criteria for wood, European Journal of Wood and Wood Products, 70(6) (2012) 871–882. 50, 51, 54

[13] L.I. Cardona, P. Paultre, J. Mazars, Damage mechanics applied to performance-based design of reinforced concrete columns, Earthq. Eng. Struct. Dyn., 46(14) (2017) 2439–2457. 44, 86, 281

[14] CEN.EN 1993-1-8, Eurocode 5: design of timber structures, Part 1—1: general-common rules and rules for buildings, (2004) 69, 177, 226

[15] CEN.EN 1993-1-8, Eurocode 3: design of steel structures, Part 1—8: design of joints, (2005). 177

[16] P. Ceresa, L. Petrini, R. Pinho, R. Sousa, A fibre flexure–shear model for seismic analysis of RC-framed structures, Earthq. Eng. Struct. Dyn., 38 (2009) 565–586. 281

[17] M. Cervera, C. Tesei, An Energy-Equivalent d+/d- Damage Model with Enhanced Microcrack Closure-Reopening Capabilities for Cohesive-Frictional Materials, Materials, 10(433) (2017). 84, 86

[18] N. Chancellor, M. Eatherton, D. Roke, T. Akbaş, Self-Centering Seismic Lateral Force Resisting Systems: High Performance Structures for the City of Tomorrow, Buildings, 4 (2014) 520–548. 34

[19] C. Christopoulos, A. Filiatrault, C.M. Uang, B. Folz, Posttensioned Energy Dissipating Connections for Moment-Resisting Steel Frames, Journal of Structural Engineering, 128 (2002) 1111–1120. 298, 299, 300

[20] C. Christopoulos, A. Filiatrault, B. Folz, Seismic response of self-centring hysteretic SDOF systems, Earthq. Eng. Struct. Dyn., 31(5) (2002) 1131–1150. 299, 303

[21] Y.H. Chui, Y. Li, Y, Modeling Timber Moment Connection under Reversed Cyclic Loading, Journal of Structural Engineering, 131(11) (2005) 1757–1763. 279

[22] Y. H. Chui, C. Ni, Load-Embedment Response of Timber to Reversed Cyclic Load, Wood and Fiber Science, 29(2) (1997) 148-–160. 226

[23] P.L. Clouston, F. Lam, Computational modeling of strand-based wood composites, Journal of Engineering Mechanics, 127(8) (2001) 844–851. 47, 48, 60

[24] P. Clouston, F. Lam, J.D. Barrett, Interaction Term of Tsai-Wu Theory for Laminated Veneer, Journal of Materials in Civil Engineering, 10(2) (1998) 112—116. 95

[25] M. Collins, B. Kasal, P. Paevere, G.C. Foliente, Three-Dimensional Model of Light Frame Wood Buildings. II: Experimental Investigation and Validation of Analytical Model, Journal of Structural Engineering, 131(4) (2005) 684–692. 34, 39

[26] C.A. Cornell, H. Krawinkler, Progress and challenges in seismic performance assessment, PEER Center News 3(2) (2000) Available online from: https://apps.peer.berkeley.edu/news/2000spring/performance.html/Last access date: February 23, 2018. 39, 40

[27] S.C. Cowin, On the strength anisotropy of bone and wood, Trans. ASME, 46(4) (1979) 832–838. 50, 51, 55, 60

[28] R. De Borst, Some recent issues in computational failure mechanics, International Journal for Numerical Methods in Engineering, 52 (2001) 63–95. 93, 100, 216

[29] R. De Borst, M.A. Crisfield, J.J.C. Remmers, C.V. Verhoosel, Non-linear Finite Element Analysis of Solids and Structures, Wiley, 2nd edition (2012). 97, 230

[30] R. De Borst, P.H. Feenstra, Studies in Anisotropic Plasticity with Reference to the Hill Criterion, International Journal of Numerical Methods in Engineering, 29 (1990) 315–336. 56

[31] R. De Borst, J. Pamin, M.G.D. Geers, On coupled gradient-dependent plasticity and damage theories with a view to localization analysis, European Journal of Mechanics A/Solids, 18 (1999) 939-–962. 80, 88, 216

[32] G.G. Deierlein, A.M. Reinhorn, M.R. Willford, Nonlinear Structural Analysis For Seismic Design: A Guide for Practicing Engineers, NEHRP Seismic Design Technical Brief, No. 4 (2010), Gaithersburg, USA. 42, 180, 187

[33] C. Demirci, C. Málaga-Chuquitaype, L. Macorini, Seismic drift demands in multi-storey cross-laminated timber buildings, Earthq. Eng. Struct. Dyn., 47(4) (2009) 1014–1031. 34

[34] E.A. De Souza Neto, D. Peric, D.R.J. Owen, Computational Methods for Plasticity – Theory and Applications, John Wiley and Sons Ltd (2008). 56, 57

[35] DIANA, User's Manual - Version 10.1, DIANA FEA BV, Delft, The Netherlands (2016). 22, 24, 25, 81, 115, 157, 201, 202, 207, 281, 282, 283, 287, 303

[36] A.M.P.G. Dias, J.W. Van de Kuilen, S. Lopes, H. Cruz, A non-linear 3D FEM model to simulate timber–concrete joints, Advances in Engineering Software, 38 (2007) 522–530. 19, 61, 63, 204, 218, 221, 222

[37] A.I. Dimopoulos, T.L. Karavasilis, G. Vasdravellis, B. Uy, Seismic design, modelling and assessment of self-centering steel frames using post-tensioned connections with web hourglass shape pins, Bulletin of Earthquake Engineering, 11(5) (2013) 1797–1816. 299, 304

[38] M. Dorn, Investigations on the Serviceability Limit State of Dowel-Type Timber Connections, PhD Thesis (2012), Vienna University of Technology, Faculty of Civil Engineering, Vienna, Austria. 19, 54, 60, 61, 62, 68, 222, 241

[39] C.L. Dos Santos, J.J.L. Morais, A.M.P.De Jesus, Mechanical behaviour of wood T-joints, Experimental and numerical investigation, Frattura Ed Integrita Strutturale, 31 (2015) 23–37. 19, 47, 48, 63, 65, 69, 222

[40] E.N. Dvorkin, R.G. Toscano, Shell Element Formulations for General Nonlinear Analysis. Modeling Techniques. In: Finite Element Analysis of the Collapse and Post-Collapse Behavior of Steel Pipes: Applications to the Oil Industry, SpringerBriefs in Applied Sciences and Technology. Springer, (2013) Berlin, Heidelberg. 282, 283, 284

[41] ECCS European Convention for Constructional Steelwork, Recommended testing procedure for assessing the behaviour of structural steel elements under cyclic loads, Brussels (1986). 177

[42] R. Faria, J. Oliver, M. Cervera, On isotropic scalar damage models for the numerical analysis of concrete structures, CIMNE Monograph, No.198 (2000) Barcelona, Spain. 85, 106, 109, 110

[43] R. Faria, J. Oliver, M. Cervera, Modeling Material Failure in Concrete Structures under Cyclic Actions, Journal of Structural Engineering, 130(12) (2004) 1997–2005. 85, 91

[44] R. Faria, X. Oliver, A rate dependent plastic-damage constitutive model for large-scale computations in concrete structures, CIMNE Monograph, No.17 (1993) Barcelona, Spain. 43

[45] R. Faria, J. Oliver, M. Cervera, A strain-based plastic viscous-damage model for massive concrete structures, International Journal of Solids and Structures 35(14) (1998) 1533–1558. 79, 86, 106, 113, 114

[46] Building Seismic Safety Council, NEHRP Guidelines for the seismic rehabilitation of buildings, FEMA-273, Federal Emergency Management Agency, Washington D.C., USA, 1997. 40

[47] DC. Feng, J. Xu, An efficient fiber beam-column element considering flexure-shear interaction and anchorage bond-slip effect for cyclic analysis of RC structures, Bull. Earthquake Eng., (2018). 44, 281

[48] G.C. Foliente, Hysteresis Modeling of Wood Joints and Structural Systems, Journal of Structural Engineering 121 (1995) 1013–1022. 39, 45

[49] G.C. Foliente, M.P. Singh, M.N. Noori, Equivalent Linearization of Generally Pinching Hysteretic, Degrading Systems, Earthq. Eng. Struct. Dyn., 25 (1996) 611–629. 39, 200, 201

[50] Forest Products Laboratory, Wood handbook—Wood as an engineering material, U.S. Department of Agriculture General Technical Report, FPL-GTR-190 (2010), WI, US. 219

[51] R.O. Foschi,Load-slip characteristics of nails, Wood Science, 7 (1974) 69–76. 45

[52] M. Fragiacomo, B. Dujic, I. Sustersic, Elastic and ductile design of multi-storey crosslam massive wooden buildings under seismic actions, Engineering Structures, 33 (2011) 3043–3053. 34

[53] B. Franke, P. Quenneville, Numerical Modeling of the Failure Behavior of Dowel Connections in Wood, Journal of Engineering Mechanics, 137(3) (2011) 186-–195. 47, 48, 117, 219

[54] C.D. Frenette, The Seismic Response of a Timber Frame with Dowel Type Connections, Master Thesis (1997), The University of British Columbia, Department of Civil Engineering, Vancouver, Canada. 19, 71, 72

[55] M.M. Garlock, J.M. Ricles, R. Sause, Experimental Studies of Full-Scale Posttensioned Steel Connections, Journal of Structural Engineering, 131(3) (2005) 438–448. 299, 307

[56] M.M. Garlock, R. Sause, J.M. Ricles, Behavior and Design of Posttensioned Steel Frame Systems, Journal of Structural Engineering, 133(3) (2007) 389–399. 299, 304

[57] N. Gattesco, I. Toffolo, Experimental study on multiple-bolt steel-to-timber tension joints, Materials and Structures, 37 (2004) 129–138. 19, 71, 73

[58] P. Grassl ,M. Jirasek M, Damage-plastic model for concrete failure, International Journal of Solids and Structures 43(22-23) (2006) 7166—7196. 79, 80, 84, 93, 100, 113, 115

[59] P. Grassl P, On a damage-plasticity approach to model concrete failure, Engineering and Computational Mechanics, 162(EM4) (2009) 221-–231. 100

[60] Z.W. Guan, E.C. Zhu, Finite element modelling of anisotropic elasto-plastic timber composite beams with openings, Engineering Structures, 31 (2009) 394–403. 49

[61] P. Guindos, Comparison of different failure approaches in knotty wood, Drewno, 57(193) (2014) 51–68. 50, 55

[62] T. Guo, L. Song, G. Zhang, Numerical Simulation and Seismic Fragility Analysis of a Self-Centering Steel MRF with Web Friction Devices, Journal of Earthquake Engineering, 19(5) (2015) 731–751. 300

[63] R.L. Hankinson, Investigation of Crushing Strength of Spruce at Varying Angles of Grain, Air Service Information Circular, No. 259 (1921), US. 51

[64] Z.G. Hasan, Inside Vancouver's Brock Commons, the World's Tallest Mass Timber Building, (2017). Available online from: https://www.archdaily.com/879625/inside-vancouvers-brock-commons-the-worlds-tallest-timber-structured-building/ Last access date: May 05, 2018. 33

[65] F. Hashagen, R. De Borst, Enhancement of the Hoffman yield criterion with an anisotropic hardening model, Computers and Structures, 79 (2001) 637-–651. 108

[66] Z. Hashin, Failure criteria for unidirectional fiber composites, Journal of Applied Mechanics, 47 (1980) 329–334. 50, 51, 54

[67] A. Hassanieh, H.R. Valipour, M.A. Bradford, Experimental and numerical study of steel-timber composite (STC) beams, Journal of Constructional Steel Research, 122 (2016) 367–378. 171, 221, 222

[68] A. Hassanieh, H.R. Valipour, M.A. Bradford, C. Sandhaas, Modelling of steel-timber composite connections : Validation of finite element model and parametric study, Engineering Structures, 138 (2017) 35–49. 19, 67, 69, 208, 218, 221, 222

[69] M. He, J. Zhang, Z. Li, Influence of cracks on the mechanical performance of dowel type glulam bolted joints, Construction and Building Materials, 153 (2017) 445-–458. 184

[70] A. Heiduschke, B. Kasal, P. Haller, Performance and Drift Levels of Tall Timber Frame, Structural Engineering International, 2 (2008) 186–191. 39

[71] A. Heiduschke, B. Kasal, P. Haller, Shake table tests of small- and full-scale laminated timber frames with moment connections, Bulletin of Earthquake Engineering, 7 (2009) 323–339. 201

[72] C.P. Heine, Simulated Response of Degrading Hysteretic Joints With Slack Behaviour, PhD thesis (2001), Virginia Polytechnic Institute and State University, Virginia, USA. 192

[73] R. Hill, A theory of the yielding and plastic flow of anisotropic materials. Proc. Roy. Soc., A193 (1947) 281–297. 48, 56, 87

[74] G. Hochreiner, T.K. Bader, M. Schweigler, J. Eberhardsteiner, Structural behaviour and design of dowel groups Experimental and numerical identification of stress states and failure mechanisms of the surrounding timber matrix, Engineering Structures, 131 (2017) 421–437. 82, 267

[75] O. Hoffman, The brittle strength of orthotropic materials, Journal Composite Materials, 1 (1967) 200–206 48, 50, 56, 219

[76] J.P. Hong, Three-dimensional nonlinear finite element model for singe and multiple dowel-type wood connections, PhD thesis (2007), Program of Forestry, University of British Columbia, Vancouver, Canada. 45

[77] A. Ibrahimbegovic, L. Davenne, D. Markovic, N. Dominguez, Performance Based Earthquake-Resistant Design: Migrating Towards Nonlinear Models and Probabilistic Framework, Fischinger M. (eds) Performance-Based Seismic Engineering: Vision for an

Earthquake Resilient Society, Geotechnical, Geological and Earthquake Engineering, vol 32, Springer(2014). 42, 43

[78] A. Iqbal, S. Pampanin, A.H. Buchanan, Seismic Performance of Full-Scale Post-Tensioned Timber Beam-Column Connections, Journal of Earthquake Engineering, 20(3) (2016) 383–405. 170, 301, 307

[79] L. Jason, A. Huerta, G. Pijaudier-Cabot, S. Ghavamian, An elastic plastic damage formulation for concrete: Application to elementary tests and comparison with an isotropic damage model, Computer Methods in Applied Mechanics and Engineering, 195(52) (2006) 7077—7092. 79, 80, 84, 85, 100

[80] J.L. Jensen, P. Quenneville, Fracture mechanics analysis of row shear failure in dowelled timber connections: asymmetric case, Materials and Structures, 44 (2011), 351–360. 88, 117, 148, 219, 241

[81] A. Jorissen, M. Fragiacomo, General notes on ductility in timber structures, Engineering Structures, 33 (2011) 2987–2997. 69

[82] J.W. Ju, On energy-based coupled elastoplastic damage theories: Constitutive modeling and computational aspects, International Journal of Solids and Structures, 25(7) (1989) 803–833. 216

[83] J.W. Ju, Isotropic and Anisotropic Damage Variables in Continuum Damage Mechanics. Journal of Engineering Mechanics ASCE 116(12) (1990) 2764–2770. 83, 84

[84] J.W. Kang, J. Lee, A new damage index for seismic fragility analysis of reinforced concrete columns, Structural Engineering and Mechanics, 60(5) (2016) 875–890. 43

[85] V. Karagiannis,C. Málaga-Chuquitaype, A.Y. Elghazouli, Modified foundation modelling of dowel embedment in glulam connections, Construction and Building Materials 102(2) (2016) 1168–1179. 19, 23, 45, 46, 225, 226, 227, 228, 232, 233, 235, 236, 239, 240, 242, 243, 244, 245, 246

[86] V. Karagiannis,C. Málaga-Chuquitaype, A.Y. Elghazouli, Behaviour of hybrid timber beam-to-tubular steel column moment connections, Engineering Structures, 131 (2017) 243—263. 170, 171, 177, 221, 268

[87] V. Karagiannis, Structural response of hybrid steel-timber joints, PhD Thesis (2017), Imperial College London, Department of Civil and Environmental Engineering, London, UK. 17, 23, 177, 179, 217, 218, 219, 246, 247, 248, 249, 275

[88] B. Kasal, S. Pospisil, I. Jirovsky, A. Heiduschke, M. Drdacky, P. Haller, Seismic performance of laminated timber frames with fiber-reinforced joints, Earthquake Engineering and Structural Dynamics, 33 (2004) 633–646. 34

[89] B. Kasal, R.J. Leichti, State of the art in multiaxial phenomenological failure criteria for wood members, Prog. Struct. Engng Mater., 7 (2005) 3—13. 45, 50, 51, 53, 59, 95

[90] N. Kharouf, G. McClure, I. Smith, Elasto-plastic modeling of wood bolted connections, Computers and Structures, 81 (2003) 747–754. 82

[91] N. Kharouf, G. McClure, I. Smith, Postelastic Behavior of Single- and Double-Bolt Timber Connections, Journal of Structural Engineering, 131 (2005) 188–196. 48, 69

[92] M. Khelifa, A. Khennane, M. El Ganaoui, A. Celzard, Numerical damage prediction in dowel connections of wooden structures, Materials and Structures 49(5) (2016) 1829–1840. 47, 49, 83

[93] A. Khennane, M. Khelifa, L. Bleron, J. Viguier, Numerical modelling of ductile damage evolution in tensile and bending tests of timber structures. Mechanics of Materials, 68 (2014) 228–236. 49

[94] H.J. Kim, C. Christopoulos, Numerical models and ductile ultimate deformation response of post-tensioned self-centering moment connections, Earthq. Eng. Struct. Dyn., 38 (2009) 1–21. 299

[95] S. Klinkel, S. Govindjee, Using finite strain 3D-material models in beam and shell elements, Engineering Computations, 19(3) (2002) 254–271. 282, 321

[96] M. Koliou, A. Filiatrault, Development of wood and steel diaphragm hysteretic connector database for performance-based earthquake engineering, Bulletin of Earthquake Engineering, 15 (2017) 4319–4347. 39, 42

[97] H. Krawinkler, G.G. Deierlein, Challenges Towards Achieving Earthquake Resilience Through Performance-Based Earthquake Engineering, Fischinger M. (eds) Performance-Based Seismic Engineering: Vision for an Earthquake Resilient Society, Geotechnical, Geological and Earthquake Engineering, vol 32, Springer(2014). 39, 40

[98] C. La Borderie, Unilateral phenomena in a damageable material: modelling and application to the analysis of concrete structures, PhD thesis (1991), Laboratoire de Mécanique et de Technologie, Univ. Paris VI, Cachan, France (in French). 43

[99] P.A. Lacourt, F.J. Crisafulli, A.E. Mirasso, Finite element modelling of hysteresis, degradation and failure of dowel type timber joints, Engineering Structures, 123 (2016) 89–96. 201

[100] F. Lam, M. Schulte-Wrede, C.C. Yao, J.J. Gu, Moment resistance of bolted timber connections with perpendicular to grain reinforcements, World Conference on Timber Engineering (2008) Miyazaki, Japan. 20, 74, 76, 184

[101] F. Lam, M. Gehloff, M. Closen, Moment-resisting bolted timber connections, Proceedings of the Institution of Civil Engineers: Structures and Buildings, 163(SB4) (2010) 267—274. 184, 192

[102] I. Lapczyk, J.A. Hurtado, Progressive damage modeling in fiber-reinforced materials, Composites Part A Applied Science Manufacture 38 (2007) 2333—2341. 106

[103] LaVision UK Ltd., https://www.lavision.de/en/ Last access date: July 01, 2018 266

[104] J. Lee, G.L. Fenves, Plastic-damage model for cyclic loading of concrete structures, J. Eng. Mech. ASCE 124 (2018) 892–900. 43

[105] F. Légeron, P. Paultre, J. Mazars, Damage Mechanics Modeling of Nonlinear Seismic Behavior of Concrete Structures, J. Struct. Eng., 131(6) (2005) 946–955. 43, 216, 281

[106] R.J. Leichti, R.C. Tang, Predicting the load capacity of wood composite I-beams using the tensor polynomial strenght theory, Wood Science and Technology, 23 (1989) 109–121. 50, 51

[107] A.J.M. Leijten, S. Ruxton, H. Prion, F. Lam, Reversed-Cyclic Behavior of a Novel Heavy Timber Tube Connection, Journal of Structural Engineering, 132(8) (2006) 1314-–1319. 190, 195, 201

[108] Z. Li, G.D. Hatzigeorgiou, Seismic damage analysis of RC structures using fiber beam-column elements, Soil Dynamics and Earthquake Engineering, 32 (2012) 103–110. 43, 281

[109] Z.X. Li, Y. Gao, Q. Zhao, A 3D flexure-shear fiber element for modeling the seismic behavior of reinforced concrete columns, Engineering Structures, 117 (2016) 372–383. 281

[110] X. Li, P.G. Duxbury, P. Lyons, Considerations for the Application and Numerical Implementation of Strain Hardening with the Hoffman Yield Criterion, Computers and Structures, 52(4) (1994) 633–644. 95

[111] H. Liang, Y.K. Wen, G.C. Foliente, Damage Modeling and Damage Limit State Criterion for Wood-Frame Buildings Subjected to Seismic Loads, Journal of Structural Engineering, 137(1) (2011) 41–48. 34, 39

[112] J.W. van de Lindt, Damage-Based Seismic Reliability Concept for Woodframe Structures, J. Struct. Eng. 131(4) (2005) 668–675. 34, 39

[113] J.W. van de Lindt, D.V. Rosowsky, W. Pang, S. Pei, Performance-Based Seismic Design of MidRise Woodframe Buildings, Journal of Structural Engineering, 139 (2013) 1294–1302. 39

[114] J.Y. Liu, Evaluation of the Tensor Polynomial Strength Theory for Wood, Journal of Composite Materials, 18 (1984) 216—226. 50, 51, 56, 60, 95

[115] P. Mackenzie-Helnwein, J. Eberhardsteiner, H.A. Mang, A multi-surface plasticity model for clear wood and its application to the finite element analysis of structural details, Computational Mechanics, 31 (2003) 204–218. 54

[116] N.T. Mascia, E.A. Nicolas, Evaluation of Tsai–Wu criterion and Hankinson's formula for a Brazilian wood species by comparison with experimental off-axis strength tests, Wood Material Science and Engineering, 7 (2012) 49–58. 55, 59, 60

[117] N.T. Mascia, R.A. Simoni, Analysis of failure criteria applied to wood, Engineering Failure Analysis, 35 (2013) 703—712. 50, 51, 55, 95

[118] A. Matzenmiller, J. Lubliner, R.L Taylor, A constitutive model for anisotropic damage in fiber-composites, Mechanics of Materials, 20 (1995) 125–152. 85, 101, 216

[119] J. Mazars, P. Kotronis, F. Ragueneau, G. Casaux, Using multifiber beams to account for shear and torsion. Applications to concrete structural elements, Computer Methods in Applied Mechanics and Engineering, 195 (2006) 7264–7281. 281

[120] J. Mazars, F. Hamon, S. Grange, A new 3D damage model for concrete under monotonic, cyclic and dynamic loadings, Materials and Structures, 48 (2015) 3779–3793. 86

[121] J. Moehle, Performance-Based Earthquake Engineering in the U.S.: A Case Study for Tall Buildings, Fischinger M. (eds) Performance-Based Seismic Engineering: Vision for an Earthquake Resilient Society, Geotechnical, Geological and Earthquake Engineering, vol 32, Springer(2014). 41

[122] D.M. Moses, H.G.L. Prion, Stress and failure analysis of wood composites: A new model, Composites: Part B, 35 (2004), 251–261. 47, 48

[123] Y.D. Murray, Manual for LS-DYNA wood material model 143, Federal Highway Administration Report, No.FHWA-HRT-04-097 (2007), VA, US. 50, 53, 54, 95, 117, 219

[124] M.P. Newcombe, S. Pampanin, A. Buchanan, A. Palermo, Section Analysis and Cyclic Behavior of Post-Tensioned Jointed Ductile Connections for Multi-Story Timber Buildings, Journal of Earthquake Engineering, 12(S1) (2008) 83–110. 300, 301

[125] C.B. Norris, Strength of Orthotropic Materials Subjected to Combined Stress, U.S. Forest Products Lab. Rep. 1816, FPL (1962) WI, US. 50, 51, 53

[126] S. Oller, E. Car, J. Lubliner, Definition of a general implicit orthotropic yield criterion, Computer Methods in Applied Mechanics and Engineering, 192(7–8) (2003) 895—912. 60, 94

[127] C. O'Loinsigh, M. Oudjene, E. Shotton, A. Pizzi, P. Fanning, Mechanical behaviour and 3D stress analysis of multi-layered wooden beams made with welded-through wood dowels, Composite Structures 94 (2012) 313–321. 49

[128] M. Oudjene, M. Khelifa, Finite element modelling of wooden structures at large deformations and brittle failure prediction, Materials and Design 30 (2009) 4081–4087. 49

[129] M. Oudjene, V.D. Tran, M. Khelifa, Cyclic and monotonic responses of double shear single dowelled timber connections made of hardwood species: Experimental investigations, Construction and Building Materials, 132 (2017) 188-–195. 190, 195

[130] A. Palermo, S. Pampanin, A. Buchanan, M. Newcombe, Seismic design of multi-storey buildings using laminated veneer lumber (LVL), NZSEE Conference (2005) Taupo, New Zealand. 300

[131] A. Papachristidis, M. Fragiadakis, M. Papadrakakis, A 3D fibre beam-column element with shear modelling for the inelastic analysis of steel structures, Computational Mechanics 45 (2010) 553–572. 281

[132] J.A. Paredes, S. Oller, A.H. Barbat, New Tension-Compression Damage Model for Complex Analysis of Concrete Structures, J. Eng. Mech. 142 (2016) 1–16. 84, 86, 101

[133] F. Parisio, S. Samat, L. Laloui, Constitutive analysis of shale: A coupled damage plasticity approach, International Journal of Solids and Structures, 75–76 (2015) 88-–98. 84, 115

[134] L. Pelà, M. Cervera, P. Roca, Continuum damage model for orthotropic materials: Application to masonry, Computer Methods in Applied Mechanics and Engineering, 200 (2011) 917-–930. 86

[135] M. Popovski, Seismic performance of braced timber frames, PhD Thesis (2000), The University of Bristish Columbia, Department of Civil Engineering, Vancouver, Canada. 21, 145, 148, 150, 152, 168

[136] M. Popovski, H.G. Prion, E. Karacabeyli, Seismic performance of connections in heavy timber construction, Canadian Journal of Civil Engineering, 29 (2002) 389-–399. 20, 21, 73, 75, 144, 145, 148, 184, 190, 194, 195

[137] M. Popovski, E. Karacabeyli, Seismic Performance of Riveted Connections in Heavy Timber Construction, 13th World Conference on Earthquake Engineering (2004) Vancouver, Canada. 201

[138] T.P.S. Reynolds, Dynamic Behaviour of Dowel-type Connections Under In-service Vibration, PhD Thesis (2013), University of Bath, Department of Architecture and Civil Engineering, Bath, UK. 20, 70, 72, 74, 201

[139] T. Reynolds, B. Sharma, K. Harries, M. Ramage, Dowelled structural connections in laminated bamboo and timber, Composites Part B: Engineering, 90 (2016) 232–240. 267

[140] J.M. Ricles, R. Sause, M.M. Garlock, C. Zhao, Posttensioned Seismic-Resistant Connections for Steel Frames, Journal of Structural Engineering, 127 (2001) 113–121. 298

[141] P.D. Rodd, The analysis of timber joints made with circular dowel connectors. PhD Thesis (1973), University of Sussex, UK. 222

[142] S. Saloustros, L. Pelá, M. Cervera, P. Roca, Finite element modelling of internal and multiple localized cracks, Comput. Mech., 59 (2017) 299-–316. 86

[143] C. Sandhaas, J.W. Van de Kuilen, H.J. Blass, Constitutive Model for Wood Based on Continuum Damage Mechanics, World Conference on Timber Engineering (2012) Auckland, New Zealand. 47, 49, 67, 83, 90, 149

[144] C. Sandhaas, Mechanical behaviour of timber joints with slotted-in steel plates, PhD Thesis (2012), Delft University of Technology, Faculty of Civil Engineering and Geosciences, Delft, The Netherlands. 54, 67, 85, 118, 204, 218, 222

[145] C.L. Santos, A.M.P. De Jesus, J.J.L. Morais, J.L.P.C Lousada, Quasi-static mechanical behaviour of a double-shear single dowel wood connection, Construction and Building Materials, 23 (2009) 171–182. 19, 62, 63, 64, 216, 222, 230

[146] C.L. Santos, A.M.P. De Jesus, J.J.L. Morais, J.L.P.C Lousada, A Comparison Between the EN 383 and ASTM D5764 Test Methods for Dowel-Bearing Strength Assessment of Wood: Experimental and Numerical Investigations, Strain, 46 (2010) 159–174. 203, 204, 218, 225, 230

[147] A. Saritas, F.C. Filippou, Numerical integration of a class of 3d plastic-damage concrete models and condensation of 3d stress-strain relations for use in beam finite elements, Engineering Structures, 31 (2009) 2327–2336. 282, 321

[148] J.C.J. Schellekens, R. De Borst, The Use of the Hoffman Yield Criterion in Finite Element Analysis of Anisotropic Composites, Computers and Structures, 37 (1990) 1087–1096. 56, 57

[149] J. Schmidt, M. Kaliske, Models for numerical failure analysis of wooden structures, Engineering Structures, 31(2) (2009) 571–579. 117, 219

[150] J. Schneider, E. Karacabeyli, M. Popovski, S.F. Stiemer, S. Tesfamariam, Damage Assessment of Connections Used in Cross-Laminated Timber Subject to Cyclic Loads, Journal of Performance of Constructed Facilities, 28(6) (2014) A4014008-1—14. 34, 39

[151] J. C. M. Schoenmakers, A.J.M. Jorissen, A.J.M. Leijten, Evaluation and modelling of perpendicular to grain embedment strength, Wood Science and Technology, 44(4) (2009) 579-–595. 226

[152] J.C.M. Schoenmakers, S. Svensson, Embedment tests perpendicular to the grain – optical measurements of deformation fields, European Journal of Wood and Wood Products, 69 (2011) 133–142. 266

[153] A.C. Schreyer, Monotonic and cyclic behaviour of slender dowel-type fasteners in wood-steel-wood connections, PhD Thesis (2002), The University of Bristish Columbia, Department of Wood Science, Vancouver, Canada. 19, 71, 72

[154] E. Serrano, Adhesive Joints in Timber Engineering: Modelling and Testing of Fracture, PhD Thesis (2000), Lund University, Department of Mechanics and Materials, Lund, Sweeden. 117, 219

[155] Y.L. Shen, J. Schneider, S. Tesfamariam, S.F. Stiemer, Z.G. Mu, Hysteresis behavior of bracket connection in cross-laminated timber shear walls, Construction Building Materials, 48 (2013) 980–991. 279

[156] Z. Shu, M.J. He, Z. Li, Estimating inelastic drift demands for wood portal frame systems considering accumulated damages, Structural Design of Tall and Special Buildings, 27(3) (2018) e1440. 34, 39

[157] J.C. Simo, R.L. Taylor, Consistent tangent operators for rate-independent elastoplasticity, Computer Methods in Applied Mechanics and Engineering, 48 (1985) 101—118. 108

[158] J.C. Simo, J.W. Ju, Strain- and stress-based continuum damage models—I. Formulation, International Journal of Solids and Structures 23(7) (1987) 821–840. 83, 93, 113

[159] L.F. Sirumbal-Zapata, C. Málaga-Chuquitaype, A.Y. Elghazouli, A three-dimensional plasticity-damage constitutive model for timber under cyclic loads, Computers and Structures, 195 (2018) 47–63. 81

[160] A.M. Sivaselvan, A.M. Reinhorn, Hysteretic Models for Deteriorating Inelastic Structures, Journal of Engineering Mechanics, 126(6) (2000) 633–640. 39

[161] J. Sjödin, E. Serrano, B. Enquist, Contact-free measurements and numerical analyses of the strain distribution in the joint area of steel-to-timber dowel joints, Holz Als Roh- Und Werkstoff, 66 (2006) 497–506. 266

[162] J. Sjödin, E. Serrano, B. Enquist, An experimental and numerical study of the effect of friction in single dowel joints, Holz Roh Werkst, 66 (2008) 363—372. 218, 266

[163] J. Sjödin, E. Serrano, A numerical study of methods to predict the capacity of multiple steel-timber dowel joints, Holz Roh Werkst, 66 (2008) 447–454. 218

[164] T. Smith, F.C. Ponzo, A. Di Cesare, S. Pampanin, D. Carradine, A.H. Buchanan, D. Nigro, Post-Tensioned Glulam Beam-Column Joints with Advanced Damping Systems: Testing and Numerical Analysis, Journal of Earthquake Engineering, 18(1) (2014) 147–167. 303

[165] SOM, Timber Tower Research Project, Skidmore, Owings and Merril, LLP Final Report (2013), IL, US. 33

[166] S. Tesfamariam, S.F. Stiemer, C. Dickof, M.A. Bezabeh, Seismic Vulnerability Assessment of Hybrid Steel-Timber Structure: Steel Moment-Resisting Frames with CLT Infill, Journal of Earthquake Engineering, 18(6) (2014) 929–944. 170

[167] P.S. Theocaris, Properties and experimental verification of the paraboloid failure criterion with transversely isotropic materials, Journal of Materials Science, 25 (1990) 1076–1085. 51

[168] P.S. Theocaris, T.P. Philippidis, On the validity of the tensor polynomial failure theory with stress interaction terms omitted, Composites Science and Technology, 40 (1991) 181–191. 51

[169] P.S. Theocaris, The elliptic paraboloid failure criterion for cellular solids and brittle foams, Acta Mechanica, 89 (1991) 93–121. 52

[170] P.S. Theocaris, The symmetric ellipsoid failure surface for the transversely isotropic body, Acta Mechanica, 92 (1992) 35–60. 52, 60

[171] S.W. Tsai, E.M. Wu, A general theory of strength for anisotropic materials, Journal of Composite Materials, 1 (1971) 558–580 47, 50, 56

[172] Architect Magazine, UBC Earth System Science Building (ESSB), (2014). Available online from: http://www.architectmagazine.com/project-gallery/ubc-earth-systems-science-building-essb-3791/ Last access date: May 05, 2018. 33

[173] United Nations, World Population Prospects: The 2017 Revision, Department of Economic and Social Affairs, Population Division (2017), NY, US. 33

[174] United Nations, World Urbanization Prospects produced: The 2018 Revision, Department of Economic and Social Affairs, Population Division (2018), NY, US. 33

[175] H. Valipour, N. Khorsandnia, K. Crews, A. Palermo, Numerical modelling of timber/timber-concrete composite frames with ductile jointed connection, Advances in Structural Engineering, 19(2) (2016) 299–313. 82, 170, 301, 302

[176] S. Valliappan, M. Yazdchi, N. Khalili, Seismic analysis of arch dams - a continuum damage mechanics approach, International Journal for Numerical Methods in Engineering 45 (1999) 1695–1724. 84

[177] T.A.C.M. van der Put, The tensor polynomial failure criterion for wood, Delft Wood Science Foundation, Publication Series 2005 nr.2 (2005) Delft, The Netherlands. 50, 51

[178] T.A.C.M. van der Put, A General Failure Criterion for Wood, IUFRO Timber Engineering Group Meeting, Paper 23 (1982) Boras, Sweden. 50, 51

[179] T.A.C.M. van der Put, Discussion and Proposal of a General Failure Criterion for Wood, International Council For Building Research Studies, CIB-W18/26-6-1 (1993) Georgia, USA. 59

[180] M. Wang, X. Song, X. Gu, Y. Zhang, L. Luo, Rotational Behavior of Bolted Beam-to-Column Connections with Locally Cross-Laminated Glulam, Journal of Structural Engineering, 141 (2015) 040141211-–7. 20, 74, 76, 184, 190, 192

[181] M. Wang, X. Song, X. Gu, Y. Wu, Mechanical Behavior of Bolted Glulam Beam-To-Column Connections With Slotted-in Steel Plates Under Pure Bending, World Conference on Timber Engineering (2016) Viena, Austria. 90, 149

[182] D.P. Welch, T.J. Sullivan, G.M. Calvi, Developing Direct Displacement-based Design and Assessment Procedures for Performance-Based Earthquake Engineering, ROSE 2012/03 (2012), IUSS Press, Pavia, Italia. 39, 40

[183] J.M: Williams, K.J. Fridley, W.F. Cofer, R.H. Falk, Failure modeling of sawn lumber with a fastener hole, Finite elements in Analysis and Design, 36 (2000) 83–98. 47, 60

[184] J.Y. Wu, J. Li, R. Faria, An energy release rate-based plastic-damage model for concrete, International Journal of Solids and Structures, 43 (2006) 583-–612. 84, 86

[185] B.H. Xu, A. Bouchaïr, M. Taazount, E.J. Vega, Numerical and experimental analyses of multiple-dowel steel-to-timber joints in tension perpendicular to grain, Engineering Structures, 31 (2009) 2357–2367. 17, 21, 22, 50, 69, 70, 144, 156, 157, 158, 159, 160, 161, 162, 164, 168, 169

[186] B.H. Xu, A. Bouchaïr, P. Racher, Analytical study and finite element modelling of timber connections with glued-in rods in bending, Construction and Building Materials, 34 (2012) 337–345. 222

[187] B.H. Xu, A. Bouchaïr, M. Taazount, P. Racher P, Numerical simulation of embedding strength of glued laminated timber for dowel-type fasteners, Journal of Wood Science, 59 (2013) 17–23. 50, 149, 204, 234

[188] B. Xu, A. Bouchair, P. Racher, Appropriate Wood Constitutive Law for Simulation of Nonlinear Behavior of Timber Joints, J. Mater. Civ. Eng. (ASCE), 26(6) (2014) 04014004-1–7. 44, 47, 50, 82

[189] B. Xu, A. Bouchair, P Racher, Mechanical Behavior and Modeling of Dowelled Steel-to-Timber Moment-Resisting Connections, J. Struct. Eng., 141(6):04014165 (2015). 19, 64, 66, 170, 171, 218, 241

[190] J. Yang, Influence of Strengthening and Repair Schemes on Dowel Type Timber Joints and Moment Resisting Frames, PhD Thesis (2013), The University of Hong Kong, Department of Civil Engineering, Hong Kong, China. 19, 70, 71

[191] H. Zhang, G.C. Foliente, Y. Yang, F. Ma, Parameter identification of inelastic structures under dynamic loads, Earthq. Eng. Struct. Dyn., 31(5) (2002) 1113–1130. 34, 39

[192] X. Zhang, M. Fairhurst, T. Tannert, Ductility Estimation for a Novel Timber–Steel Hybrid System, J. Struct. Eng., 142(4):E4015001 (2016). 170, 171

[193] T. Zhou, Z. Guan, Review of existing newly developed approaches to obtain timber embedding strength, Progress in Structural Engineering Materials, 8 (2006) 49–67. 19, 70

Appendices

Appendix A

Derivatives of the Jacobian matrix of the plasticity algorithm

The solution of the system of equations 3.54 can be obtained by means of the iterative Newton-Raphson method:

$$\boldsymbol{b}_{j+1}^{i+1} = \boldsymbol{b}_{j+1}^{i} - \left(\boldsymbol{J}_{j+1}^{i}\right)^{-1} \boldsymbol{r}_{j+1}^{i} \tag{A.1}$$

where i is the iteration number, j is the previous load step, $\boldsymbol{b}$ is the unknown variables vector, $\boldsymbol{r}$ is the residuals vector, and $\boldsymbol{J}$ is the Jacobian matrix:

$$\boldsymbol{b}_{j+1}^{i} = \begin{bmatrix} \Delta\lambda_{j+1}^{i} \\ \Delta k_{j+1}^{i} \end{bmatrix} \tag{A.2}$$

$$\boldsymbol{r}_{j+1}^{i} = \begin{bmatrix} f_p\left(\Delta\lambda_{j+1}^{i}, \Delta k_{j+1}^{i}\right) \\ F\left(\Delta\lambda_{j+1}^{i}, \Delta k_{j+1}^{i}\right) \end{bmatrix} \tag{A.3}$$

$$\boldsymbol{J}_{j+1}^{i} = \begin{bmatrix} \frac{\mathrm{d}f_p}{\mathrm{d}\Delta\lambda}\left(\Delta\lambda_{j+1}^{i}, \Delta k_{j+1}^{i}\right) & \frac{\mathrm{d}f_p}{\mathrm{d}\Delta k}\left(\Delta\lambda_{j+1}^{i}, \Delta k_{j+1}^{i}\right) \\ \frac{\mathrm{d}F}{\mathrm{d}\Delta\lambda}\left(\Delta\lambda_{j+1}^{i}, \Delta k_{j+1}^{i}\right) & \frac{\mathrm{d}F}{\mathrm{d}\Delta k}\left(\Delta\lambda_{j+1}^{i}, \Delta k_{j+1}^{i}\right) \end{bmatrix} \tag{A.4}$$

The expressions to calculate the four total derivatives of the Jacobian matrix are:

$$\frac{\mathrm{d}f_p}{\mathrm{d}\Delta\lambda} = \frac{\partial f_p}{\partial\bar{\boldsymbol{\sigma}}^{-}}\frac{\partial\bar{\boldsymbol{\sigma}}^{-}}{\partial\Delta\lambda} = \boldsymbol{n}^{T}\frac{\partial\bar{\boldsymbol{\sigma}}^{-}}{\partial\Delta\lambda} \tag{A.5}$$

$$\frac{\mathrm{d}f_p}{\mathrm{d}\Delta k} = \frac{\partial f_p}{\partial \bar{\boldsymbol{\sigma}}^-}\frac{\partial \bar{\boldsymbol{\sigma}}^-}{\partial \Delta k} + \frac{\partial f_p}{\partial \boldsymbol{q}}\frac{\partial \boldsymbol{q}}{\partial \Delta k} + \frac{\partial f_p}{\partial \bar{\sigma}_y}\frac{\partial \bar{\sigma}_y}{\partial \Delta k} = \boldsymbol{n}^T\frac{\partial \bar{\boldsymbol{\sigma}}^-}{\partial \Delta k} + \bar{\boldsymbol{\sigma}}^{-T}\frac{\partial \boldsymbol{q}}{\partial \Delta k} - 2\bar{\sigma}_y h \tag{A.6}$$

$$\frac{\mathrm{d}F}{\mathrm{d}\Delta \lambda} = \frac{\partial F}{\partial \boldsymbol{n}}\frac{\partial \boldsymbol{n}}{\partial \Delta \lambda} + \frac{\partial F}{\partial \Delta \lambda} = \frac{\partial F}{\partial \boldsymbol{n}}\left(\frac{\partial \boldsymbol{n}}{\partial \bar{\boldsymbol{\sigma}}^-}\frac{\partial \bar{\boldsymbol{\sigma}}^-}{\partial \Delta \lambda}\right) - \sqrt{\boldsymbol{n}^T\boldsymbol{T}\boldsymbol{n}} \tag{A.7}$$

$$\frac{\mathrm{d}F}{\mathrm{d}\Delta k} = \frac{\partial F}{\partial \boldsymbol{n}}\frac{\partial \boldsymbol{n}}{\partial \Delta k} + \frac{\partial F}{\partial \Delta k} = \frac{\partial F}{\partial \boldsymbol{n}}\left(\frac{\partial \boldsymbol{n}}{\partial \bar{\boldsymbol{\sigma}}^-}\frac{\partial \bar{\boldsymbol{\sigma}}^-}{\partial \Delta k} + \frac{\partial \boldsymbol{n}}{\partial \Delta k}\right) + 1 \tag{A.8}$$

While the expressions of the partial derivatives in Eqs. A.5 to A.8 are defined as follows:

$$\frac{\partial \bar{\boldsymbol{\sigma}}^-}{\partial \Delta \lambda} = \boldsymbol{A}^{-2}\left[\boldsymbol{P}\left(\boldsymbol{D}^{e^{-1}}\bar{\boldsymbol{\sigma}}^{e^-} - \Delta\lambda \boldsymbol{q}\right) + \boldsymbol{A}\boldsymbol{q}\right] \tag{A.9}$$

$$\frac{\partial \bar{\boldsymbol{\sigma}}^-}{\partial \Delta k} = -\Delta\lambda \boldsymbol{A}^{-1}\frac{\partial \boldsymbol{q}}{\partial \Delta k} \tag{A.10}$$

$$\frac{\partial \boldsymbol{q}}{\partial \Delta k} = h\begin{bmatrix} \chi_{10,0} & \chi_{11,0} & \chi_{12,0} & 0 & 0 & 0 \end{bmatrix}^T \tag{A.11}$$

$$\frac{\partial F}{\partial \boldsymbol{n}} = -\frac{\Delta\lambda}{\sqrt{\boldsymbol{n}^T\boldsymbol{T}\boldsymbol{n}}}\boldsymbol{n}^T\boldsymbol{T} \tag{A.12}$$

$$\frac{\partial \boldsymbol{n}}{\partial \bar{\boldsymbol{\sigma}}^-} = \boldsymbol{P} \tag{A.13}$$

$$\frac{\partial \boldsymbol{n}}{\partial \Delta k} = \frac{\partial \boldsymbol{q}}{\partial \Delta k} \tag{A.14}$$

Similarly, the other partial derivatives required for the calculation of the consistent elasto-plastic tangent stiffness matrix in Eq. 3.67 are:

$$\frac{\partial \bar{\boldsymbol{\sigma}}^-}{\partial \boldsymbol{\epsilon}^-} = \frac{\partial \bar{\boldsymbol{\sigma}}^-}{\partial \bar{\boldsymbol{\sigma}}^{e^-}}\frac{\partial \bar{\boldsymbol{\sigma}}^{e^-}}{\partial \boldsymbol{\epsilon}^-} = \boldsymbol{A}^{-1} \tag{A.15}$$

$$\frac{\partial f_p}{\partial \boldsymbol{\epsilon}^-} = \frac{\partial f_p}{\partial \bar{\boldsymbol{\sigma}}^-}\frac{\partial \bar{\boldsymbol{\sigma}}^-}{\partial \boldsymbol{\epsilon}^-} = \boldsymbol{n}^T\boldsymbol{A}^{-1} \tag{A.16}$$

$$\frac{\partial F}{\partial \boldsymbol{\epsilon}^-} = \frac{\partial F}{\partial \boldsymbol{n}}\frac{\partial \boldsymbol{n}}{\partial \bar{\boldsymbol{\sigma}}^-}\frac{\partial \bar{\boldsymbol{\sigma}}^-}{\partial \boldsymbol{\epsilon}^-} = -\frac{\Delta\lambda}{\sqrt{\boldsymbol{n}^T\boldsymbol{T}\boldsymbol{n}}}\boldsymbol{n}^T\boldsymbol{T}\boldsymbol{P}\boldsymbol{A}^{-1} \tag{A.17}$$

After convergence, all the derivatives in Eq. 3.67 employed for the calculation of the consistent elasto-plastic tangent stiffness matrix, D^{ep}, should be evaluated again for the given converged solution values.

APPENDIX A. DERIVATIVES OF THE JACOBIAN MATRIX OF THE PLASTICITY ALGORITHM